

Redox-engineered photosystems and tailor-made  
electron pathways for in vitro biocatalysis

Redox-manipulierte Photosysteme und  
maßgeschneiderte Elektronenwege für die in vitro  
Biokatalyse

Hitesh Kumar Reddy Medipally

## **Propositions**

1. Photosystem I was successfully applied in Biocatalysis.  
(this thesis)
2. Clickable photosystem I model was successfully created for cofactor regeneration. (this thesis)
3. Artificial intelligence adds more versatility to gene editing than nature itself.
4. Novelty and practical application should be weighed equally in science.
5. Climate change calls for sustainable choices in our daily lives.
6. The universe is one family, co-existing by sharing and bonding.
7. Civic sense should be taught as a mandatory subject.

Propositions belonging to the thesis, entitled

### **Redox-engineered photosystems and tailor-made electron transfer pathways for in vitro biocatalysis**

Hitesh Kumar Reddy Medipally

Bochum, 08 Feb 2024

## **Thesis committee**

### **Promotors**

Prof. Dr Marc Nowaczyk  
Professor, Department of Plant Biochemistry  
Ruhr University Bochum

Prof. Dr Willem J. H. van Berkel  
Emeritus Personal Chair at the Laboratory of Biochemistry  
Wageningen University & Research

### **Other members**

Prof. Dr Dirk Tischler, Ruhr University Bochum  
Prof. Dr Herbert van Amerongen, Wageningen University & Research  
Prof. Dr Franz Naberhaus, Ruhr University Bochum (Chair of the committee)  
Prof. Dr Frank Hollmann, Delft University of Technology  
Junior Prof. Dr Mirko Basen, University of Rostock

This research was conducted under the auspices of the International Graduate School Biosciences (IGB) at Ruhr-University Bochum, Germany, and the VLAG Graduate School (Biobased, Biomolecular, Chemical, Food and Nutrition Sciences), The Netherlands, and within the framework of the joint Ph.D. program PhotoBioCat (Light-driven sustainable biocatalysis training network).

# Redox-engineered photosystems and tailor-made electron pathways for in vitro biocatalysis

## Redox-manipulierte Photosysteme und maßgeschneiderte Elektronenwege für die in vitro Biokatalyse

Hitesh Kumar Reddy Medipally

### **Thesis**

submitted in fulfilment of the requirements for the joint degree of doctor  
between

**Ruhr University Bochum**

by the authority of the Rector Magnificus, Prof. Dr M. Paul,  
and

**Wageningen University**

by the authority of the Rector Magnificus, Prof. Dr A.P.J. Mol,  
in the presence of the

Thesis Committee appointed by the Academic Boards of both universities  
to be defended in public

on Thursday, 08 February 2024

at 02.00 p.m. in the lecture hall (ND 2/99) of Ruhr University Bochum



Hitesh Kumar Reddy Medipally

Redox-engineered photosystems and tailor-made electron transfer pathways for in vitro biocatalysis  
244 pages.

Joint PhD thesis, Ruhr-University Bochum, Bochum, Germany, and Wageningen University,  
Wageningen, the Netherlands (2024).

With references, with a summary in English and German.

DOI: <https://doi.org/10.18174/671930>

# Summary

Photosynthesis is a process in which light is converted into chemical energy and is a fundamental source of our planet's food needs. Applying photosynthetic organisms for the sustainable production of biohydrogen, commodity chemicals, and pharmaceuticals is a promising approach. This is due to the dependency of photosynthetic microorganisms on cheap and abundant resources like sunlight, water and CO<sub>2</sub>. In recent years, considerable interest has been developed in applying isolated components of the photosynthetic apparatus, such as using photosystems for building photovoltaic devices or modifying photosystems as photocatalytic modules for chemical production. In Chapter 2, the exciting aspects of applied photosynthesis were summarized, mainly focusing on describing the biotechnological application and strategies to improve and fine-tune photosynthesis toward biocatalysis or biohydrogen production (**Chapter 2, Medipally et al., 2021**).

In light of applied photosynthesis, significant attention has been drawn to mimicking photosynthesis in vitro. This is achieved by integrating photosynthetic membrane complexes with the conductive materials to develop biosolar devices. Especially photosystem I (PSI) is considered as a potential candidate for in vitro applications. This is due to the natural abundance, remarkable stability, and the highest light-induced charge separation activity of P700 (reaction-center chlorophyll a) with the potential of -1.3 V vs SHE. In this study, we explored the application of PSI as a photocatalyst in biocatalytic reactions. A PSI-ferredoxin-ferredoxin NADP<sup>+</sup> reductase (PSI-Fd-FNR) recycling system was established by artificial reconstitution of the photosynthetic electron transport chain in vitro (**Chapter 3, Medipally et al., 2023a**) for the regeneration of nicotinamide adenine dinucleotide phosphate hydride (NADPH). Upon light illumination, the NADPH production rate of the cascade at pH 7.5 was estimated to be 1.73 mM/h. Further, different NAD(P)H-dependent oxidoreductases: *Nicotiana tabacum* double bond reductase, *Lactobacillus bervis* alcohol dehydrogenase, *Actinorhadin* ketoreductase were coupled to the PSI-Fd-FNR NADPH recycling system to perform the asymmetric reduction of *trans*-cinnamaldehyde, *trans*-1-decalone, and acetophenone, respectively, reaching up to 99% conversion and retaining enantioselectivity.

Furthermore, to circumvent diffusion-dependent electron transfer and achieve molecular confinement between PSI, Fd, and FNR, a clickable PSI-Fd-FNR fusion system for light-driven NADPH regeneration was developed. For this, we first created a mutant in which immunity protein 7 (Im7) was fused to the C-terminus of the PsaE subunit of PSI in the cyanobacterium *Synechocystis* sp. PCC 6803. The biochemical characterization of the isolated Im7-PSI complex revealed that it is structurally and functionally similar to PSI-Wt. Next, colicin DNase E7 (E7) fusion chimeras of Fd and FNR with varying linker domains were constructed and prepared from recombinant *E. coli*. UV-VIS-absorption spectroscopy studies on E7-Fd and E7-Fd-FNR revealed the successful assembly of FeS and FAD units in E7-Fd and E7-Fd-FNR fusion proteins. Isolated Im7-PSI was then coupled with E7-Fd or E7-Fd-FNR constructs through high-affinity binding of the E7/Im7 protein pair. The bi- and tri-partite module variants were characterized based on the light-driven NADPH production rate.

All systems successfully produced NADPH, indicating the general applicability of the strategy (**Chapter 4, Medipally et al., 2023b**).

Ultimately, in Chapter 5, we demonstrate, using in vivo ultrafast transient absorption spectroscopy, that it is possible to extract electrons directly from photoexcited PSI and PSII, using both live cyanobacterial cells and isolated photosystems, with the exogenous electron mediator 2,6-dichloro-1,4-benzoquinone (DCBQ) (**Chapter 5, Baikie & Wey et al., 2023**). We postulate that DCBQ can oxidize peripheral chlorophyll pigments participating in highly delocalized charge transfer states after initial photoexcitation. These results open new avenues to study and re-wire photosynthesis for bioenergy and semi-artificial photosynthesis.

**Chapter 6** presents a general discussion on the topics of this thesis and a reflection on the future perspectives of in vitro photobiocatalysis.

In summary, this thesis asserts the importance of integrating PSI for in vitro biocatalysis or biosolar cell development by exploring the possibilities of tailored electron transfer pathways.

# Zusammenfassung

Die Photosynthese ist ein Prozess, bei dem Lichtenergie in chemische Energie umgewandelt wird und stellt damit eine grundlegende Quelle für den Nahrungsbedarf unseres Planeten dar. Der Einsatz photosynthetischer (Mikro-)Organismen ist ein vielversprechender Ansatz zur nachhaltigen Erzeugung von Biowasserstoff, chemischen Grundstoffen sowie Pharmazeutika, da sie lediglich auf kostengünstige und reichlich vorhandene Ressourcen wie Sonnenlicht, Wasser und CO<sub>2</sub> angewiesen sind. In den letzten Jahren hat sich ein erhebliches Interesse an der Anwendung isolierter Komponenten des Photosyntheseapparates entwickelt, wie z. B. der Einsatz von Photosystemen in photovoltaischen Geräten oder die Modifizierung von Photosystemen als photokatalytische Module für die Wasserstoffproduktion. Der erste Teil dieser Arbeit umfasst Aspekte der angewandten Photosynthese mit Fokus auf biotechnologische Anwendung sowie Strategien zur Verbesserung und Feinabstimmung der Photosynthese für die Biokatalyse oder Biowasserstoffproduktion (**Kapitel 2, Medipally et al., 2021**).

Angewandte Photosynthese zielt darauf ab, die natürliche Photosynthese in einer kontrollierten Umgebung in vitro nachzuahmen. Dabei kommen isolierte, photosynthetische Membranproteinkomplexe zum Einsatz, um sogenannte biosolare Systeme zu konstruieren. Insbesondere das Photosystem I (PSI) gilt als potenzieller Kandidat für in vitro Anwendungen. Gründe hierfür sind sein abundantes Vorkommen in der Natur, die bemerkenswerte Stabilität und die hohe lichtinduzierte Ladungstrennungsaktivität von PSI-Reaktionszentren mit einem Potential von -1,3 V gegenüber der Standardwasserstoffelektrode. Im zweiten Teil dieser Arbeit steht die Anwendung von PSI als Photokatalysator in biokatalytischen Reaktionen im Vordergrund: Durch künstliche Rekonstitution der photosynthetischen Elektronentransportkette wurde ein PSI-Ferredoxin-Ferredoxin NADP<sup>+</sup> Reduktase (PSI-Fd-FNR)-Recyclingsystem zur Regeneration von Nicotinamadenindinukleotidphosphat (NADPH) aufgebaut (**Kapitel 3, Medipally et al., 2023a**). Der finale Elektronendonator hierbei ist Natriumascorbat, und der finale Elektronenakzeptor ist NADP<sup>+</sup>. Die NADPH-Produktionsrate dieser Kaskade bei pH 7,5 unter Lichteinwirkung wurde dabei auf 1,73 mM/h geschätzt und mit anderen bekannten enzymatischen NADPH-Recycling-Systemen auf der Grundlage ihrer Umsatzhäufigkeit verglichen. Darüber hinaus wurden verschiedene NAD(P)H-abhängige Oxidoreduktasen untersucht: Die *Nicotiana tabacum* Doppelbindungsreduktase, die *Lactobacillus brevis* Alkoholdehydrogenase sowie die *Actinorhodin* Ketoreduktase wurden mit dem PSI-Fd-FNR-NADPH-Recyclingsystem gekoppelt, um die asymmetrische Reduktion von trans-Zimtaldehyd, trans-1-Decalon bzw. Acetophenon durchzuführen, wobei bis zu 99 % Umwandlung bei vollständiger Enantioselektivität erzielt wurden.

Um den diffusionsabhängigen Elektronentransport zu umgehen und einen molekularen Einschluss zwischen PSI, Fd und FNR zu erreichen, wurde im Rahmen dieser Arbeit ein chemisch „klickbares“ PSI-Fd-FNR-Fusionssystem für die lichtgesteuerte NADPH-Regeneration entwickelt. Dazu wurde zunächst eine Mutante erzeugt, bei der das Immunprotein 7 (Im7) mit dem C-Terminus der PsaE-Untereinheit des PSI im

Cyanobakterium *Synechocystis* sp. PCC 6803 fusioniert worden ist. Die biochemische Charakterisierung des isolierten Im7-PSI-Komplexes ergab, dass dieser strukturell und physiologisch dem Wildtyp-PSI-Komplex ähnelt. Anschließend wurden Colicin-DNase-E7 (E7)-Fusionschimären aus Fd und FNR mit unterschiedlichen Linkerdomänen in *E. coli* hergestellt. UV-Absorptionsspektroskopische Untersuchungen an E7-Fd und E7-Fd-FNR zeigten die erfolgreiche Integration der Eisen-Schwefel und Flavin-Adenin-Dinukleotid-Kofaktoren in die Fusionsproteine E7-Fd und E7-Fd-FNR. Isoliertes Im7-PSI wurde dann durch hochaffine Bindung des E7/Im7-Proteinpaares mit den Fusionsproteinen E7-Fd oder E7-Fd-FNR gekoppelt. Die zwei- und dreigliedrigen Modulvarianten wurden charakterisiert und hinsichtlich ihrer photoinduzierten NADPH-Produktionsraten hin untersucht. Dabei konnte gezeigt werden, dass sowohl die zwei- als auch die dreigliedrigen Systeme unter Lichteinwirkung erfolgreich NADPH produzieren, was auf die Funktionalität und Anwendbarkeit der Strategie hinweist (**Kapitel 4, Medipally et al., 2023b**).

Abschließend konnte mit Hilfe ultraschneller transientser Absorptionsspektroskopie in vivo gezeigt werden, dass es möglich ist, Elektronen direkt aus photoangeregtem PSI bzw. PSII zu extrahieren. Dies war sowohl in lebenden Cyanobakterienzellen als auch mit isolierten Photosystemen mit dem exogenen Elektronenmediator 2,6-Dichlor-1,4-benzochinon (DCBQ) möglich (**Kapitel 5, Baikie & Wey et al., 2023**). Die Ergebnisse dieser Arbeit legen nahe, dass DCBQ periphere Chlorophyllpigmente oxidieren kann, die nach der initialen Photoanregung an hoch delokalisierten Ladungstransferzuständen beteiligt sind. Diese Ergebnisse eröffnen neue Wege für die Erforschung und Neukonzeption der Photosynthese für die Gewinnung von Bioenergie und für den Einsatz in semi-artifiziellen Systemen.

**Kapitel 6** enthält eine allgemeine Diskussion über die Themen dieser Arbeit und Überlegungen zu den künftigen Perspektiven der in vitro Photobiokatalyse.

Zusammengefasst zeigt diese Arbeit verschiedene Möglichkeiten maßgeschneiderter Elektronentransferpfade auf und verdeutlicht damit die Bedeutung von PSI und seine Anwendung für die in vitro Biokatalyse sowie für die Entwicklung von Biosolarzellen.

# List of abbreviations

Actinorodin ketoreductase	<i>Act</i> KR
Adenosine triphosphate	ATP
Adenosine monophosphate	AMP
Alcohol dehydrogenase	ADH
Baeyer-Villiger monooxygenase	BVMO
Biophotovoltaics	BPV
<i>Candida parapsilosis</i> alcohol dehydrogenase	<i>Cp</i> ADH
Cytochrome <i>b<sub>6</sub>f</i> complex	Cyt <i>b<sub>6</sub>f</i>
Cytochrome <i>c<sub>6</sub></i>	Cyt <i>c<sub>6</sub></i>
Cytochrome P450 monooxygenase	CYP124
Dichlorophenolindophenol	DCPIP
Dichlorobenzoquinone	DCBQ
3-(3,4-Dichlorophenyl)-1,1-dimethylurea	DCMU
Dissociation constant	$K_d$
Ferredoxin	Fd
Ferredoxin oxidized	Fd <sub>ox</sub>
Ferredoxin reduced	Fd <sub>red</sub>
Ferredoxin NADP <sup>+</sup> oxidoreductase	FNR
Ferredoxin NADP <sup>+</sup> oxidoreductase oxidized	FNR <sub>ox</sub>
Ferredoxin NADP <sup>+</sup> oxidoreductase reduced	FNR <sub>red</sub>
Flavodoxin	Fld
Flavodiiron protein	Flv
Flavin adenine dinucleotide	FAD
Formate dehydrogenase	FDH
Fullerene	C <sub>60</sub>
Glucose dehydrogenase	GDH
Glucose 6-phosphate dehydrogenase	G6PDH
Glucose tolerant	GT
Horse liver alcohol dehydrogenase	HLADH
Hydrogenase	Hyd
Imine reductase	IRED
Isothermal titration calorimetry	ITC
<i>Lactobacillus bervis</i> alcohol dehydrogenase	<i>Lb</i> ADH
<i>Lactobacillus kefir</i> alcohol dehydrogenase	<i>Lk</i> ADH
Light harvesting complex I	LHCI
Light harvesting complex II	LHCII
Methyl viologen	MV
<i>N, N, N, N'</i> -tetramethyl- <i>p</i> -phenylenediamine	TMPD
Dihyronicotinamide adenine dinucleotide	NADH
NADH dehydrogenase complex	NDH
Dihyronicotinamide adenine dinucleotide phosphate	NADPH
Nicotinamide adenine dinucleotide	NAD <sup>+</sup>
Nicotinamide adenine dinucleotide phosphate	NADP <sup>+</sup>
<i>Nicotiana tabacum</i> double bond reductase	<i>Nt</i> DBR
Oxygen-evolving complex	OEC
Phosphite dehydrogenase	PTDH
Photosystem I	PSI
Photosystem II	PSII

Photosystem I primary electron donor	P700
Phylloquinone	A <sub>1</sub>
Plastoquinone	PQ
Proton gradient regulation-like protein	PGRL
Phycocyanin	PC
Quinone	Q <sub>A</sub> and Q <sub>B</sub>
Sodium ascorbate	NaAsc
Single-walled carbon nanotubes	SWCNTs
Thylakoid rhodanese-like protein	TROL
Titanium dioxide	TiO <sub>2</sub>
Translocon on the inner chloroplast membrane protein 62	TIC62
Tyrosine	Y <sub>z</sub>
Ene reductase from <i>Bacillus subtilis</i>	YqjM
Zinc oxide	ZnO

## Table of Content

<b>Summary.....</b>	<b>iii</b>
<b>Zusammenfassung .....</b>	<b>v</b>
<b>List of abbreviations.....</b>	<b>vii</b>
<b>Chapter 1: General Introduction.....</b>	<b>1</b>
<b>1.1 Applications and challenges of biotransformation .....</b>	<b>2</b>
<b>1.2 Cofactor regeneration systems .....</b>	<b>3</b>
<b>1.3 Application of cyanobacteria for biotransformations .....</b>	<b>6</b>
1.3.1 <i>Synechocystis</i> : A model organism.....	6
1.3.2 Application of cyanobacterial whole cells for biotransformations.....	7
1.3.3 Application of PSI in biocatalysis .....	11
<b>1.4 Photosynthetic electron transport .....</b>	<b>14</b>
1.4.1 Photosystem I structure and function.....	15
1.4.2 Ferredoxin structure and function.....	19
1.4.3 Ferredoxin NADP <sup>+</sup> oxidoreductase structure and function.....	21
<b>1.5 Enzyme fusion-A typical way for diffusion independent electron transfer .....</b>	<b>24</b>
1.5.1 Engineering PSI for molecular confinement .....	26
<b>1.6 A novel colicin-based PSI fusion for NADPH regeneration.....</b>	<b>32</b>
<b>1.7 Objectives of the thesis .....</b>	<b>34</b>
<b>1.8 References .....</b>	<b>35</b>
<b>Chapter 2: Parameters of photosynthesis relevant for a biotechnological application...</b>	<b>40</b>
<b>Chapter 3: Light-driven NADPH cofactor recycling by photosystem I for biocatalytic reactions.....</b>	<b>73</b>
<b>Chapter 4: A clickable photosystem I, ferredoxin, and ferredoxin NADP<sup>+</sup> reductase Fusion system for light-driven NADPH regeneration .....</b>	<b>99</b>
<b>Chapter 5: Photosynthesis re-wired on the pico-second timescale .....</b>	<b>138</b>
<b>Chapter 6: Discussion.....</b>	<b>202</b>
6.1 Functional and structural significance of PSI in biocatalysis .....	203
6.2 PSI-based light-driven biocatalysis .....	203



6.3 Upscaling of PSI-Fd-FNR biocascade .....	205
6.4 Clickable PSI: A plug-and-play approach .....	211
6.5 Capturing electrons from whole-cells.....	213
6.6 Clickable PSI-based rational electron partitioning for efficient chemical production in Cyanobacteria.....	215
6.7 References .....	218
<b>Publications.....</b>	<b>221</b>
<b>Published research articles.....</b>	<b>222</b>
<b>Conference contributions .....</b>	<b>223</b>
<b>Contribution to the publications .....</b>	<b>224</b>

Appendix

Acknowledgment

Curriculum vitae

Erklärung

# Chapter 1: General Introduction

### 1.1 Applications and challenges of biotransformation

Increased concern for the environment has led to the development of biotechnological processes for the production of fuels and commodity chemicals as sustainable alternatives. <sup>[1]</sup> The production of chemicals using conventional chemistry is often high yielding but requires harsh reaction conditions and produces unwanted byproducts that increase downstream costs. Less hazardous chemical synthesis and atom economy are the two fundamental principles of green chemistry that emphasize the need for sustainable chemical processes with high atom efficiency. <sup>[2]</sup> In general, the production of chemicals by biotechnological processes can be divided into two categories: fermentation and biotransformation. In fermentation processes, microbial systems are employed in conversion of the carbon source or growth substances into the final product. <sup>[3]</sup> Fermentation is widely used in the production of secondary metabolites like antibiotics and vitamins. <sup>[4,5]</sup> Improvements in strain development and fermentation technology for controlling the growth conditions (e.g. pH, nutrients and pressure) have optimized the production rates of heterotrophic systems. <sup>[6-8]</sup>

Catalysis of chemical reactions using biological resources like enzymes or whole cells is defined as biocatalysis or biotransformation. <sup>[9]</sup> In whole cell biotransformation reactions, a specific substrate is converted into a product by one enzyme or a multi-enzyme cascade while the supplemented carbon source is mainly involved in cell growth. In recent years, biocatalysis has developed into an environmentally friendly method to produce a vast variety of chemicals, ranging from commodity chemicals to pharmaceuticals. Thanks to a huge improvement in genetic engineering and sequencing tools, many different enzymes can now be obtained from all kinds of organisms by cloning and overexpression in microbial cell factories. Biocatalysis is successfully used in producing pharmaceutical products at a commercial scale, either the drug itself or the pharmaceutical intermediate. <sup>[9]</sup> For example:  $\beta$ -hydroxy-*n*-butyric acid, and 11 $\alpha$ -hydroxyprogesterone produced by biotransformation are used in the production of captopril, carbapenem, and cortisone drugs, respectively. <sup>[10]</sup> Genetically engineered microorganisms are also used to produce 2-carboxylic acid <sup>[11]</sup> and L-carnitine. <sup>[12]</sup> Hence, biocatalysis can be a potential complementary tool in organic synthesis for various chemical synthesis processes. <sup>[9,13]</sup> However, the major obstacle to commercial application is the high production cost, this is due to low time-space yield of the reaction, substrate toxicity, product inhibition of the enzyme(s), enzyme instability, byproduct formation, and product separation (workup) and dependency on expensive cofactors. Most of these problems can be addressed by genetic

engineering of an enzyme or by reaction engineering.<sup>[14]</sup> Especially, the dependency of enzymes on expensive cofactors, including oxidoreductases can be addressed by establishing a continuous cofactor regeneration system.<sup>[14]</sup>

### 1.2 Cofactor regeneration systems

Oxidoreductases are an interesting enzyme class with a wide range of applications in chemical synthesis, mainly due to their stereo-, regio- and enantioselectivity. Oxidoreductases catalyze the reduction or oxidation of a chemical compound by simultaneously oxidizing or reducing another compound. Many oxidoreductases depend on coenzymes like NAD(P)H as reductant source. In nature, nicotinamide adenine dinucleotide (NAD<sup>+</sup>) is synthesized by salvage or de-novo pathways<sup>[15]</sup> and later converted based on the metabolic need to nicotinamide adenine dinucleotide phosphate (NADP<sup>+</sup>) by NAD<sup>+</sup> kinase.<sup>[16]</sup> This enzyme introduces the extra phosphate group at the C-2 position of the ribose ring (**Figure 1**).<sup>[17][18]</sup> In heterotrophic organisms, dihydronicotinamide adenine dinucleotide hydride (NADH) is recycled by the Krebs cycle while dihydronicotinamide adenine dinucleotide phosphate hydride (NADPH) is recycled by the pentose phosphate pathway, the Entner-Doudoroff pathway, and the isocitrate dehydrogenase catalyzed step of the Krebs cycle.<sup>[19]</sup> Biotransformation performed via heterologous recombinant expression of oxidoreductases requires a continuous supply of NAD(P)H. Depending on the reaction, dehydrogenases use NAD<sup>+</sup> or NADP<sup>+</sup>, some reductases, and monooxygenases utilize NADH or NADPH and some accept both cofactors equally. Addition of NAD(P)H in stoichiometric amounts equivalent to the substrate concentration of the reaction is not economically feasible. This is due to the high cost of NAD<sup>+</sup>/NADH and especially NADP<sup>+</sup>/NADPH, being 663/1270 and 621/1808 € per mmol, respectively.<sup>[20]</sup> However, the price may differ based on the quality and market situation. In recent years, several NAD(P)H regeneration strategies were proposed based on the following methodologies: 1) enzymatic regeneration, 2) chemical regeneration, 3) metal-based catalytic regeneration, 4) electrochemical regeneration, 5) photocatalytic regeneration, 6) heterogeneous catalytic regeneration. Enzymatic NAD(P)H regeneration is the only industrially applied method because of the use of mild reaction conditions and high specific activity.<sup>[21]</sup> The enzymatic regeneration approach can be divided into the coupled-substrate approach and the coupled-enzyme approach. In the coupled-substrate approach, one single enzyme catalyzes both cofactor regeneration and substrate conversion.<sup>[21]</sup> An example is the synthesis of commodity chemical (2S-5S)-hexanediol using alcohol dehydrogenase (ADH) (**Figure 2A**).<sup>[22]</sup> This approach is mainly reported for ADH and may not be applicable to other cofactor regenerating enzymes. In

## Chapter 1

the coupled-enzyme approach, the NAD(P)H-dependent enzyme relies on cofactor regenerating enzymes. An example is GDH, which uses glucose as a hydride donor (**Figure 2B**). The most widely reported NAD(P)H regenerating enzymes are formate dehydrogenase (FDH), glucose dehydrogenase (GDH), glucose 6-phosphate dehydrogenase (G6PDH), phosphite dehydrogenase (PTDH) and hydrogenase (Hyd).<sup>[21]</sup> FDH reduces  $\text{NAD(P)}^+$  to NAD(P)H, using formate as a sacrificial substrate. In this process, gaseous  $\text{CO}_2$  is formed as a byproduct, which is easily separated from the reaction medium, thus pushing the reaction equilibrium forward to reduce  $\text{NAD(P)}^+$  with the least possibility of the reverse reaction.<sup>[23]</sup> Interestingly, FDH is commercially used to produce L-methionine by Degussa Company.<sup>[23]</sup> In case of GDH, which uses glucose as a sacrificial substrate and produce a side product, gluconic acid, as a result, the downstream process for separation of the byproduct is less easy. On the other hand, GDH is reported to have a high NADH reduction capacity of  $550 \text{ U mg}^{-1}$ .<sup>[24]</sup> In case of G6PDH, expensive glucose-6-phosphate is used as a sacrificial substrate to produce NADPH, in this process 6-phospho-gluconic acid is formed as a byproduct and this reaction is also atom inefficient. Thus, expensive sacrificial substrate and tedious downstream processing for easy product workup remain major obstacles in large scale application of G6PDH. However, the NADPH reduction capacity of G6PDH is  $2890 \text{ U mg}^{-1}$ <sup>[25]</sup>, which is very high compared to other cofactor regenerating enzymes. In case of PTDH, phosphite is used as a sacrificial substrate to produce NADPH. The byproduct phosphate can act as a buffering module in the reaction or can be easily removed by calcium precipitation. Though the workup of the reaction of PDH is rather easy, the specific activity of PTDH is quite low.<sup>[26,27]</sup> In case of Hyd, hydrogen is used as a sacrificial substrate to produce NADPH. Here also, the downstream process is inexpensive, but the specific activity of Hyd is very low.<sup>[28]</sup> In the above-mentioned enzymatic reactions, except for those with Hyd and PTDH, all the approaches are atom inefficient, i.e., most substrate atoms are involved in byproduct formation. Alternatively, photosynthetic organisms regenerate NADPH by obtaining electrons from water oxidation. In doing so, the byproduct formed is just protons, thus making this process atom efficient. In recent years, considerable interest was drawn in using photosynthetic organisms like cyanobacteria as a host for oxidoreductases based biotransformations.

## Chapter 1

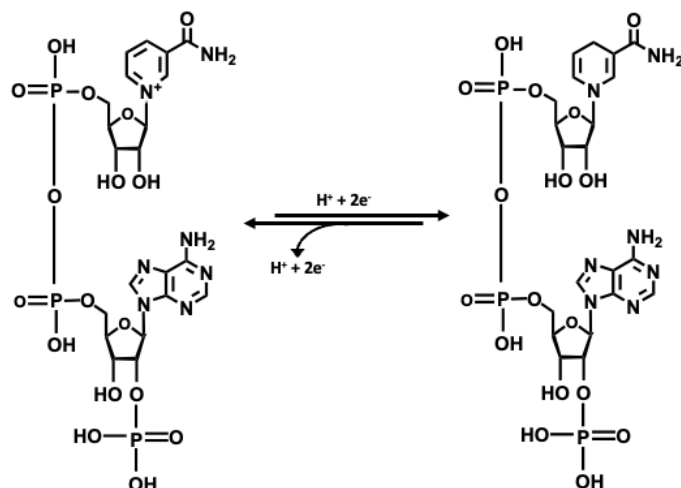


**Figure 1: Structural representation of reduction of NADP<sup>+</sup> to NADPH.** <sup>[21] [17]</sup>

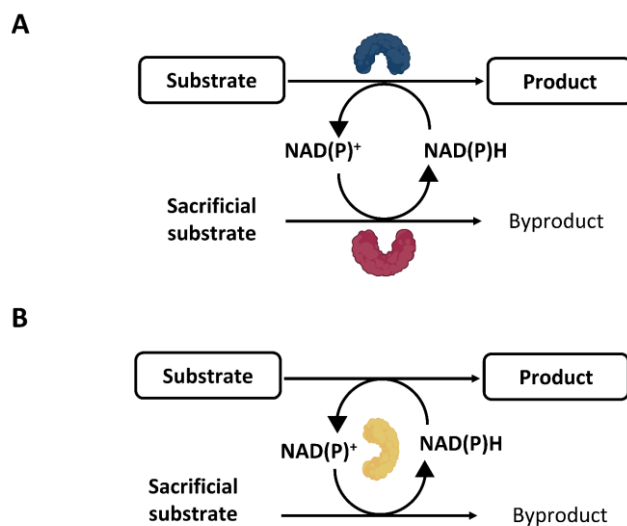


**Figure 2: Schematic representation of enzymatic NAD(P)H recycling systems.** A) Coupled-enzyme approach: In this system, NAD(P)H-dependent oxidoreductases (blue) are hinged on other NAD(P)H regenerating enzymes (red) and ultimate electron donors. B) Coupled-substrate approach: In this system, only one enzyme (yellow) catalyzes the formation of NAD(P)H and converts the substrate of interest to the product. This scheme is adapted from previous literature. <sup>[21]</sup>

**Table 1: Various enzymatic recycling systems**

Type	Substrate	Byproduct	Specificity	Literature
GDH	D-Glucose	D-glucono-1,5-lactone	NAD(P) <sup>+</sup>	[29]
G6DH	Glucose-6-phosphate	6-phosphogluconate	NAD(P) <sup>+</sup>	[30]
ADH	2-Propanol	Acetone	NAD(P) <sup>+</sup>	[31]
FDH	Formate	Carbon dioxide	NAD(P) <sup>+</sup>	[32]
PTDH	Phosphite	Phosphate	NAD(P) <sup>+</sup>	[26]
Hyd	Hydrogen	Protons	NAD(P) <sup>+</sup>	[28]

## 1.3 Application of cyanobacteria for biotransformations

### 1.3.1 *Synechocystis*: A model organism

Here we described one of the most studied cyanobacteria: *Synechocystis* sp., which is a unicellular, non-nitrogen fixing cyanobacterium. *Synechocystis* sp. has been extensively used as a host for various biotransformation reactions and for various physiological aspects of photosynthesis. This is because of its natural transformation ability and its capacity to grow heterotrophically on glucose as a carbon source. There are several substrains of *Synechocystis* sp., for example, ATCC, glucose tolerant (GT), and Kazusa. However, all these strains are derived from Berkley strain 6803, which was isolated from freshwater in California. <sup>[33,34]</sup> Subculturing and growing in laboratory conditions introduced mutations in these strains, and subtle phenotypic differences were observed. PCC and Berkeley are motile while GT and Kazusa are non-motile. <sup>[34]</sup> PCC and ATCC are glucose sensitive, whereas GT was unintentionally generated. <sup>[35]</sup> In fact, some laboratories reported that even under controlled conditions strain GT became glucose intolerant, indicating that the critical phenotypic assessment needs to be checked regularly. <sup>[35]</sup> Interestingly, *Synechocystis* sp. PCC 6803 was also the first phototrophic organism to be fully sequenced. In *Synechocystis* sp. PCC 6803, 3167 constituent genes and their relative map positions were revealed by genome sequencing. <sup>[35]</sup> For about fifty percent of these genes and their functions were revealed by a similarity search. This enabled the establishment of two gene databases, Cyanobase and Cyanomutant, which were used as dynamic tools in studying photosynthetic organisms. <sup>[35]</sup>

### 1.3.2 Application of cyanobacterial whole cells for biotransformation

In recent years cyanobacteria have been extensively modified to host oxidoreductases for biotransformations.<sup>[3,36–40]</sup> NADPH regeneration in cyanobacteria is mainly dependent on the photosynthetic electron transport chain. The ultimate source of electrons for photosynthetic electron transport is the water splitting activity of photosystem II (PSII), making the process atom efficient. The dependency of cyanobacteria on other abundant and cheap resources like light and CO<sub>2</sub> for growth makes these photoautotrophic prokaryotes attractive candidates for biotransformations. Increasingly available methods for genetic manipulation and critical understanding of their physiology have unleashed potential of application of cyanobacteria in biotransformations. Intensive research is being performed to address various issues of whole cell biotransformation with cyanobacteria: increasing the intracellular concentration of enzymes of interest, increasing the photosynthetic efficiency and the design and development of photobioreactors for specific reactions.<sup>[3]</sup> Especially, *Synechococcus elongatus* sp. PCC 7942 (*Synechococcus* sp.) and *Synechocystis* sp. PCC 6803 (*Synechocystis* sp.) are extensively studied in respect to whole cell biotransformations.<sup>[3,40] [41]</sup>

It was reported that *Synechococcus* sp. selectively reduces various aryl methyl ketones with different electron withdrawing moieties like halogens and methoxides to the corresponding (*S*)-alcohols.<sup>[3]</sup> Pentafluoroacetophenone (**1a**) was converted to (*S*)-pentafluoro(phenyl)ethanol (**1b**) with 82 % conversion in 48 h and with 99 % enantioselectivity.<sup>[42]</sup> In addition, *Synechococcus* sp. was observed to convert (+)- and (-) camphorquinone (**2a**) to (-) -(3*S*)-*exo*-hydroxycamphor (**2b**) with 86 % conversion in 48 h.<sup>[43]</sup> The alcohol production in *Synechococcus* sp. was attributed to the action of a NADPH-dependent ADH. Furthermore, *Synechococcus* sp. was observed to contain ene-reductase activity, thereby reducing cyclic enones like 2-methyl-cyclopenten-1-one and (*R*)- and (*S*)-carvones, as well as  $\alpha,\beta$ -unsaturated aldehydes.<sup>[44]</sup> *Synechococcus* sp. was also capable of oxyfunctionalization thereby converting (*S*)-limonene (**3a**) to *cis*-carveol (**3b**) and *trans*-carveol (**3c**) with 28-32% and 7-9% yield (**Figure 3**).<sup>[45]</sup> Significant improvements in product formation yields were achieved by expressing foreign genes within cyanobacteria (**Figure 4**). Königer et al. expressed an ene-reductase from *Bacillus subtilis* (YqjM) in *Synechocystis* sp. by homologous recombination of the YqjM gene at gene locus *slr0168* of *Synechocystis* sp. This flavin-dependent ene-reductase



## Chapter 1

is known to catalyze the *trans*-hydrogenation of C=C double bonds. Recombinant YqjM *Synechocystis* sp. reduced N-methylmaleimide (**4a**) to N-methylsuccinimide (**4b**) with  $1.8 \text{ g}_{\text{cdw}}^{-1}$ .<sup>[39]</sup>

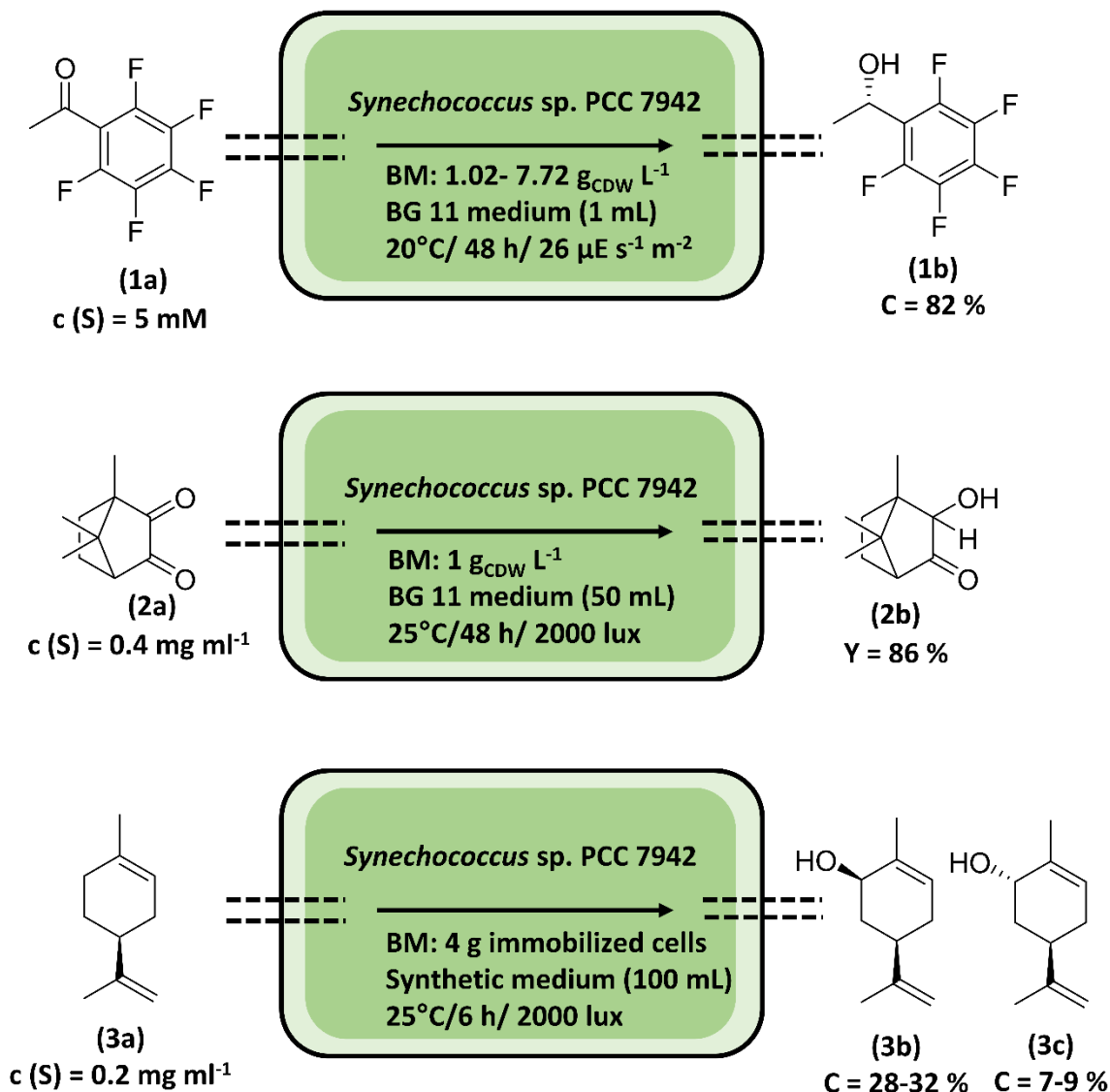


**Figure 3:** Whole cell-based biotransformation with *Synechococcus* sp. PCC 7942 via reduction of various compounds.<sup>[3,40,42,44,45]</sup> c: concentration, C: conversion, Y: Yield.

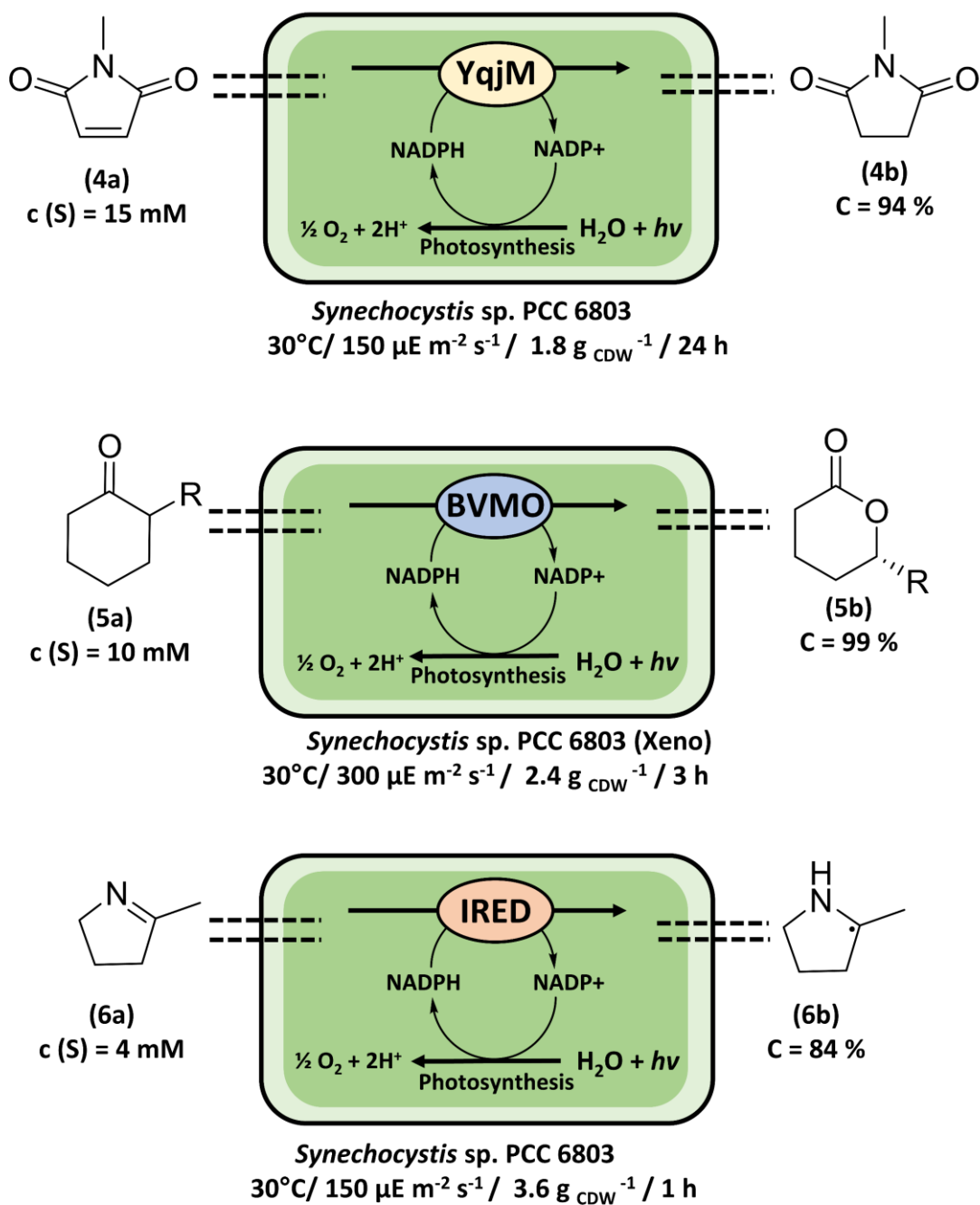


**Figure 4:** Whole cell-based biotransformation with genetically modified *Synechocystis* sp. PCC 6803 containing heterologously expressed reductases like YqjM<sup>[39]</sup>, BVMO<sup>[37]</sup>, IRED<sup>[36]</sup>. c: concentration, C: conversion.

## Chapter 1

YqjM requires continuous supply of NADPH, which was generated by the photosynthetic electron transport chain. Initially, the specific activity of YqjM expressed in *Synechocystis* sp. for conversion of N-methylmaleimide to N-methylsuccinimide was 53 U g<sub>CDW</sub><sup>-1</sup>.<sup>[39]</sup> However, deletion of the alternative electron sink sources such as Flavodiiron protein 1 (Flv1), which is involved in protection mechanisms, boosted the NADPH production by diverting the high energy electrons produced by light-excited photosystem I (PSI) to ferredoxin NADP<sup>+</sup> oxidoreductase (FNR) via ferredoxin (Fd). In the Flv1 deletion mutants of YqjM *Synechocystis* sp. the specific activity of the conversion of N-methylmaleimide into N-methylsuccinimide was reported to be 107.1 U g<sub>CDW</sub><sup>-1</sup>, indicating an increase in activity to ~50%.<sup>[38]</sup> NADPH production by linear photosynthetic electron transport chain was also coupled with other recombinant enzymes expressed in *Synechocystis* sp. like Baeyer-Villiger monooxygenase (BVMO) for oxyfunctionalization of cyclohexanone (**5a**) to  $\epsilon$ -caprolactone (**5b**) with 99% conversion within 3 h<sup>[37]</sup> and imine reductase (IRED) for imine reduction of 2-methylpyrroline (**6a**) to 2-methylpyrrolidine (**6b**) with 84% conversion within 1 h.<sup>[36]</sup>

Recently, ADH overexpressed *Synechocystis* sp. was used in a photo-electron shuttle system. In this method, a multi-enzyme reaction takes place in three modules (**Figure 5**). In module I, ADH overexpressed *Synechocystis* sp. reduces ketones to alcohols by using NADPH generated from the photosynthetic electron transport chain. The produced alcohol from module I is exported out of the cell and converted back into ketone in module II with external ADH by reducing NADP<sup>+</sup> to NADPH. Lastly, in module III, NADPH produced in module II is oxidized by coupled oxidoreductase for conversion of substrate to product. In this system, various NADPH-dependent redox enzymes were used in module III, yielding up to 99% conversion.<sup>[46]</sup> By this method, mass transfer limitation of certain substrates and toxicity can be reduced, and multiple oxidoreductases in combination with cyanobacteria can be used without genetic modification.

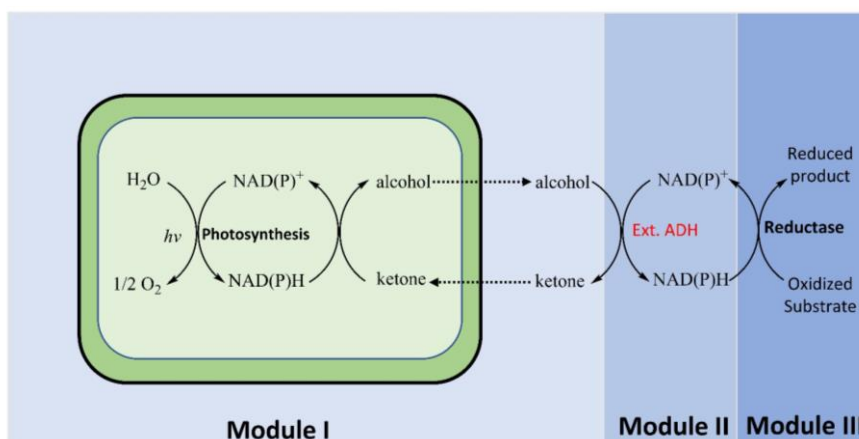


**Figure 5: NADPH regeneration using cyanobacteria.** **Module I:** Photosynthetically produced NADPH via water oxidation is supplied to internal (Int.) ADH to reduce ketone to alcohol and produced alcohol is exported out of the cell. **Module II:** The exported alcohol is converted to ketone by external (Ext.) ADH, simultaneously reducing  $\text{NADP}^+$  to NADPH. **Module III:** The produced NADPH in module II is coupled to a reductase. <sup>[46]</sup>

### 1.3.3 Application of PSI in biocatalysis

In contrast to conventional cyanobacteria based whole cell biotransformations, the use of isolated PSI from the photosynthetic apparatus for driving photobiocatalytic reactions is also becoming prominent. <sup>[47–49]</sup> In these cascade reactions, sodium ascorbate (NaAsc) was used as an ultimate electron donor. Upon light illumination, excited PSI reduces Fd. Jenssen et al. combined this system with cytochrome P450 monooxygenase (CYP124). <sup>[48]</sup> In this reaction, CYP124 catalyzes the hydroxylation of cholest-4-en-3-one with a rate of 3 nmol/min. In another study conducted by Ihara et al., PSI was coupled to FNR via Fd for NADPH production. The produced NADPH was supplied to FDH from *Pseudomonas* sp. (*Ps*FDH) for conversion of  $\text{CO}_2$  into formate, yielding 30  $\mu\text{M}$  of formate after 3 h reaction. <sup>[50]</sup> Several studies have reported  $\alpha$  the integration of PSI on electrode surfaces and the delivery of light-induced high energy electrons from PSI to hydrogenase to produce hydrogen gas. <sup>[51–53]</sup> In this PhD thesis, for the regeneration of NADPH, a photosynthetic electron transport chain was artificially reconstituted using PSI, Fd, and FNR with NaAsc as ultimate electron donor and  $\text{NADP}^+$  as terminal electron acceptor. Next, the produced NADPH was supplied to different NADPH-dependent oxidoreductases (**Figure 6**).

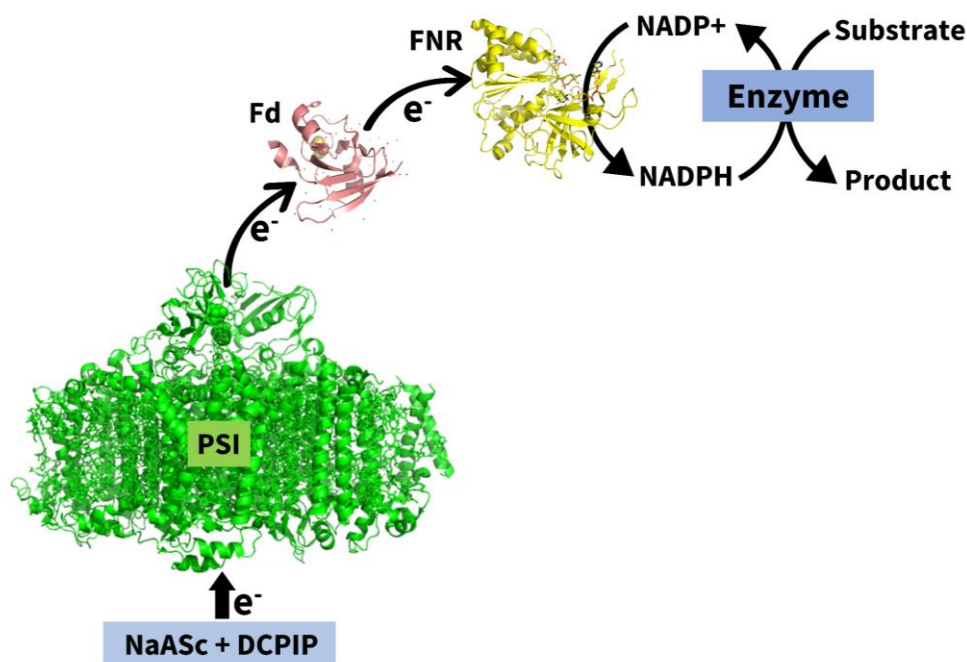


**Figure 6: Artificially reconstituted photosynthetic electron transport chain for NADPH recycling.** In this cascade system, sodium ascorbate (NaAsc) is an ultimate electron donor and nicotinamide adenine dinucleotide phosphate (NADP<sup>+</sup>) is an ultimate electron acceptor.

In conventional organic chemistry, carbonyl reduction is achieved by the usage of strong chemical reducing agents such as lithium aluminium hydride and alkoxy borohydrides.<sup>[54]</sup> These reactions also use organic solvents, which makes them unsustainable. Alternatively, ADHs (EC 1.1.1.x) are typically employed for the asymmetric reduction of ketones to obtain enantiopure alcohols.<sup>[55,56]</sup> The stereochemistry of the product produced with ADH is according to Prelog and anti-Prelog rules. In an ADH catalyzed reduction reaction, four stereochemical hydride transfer pathways are possible. If the hydride is transferred to the *si*-face of the ketone, (*R*)-alcohols are formed, and if the hydride is transferred to the *re*-face of the ketone, (*S*)-alcohols are formed (**Figure 7**). The transferred hydride stems from the *re*- or *si*-face of the nicotinamide cofactor. Depending on the need, different sets of ADHs are available for either (*S*)- or (*R*)-enantioselectivity.<sup>[57]</sup> Horse liver alcohol dehydrogenase (*HLADH*) and *TbADH* are Prelog ADHs, whereas *Lactobacillus kefir* alcohol dehydrogenase (*LkADH*), *Lactobacillus bervis* alcohol dehydrogenase (*LbADH*) and *Candida parapsilosis* alcohol dehydrogenase (*CpADH*) are anti-Prelog ADHs.<sup>[58]</sup> In this study, a *Lactobacillus bervis* alcohol dehydrogenase (*LbADH*) for reduction of acetophenone to phenylethanol was used. However, *LbADH* has very broad substrate scope including among others  $\alpha$ -ketoesters,  $\beta$ -ketoesters<sup>[59]</sup> and diketones.<sup>[60]</sup> Interestingly, *LbADH* is employed for the industrial synthesis of ethyl-3*R*-hydroxybutanoate at a scale of one ton per year. In this enzyme-coupled approach (see above),

## Chapter 1

propanol was used as a reducing agent.<sup>[61]</sup> Furthermore, *Lb*ADH was also coupled with NAD(P)H regenerating enzymes like FDH and GDH for the synthesis of 4-chloroacetophenone<sup>[62]</sup> and 2-octanone<sup>[63]</sup>, respectively. However, *Lb*ADH was limited in its catalytic performance because of its preference for NADP<sup>+</sup> rather than NAD<sup>+</sup>.<sup>[64]</sup> Therefore, a robust NADPH recycling system is required. The light-driven artificially reconstituted photosynthetic electron transport chain with PSI, Fd, and FNR for NADPH regeneration would be an attractive alternative for *Lb*ADH.

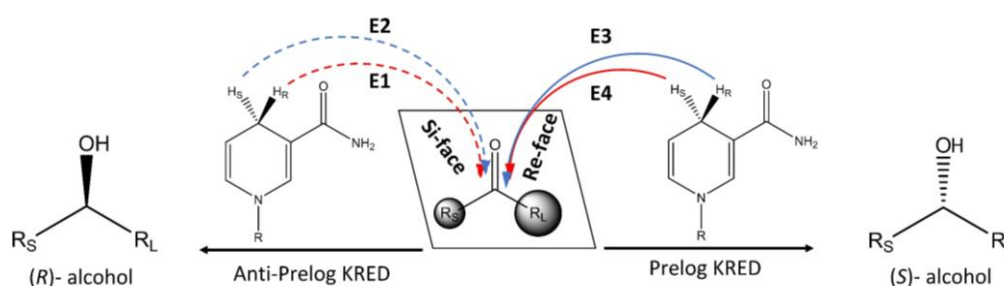


**Figure 7: KRED catalyzed reduction mechanism to produce enantiopure chemicals according to Prelog and anti-Prelog rule.**

Another interesting NADPH-dependent enzyme coupled to the PSI-Fd-FNR recycling system is ene-reductase. Ene-reductases catalyze asymmetric hydrogenation reactions, which is of high value for synthetic chemistry. Ene-reductases are well-known to catalyze the asymmetric reduction of  $\alpha,\beta$ -unsaturated compounds containing electron-withdrawing groups such as aldehydes and ketones.<sup>[65]</sup> The biocatalytic reduction with ene-reductases results in the formation of chiral compounds with up to two tetrahedral stereogenic centers. For example, ene-reductase YqjM was previously used in the production of enantiomerically pure (*R*)-profen, which is used in the synthesis of (*R*)-flurbiprofen methyl ester. Flurbiprofen is used to combat dental pain and sore throat.<sup>[66]</sup> Several other ene-reductases were used in the asymmetric reduction of  $\beta$ -cyanoacrylate esters that are used as precursors in the synthesis of drugs like pregabalin and baclofen.<sup>[66,67]</sup> Ene-reductases rely on NAD(P)H as the hydride source. Previously, ene-reductases were coupled to other NAD(P)H regenerating enzymes for an inexhaustible supply of NAD(P)H, for example, ADH and FDH.<sup>[68]</sup> In this PhD study, an alternative light-driven PSI-Fd-FNR NADPH regenerating system was established to reduce *trans*-cinnamaldehyde to dihydrocinnamaldehyde using *Nicotiana tabacum* double bond reductase (*Nt*DBR). This light-driven enzymatic recycling system retained the stereochemistry of the reactions and enantiopurity of the product, demonstrating its applicability in future studies.

## 1.4 Photosynthetic electron transport

NADPH produced by photosynthetic organisms based on the photosynthetic electron transport chain (PET), and a detailed explanation on the key components of the artificially reconstituted PET for in vitro NADPH recycling is provided here. Photosynthetic organisms utilize light as a source of energy to fix  $\text{CO}_2$ . Organisms that can perform this process are called photoautotrophs. Oxygenic photosynthesis occurs in two phases. In the light phase, reactions ultimately lead to the formation of NADPH and adenosine triphosphate (ATP), along with oxygen as a byproduct. In the light-independent phase,  $\text{CO}_2$  is converted into triose phosphate via the Calvin-Benson cycle by utilizing NADPH and ATP produced in the light phase. The key players in the light phase, such as PSII, PSI, cytochrome *b<sub>6</sub>f* complex (Cyt *b<sub>6</sub>f*), and ATP synthase, are embedded in the thylakoid membrane. Two types of electron transfer pathways take place between these components: a linear electron transfer pathway and a cyclic electron transfer pathway. Here, only the linear electron transfer pathway will be discussed.

Light-induced linear electron flow is initiated by simultaneous excitation of PSII and PSI. In this process, the ultimate electron donor is water, and the final electron acceptor is  $\text{NADP}^+$ . Upon light absorption, P680, a reaction center chlorophyll molecule ensemble, acts as the primary electron donor and transfers electrons to tightly bound quinone ( $\text{Q}_\text{A}$ ) via pheophytin. <sup>[69]</sup> In the following,  $\text{Q}_\text{A}$  reduces mobile  $\text{Q}_\text{B}$ . Oxidized P680<sup>+</sup> ( $E_\text{m} > 1\text{V}$ , the most potent oxidizing biological agent) further oxidizes a nearby tyrosine residue ( $\text{Y}_\text{z}$ ). <sup>[69]</sup> Oxidized  $\text{Y}_\text{z}$  extracts electrons from water via oxygen-evolving complex (OEC). After the second round of light-induced charge separation,  $\text{Q}_\text{B}^-$  is further reduced to form  $\text{Q}_\text{B}^{2-}$ , which is protonated by two protons from the stroma, forming  $\text{Q}_\text{B}\text{H}_2$ . Then,  $\text{Q}_\text{B}\text{H}_2$  enters the lipid bilayer and is replaced by oxidized quinone. <sup>[69]</sup> In the next step, plastoquinone ( $\text{PQH}_2$ ) is oxidized at the  $\text{Q}_0$  site of the Cyt *b<sub>6</sub>f* complex. One electron is transferred to phycocyanin (PC)/cytochrome  $c_6$  (Cyt  $c_6$ ) via the Rieske iron-sulfur protein and Cyt *f*. The second electron is passed across the membrane through two heme groups of Cyt *b<sub>6</sub>f* to reduce quinone bound to the  $\text{Q}_\text{i}$  site. This reduction results in the uptake of two protons from the stroma and their release into the lumen. As a result, proton motive force is generated across the membrane, which is used to drive ATP synthesis. Due to this function, Cyt *b<sub>6</sub>f* is regarded as a molecular orchestrator of photosynthesis. <sup>[69]</sup> The second electron is finally also transferred to PC/ Cyt  $c_6$ . The reduced PC/ Cyt  $c_6$  further transfers the electrons to oxidized P700 (reaction center chlorophylls) of PSI. Due to the light excitation property of PSI, another charge separation activity takes place, which generates electrons with high reduction potential. <sup>[69]</sup> The primary natural electron acceptor of PSI is Fd or flavodoxin



(Fld). Fd or Fld acts as an electron mediator to several oxidoreductases; however, most of the reduced Fd is utilized by FNR to regenerate NADPH that is spent in the Calvin Benson cycle for CO<sub>2</sub> fixation. The major players involved in NADPH regeneration in vivo are PSI, Fd, FNR (**Figure 8**).<sup>[69] [70] [71]</sup> The ultimate electron acceptor of the photosynthetic electron transport chain is NADP<sup>+</sup>. The concentration of NADPH in cyanobacteria, plant protoplast, and chloroplast is determined to be approximately 19-40 nmol mg<sup>-1</sup> Chl<sup>-1</sup>.<sup>[72–73]</sup> In this study, PET was artificially reconstituted using PSI, Fd and FNR. Further, a glimpse on structure and function of the individual proteins is provided.

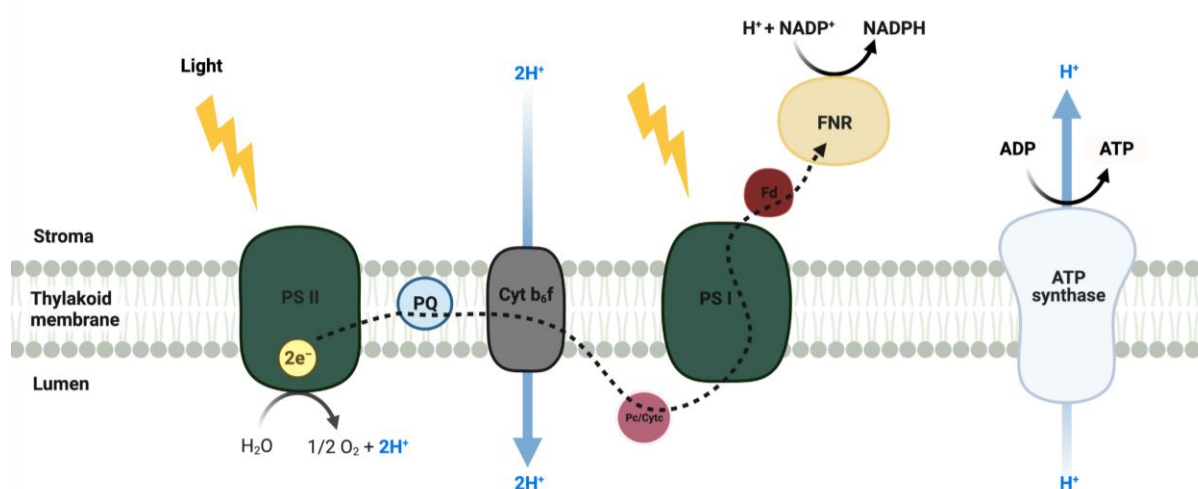


**Figure 8: Schematic representation of the photosynthetic electron transport chain.**, PSII: Photosystem II, PQ: Plastoquinone Cyt *b<sub>6</sub>f*: Cytochrome *b<sub>6</sub>f* complex, Pc: Phycocyanin, Cyt *c<sub>6</sub>*: Cytochrome *c<sub>6</sub>*, PSI: Photosystem I, Fd: Ferredoxin, FNR: Ferredoxin NADP<sup>+</sup> oxidoreductase, ATP synthase: Adenosine triphosphate synthase.

### 1.4.1 Photosystem I structure and function

PSI, a natural photocatalyst used in artificial reconstitution of PET in this PhD study, is a multiprotein complex that exists in trimeric and tetrameric forms in cyanobacteria<sup>[74]</sup> and is embedded in the thylakoid membrane. The PSI consists of an iron-sulfur (Fe<sub>4</sub>S<sub>4</sub>) cluster as a terminal electron acceptor, which is classified as a type 1 reaction center.<sup>[12]</sup> The three-dimensional structure of PSI at a resolution of 2.5 Å is described in Fromme et al., 2001.<sup>[75]</sup> The monomeric complex of PSI from *Thermosynechococcus vestitus* BP-1 (hereafter *T. vestitus* BP1) consists of 12 protein subunits (PsaA, PsaB, PsaC, PsaD, PsaE, PsaF, PsaI, PsaJ, PsaK, PsaL, PsaM, PsaX), 96 chlorophylls, 2 phylloquinones, 3 (4Fe-4S) clusters, 22 carotenoids, 4 lipids, and calcium ions (**Figure 9A & 9B**).<sup>[76]</sup> Trimeric PSI has a diameter of 210 Å and a height of 90 Å in height. The core of the PSI monomer consists of the subunits PsaA and PsaB, which coordinate cofactors of the internal electron transfer chain. The five C-terminal transmembrane helices (A/B-g to A/B-k) of PsaA and PsaB surround the cofactors of the



## Chapter 1

electron transfer chain, forming its central core. A/B-a to A/B-d are separated from the core by a broad elliptical belt containing chlorophyll and carotenoids, while the N-terminal transmembrane  $\alpha$ -helices of each PsaA and PsaB are organized in the form of "trimers of dimers". Both N- and C-terminal domains of PsaA and PsaB are involved in the coordination of chlorophyll molecules. Apart from this, PsaA and PsaB also accommodate three phospholipids and one galactolipid molecule. The luminal surface of PSI is formed mainly by the loop region of PsaA and PsaB, which is responsible for creating a putative binding pocket for Cyt  $c_6$  and PC. In addition, there are seven small membrane integral subunits (PsaF, PsaI, PsaJ, PsaK, PsaL, PsaM, PsaX) in PSI.<sup>[76]</sup> These subunits are located distally or peripherally to the PsaA/PsaB subunits. The primary function of these subunits is stabilization of the antenna system and the structure of the overall complex. The stromal region of PSI is protruded out of the membrane, the so-called stromal hump (**Figure 9C**), formed by the subunits PsaC, PsaD, and PsaE.<sup>[76]</sup> All three subunits are attached to the stromal loops of PsaA/PsaB and do not consist of transmembrane  $\alpha$ -helices.<sup>[76]</sup><sup>[77]</sup> PsaC binds two (4Fe-4S) clusters, F<sub>A</sub> and F<sub>B</sub>, and acts as an electron channel between F<sub>x</sub> and Fd.<sup>[76]</sup> The PsaC subunit shows structural similarities with bacterial Fd and additionally contains an internal loop with C-terminal extension.<sup>[78]</sup> The C-terminal extension supports the interaction of PsaC with subunits PsaA/PsaB and PsaD.<sup>[78]</sup> This is considered to be necessary for the assembly of PsaC within PSI.<sup>[78]</sup> PsaD plays a crucial role in the proper docking of Fd and Fld to PSI and is also known to be necessary for the correct orientation of PsaC.<sup>[76]</sup> All this suggests the stabilizing role of PsaD in the stromal ridge.<sup>[77]</sup> PsaE is located in the periphery of the stromal hump and is observed to be involved in the docking of soluble electron acceptors as well as to play a crucial role in avoiding electron transfer to oxygen.<sup>[79]</sup> The  $\Delta$ PsaE mutant of *Synechocystis* sp. does not seem to have any profound phenotypic effect.<sup>[79]</sup> However, careful physiological examination revealed that  $\Delta$ PsaE mutants of *Synechocystis* sp. have increased expression of genes such as PetH and CatG, indicating a defence mechanism of the cells to achieve the usual NADP<sup>+</sup> photoreduction and quench ROS.<sup>[79,80]</sup> Recent PSI-Fd structural insights revealed the detailed involvement of the PsaE subunit in Fd binding.<sup>[81]</sup> On the other hand, an in vitro study performed by Cassan et. al via artificial reconstitution of photosynthetic electron transport chain yielded contradictory results.<sup>[83]</sup>

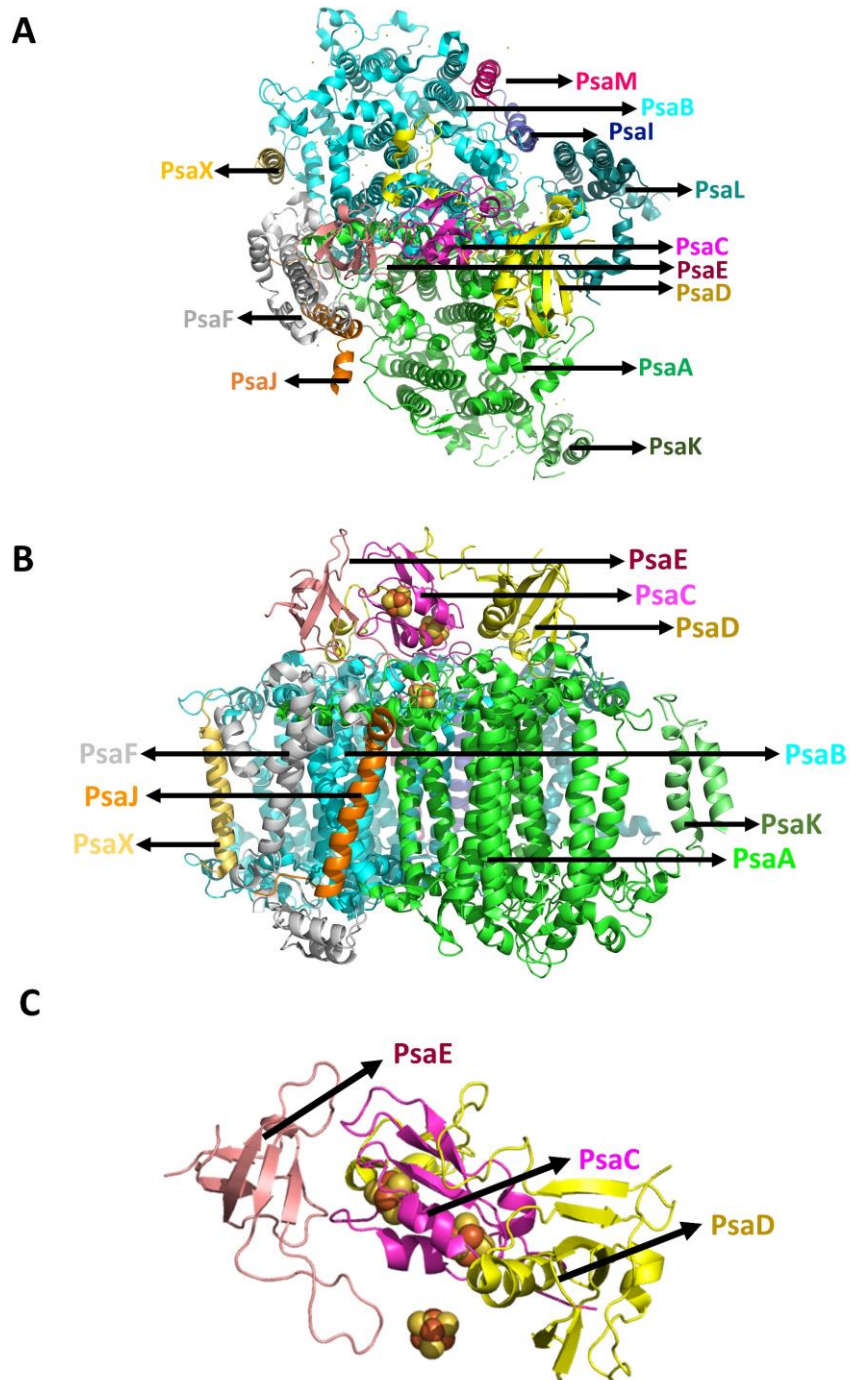


**Figure 9: Crystal structure of cyanobacterial PSI.** A) Monomeric crystal structure of PSI from *Thermosynechococcus vestitus* BP-1 (Top view, PDB-ID: 1JB0), B) Monomeric crystal structure of PSI (Side view, PDB-ID: 1JB0), C) Stromal hump of PSI consists of three subunits (PsaE, PsaC, PsaD). PsaA: light green; PsaB: ocean blue, PsaC: pink, PsaD: dark yellow, PsaE: light brown, PsaF: ash, PsaI: dark blue, PsaJ: orange, PsaK: drak green, PsaL: cyano-blue, PsaL: shiny blue, PsaX: light yellow.

## Chapter 1

PSI is involved in the oxidation of Cyt *c*<sub>6</sub> and the reduction of Fd at the stromal and luminal side of the thylakoid membrane, respectively. A serial electron transfer pathway is established within PSI, as shown (**Figure 10A**), where the schematic representation of the arrangement of cofactors within PSI is presented.<sup>[75]</sup> Upon photoinduced excitation of P700, a unique chlorophyll pair within PSI serving as primary electron donor, an electron from P700\* is transferred to A<sub>0</sub>, a chlorophyll molecule that acts as primary electron acceptor, and then to phylloquinone (A<sub>1</sub>), F<sub>x</sub>, F<sub>A</sub>, and F<sub>B</sub>, respectively.<sup>[77]</sup> P700, A<sub>0</sub>, A<sub>1</sub>, and F<sub>x</sub> are bound to PsaA/PsaB, whereas F<sub>A</sub> and F<sub>B</sub> clusters are bound to extrinsic subunit PsaC.<sup>[77]</sup> The electron transfer between P700\*, A<sub>0</sub> and A<sub>1</sub> is a fast process and occurs in picoseconds. Further electron transfers between A<sub>1</sub>, F<sub>x</sub>, F<sub>A</sub> and F<sub>B</sub> are relatively slow and occurs in nanoseconds (**Figure 10B**).<sup>[83]</sup> It is estimated that PSI in its natural environment can transfer electrons with a speed of 47 e<sup>-</sup> PSI<sup>-1</sup> s<sup>-1</sup>.<sup>[52]</sup> However, applying PSI on an electrode surface, electron transfer rate is much more improved with the design and development of a suitable redox interface between PSI and electrode surface.<sup>[84]</sup> Along with its remarkable electron transfer ability, P700 is also known to undergo charge separation with the highest reduction potential of -1.3 V.<sup>[84]</sup> This makes PSI the most potent biological reductant, and this feature motivates the application of PSI as a photocatalyst for hydrogen production or in the field of biophotovoltaics.

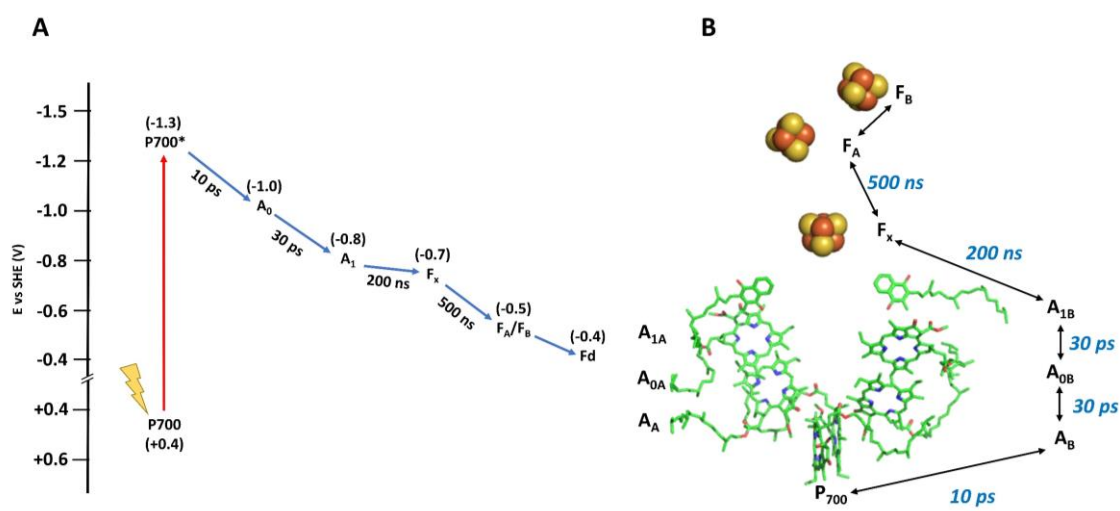


**Figure 10: Schematic representation of electron transfer within PSI.** The electron transfer within PSI is light induced. A) Reduction potential dependent sequential electron transfer from P700 to Fd (capturing the complete electron transfer events within PSI). B) Cofactor arrangement within the PSI complex. P700: Primary electron donor, A<sub>0</sub>: Chlorophyll (Primary electron acceptor). A<sub>1</sub>: phylloquinone. F<sub>x</sub>, F<sub>A</sub>, F<sub>B</sub>: Fe<sub>4</sub>S<sub>4</sub> clusters. Reduction potential and pictures are adapted from the following sources.

Apart from outstanding light capture and reduction potential, PSI has its cofactors ( $F_x$ ,  $F_A$ ,  $F_B$ ) close to the surface. This feature enables PSI to donate electrons to various natural and artificial electron mediators such as Fd, Fld<sup>[87]</sup>, methyl viologen (MV)<sup>[88]</sup>, fullerene ( $C_{60}$ )<sup>[89]</sup>, titanium dioxide ( $TiO_2$ )<sup>[90]</sup>, zinc oxide (ZnO)<sup>[90]</sup>, or  $O_2$ <sup>[88]</sup>. On the other hand, PSI is also capable of obtaining electrons from various donor systems such as Cyt  $c_6$ <sup>[91]</sup>, PC<sup>[91]</sup>, Dichlorophenolindophenol (DCPIP)<sup>[88]</sup>, *N,N,N,N'*-tetramethyl-*p*-phenylenediamine (TMPD)<sup>[88]</sup>, NaAsc<sup>[92]</sup>, synthetic redox-active polymer  $Os(bpy)_2Cl_2$ <sup>[93]</sup>, gold (Au)<sup>[94]</sup>, graphene<sup>[95]</sup>, or indium tin oxide (ITO)<sup>[96]</sup>. This promiscuous redox interface makes PSI a suitable candidate for applied chemistry, especially in the fields of photovoltaics and biocatalysis.

### 1.4.2 Ferredoxin structure and function

Ferredoxin (Fd) acts as an electron mediator in artificial reconstituted PET between PSI and FNR. Ferredoxin is a general term used for small iron-containing soluble acidic proteins that are ubiquitous in all biological organisms. They contain an Fe-S cluster as a prosthetic group based on which different Fd variants can be classified: ([2Fe-2S], [3Fe-4S] and [4Fe-2S]).<sup>[97]</sup> [2Fe-2S] Fd is considered a plant-type Fd (**Figure 11A**), although some bacterial Fds also harbor a [2Fe-2S]-type cluster.<sup>[97]</sup> All the plant-type Fds contain a conserved amino acid motif (CX<sub>4</sub>CX<sub>2</sub>CX<sub>n</sub>C) for the assembly of [2Fe-2S], which is specific for the photosynthetic Fds.<sup>[98]</sup>

Fd plays a pivotal role in electron mediation from PSI embedded in thylakoids to various oxidoreductases (example: FNR). It is also known to interact with the NADH dehydrogenase (NDH) complex in cyanobacteria and plant chloroplasts, playing a crucial role in the cyclic electron flow.<sup>[99]</sup> Furthermore, Fd is involved in many other metabolic activities such as the biosynthesis of chlorophyll and glutamate, fatty acid metabolism, and nitrogen and sulfur assimilation.<sup>[98]</sup> Plant-type Fds can be differentiated by their small size (~10kDa) and a relatively high proportion of acidic amino acid residues.<sup>[100]</sup> This pattern is observed from cyanobacteria to higher plants. Structurally, Fds consist of 1 to 3  $\alpha$ -helices and 3 to 5  $\beta$ -strands (**Figure 11B**). The iron-sulfur cluster in Fd is surrounded by a hydrophobic patch. The protein surface of Fd is rich in negatively charged glutamic acid and aspartic acid residues. Therefore, their enzyme interaction partners tend to have positively charged amino acid residues in their interaction site<sup>[100]</sup>, e.g., the Fd-interaction site of PSI.<sup>[98]</sup> However, Fd is known to have different possible orientations while interacting with HydA1 or HydA2, although the latter enzymes have only one Fd binding site.<sup>[98]</sup>

## Chapter 1

*Synechocystis* sp. contains nine different types of Fds, Fd 1 to Fd 9. Fd 1-6 genes encode a [2Fe-2S] cluster, the Fd 7 gene encodes a [4Fe-4S] cluster, whereas the Fd 8 and Fd 9 genes encode a [2Fe-2S] or [4Fe-4S] cluster.<sup>[97]</sup> Designated Fd genes in *Synechocystis* are: Fd 1 (*ssl0020* or *PetF*) [5], Fd 2 (*sll1382*), Fd 3 (*slr1828*), Fd 4 (*slr0150*), Fd 5 (*slr0148*), Fd 6 (*ssl2559*), Fd7 (*sll0662*), Fd 8 (*ssr3184*) and Fd 9 (*slr2059*).<sup>[97]</sup> All Fd genes are part of well conserved gene clusters indicating their specific function. Fd 1 is highly abundant in the cells and known to be involved in photoautotrophic metabolism. The gene expression of Fd 1 is light-induced and positively regulated by carbon concentration.<sup>[97]</sup> Fd 2 to Fd 9 are less abundant in the cell and their expression is controlled by external cell environments.<sup>[97]</sup> Independent knockouts of Fd, produced by replacing each Fd-coding sequence by homologous recombination with the  $Km^R$  gene revealed the phenotypic and physiological significance of each Fd.<sup>[97]</sup> A  $\Delta fd1$ :  $Km^R$  insertion mutant could not be generated in *Synechocystis* indicating the significance of Fd1 for viability.<sup>[98]</sup> Based on the knockout study, Fd 2, 3, 6, 8 appeared to be important for the photoautotrophic growth of cyanobacteria. Individual knockouts of Fd 4, Fd 5, Fd 7, Fd 9 did not influence the viability of *Synechocystis*, indicating that these Fds are dispensable under normal growth conditions.<sup>[102–104]</sup> However, a study conducted by Chauvat et.al reported that Fd 7 and Fd 9 play a crucial role in oxidative and metal stress conditions.<sup>[97]</sup> Irrespective of physiological relevance, more details about the function of each Fd in cyanobacteria remain to be elucidated.

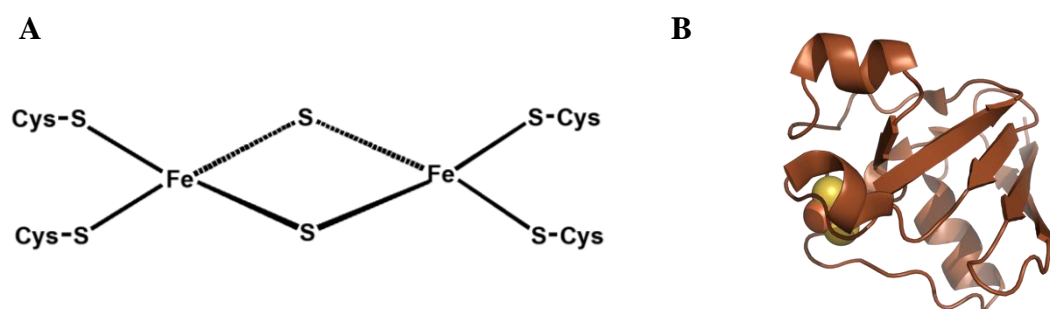


**Figure 11: Structural representation of ferredoxin (Fd) and its [2Fe-2S cluster] cofactor.** A) Schematic representation of the [2Fe-2S] cluster. B) Crystal structure of Fd from *T. vestitus* BP1 (PDB-ID:5AUI).

Recently, the cryo-EM structure of *T. vestitus* BP1 PSI in complex with type 1 Fd and a loosely bound Cyt  $c_6$  was obtained at 1.97 Å resolution as described in Li et.al.<sup>[81]</sup> This study revealed that Fd binds to the stromal side subunits of PSI, and in particularly to PsaC and PsaE. Fd was also observed to interact with the PsaA subunit of PSI. A wide range of electrostatic and

hydrophobic interactions were found to be crucial for complex formation between Fd and PSI. From a thermodynamic perspective, these interactions decrease the enthalpy.<sup>[81]</sup> On the other hand, upon complex formation, the dissociation of water molecules surrounding the interfaces of Fd and PSI energetically contributes to an increase in entropy which favors the complexation between Fd and PSI.<sup>[81]</sup> Thus, the binding of Fd with PSI is entropy driven. Additionally, this was confirmed by isothermal titration calorimetry (ITC), and the dissociation constant ( $K_d$ ) of the PSI-Fd complex was determined to be about 0.8  $\mu$ M.<sup>[81,105]</sup> According to Li et.al, after the electron transfer from PSI to Fd, the dissociation of Fd from PSI is driven by conformational changes in the proteins.<sup>[81]</sup> Upon reduction of Fd, a flip in the peptide bond at Cys45 results in the disruption of interaction between Cys45 of Fd and Glu15 of PsaC, while the C-terminal Tyr97 of Fd would dislodge water-mediated hydrogen bonds associated with Glu15.<sup>[81]</sup> The high enthalpic energy cost with loss of this interaction might favor the dissociation of the PSI-Fd complex. Additionally, in this study, the interaction of Fd with PSI- Cyt  $c_6$  was predicted to be indirectly controlled by the interaction of Fd on the stromal side of the PSI.<sup>[81]</sup> The subunit PsaF of PSI acts as a transmembrane signal transducer from the stromal side to the luminal side that prevents the interaction of to Cyt  $c_6$  and PSI for Fd reduction, thus preventing the over-reduction of the  $F_A$ - $F_B$  cluster of PSI.<sup>[81]</sup>

### 1.4.3 Ferredoxin $NADP^+$ oxidoreductase structure and function

In PET, FNR obtains electrons from Fd and reduces  $NADP^+$ . FNR is classified in the Enzyme Nomenclature system (McDonald and Tipton FEBS J 2021) as EC 1.18.1.2.<sup>[106]</sup> It is a soluble cytosolic protein, containing a non-covalently bound flavin adenine dinucleotide (FAD) cofactor as prosthetic group (**Figure 12A**). FNR plays a crucial role in the photosynthetic electron transport chain by catalyzing the reduction of  $NADP^+$  to NADPH. The reversibility of this reaction depends on the ratio of  $Fd_{ox}/Fd_{red}$ . The function of FNR in photosynthetic cells is the regeneration of NADPH for  $CO_2$  assimilation. The NADPH produced is then used to drive other metabolic activities such as nitrogen assimilation, steroid hydroxylation, hydrogen fixation, or fatty acid desaturation.<sup>[107]</sup> In photosynthesis, most of the reduced Fd is channelled towards FNR, mainly because of the higher affinity of  $Fd_{red}$  towards FNR<sup>[108]</sup> and molecular confinement by anchoring FNR to phycobilisomes<sup>[109]</sup> or directly on thylakoids<sup>[110]</sup> in cyanobacteria, and through accessory proteins such as the translocon on the inner chloroplast membrane protein 62 (TIC62)<sup>[111]</sup>, or the thylakoid rhodanese-like protein (TROL) in plants.<sup>[112]</sup> These association models have been shown to expose FNR more towards  $Fd_{red}$  and may ultimately lead to higher NADPH production. It has also been reported that FNR plays a crucial



## Chapter 1

role in cyclic electron flow by forming a supercomplex with PSI, light harvesting complex I (LHCI), light harvesting complex II (LHCII) of PSII and the proton gradient regulation-like protein (PGRL1).<sup>[113]</sup> FNR is highly specific for NADP<sup>+</sup>.<sup>[114]</sup> For FNR from *Anabaena*, it was shown by site-directed mutagenesis that both the pyrophosphate and 2'-phosphate moieties of NADP<sup>+</sup> are involved in determining the pyridine nucleotide specificity.<sup>[114]</sup> Within the NADP(H) binding domain of FNR (**Figure 12B**), a large cavity is present to accommodate the 2'-P-AMP moieties of NADP(H). Upon binding of the pyridine nucleotide, this cavity is rearranged to have an optimal shape and charge match.<sup>[114]</sup>

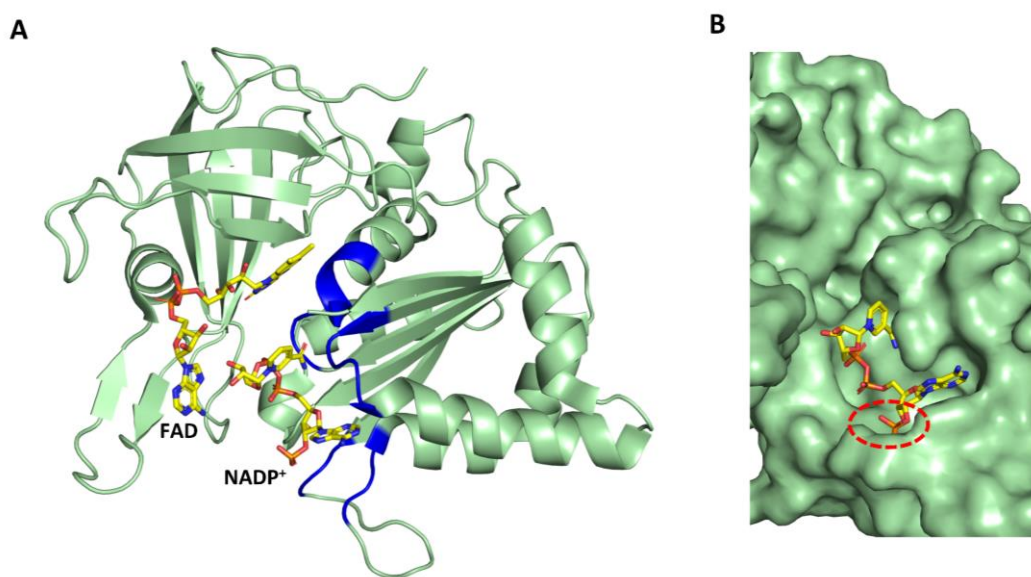


**Figure 12: Crystal structure of FNR from *Anabaena* sp. (PDB-ID:1GJR).** A) Co-crystallized form of FNR with NADP<sup>+</sup>. Residues involved in the interaction with NADP<sup>+</sup> are high-lighted in blue. B) Cavity formation in FNR upon NADP<sup>+</sup> binding (high-lighted by a red circle).

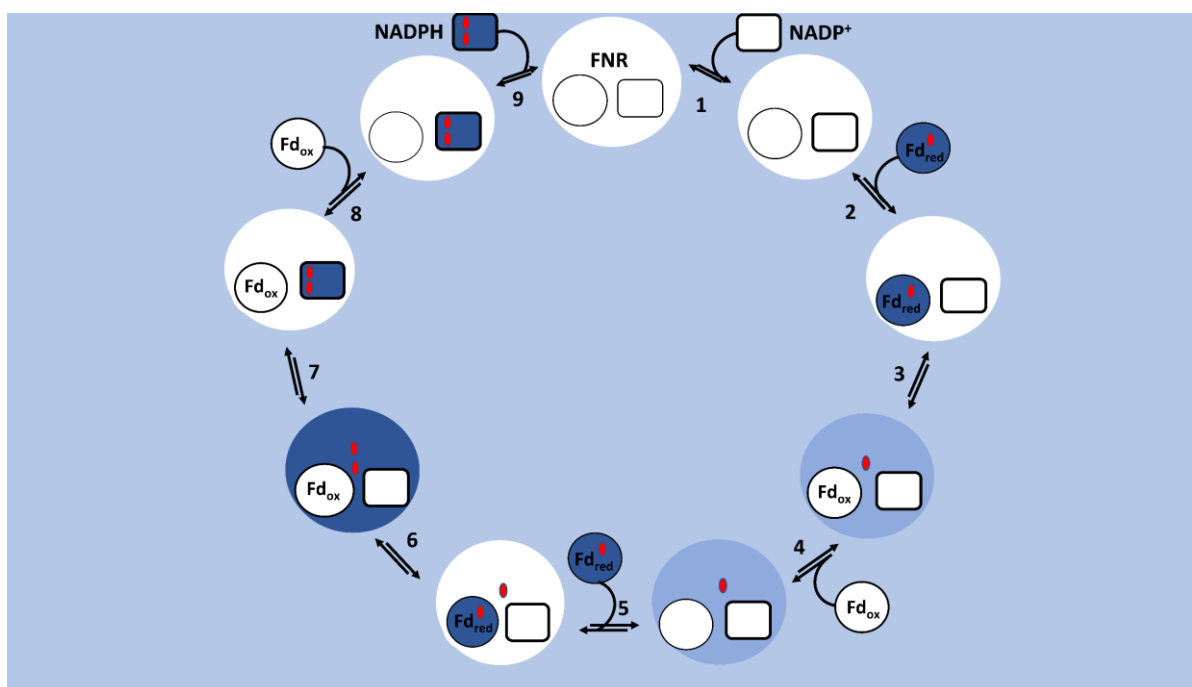


**Figure 13. Catalytic cycle of ferredoxin NADP<sup>+</sup> oxidoreductase (FNR).** The various steps of the catalytic cycle were proposed based on kinetic and binding experiments of spinach and *Anabaena* PCC 7119 FNR. FNR is represented as large ball, NADP<sup>+</sup> is represented as a square, Fd is represented as a small ball. The oxidized state is represented by white color, the half-reduced state is represented by light blue, and the fully reduced state is represented by dark blue. <sup>[107,115]</sup>

A brief series of events involved in the process of NADPH formation by FNR is depicted in **Figure 13**. <sup>[107]</sup> During the catalytic cycle, the FAD cofactor in FNR transits into three different redox states: oxidized (quinone), one-electron reduced (semiquinone), and two-electron reduced (hydroquinone). Several intermediate steps occur during the reduction of NADP<sup>+</sup> by using electrons from Fd<sub>red</sub> (**Figure 13**). <sup>[107]</sup> Interaction with Fd<sub>red</sub> necessitates the presence of NADP<sup>+</sup> in the FNR active site. <sup>[107]</sup> Interaction of NADP<sup>+</sup> to FNR (**Step 1**) occurs in two stages. The adenosine part of NADP<sup>+</sup> binds to FNR and subsequently isomerizes, thus leading to nicotinamide docking. In this process, the nicotinamide ring is stacked onto the *re*-face of the isoalloxazine moiety of the flavin cofactor, which requires the displacement of the aromatic side chain of the terminal tyrosine. <sup>[107]</sup> Next, Fd<sub>red</sub> binds to FNR<sub>ox</sub>. This initiates the FAD cofactor of FNR undergoes a one-electron reduction and acquires a neutral (light blue) semiquinone state (**Step 2&3**), which is relatively unstable. <sup>[107]</sup> Fd interacts at a concave region of the FAD domain of FNR. Interaction of Fd with the FAD domain, places the [2Fe-2S] cluster of Fd at close distance, almost 6 Å, from the isoalloxazine ring of FAD, such that direct electron transfer occurs between these two prosthetic groups. <sup>[107]</sup> After dissociation of Fd<sub>ox</sub> (**Step 4**) and re-association and electron transfer of Fd<sub>red</sub> to FNR<sub>sq</sub> (**Step 5**), FNR attains the fully reduced state (FNR<sub>red</sub>) (**Step 6**). <sup>[107]</sup> The electron transfer from Fd<sub>red</sub> to FNR<sub>sq</sub> is a relatively slow process because Fd<sub>ox</sub> strongly inhibits the second electron transfer by binding to FNR<sub>sq</sub>. <sup>[107]</sup>



However, the presence of  $\text{NADP}^+$  stimulates the release of  $\text{Fd}_{\text{ox}}$ . Thus, the presence of  $\text{NADP}^+$  facilitates the process from step 4 to 8 and step 4 is a rate limiting step in this catalytic cycle. <sup>[110]</sup> A ternary protein complex with  $\text{Fd}_{\text{ox}}$ ,  $\text{FNR}_{\text{red}}\text{-NADP}^+$  formation was measured in vitro by difference spectroscopy. In the next steps, dissociation of  $\text{Fd}_{\text{ox}}$  from the  $\text{FNR}_{\text{red}}\text{-NADP}^+$  complex and hydride transfer from  $\text{FNR}_{\text{red}}$  to  $\text{NADP}^+$  occurs (**Step 7 and 8**). Finally, dissociation of the  $\text{FNR}_{\text{ox}}\text{-NADPH}$  complex (**Step 9**) closes the catalytic cycle. <sup>[107]</sup>

### 1.5 Enzyme fusion- A typical way for diffusion independent electron transfer

The NADPH regeneration capacity of an artificially reconstituted PET cascade comprising PSI, Fd and FNR depends on the interaction frequency between the protein partners. Minimizing the physical distance between the catalytic entities may lead to faster electron (substrate) transfer via molecular confinement. Molecular confinement can be achieved by enzyme fusion, which is performed by combining two or more genes. Here, general advantages and disadvantages of the application of enzyme fusion and what determines the optimal linker for a fusion is described. Fusion of enzymes may lead to substrate channelling, which improves the overall reaction rate of the cascade, and this process is essential if the concentration of intermediate products is low or if the intermediate compounds are unstable or susceptible to side reactions. <sup>[116]</sup> Fusion technology is applied in different fields, such as biocatalytic applications to improve reaction efficacy, in whole cell cascade reactions, and for boosting protein expression by tethering solubility tags. <sup>[116]</sup> For instance, in the PTDH-BMVO fusion BVMO steadily catalyzes the conversion of ketones to lactones or esters by using the NADPH regenerated by the covalently linked auxiliary enzyme PTDH (**Figure 14**). <sup>[117]</sup> By this method a separate expression of both enzymes can be avoided and, as a result, a one-pot, self-sufficient system is established. However, one noticeable observation was a decrease in the affinity of PTDH for phosphite when fused to BVMO. <sup>[117]</sup> Another fusion construct is the ADH-BVMO fusion. <sup>[118]</sup> In this system, ADH generates NADPH from  $\text{NADP}^+$  via transformation of alcohol into ketone. Ketone and NADPH are further used as substrates for BVMO, which leads to the formation of esters. To create the ADH-BVMO fusion, a glycine-rich linker was introduced to connect the single enzymes. <sup>[118]</sup> The catalytic rate of this fusion construct was higher when compared to the system having both enzymes as individual entities. <sup>[118]</sup>

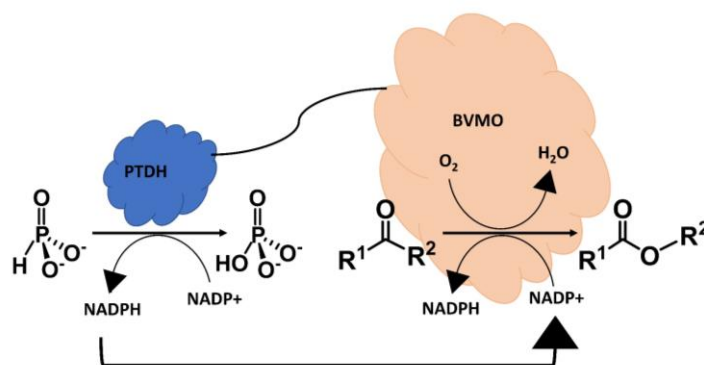


**Figure 14: Schematic representation of enzyme fusion PTDH-BVMO.** The fused construct with bifunctional protein entities promotes the production of NADPH and simultaneous conversion of the ketone to ester. This picture is adapted from previous literature. <sup>[116]</sup>

Enzyme fusions need to be designed carefully considering various parameters, like type of amino acids in the linker, length of the linker and fusion orientation i.e. at the N- or C-terminus. In the case of the PTDH-BVMO fusion, the fusion orientation did not change the catalytic activity, but in other cases, a change of orientation may lead to improper folding or enzyme inactivation. <sup>[116]</sup> For instance, a C-terminal fusion to ADH was reported to cause inactivation. <sup>[118]</sup> In fusion design, the length of the linker may also play a crucial role. In a study conducted by George et al. 2002, 1280 linkers were extracted out of naturally occurring 630 multidomain protein chains. <sup>[119]</sup> The average linker length was found to have  $10.0 \pm 5.8$  residues and the linkers were classified as large, medium, and small based on the average number of amino acid residues  $21.0 \pm 7.6$ ,  $9.1 \pm 2.4$ , and  $4.5 \pm 0.7$ , respectively. <sup>[119]</sup> However, most of the linker lengths in the design of fusion proteins are chosen arbitrarily or in a state of proximity. For example, in a study of the Fd and PSI fusion model, the linker length was chosen based on the electron transfer distance between these two proteins as individual entities. <sup>[92]</sup> Another key factor in fusion design is the amino acid composition of the linker, which determines its flexibility and rigidity. <sup>[120]</sup> Flexible linkers usually consist of small non-polar (glycine) and neutral polar (serine or threonine) amino acids. The inclusion of serine and threonine in the glycine linker was observed to enhance the stability of the linker by hydrogen bond formation with water. <sup>[120]</sup> (GGGGS)<sub>n</sub> is a commonly used pattern. <sup>[120]</sup> For example, the PSI-Fd fusion containing a (GGGS)<sub>n</sub> linker was observed to perform better than the free protein system. <sup>[121]</sup> Nevertheless, there are also other flexible linkers reported such as EGKSSSGSGESKST. This linker is flexible due to the high number of serine and glycine residues, thus increasing the solubility. This linker was developed by protein modelling for construction of a fusion protein of the variable regions of the heavy and light chains of an antibody. <sup>[122]</sup> In contrast to flexible

linkers, rigid linkers are the choice of interest to achieve minimal interaction or minimal intervention between the proteins or protein domains of interest <sup>[123]</sup>.  $\alpha$ -Helix linkers are rigid spacers due to their ability to create an intra-hydrogen bond. Typical amino acid constituents of  $\alpha$ -helix linkers are Pro, Ala, Lys, or Gln. <sup>[119]</sup>

### 1.5.1 Engineering PSI for molecular confinement

Designing the proper fusion model for a large membrane complex like PSI is challenging. However, the remarkable stability, light-dependent highest charge separation activity and easy genetic manipulation of the redox interface have stimulated many research groups to develop fusion strategies to efficiently extract the electrons from the redox interface of PSI. <sup>[84]</sup> Here, the general function, advantages and disadvantages of various PSI fusion strategies and PSI fusion strategy explored in this PhD study is discussed and explained.

#### Indirect metallic immobilization on PSI for hydrogen production

Greenbaum et al. 1985 pioneered the immobilization of metals on PSI by precipitating platinum colloid particles on thylakoids. <sup>[124]</sup> Since then, several studies have been reported for hydrogen production using isolated components of photosynthetic apparatus. This is achieved by immobilization of thylakoids with  $[\text{Pt Cl}_6]^{2-}$  and  $[\text{OsCl}_6]^{2-}$  ligands (**Figure 15A**). <sup>[125]</sup> Also, isolated PSI with  $[\text{Pt Cl}_6]^{2-}$  was used (**Figure 15B**), resulting in hydrogen production rate of  $0.08 \mu\text{mol H}_2 \text{ mg}^{-1} \text{ Chl}^{-1} \text{ h}^{-1}$ . <sup>[126]</sup> In recent years, platinized PSI was also deposited on an electrode for  $\text{H}_2$  production. <sup>[53]</sup> However, the disadvantage of this model is that the deposition of Pt on the thylakoids or PSI is not site-specific. As a result, the photo-energized electrons obtained from light-excited PSI were not channelized properly.

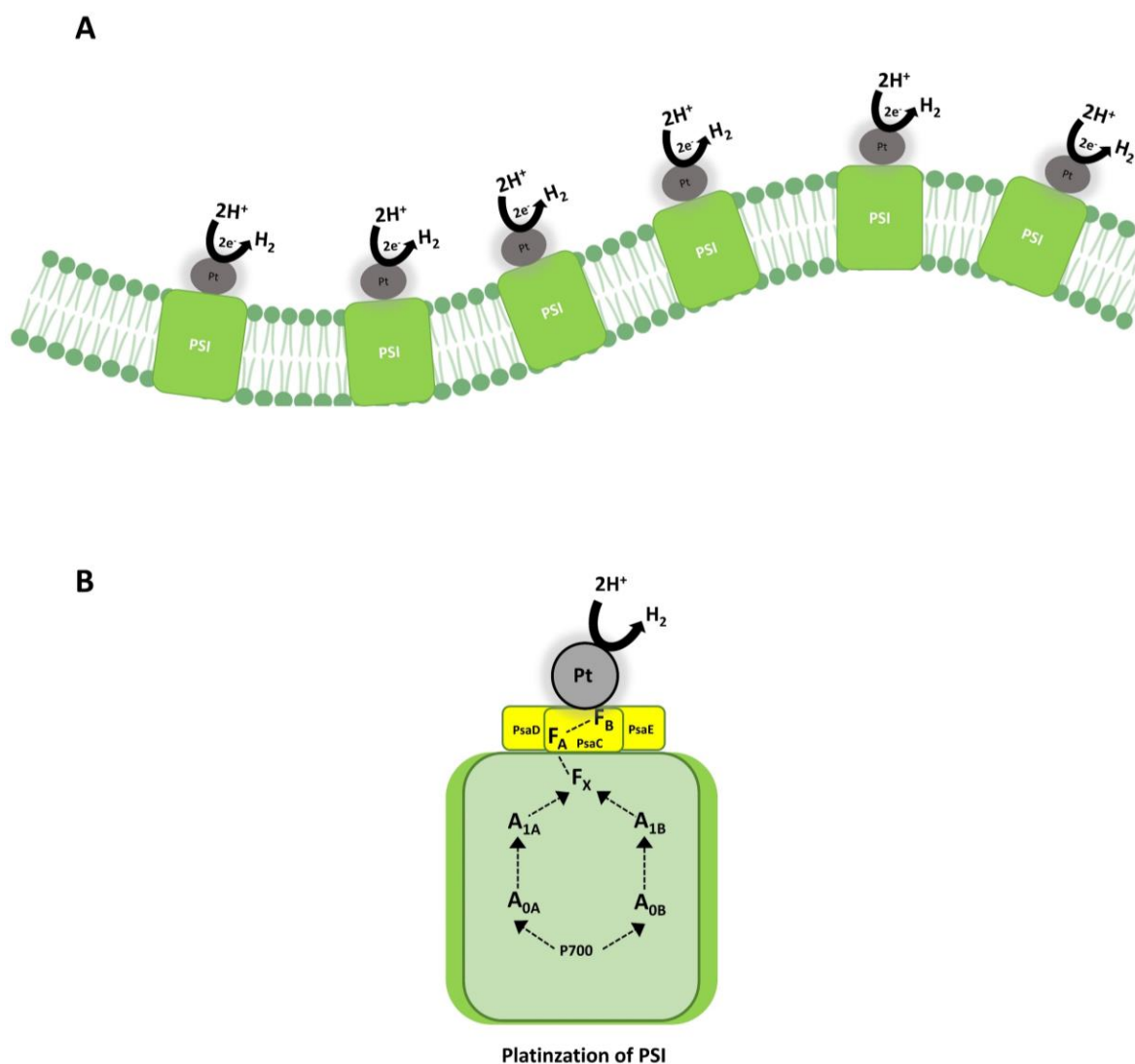


**Figure 15: Immobilization of Pt on thylakoids and isolated PSI.** A) Schematic representation of deposition of platinum colloid particles on thylakoids for light-dependent production of hydrogen <sup>[125]</sup>. B) Deposition of Pt on isolated PSI for hydrogen production. <sup>[126]</sup>

### Direct wiring of F<sub>B</sub> cluster of PSI to the catalyst for hydrogen production

In a study conducted by Yu et al. 1993, direct wiring of the F<sub>B</sub> cluster of PsaC to a metal catalyst was achieved. <sup>[127]</sup> In this study, based on the structural and functional knowledge of PSI in those days, a novel fusion strategy was designed. PSI harbors two [4Fe-4S] clusters, which are coordinated by 4 Cys residues each to form the F<sub>A</sub> and F<sub>B</sub> cluster, respectively. PsaC has a signature motif CxxC<sub>13</sub>xxCxxxCP. When Cys<sub>13</sub> was replaced by Gly only one Fe-S cluster (F<sub>A</sub>) was assembled. This PsaC variant was expressed and purified as an inclusion body from *E. coli* and later reconstituted with [4Fe-4S]. [S-(CH<sub>2</sub>)<sub>2</sub>-OH]<sub>4</sub>. <sup>[127]</sup> The reconstituted PsaC contained two Fe-S clusters, one at the F<sub>A</sub> site as [4Fe-4S]. (Cys)<sub>4</sub> and another at the F<sub>B</sub> site as

## Chapter 1

[4Fe-4S].[(Cys)<sub>3</sub>S-(CH<sub>2</sub>)<sub>2</sub>-OH].<sup>[127]</sup> The thiolate group could be replaced by another dipyridinium (viologen derivative) or another thiolate.<sup>[128]</sup> This approach enabled the site-specific bridging of the catalytic module on to the photochemical module of PSI. Pt and Au nanoparticles were conjugated to PSI by this approach.<sup>[51]</sup> In a study conducted by Grimme et al. 2009, based on the PsaC-C13G variant mentioned above, a reconstituted spinach PSI was tethered with metal catalyst via dithiol linkers (aliphatic and aromatic) (**Figure 16**). A linker with one benzene ring was performing better than several aliphatic linkers. With the aliphatic linkers, an increase in linker length resulted in a decrease in hydrogen production. PSI-linker-1,4-benzenedithiol-Pt showed the highest hydrogen production with 150.5  $\mu\text{mol H}_2 \text{ mg}^{-1} \text{ Chl}^{-1} \text{ h}^{-1}$ , presumably due to less steric hinderance.<sup>[129]</sup>

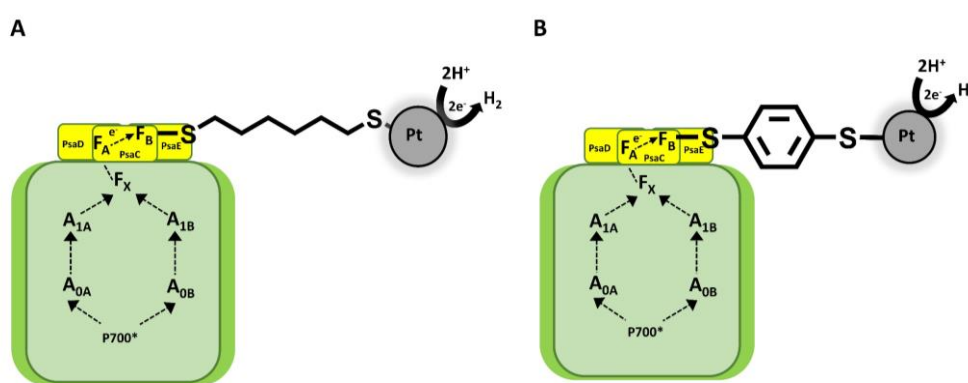


**Figure 16: Molecular tethering of metallic catalytic module to PSI.** PSI (PsaC-C13G variant) was tethered with linker 1,8-hexanedithiol (A), 1,4-benzenedithiol (B). The other end of the linker is fused to platinum (Pt). This picture was adapted from previous literature.<sup>[51]</sup>

The above concept was further extended by tethering an enzyme catalyst. In a study conducted by Lubner et al. 2011, hydrogenase was tethered to PSI with dithiol linkers (**Figure 17**).<sup>[52]</sup> In this study, luminal and stromal sides of PSI were tethered to [FeFe]-Hyd C97G and, Cyt *c*<sub>6</sub>, respectively (Figure 17 only indicates Hyd tethering). Three different linker lengths were used to tether hydrogenase to PSI (1,6-hexanedithiol; 1,8-octanedithiol; 1,10-decanedithiol). The 1,8-octanedithiol linked Hyd-PSI fusion was observed to outperform the other variants by producing 2,200  $\text{mmol H}_2 \text{ mg}^{-1} \text{ Chl}^{-1} \text{ h}^{-1}$ . Presumably, this linker length was sufficient to avoid steric hindrance. Interestingly, the electron transfer rate within this PSI fusion was higher ( $105 \pm 22 \text{ e}^- \text{ PSI}^{-1} \text{ s}^{-1}$ ) than the process of natural photosynthesis ( $47 \text{ e}^- \text{ PSI}^{-1} \text{ s}^{-1}$ ).<sup>[52]</sup> However, the in vivo application of this model appeared to be lethal.<sup>[51]</sup>

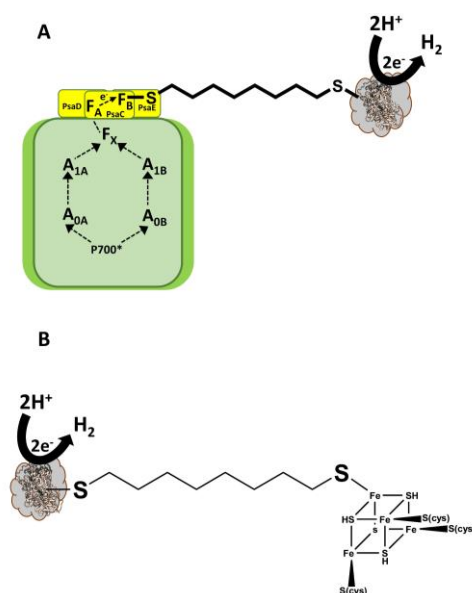


**Figure 17: Molecular tethering of enzymatic catalytic module to PSI.** **A:** PSI (PsaC-C13G variant) was tethered with linker 1,8-octanedithiol and the other end of the linker was fused with Hyd.<sup>[52]</sup> **B:** Schematic representation of Hyd-tethered 1,8-octanedithiol to [2Fe-2S] cluster.

## In vivo PSI-hydrogenase fusions for hydrogen production

One of the major problems of in vivo hydrogen production using cyanobacteria is the sensitivity of Hyd to oxygen (oxygen produced by water splitting activity of PSII) and competition of Hyd for redox flux with so far established molecular inter-networks.<sup>[130]</sup> These issues were addressed by using oxygen tolerant [NiFe]-Hyd and direct fusion of Hyd to PSI for channelized electron supply.<sup>[130]</sup> Redox coupling of Hyd and PSI fusion is thermodynamically feasible because the redox potential of terminal F<sub>A</sub> and F<sub>B</sub> is between -440 and -480 mV vs. SHE and the 2H<sup>+</sup>/H<sub>2</sub> reaction potential is -420 mV vs SHE.<sup>[130]</sup> Different Hyd-PSI fusion models proposed in recent years are: [NiFe]-Hyd (HoxGK from *Cupriavidus necator*)-PsaE fusion mutant was expressed and successfully recombined to PsaE-depleted PSI mutant in *T. vestitus*.<sup>[130]</sup> The light-driven hydrogen production of isolated Hyd-PSI complex was reported to be 0.58 mmol H<sub>2</sub> mg Chl<sup>-1</sup> h<sup>-1</sup>.<sup>[130]</sup> No in vivo photohydrogen experiments were performed with this fusion model because for this, they would have to introduce the whole Hyd maturation operon in *T. vestitus* BP1.<sup>[130]</sup> In another study, [NiFe]-Hyd (HoxYH from *Synechocystis* sp. PCC 6803) was fused to PsaD subunit of PSI, and this mutant was created in *Synechocystis* sp. PCC 6803.<sup>[131]</sup>

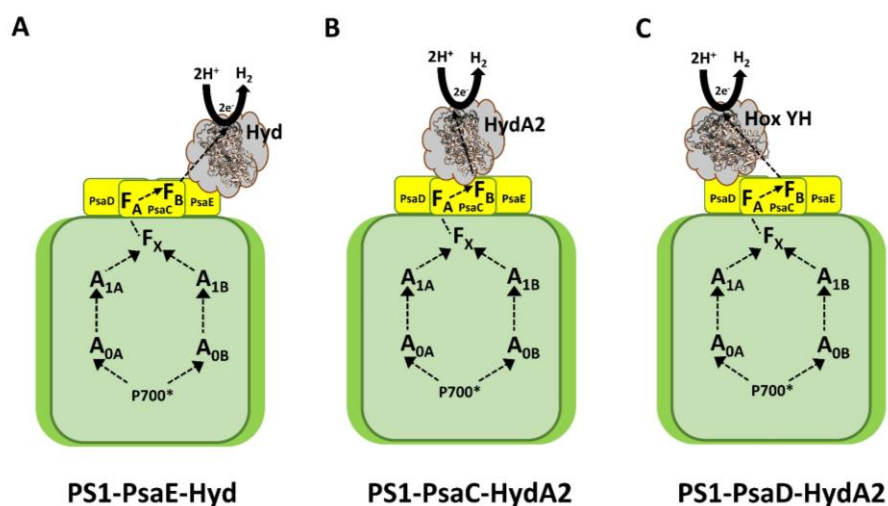


**Figure 18. Schematic representation of chimeric PSI-hydrogenase fusion models.** A: [NiFe]-Hyd (HoxGK from *Cupriavidus necator*) was recombinantly fused to PsaE subunit of PSI. <sup>[130]</sup> B: *Chlamydomonas reinhardtii* [Fe-Fe]-HydA2 was recombinantly fused to PsaC subunit of PSI. <sup>[132]</sup> C: *Synechocystis* sp. PCC 6803 [NiFe]-Hyd (HoxYH) was recombinantly fused to PsaD subunit of PSI. <sup>[131]</sup>

This model argues the presence of Hyd near a 4Fe-4S cluster of F<sub>x</sub> site by fusing it to the PsaD subunit <sup>[133]</sup>. In this study, photoautotrophic hydrogen production up to 500  $\mu$ M was observed in vivo (standard units are missing). <sup>[131]</sup> Next to both cyanobacterial systems, a PSI fusion model with an oxygen-sensitive Hyd from a green alga was reported. In this model, [FeFe]-HydA2 from *Chlamydomonas reinhardtii*) was fused to the PsaC subunit of PSI. <sup>[132]</sup> Successful photoautotrophic hydrogen production was observed in vivo and was estimated to be 300 nmol H<sub>2</sub> mg<sup>-1</sup> Chl<sup>-1</sup> h<sup>-1</sup>. <sup>[134]</sup>

## Stripping and reconstitution of PSI-Fd fusion for NADPH regeneration

In the study conducted by Wittenberg et al. 2013, a PSI-Fd fusion was achieved by stripping of stromal hump followed by reconstitution. <sup>[121]</sup> Firstly, the stromal ridge (PsaC, PsaD, PsaE) of PSI was removed by treating PSI with 7 M urea at 42 °C. Then, stripped PSI along with Fd-PsaE fusion and PsaD and PsaC components were reconstituted into PSI-Fd (**Figure 19**). PSI and Fd were separated by three different linker lengths of 14, 19 and 25 amino acids. The linker consisted of repeats of (GGSGS)<sub>n</sub>, and the linker length was chosen based on computational modelling. The PSI-Fd fusion with a linker of 14 amino acid residues between Fd and PsaE was observed to perform better than the protein system where PSI and Fd were present as individual components. <sup>[121]</sup>



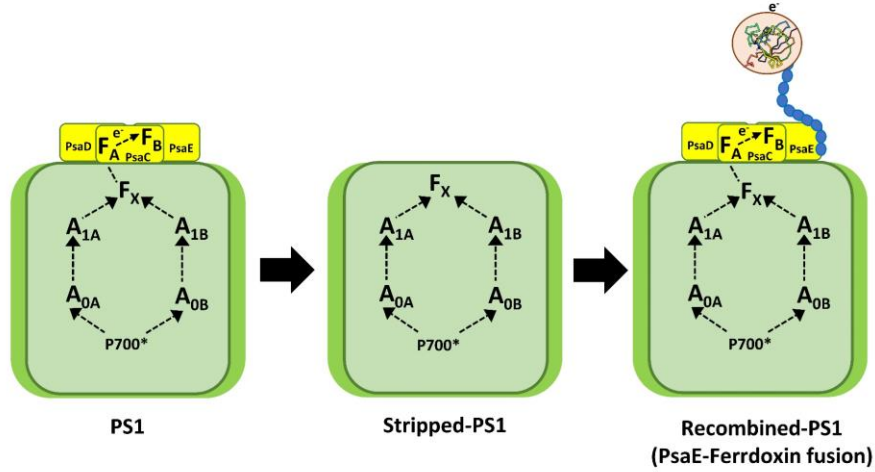


**Figure 19: Schematic representation of creation of PSI-Fd fusion.** In this process, stromal ridge of PSI was stripped and then the stromal subunits (PsaC, PsaD, PsaE-Fd) were reconstituted with stripped PSI. <sup>[121]</sup>

### Recombination based PSI-Fd fusion for NADPH regeneration

In a study conducted by Moal et al. 2012, a PSI-Fd fusion (**Figure 20**) was developed based on recombination of PsaE of PSI in vitro. <sup>[92]</sup> First, PSI- $\Delta$ PsaE mutant was created and isolated from *Synechocystis* sp. and recombined with PsaE-Fd fusion protein, which was heterologously expressed and purified from *E. coli*. <sup>[92]</sup> PSI and Fd were separated by three different linker lengths of 5, 7, and 10 amino acids and consisted of a mutation of R39Q on PsaE. <sup>[92]</sup> Out of three chimeras, PS1-Fd fusion with a linker of 10 amino acids outperformed the free protein system and the other linker variants. <sup>[92]</sup>

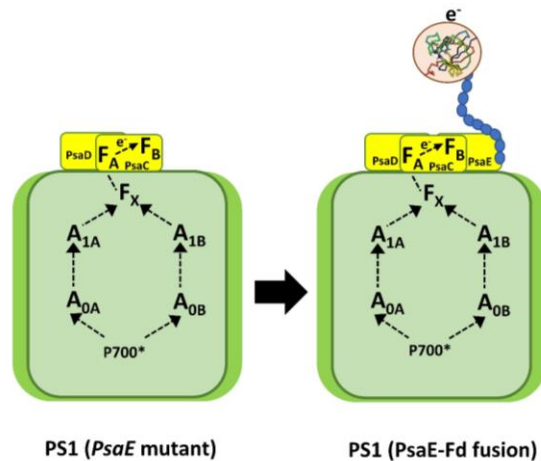


**Figure 20: Schematic representation of creation of Fd-fused PSI.** <sup>[92]</sup> For details see main text.



## 1.6 A novel colicin-based PSI fusion for NADPH regeneration

One of the goals of this PhD study was to develop a clickable PSI system for light-driven NADPH regeneration and biocatalytic applications. This was established using E7 Colicin DNase and corresponding immunity protein as an in vitro affinity system. For this, PSI of *Synechocystis* sp. PCC. 6803 was genetically modified through recombinant expression of Im7 with the PsaE subunit of PSI and, on the other hand, E7 DNase was fused with Fd or Fd-FNR genetic elements and expressed in *E. coli*. Further, PSI-Im7 was coupled to E7-Fd-FNR via the E7-Im7 affinity system to form the PSI-Fd-FNR complex. Here the general structure and function of the E7-Im7 system is described.

Colicins are mostly plasmid-encoded antimicrobials produced by *E. coli* and are defensive against sensitive *E. coli* and other coliform bacteria to reduce natural competitors for acquiring nutrients.<sup>[133]</sup> Apart from colicins, an immunity protein is co-expressed in host cells and other colicin-resistant bacterial cells.<sup>[133]</sup> This immunity protein binds with colicins by non-covalent interaction and avoids the toxication from self-produced colicin.<sup>[133]</sup> A typical gene cluster of colicin encodes toxin protein, immunity protein, and a lysis gene, which encodes a protein helpful in the release of colicin from bacteria. In colicin-resistant strains corresponding to toxic colicin, an immunity protein is simultaneously produced.<sup>[133]</sup> Based on the type of protein that colicins use for penetration into the outer membrane of colicin-sensitive *E. coli*, colicins are divided into two groups: Group A: Tol system uses Tol protein for penetration and is subdivided into colicins E1 to E9, A, K, N based on the membrane receptor they bind.<sup>[133]</sup> Group B: uses Ton protein for penetration and are subdivided into colicins 5, 10, B, D, M, V, Ia, Ib.<sup>[133]</sup> Here the focus will be set only on E7 colicin, which is known to bind to the BtuB receptor (vitamin B12 receptor) and has a DNase-based antimicrobial activity.<sup>[134]</sup>

**Structure of E7 colicin:** Colicin has three domains: a receptor binding domain, a membrane translocation domain, and a cytotoxic DNase domain.<sup>[134]</sup> The DNase domain of ColE7 consists of five  $\alpha$ -helices ( $\alpha 1$ - $\alpha 5$ ) and two antiparallel  $\beta$ -sheets ( $\beta e$  and  $\beta d$ ) placed against it (**Figure 21**).<sup>[134]</sup> A hydrophobic core is made between  $\beta e$  and a layered sheet of  $\alpha$ -helices. The core is comprised of 22 residues (mainly with Met, Phe, Trp).<sup>[134]</sup> A  $Zn^{2+}$  ion is located between sheet  $\beta d$  and  $\alpha 5$ . The metal ion, which plays an important role in DNase activity, is coordinated by one water molecule and three histidine residues.<sup>[134]</sup>

## Chapter 1

**Structure of Im7:** The Im7 protein consists of four antiparallel  $\alpha$ -helices ( $\alpha 1^*$ – $\alpha 4^*$ ). The topology of this protein is similar to the four-helix bundle structure (**Figure 21**).<sup>[136]</sup> All four helices differ in length, position, and orientation. Helix  $\alpha 3^*$  is very short and has one turn, helix  $\alpha 4^*$  is slide downwards and tilted away from both  $\alpha 1$  and  $\alpha 2$ , making Im7 to appear as a V-shaped protein.<sup>[134]</sup> All four helices are connected by loops present up and down (loop 12, loop 34, loop 23).<sup>[134]</sup>

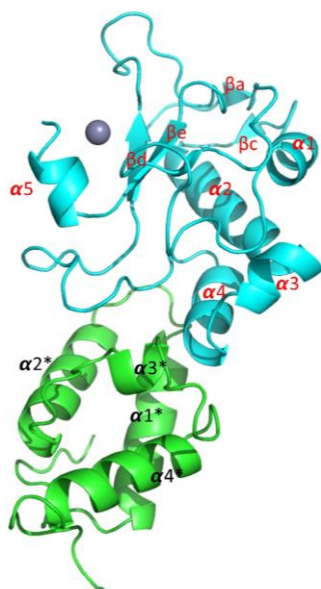


**Figure 21: Structural representation of the interaction of E7-Im7.** This protein interaction model is adapted from PDB: 7CEI. Immunity protein 7 (Im7) is represented in green color. ColE7 DNase is represented in ocean blue. The V-shaped Im7 arm clamps the DNase domain of ColE7 and inhibits the colicin's DNase activity.

Im7 is a V-shaped protein, and E7 clamps around it, two arms of Im7 play a crucial role in protein recognition. One arm is present at the  $\alpha 1^*$ –loop 12– $\alpha 2^*$  region (sequence of this region is variable) and another arm is present at the loop 23– $\alpha 3^*$ –loop 34 region (sequence of this region is more conserved).<sup>[134]</sup> E7 has a highly variable protein recognition site ( $\alpha 4$  and long continuous loop). This variable recognition region of E7 interacts with both conserved and variable recognition regions of Im7.<sup>[134]</sup> Most of the hydrogen bonds of the variable arm of Im7 interact with side chains of E7, and there is one hydrogen bond to a main chain atom of E7. The conserved arm of Im7 interacts with four water-mediated and three direct hydrogen bonds involving the main chain residues of E7.<sup>[134]</sup> The E7-Im7 complex has a  $K_d$  of  $9.3 \times 10^{-17}$  M<sup>[135]</sup>, indicative for extremely tight binding. In this PhD study, the E7-Im7 system was used as an affinity system; for this, the DNase activity of E7 DNase was inactivated by point mutations without comprising the binding ability of the E7-Im7 system.

### 1.7 Objectives of the thesis

The large part of materials and electricity for our everyday life is provided by chemical industries and power industries, respectively. At the same time these industries are also the most polluting industries. Even today, there are processes which produce 100-fold more waste than the product exists. Alternatively, biocatalysis and biophotovoltaics offer clean and sustainable solutions. This thesis will explore the potential for application of components of photosynthetic apparatus and photosynthetic organisms for sustainable chemical production and biophotovoltaics. Particularly, PSI will be used as a photocatalyst for sustainable chemical production. Also, photodynamics of PSI and PSII, isolated or within the live *synechocystis sp.* cells will be investigated to understand the electron transfer.

Firstly, a PSI-Fd-FNR cascade shall be investigated for the light-driven production of NADPH. In this study, various aspects determining the rate of NADPH production will be investigated. The NADPH production will be examined by fluorescence spectroscopy. After finding the optimal reaction conditions, the PSI-Fd-FNR cascade will be coupled with different NADPH dependent oxidoreductases. The yield and enantiopurity of the chiral products will be quantified based on gas chromatography. Additionally, the PSI-Fd-FNR cascade will be deposited on the electrode aiming to establish a photocathode for various purposes.

Secondly, to achieve diffusion limited faster electron transfer between PSI, Fd, and FNR, molecular confinement of these proteins shall be performed. For this, a clickable PSI shall be created by fusing Im7 to the C-terminus of the PsaE subunit of PSI in *Synechocystis sp.* PCC 6803. The isolated PSI-Im7 will be biochemically and spectroscopically characterized. Further, E7 fusion chimeras with only Fd and Fd-FNR consisting of varying linker domains will be created and expressed in *E. coli*. The isolated Im7-PSI will be coupled with the E7-Fd or E7-Fd-FNR fusion proteins through high-affinity binding of the E7/Im7 protein pair. The fusion complexes will be characterized by photo-induced NADPH formation via fluorescence spectroscopy.

Moreover, these fusion complexes shall be deposited in an oriented manner on the electrode surface via the Langmuir Blodgett technique aiming for direct electron transfer with minimal charge recombination and short circuit effect.

## 1.8 References

- [1] M. J. Burk, S. van Dien, *Trends Biotechnol* **2016**, *34*, 187–190.
- [2] P. Anastas, N. Eghbali, *Chem. Soc. Rev.* **2010**, *39*, 301–312.
- [3] H. C. Grimm, R. Kourist, in *Photosynthesis*, De Gruyter, **2021**, pp. 57–92.
- [4] R. Sharma, P. Garg, P. Kumar, S. K. Bhatia, S. Kulshrestha, *Fermentation* **2020**, *6*, 106.
- [5] C. Visvanathan, X. Li, S. Shi, L. A. Averianova, L. A. Balabanova, O. M. Son, A. B. Podvolotskaya, L. A. Tekutyeva, *Front. Bioeng. Biotechnol* **2020**, *8*, 570828.
- [6] S. Parekh, V. A. Vinci, R. J. Strobel, *Appl Microbiol Biotechnol* **2000**, *54*, 287–301.
- [7] Y.-H. Wang, J.-T. Feng, Q. Zhang, X. Zhang, *J Appl Microbiol* **2008**, *104*, 735–744.
- [8] S. Sánchez, A. Chávez, A. Forero, Y. García-Huante, A. Romero, M. Sánchez, D. Rocha, B. Sánchez, M. A. Valos, S. Guzmán-Trampe, R. Rodríguez-Sanoja, E. Langley, B. Ruiz, *J Antibiot* **2010**, *63*, 442–459.
- [9] K. S. Lam, *Biocatalysis for the Pharmaceutical Industry*, John Wiley & Sons, Ltd, Chichester, UK, **2009**, pp. 213–227.
- [10] K. Kieslich, *Acta Biotechnol* **1991**, *11*, 559–570.
- [11] A. Zaks, D. R. Dodds, *Drug Discov Today* **1997**, *2*, 513–531.
- [12] N. M. Shaw, K. T. Robins, A. Kiener, *Adv Synth Catal* **2003**, *345*, 425–435.
- [13] S. M. A. de Wildeman, T. Sonke, H. E. Schoemaker, O. May, *Acc Chem Res* **2007**, *40*, 1260–1266.
- [14] S. Wu, R. Snajdrova, J. C. Moore, K. Baldenius, U. T. Bornscheuer, *Angew. Chem. Int. Ed* **2021**, *60*, 88–119.
- [15] J. Sporty, S.-J. Lin, M. Kato, T. Ognibene, B. Stewart, K. Turteltaub, G. Bench, *Yeast* **2009**, *26*, 363–369.
- [16] B. B. Li, X. Wang, L. Tai, T.-T. Ma, A. Shalmani, W.-T. Liu, W.-Q. Li, K.-M. Chen, *Front Plant Sci* **2018**, *9*, 379.
- [17] C. E. Paul, I. W. C. E. Arends, F. Hollmann, *ACS Catal* **2014**, *4*, 788–797.
- [18] T. Knaus, C. E. Paul, C. W. Levy, S. De Vries, F. G. Mutti, F. Hollmann, N. S. Scrutton, *J Am Chem Soc* **2016**, *138*, 1033–1039.
- [19] S. K. Spaans, R. A. Weusthuis, J. van der Oost, S. W. M. Kengen, *Front Microbiol* **2015**, *6*, 742.
- [20] S. Mordhorst, J. N. Andexer, *Nat Prod Rep* **2020**, *37*, 1316–1333.
- [21] X. Wang, T. Saba, H. H. P. Yiu, R. F. Howe, J. A. Anderson, J. Shi, *Chem* **2017**, *2*, 621–654.
- [22] R. Machielsen, N. G. H. Leferink, A. Hendriks, S. J. J. Brouns, H.-G. Hennemann, T. Daubmann, J. van der Oost, *Extremophiles* **2008**, *12*, 587–594.
- [23] V. I. Tishkov, V. O. Popov, *Biomol Eng* **2006**, *23*, 89–110.
- [24] P. Giardina, M. G. de Biasi, M. de Rosa, A. Gambacorta, V. Buonocore, *Biochemical Journal* **1986**, *239*, 517–522.
- [25] R. B. Iyer, J. Wang, L. G. Bachas, *Extremophiles* **2002**, *6*, 283–289.
- [26] T. W. Johannes, R. D. Woodyer, H. Zhao, *Biotechnol Bioeng* **2007**, *96*, 18–26.
- [27] R. Woodyer, W. van der Donk, H. Zhao, *Comb Chem High Throughput Screen* **2006**, *9*, 237–245.
- [28] L. Lauterbach, O. Lenz, K. A. Vincent, *FEBS Journal* **2013**, *280*, 3058–3068.
- [29] F. Gao, H. Ding, X. Xu, Y. Zhao, *Environ. Sci. Pollut Re.* **2016**, *23*, 21319–21326.
- [30] R. Huang, & H. Chen, W. Zhou, C. Ma, Y.-H. P. Zhang, *Appl Microbiol Biotechnol* **2018**, *102*, 3203–3215.
- [31] K. Tauber, M. Hall, W. Kroutil, W. M. F. Fabian, K. Faber, S. M. Glueck, *Biotechnol Bioeng* **2011**, *108*, 1462–1467.

- [32] H.-T. Ding, D.-F. Liu, Z.-L. Li, Y.-Q. Du, X.-H. Xu, Y.-H. Zhao, *J Appl Microbiol* **2011**, *111*, 1075–1085.
- [33] R. Y. Stanier, R. Kunisawa, M. Mandel, G. Cohen-Bazire, *Bacteriol Rev* **1971**, *35*, 171–205.
- [34] T. Zavřel, P. Očenášová, J. Červený, *PLoS One* **2017**, *12*, 1–21.
- [35] M. Ikeuchi, & Satoshi Tabata, *Photosynth Res* **2001**, *70*, 73–83.
- [36] H. C. Büchschütz, V. Vidimce-Risteski, B. Eggbauer, S. Schmidt, C. K. Winkler, J. H. Schrittwieser, W. Kroutil, R. Kourist, *ChemCatChem* **2020**, *12*, 726–730.
- [37] E. Erdem, L. Malihan-Yap, L. Assil-Companioni, H. Grimm, G. D. Barone, C. Serveau-Avesque, A. Amouric, K. Duquesne, V. de Berardinis, Y. Allahverdiyeva, V. Alphan, R. Kourist, *ACS Catal* **2022**, *12*, 66–72.
- [38] L. Assil-Companioni, H. C. Büchschütz, D. Solymosi, N. G. Dyczmons-Nowaczyk, K. K. F. Bauer, S. Wallner, P. Macheroux, Y. Allahverdiyeva, M. M. Nowaczyk, R. Kourist, *ACS Catal* **2020**, *10*, 11864–11877.
- [39] K. Köninger, Á. Gómez Baraibar, C. Mügge, C. E. Paul, F. Hollmann, M. M. Nowaczyk, R. Kourist, *Angew. Chem. Int. Ed* **2016**, *55*, 5582–5585.
- [40] L. Malihan-Yap, H. C. Grimm, R. Kourist, *Chem Ing Tech* **2022**, *94*, 1628–1644.
- [41] R. Yamanaka, K. Nakamura, A. Murakami, *AMB Express* **2011**, *1*, 24.
- [42] J. Havel, D. Weuster-Botz, *Eng Life Sci* **2006**, *6*, 175–179.
- [43] T. Utsukihara, W. Chai, N. Kato, K. Nakamura, C. A. Horiuchi, *J Mol Catal B Enzym* **2004**, *31*, 19–24.
- [44] K. Shimoda, N. Kubota, H. Hamada, M. Kaji, T. Hirata, *Tetrahedron Asymmetry* **2004**, *15*, 1677–1679.
- [45] S. Rasoul-Amini, E. Fotooh-Abadi, Y. Ghasemi, *J Appl Phycol* **2011**, *23*, 975–981.
- [46] V. Jurkaš, F. Weissensteiner, P. de Santis, S. Vrabl, F. A. Sorgenfrei, S. Bierbaumer, S. Kara, R. Kourist, P. P. Wangikar, C. K. Winkler, W. Kroutil, *Angew. Chem. Int. Ed* **2022**, *61*, 1–10.
- [47] H. Medipally, M. Mann, C. Kötting, W. J. H. van Berkel, M. M. Nowaczyk, *ChemBioChem* **2023**, *24*, 1–10.
- [48] K. Jensen, J. B. Johnston, P. R. O. de Montellano, B. L. Møller, *Biotechnol Lett* **2012**, *34*, 239–245.
- [49] K. P. Sokol, W. E. Robinson, A. R. Oliveira, J. Warnan, M. M. Nowaczyk, A. Ruff, I. A. C. Pereira, E. Reisner, *J Am Chem Soc* **2018**, *140*, 16418–16422.
- [50] M. Ihara, Y. Kawano, M. Urano, A. Okabe, *PLoS One* **2013**, *8*, 1–8.
- [51] C. E. Lubner, R. Grimme, D. A. Bryant, J. H. Golbeck, *Biochemistry* **2010**, *49*, 404–414.
- [52] C. E. Lubner, A. M. Applegate, P. Knörzer, A. Ganago, D. A. Bryant, T. Happe, J. H. Golbeck, *Proc Natl Acad Sci U S A* **2011**, *108*, 20988–20991.
- [53] F. Zhao, F. Conzuelo, V. Hartmann, H. Li, M. M. Nowaczyk, N. Plumeré, M. Rögner, W. Schuhmann, *J Phys Chem B* **2015**, *119*, 13726–13731.
- [54] H. C. Brown, P. Veeraraghavan Ramachandran, *Sixty Years of Hydride Reductions*, ACS Publications, 1996, 1–30.
- [55] J. Dong, E. Fernández-Fueyo, F. Hollmann, C. E. Paul, M. Pesic, S. Schmidt, Y. Wang, S. Younes, W. Zhang, *Angew. Chem. Int. Ed* **2018**, *57*, 9238–9261.
- [56] F. Hollmann, D. J. Opperman, C. E. Paul, *Angew. Chem. Int. Ed* **2021**, *60*, 5644–5665.
- [57] Z. Li, H. Yang, J. Liu, Z. Huang, F. Chen, P. Account, *Chem. Rec* **2021**, *21*, 1611–1630.
- [58] A. S. de Miranda, C. D. F. Milagre, F. Hollmann, *Frontiers in Catalysis* **2022**, *2*, 1–32.
- [59] W. Hummel, *Adv Biochem Eng Biotechnol* **1997**, 145–184.
- [60] M. Kurina-Sanz, F. R. Bisogno, I. Lavandera, A. A. Orden, V. Gotor, *Adv Synth Catal* **2009**, *351*, 1842–1848.



- [61] S. Leuchs, S. Leuchs, L. Greiner, *Chem Biochem Eng Q* **2011**, 25, 267–281.
- [62] S. Bräutigam, D. Dennewald, M. Schürmann, J. Lutje-Spelberg, W. R. Pitner, D. Weuster-Botz, *Enzyme Microb Technol* **2009**, 45, 310–316.
- [63] C. Kohlmann, N. Robertz, S. Leuchs, Z. Dogan, S. Lütz, K. Bitzer, S. Na Amnieh, L. Greiner, *J Mol Catal B Enzym* **2011**, 68, 147–153.
- [64] N. H. Schlieben, K. Niefind, J. Müller, B. Riebel, W. Hummel, D. Schomburg, *J Mol Biol* **2005**, 349, 801–813.
- [65] M. K. Peers, H. S. Toogood, D. J. Heyes, D. Mansell, B. J. Coe, N. S. Scrutton, *Catal Sci Technol* **2016**, 6, 169–177.
- [66] J. Pietruszka, M. Schölzel, *Adv Synth Catal* **2012**, 354, 751–756.
- [67] C. K. Winkler, D. Clay, S. Davies, P. O'Neill, P. McDaid, S. Debarge, J. Steflik, M. Karmilowicz, J. W. Wong, K. Faber, *J Org Chem* **2013**, 78, 1525–1533.
- [68] H. S. Toogood, N. S. Scrutton, *ACS Catal* **2018**, 8, 3532–3549.
- [69] N. N. and A. Ben-Shem, *Nature reviews* **2004**, 5, 1–12.
- [70] R. E. Blankenship, *Molecular Mechanisms of Photosynthesis*, Blackwell Science Ltd, **2002**.
- [71] R. E. Blankenship, R. C. Prince, *Trends Biochem Sci* **1985**, 10, 382–383.
- [72] K. Lendzian, J. A. Bassham, *Biochim et Biophys Acta Bioenerg* **1975**, 396, 260–275.
- [73] B. Wigge, S. Kromer, P. Gardestrom, *Physiol Plant* **1993**, 88, 10–18.
- [74] D. A. Semchonok, M. Li, B. D. Bruce, G. T. Oostergetel, E. J. Boekema, *Biochim et Biophys Acta Bioenerg* **2016**, 1857, 1619–1626.
- [75] P. Jordan, P. Fromme, H. T. Witt, O. Klukas, W. Saenger, N. Krauss, *Nature* **2001**, 411, 909–917.
- [76] P. Fromme, P. Jordan, N. Krauß, *Biochim et Biophys Acta Bioenerg* **2001**, 1507, 5–31.
- [77] K. Brettel, W. Leibl, *Biochim et Biophys Acta Bioenerg* **2001**, 1507, 100–114.
- [78] N. Fischer, M. Hippler, P. Sétif, J. P. Jacquot, J. D. Rochaix, *EMBO Journal* **1998**, 17, 849–858.
- [79] R. Jeanjean, A. Latifi, H. C. P. Matthijs, M. Havaux, *Biochim et Biophys Acta Bioenerg* **2008**, 1777, 308–316.
- [80] J. J. Van Thor, T. H. Geerlings, H. C. P. Matthijs, K. J. Hellingwerf, **1999**, 38, 12735–12746
- [81] J. Li, N. Hamaoka, F. Makino, A. Kawamoto, Y. Lin, M. Rögner, M. M. Nowaczyk, Y.-H. Lee, K. Namba, C. Gerle, G. Kurisu, *Commun Biol* **2022**, 5, 951.
- [82] N. Cassan, B. Lagoutte, P. Sétif, *J Biol Chem* **2005**, 280, 25960–25972.
- [83] A. H. Teodor, B. D. Bruce, *Trends Biotechnol* **2020**, 38, 1329–1342.
- [84] K. Nguyen, B. D. Bruce, *Biochim Biophys Acta Bioenerg* **2014**, 1837, 1553–1566.
- [85] D. Nii, M. Miyachi, Y. Shimada, Y. Nozawa, M. Ito, Y. Homma, S. Ikehira, Y. Yamanoi, H. Nishihara, T. Tomo, *Photosynth Res* **2017**, 133, 155–162.
- [86] T. Kothe, N. Plumeré, A. Badura, M. M. Nowaczyk, D. A. Guschin, M. Rögner, W. Schuhmann, *Angew. Chem. Int. Ed* **2013**, 52, 14233–14236.
- [87] U. Muhlenhoff, J. Zhao, D. A. Bryant, *Eur J Biochem* **1996**, 235, 324–331.
- [88] A. Petrova, M. Mamedov, B. Ivanov, A. Semenov, M. Kozuleva, *Photosynth Res* **2018**, 137, 421–429.
- [89] N. Torabi, X. Qiu, M. López-Ortiz, M. Loznik, A. Herrmann, A. Kermanpur, A. Ashrafi, R. C. Chiechi, *Langmuir* **2021**, 37, 11465–11473.
- [90] A. Mershin, K. Matsumoto, L. Kaiser, D. Yu, M. Vaughn, K. Nazeeruddin, B. D. Bruce, M. Graetzel, S. Zhang, *Sci. Rep* **2012**, 2, 1–7.
- [91] M. Hervás, J. A. Navarro, B. De La Cerda, A. Díaz, M. A. De La Rosa, *Bioelectrochemistry* **1997**, 42, 249–254.
- [92] G. Moal, B. Lagoutte, *Biochim Biophys Acta Bioenerg* **2012**, 1817, 1635–1645.

- [93] F. Zhao, S. Hardt, V. Hartmann, H. Zhang, M. M. Nowaczyk, M. Rögner, N. Plumeré, W. Schuhmann, F. Conzuelo, *Nat Commun* **2018**, 9, 1973.
- [94] N. Terasaki, N. Yamamoto, T. Hiraga, Y. Yamanoi, T. Yonezawa, H. Nishihara, T. Ohmori, M. Sakai, M. Fujii, A. Tohri, M. Iwai, Y. Inoue, S. Yoneyama, M. Minakata, I. Enami, *Angew. Chem. Int. Ed* **2009**, 48, 1585–1587.
- [95] D. Gunther, G. Leblanc, D. Prasai, J. R. Zhang, D. E. Cliffel, K. I. Bolotin, G. K. Jennings, *Langmuir ACS* **2013**, 29, 4177–4180.
- [96] K. D. Wolfe, D. Dervishogullari, C. D. Stachurski, J. M. Passantino, G. Kane Jennings, D. E. Cliffel, *ChemElectroChem* **2020**, 7, 596–603.
- [97] C. Cassier-Chauvat, F. Chauvat, *Life* **2014**, 4, 666–680.
- [98] J. Mondal, B. D. Bruce, *Photosynthetica* **2018**, 56, 279–293.
- [99] J. M. Schuller, J. A. Birrell, H. Tanaka, T. Konuma, H. Wulfhorst, N. Cox, S. K. Schuller, J. Thiemann, W. Lubitz, P. Sétif, T. Ikegami, B. D. Engel, G. Kurisu, M. M. Nowaczyk, *Science* **2019**, 363, 257–260.
- [100] G. Hanke, P. Mulo, *Plant Cell Environ* **2013**, 36, 1071–1084.
- [101] S. Rumpel, J. S. Iebel, M. Iallo, C. Far, E. J. Reijerse, W. Ubitz, *ChembioChem* **2015**, 16, 1663–1669.
- [102] H. Mustila, Y. Allahverdiyeva, J. Isojärvi, E. M. Aro, M. Eisenhut, *Biochim Biophys Acta Bioenerg* **2014**, 1837, 1293–1304.
- [103] B. Marteyn, F. Domain, P. Legrain, F. Chauvat, C. Cassier-Chauvat, *Mol Microbiol* **2009**, 71, 520–532.
- [104] K. Gutekunst, X. Chen, K. Schreiber, U. Kaspar, S. Makam, J. Appel, *J Biol Chem* **2014**, 289, 1930–1937.
- [105] H. Kubota-Kawai, R. Mutoh, K. Shinmura, P. Sétif, M. M. Nowaczyk, M. Rögner, T. Ikegami, H. Tanaka, G. Kurisu, *Nat Plants* **2018**, 4, 218–224.
- [106] A. G. McDonald, K. F. Tipton, *FEBS J* **2023**, 2214–2231.
- [107] N. Carrillo, E. A. Ceccarelli, *Eur J Biochem* **2003**, 270, 1900–1915.
- [108] D. Kannchen, J. Zabret, R. Oworah-Nkruma, N. Dyczmons-Nowaczyk, K. Wiegand, P. Löbber, A. Frank, M. M. Nowaczyk, S. Rexroth, M. Rögner, *Biochim Biophys Acta Bioenerg* **2020**, 1861, 1–11.
- [109] H. Liu, D. A. Weisz, M. M. Zhang, M. Cheng, B. Zhang, H. Zhang, G. S. Gerstenecker, H. B. Pakrasi, M. L. Gross, R. E. Blankenship, *mBio* **2019**, 10, 1–12.
- [110] H. C. P. Matthijs, S. J. Coughlan, G. Hind, *J Biol Chem* **1986**, 261, 12154–12158.
- [111] J. P. Benz, A. Stengel, M. Lintala, Y.-H. Lee, A. Weber, K. Philipp, I. L. Gü Gel, S. Kaieda, T. Ikegami, P. Mulo, J. Soll, B. Bölker, *Plant Cell* **2009**, 21, 3965–3983.
- [112] I. Yacoby, S. Pochekailov, H. Toporik, M. L. Ghirardi, P. W. King, S. Zhang, *Proc. Natl Acad. Sci. USA* **2011**, 108, 9396–9401.
- [113] M. Iwai, K. Takizawa, R. Tokutsu, A. Okamuro, Y. Takahashi, J. Minagawa, *Nature* **2010**, 464, 1210–1213.
- [114] J. Tejero, M. Martínez-Júlvez, T. Mayoral, A. Luquita, J. Sanz-Aparicio, J. A. Hermoso, J. K. Hurley, G. Tollin, C. Gómez-Moreno, M. Medina, *J Biol Chem* **2003**, 278, 49203–49214.
- [115] C. J. Batie, H. Kamin, *J Biol Chem* **1984**, 259, 11976–11985.
- [116] F. S. Aalbers, M. W. Fraaije, *ChemBioChem* **2019**, 20, 20–28.
- [117] D. E. Torres Pazmiño, R. Snajdrova, B.-J. Baas, M. Ghobrial, M. D. Mihovilovic, M. W. Fraaije, *Angew. Chem. Int. Ed* **2008**, 120, 2307–2310.
- [118] F. S. Aalbers, M. W. Fraaije, *Appl Microbiol Biotechnol* **2017**, 101, 7557–7565.
- [119] R. A. George, J. Heringa, *Protein Eng, Des and Sel.* **2002**, 15, 871–879.
- [120] X. Chen, J. L. Zaro, W. C. Shen, *Adv Drug Deliv Rev* **2013**, 65, 1357–1369.
- [121] G. Wittenberg, W. Sheffler, D. Darchi, D. Baker, D. Noy, *Phys. Chem Chem Phys* **2013**, 15, 19608–19614.

## Chapter 1

- [122] R. E. Bird, K. D. Hardman, J. W. Jacobson, S. Y. D. Johnson, B. M. Kaufman, S. Lee, T. Lee, S. H. Pope, G. S. Riordan, M. Whitlow, *Science* **1988**, 242, 423–426.
- [123] N. Amet, H.F. Lee, W.C. Shen, *Pharm Res* **2009**, 26, 523–528.
- [124] E. Greenbaum, *Science* **1985**, 230, 1373–1375.
- [125] J. W. Lee, C. V. Tevault, S. L. Blankinship, R. T. Collins, E. Greenbaum, *Energy & Fuels* **1994**, 8, 770–773.
- [126] B. R. Evans, H. M. O’neill, S. A. Hutchens, B. D. Bruce, E. Greenbaum, *Nano Letter* **2004**, 4, 1815–1819.
- [127] L. Yu, J. Zhao, W. Lu, D. A. Bryant, J. H. Golbeck, *Biochemistry* **1993**, 32, 8251–8258.
- [128] L. Yu, I. R. Vassiliev, Y. S. Jung, D. A. Bryant, J. H. Golbeck, *J Biol Chem* **1995**, 270, 28118–28125.
- [129] R. A. Grimme, C. E. Lubner, J. H. Golbeck, *Dalton Trans* **2009**, 10106–10113.
- [130] M. Ihara, H. Nishihara, K.-S. Yoon, O. Lenz, B. Friedrich, H. Nakamoto, K. Kojima, D. Honma, T. Kamachi, I. Okura, *Photochem Photobiol* **2006**, 82, 676-682.
- [131] J. Appel, V. Hueren, M. Boehm, K. Gutekunst, *Nat Energy* **2020**, 5, 458–467.
- [132] A. Kanygin, Y. Milrad, C. Thummala, K. Reifschneider, P. Baker, P. Marco, I. Yacoby, K. E. Redding, *Energy Environ Sci* **2020**, 13, 2903–2914.
- [133] S.C. Yang, C.H. Lin, C. T. Sung, J.Y. Fang, *Front Microbiol* **2014**, 5, 1–10.
- [134] T.P. Ko, C.C. Liao, W.Y. Ku, K.F. Chak, H. S. Yuan, *Structure* **1999**, 7, 91–102.
- [135] R. Wallis, G. R. Moore, R. James, C. Kleanthous, *Biochemistry* **1995**, 34, 13743–13750



## Chapter 2: Parameters of photosynthesis relevant for a biotechnological application

Hitesh Medipally, Marc M. Nowaczyk, Matthias Rögner

### Publication 1

**Photosynthesis: Biotechnological Applications with  
Microalgae,  
De Gruyter, 2021, pp. 1-30.**

**<https://doi.org/10.1515/9783110716979-001>**

**Abstract:** This chapter introduces natural photosynthesis and the potential of its redesign in living organisms. Due to their high application potential in biotechnology, microalgae are the focus of this chapter. We do not cover the potential of semi-artificial and artificial photosynthesis as this was recently laid out in a detailed report of Acatech.<sup>[1]</sup> Instead, we emphasize the significance of such systems for the development and improvement of modified natural systems and show their potential and limitations. Besides the design of such self-reproducing organisms and the state-of-the-art methods involved, we also focus on the design of the environment, especially on the optimization of photobioreactors and new developments.

## 2.1 Photosynthesis in microalgae – evolution and limitations

### 2.1.1 What are “microalgae”?

Microalgae comprise both pro- and eukaryotic single cell organisms living either in seawater or freshwater (Fig. 1). Their sizes range between about 1 and 50  $\mu\text{m}$  with some colonies consisting of cell clusters. As phototrophs, they are capable to survive through photosynthesis, synthesizing high energy organic compounds from inorganic materials using light as an energy source. Notably, microalgae are primary producers in aquatic environments with tens of thousands of species growing far more quickly than land plants (Fig. 2). As they can easily be (mass) cultivated, they have a great potential to be used in bioindustry, provided they are purified and isolated. Under stable conditions, their energy production efficiency is reportedly around ten times higher than for land plants.<sup>[2,3]</sup>

### 2.1.2 Which premises are relevant for picking a suitable model organism?

For biotechnological applications depending on the desired product, it may be mandatory that the organism is genetically transformable, has a low doubling time, is genetically stable and is robust. Additionally, the large range of microalgae existing in nature (most still being uncharacterized) also allows to choose species adapted to extreme environmental conditions such as psychrophilic algae ( $<15\text{ }^{\circ}\text{C}$ ) (tolerating low temperatures) and thermophiles ( $45\text{--}70\text{ }^{\circ}\text{C}$ ) which may be advantageous for various biotechnological applications.

## Chapter 2

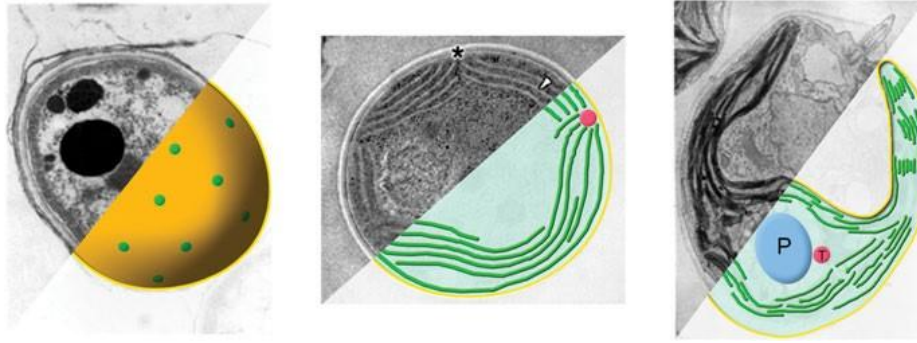


**Figure 1: Three microalgae species representing various levels of complexity:** evolutionarily *Gloeobacter* represents one of the most simple structured cells (left, lacking an internal membrane system), followed by *Synechocystis* PCC 6803 (middle, with internal membrane system consisting of various layers). In contrast to these two bacterial species, *Chlamydomonas reinhardtii* (right) belongs to the eukaryotes and provides a chloroplast as organelle. Common to all three species is the presence of thylakoid membranes (green), which harbor the components of the photosynthetic electron transport chain (Fig. acc. to ref. 4).

In this context, it may be useful to mention that the upper limit of microalgae performing oxygenic photosynthesis may be around 70-75 °C, while in case of thermophiles individual components like isolated photosystems (i.e., PS1) can tolerate much higher temperatures. With respect to future mass cultivation and to the final economic evaluation of the process costs it may be important whether a freshwater or a seawater/marine organism is chosen: In case of a location close to the sea, choosing a marine organism may save considerable costs, especially as freshwater is becoming more and more limiting (current global percentages of seawater vs. freshwater being approx. 97.5%/ 2.5%).

Here, we have chosen *Synechocystis* sp. PCC 6803 (see above, hereafter *Synechocystis*) as a model organism to illustrate the internal composition of the photosynthetic machinery and the most decisive parameters for future biotechnological applications. However, in principle, most of these parameters are valid for all kinds of microalgae (and even with some minor deviations for higher plants).

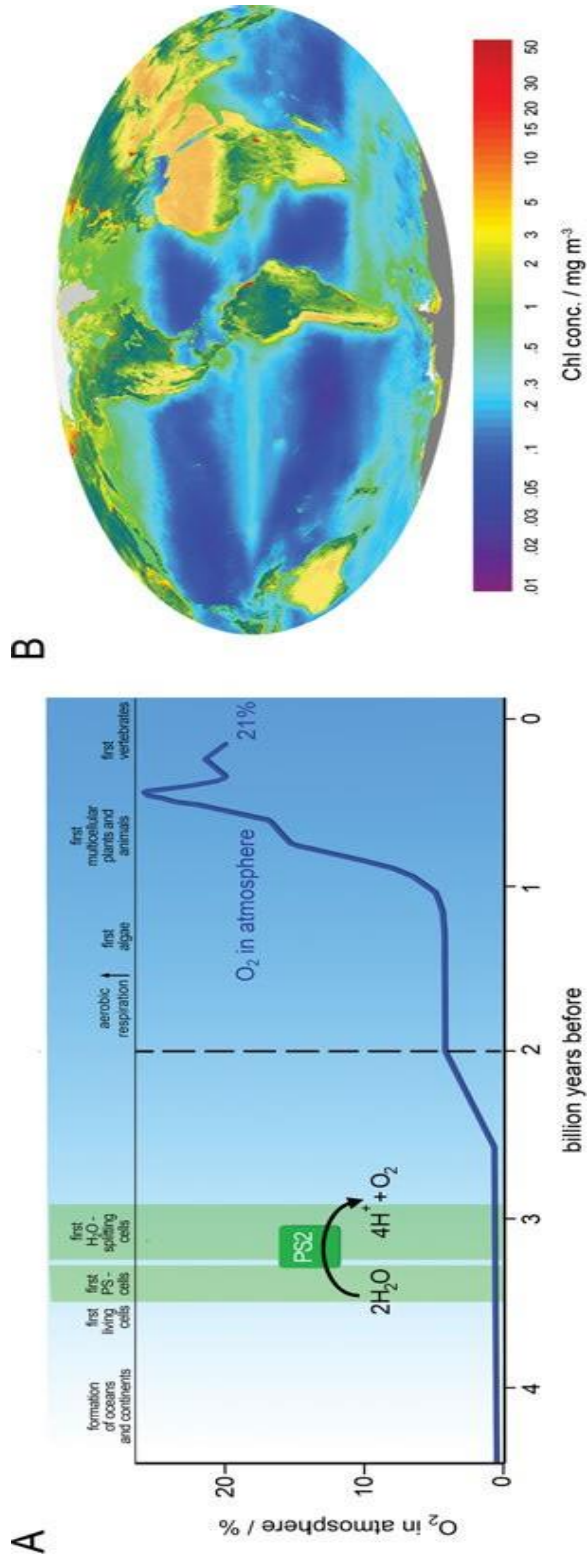


**Figure 2:** (A) Evolution of water-splitting photosynthesis goes in line with a transformation of the atmosphere. (B) Distribution of photosynthetic organisms worldwide according to chlorophyll measurements from space (figures from ref. 5, 6).

### 2.1.3 What are the rate-limiting aspects of photosynthetic efficiency?

Figure 3A shows the major electron transport (ET) routes in cyanobacterial membranes: while the outer cytoplasmic membrane provides the respiratory ET chain but lacks both photosystems, the focus of biotechnological engineering should be the thylakoid membrane (TM) which contains the complete photosynthetic ET chain, starting with the light-triggered water-splitting reaction at PS2 up to the acceptor side of PS1, which plays a central role in energy distribution, depending on physiological requirements.

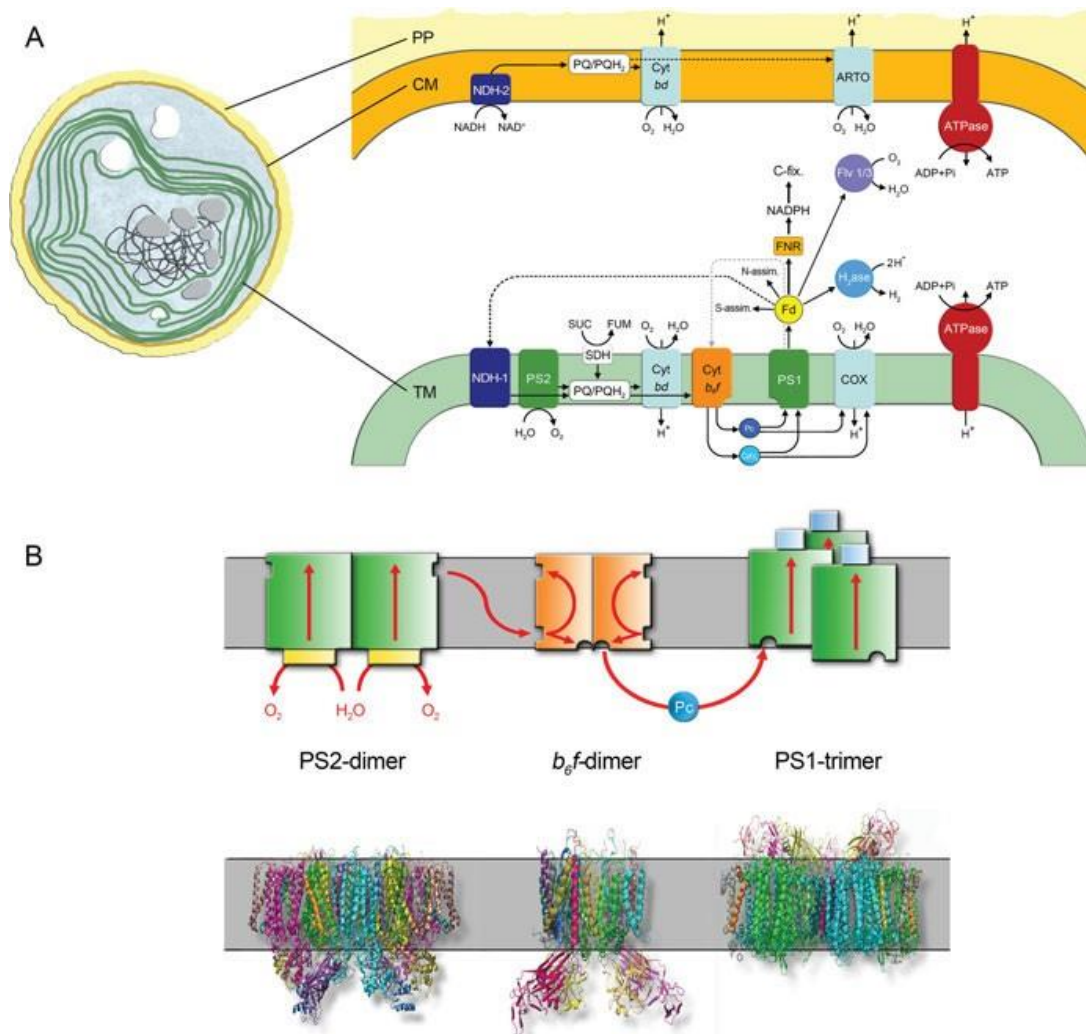


**Figure 3:** (A) Membrane systems in the cyanobacterial *Synechocystis* cell and major electron flows in cytoplasmic (CM) and thylakoid (TM) membrane. (B) Crystal structures of the three major photosynthetic electron transport complexes (PS2, *b*<sub>6</sub>*f* and PS1<sup>[7-9]</sup>) and schematic view of their electron transport routes.

## Chapter 2

Figure 3B, based on structural investigations on the molecular level, reveals that all three intrinsic membrane protein complexes (PS2, Cyt. *b<sub>6</sub>f* complex and PS1) form oligomeric complexes, which in case of PS1 and PS2 are also active as (isolated) monomers, whereas the *b<sub>6</sub>f* complex requires a dimeric state to function. Within the TM, depending on the light conditions, the oligomeric complexes of PS2 and PS1 are in equilibrium with the respective monomers.

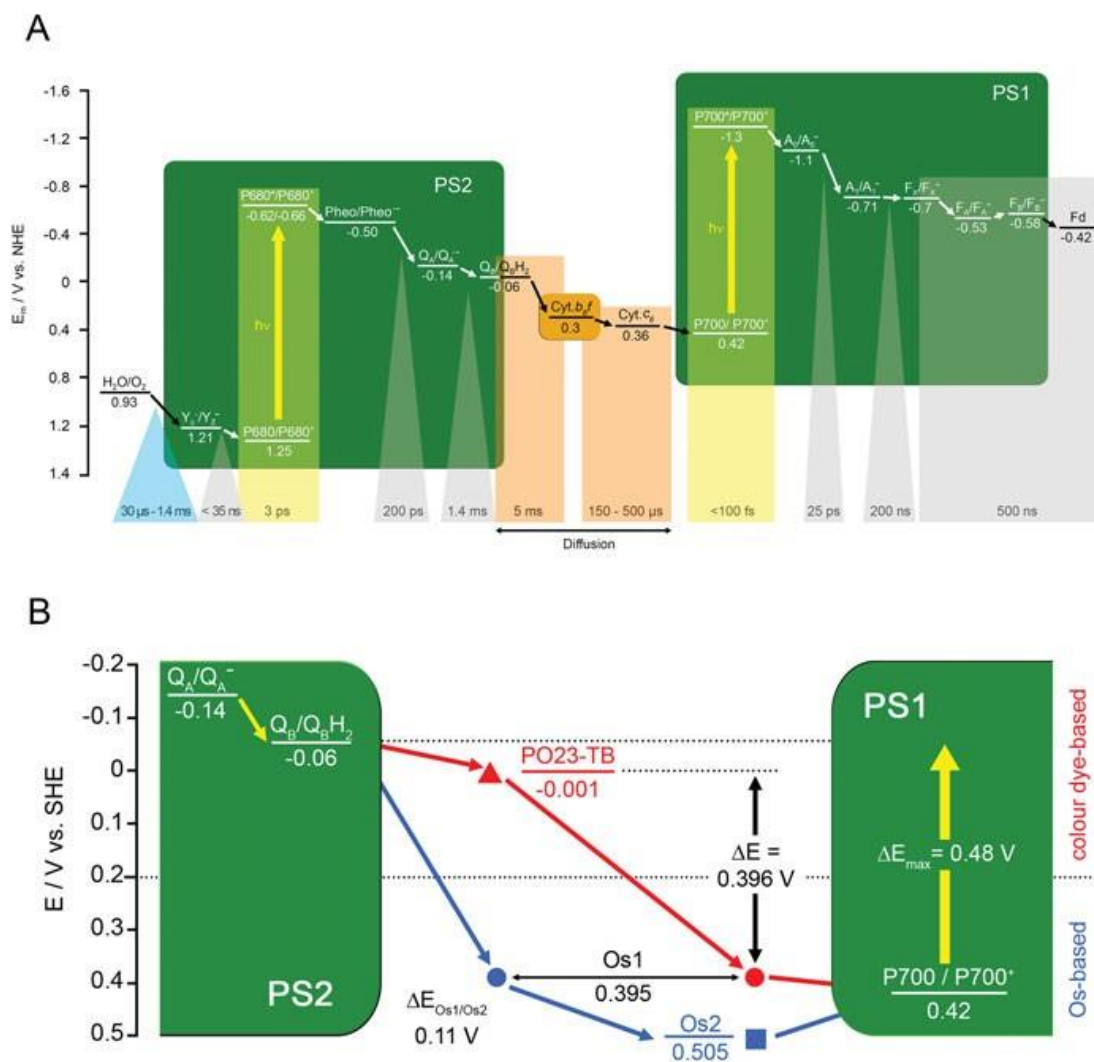


**Figure 4:** (A) Redox components and kinetics of the photosynthetic light reactions in the thylakoid membrane, involving PS2, Cyt. *b<sub>6</sub>f* and PS1, arranged in sequence for linear electron transport. <sup>[4]</sup> (B) Redox situation in a semiartificial minimal device supplemented by synthetic components ("biobattery"): PS2-based photoanode and PS1-based photocathode, being connected by Os polymers (Os1 and Os2) or, alternatively, by a phenothiazine-modified polymer in combination with Os1, realizing a semiartificial Z-scheme. <sup>[11]</sup>



This reflects the high adaptability of the cellular system to changing light conditions which is difficult/impossible to imitate in a semiartificial system. Figure 4 shows the kinetics of electron flow through this light-powered ET chain. Apparently, PQ reduction at PS2 is the rate-limiting step for the light reaction.<sup>[10]</sup> In the absence of this step and other limitations, the light-triggered reactions of PS2 and PS1 could proceed with much higher speed, which is decisive for an evaluation of the capacity of photosynthetic systems and their potential for biotechnological applications. This can be convincingly demonstrated with a semiartificial system, consisting of isolated photosystems which are immobilized on gold electrodes (Figs. 4 and 5, respectively).<sup>[11]</sup> In this case, the function of the Cyt. *b<sub>6</sub>f* complex is replaced by an artificial tailor-made redox polymer, that is, osmium polymers and/or phenothiazine, respectively, which enable to immobilize photosystems on the electrode surfaces.<sup>[12]</sup> They are not rate limiting and guarantee an optimized downhill electrode transport (Fig. 4B). It was shown that in case of PS1 the ET rate under these conditions could be extended by at least a factor of 6<sup>[13]</sup>. In case of PS2, the water-splitting reaction occurring in a time range of about 1.4 ms is rate limiting, but under the conditions of the semiartificial device this could be compensated by using larger amounts of PS2 at the anode side than PS1 at the cathode side. In contrast, natural *Synechocystis* cells contain up to 10-fold more PS1 than PS2<sup>[14]</sup>; thus, the ET is not balanced and the much smaller amount of PS2 is limiting the whole ET reaction.

The semiartificial device is an extremely useful model system to simulate the most effective transformation of harvested light energy into electric energy, especially as all components of this minimalized system can be optimized separately. However, despite a considerable stabilization of the photosystems by embedding them in polymer systems with appropriate redox polymers, the stability of this biobattery is limited by PS2 being subject to photooxidative damage.<sup>[15]</sup> In contrast, the natural cell has developed some protection strategies such as replacement of the damaged parts (especially subunit D1 of PS2) within very short time periods, that is, 20-30 min. Such an efficient biogenesis and repair system<sup>[16]</sup> is difficult or impossible to realize in an engineered or semiartificial system but very important for a biotechnological application of photosynthesis. Another advantage of the cellular system is the dynamic adjustment to external light conditions by switching between D1 variants with different properties.<sup>[17]</sup> under low light, the more efficient D1 copy is used (PsbA1), being however not very light tolerant. In contrast, under high light (HL) a slightly less efficient D1 copy (PsbA3) enables more light protection due to faster charge recombination.<sup>[18]</sup> Figure 6 shows the resulting different reactions of PS2 due to the exchange of D1 copies under HL conditions.

## Chapter 2

An extremely efficient system was recently found in algae growing on desert sand crusts under harsh environmental conditions (filamentous cyanobacteria *Microcoleus* sp., Fig. 7A) which are immediately lethal for “normal” (mesophilic) algae. Apparently, their survival strategy involves alterations in energy transfer from the antennae to the reaction centers in dependence of the diurnal desiccation/rehydration cycles and the activation of a nonradiative charge recombination due to a smaller redox gap between  $P_{680}^{+}$  and  $Q_A^{-}$  (Fig. 7B).<sup>[20]</sup> In consequence, an alternative pheophytin-independent recombination may minimize the damaging  $^1O_2$  production associated with radiative recombination.<sup>[21]</sup> These desert organisms could be the blueprint for strategies to overcome damage by extreme HL intensities and dryness, especially as deserts provide unlimited space for mass cultivation of algae under HL conditions.



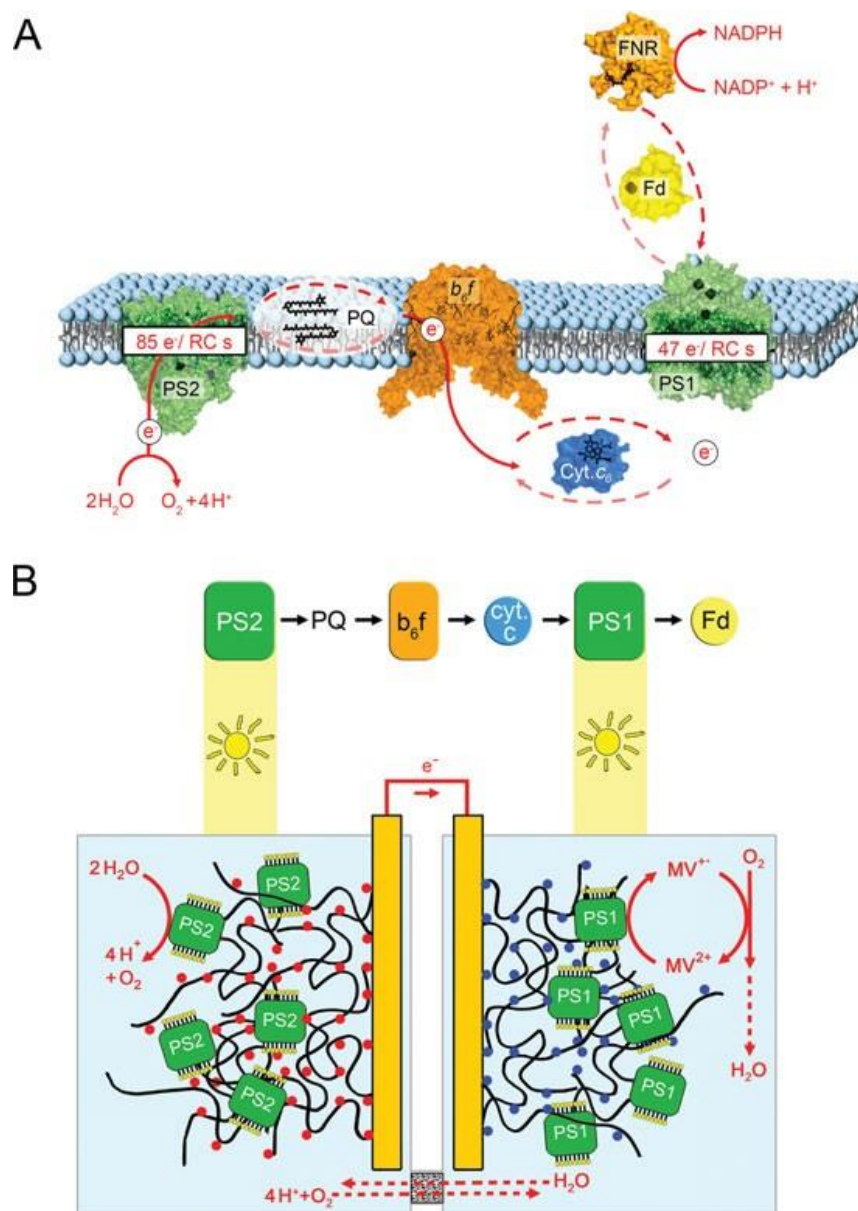


**Figure 5:** Kinetics of photosynthetic electron flow in native thylakoid membranes (A) in comparison with a semiartificial device (biobattery). (B) with isolated photosystems embedded and immobilized into a matrix of two osmium polymers with appropriate redox potentials at the acceptor side of PS2 (red) and at the donor side of PS1 (blue), respectively. <sup>[11]</sup>

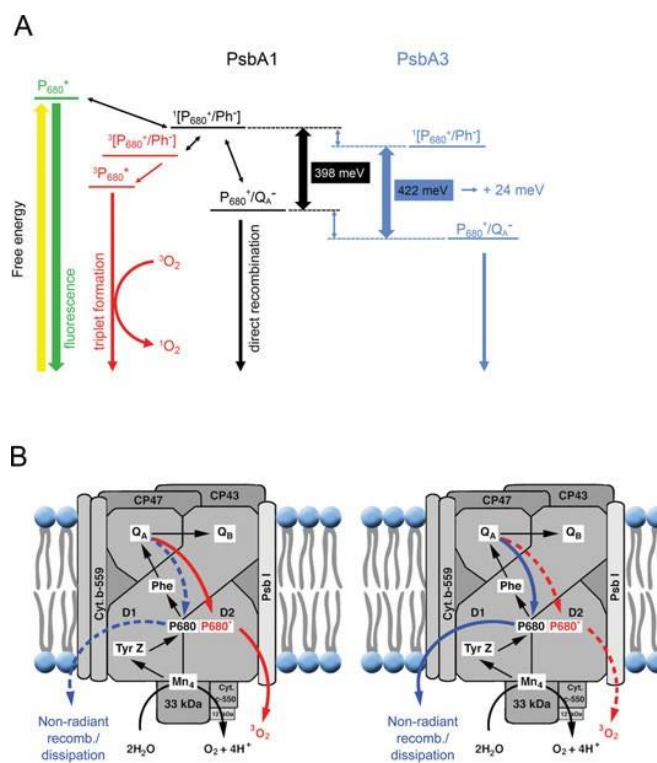


**Figure 6:** (A) High light (PsbA1) and low light (PsbA3) copies of the D1 subunit in PS2 on the redox scale <sup>[19]</sup> and (B) with correlated reactions of PS2 electron flow. <sup>[17]</sup>

In the cellular environment, the above introduced light reactions are combined with the so-called dark reactions, which are better designated as “C-fixation reactions.” Essentially, they use energy (ATP), and redox equivalents (NADPH) generated during the light reaction and CO<sub>2</sub> (from the air) to synthesize sugar compounds as energy storage for periods without light (i.e., nighttime, shading, etc.). Considering the efficiency of photosynthesis-dependent biotechnological processes, it would be reasonable to rate “quantum efficiency” as the efficiency of each light quantum which hits the TM to trigger a primary reaction in PS1 and PS2 especially as (sun) light is available in large excess and for free. Following this definition, the efficiency of PS1 and PS2 is beyond 99% according to a measurable charge separation across the TM occurring within a few nanoseconds. However, if compared with technical systems such as solar cells <sup>[22]</sup>, efficiency must be based on the full solar spectrum of which the photosynthetically active radiation (PAR) corresponds to approximately 45%. For this reason, primary photosynthetic events start with an efficiency of max. 45%, which decreases with the following ET chain between PS2 and PS1 to theoretically max. 17% (Fig. 8). Due to loss of energy during each electron transfer step, the efficiency of one of the first measurable final products, “sugar,” is typically less than 1%. However, for microalgae in bubbled bioreactors a maximum of 5–7% under optimal conditions has been estimated. <sup>[23]</sup>

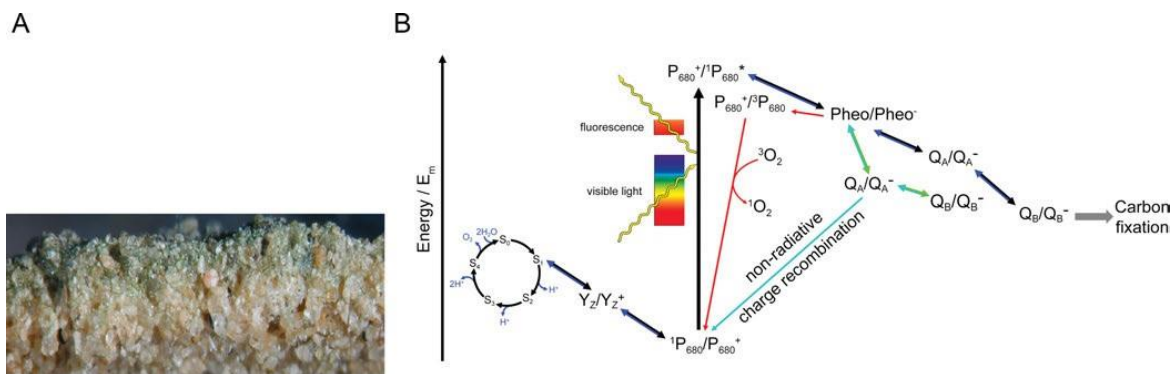


**Figure 7:** (A) Side view perpendicular to the surface of a natural sand crust with a cyanobacterial filament layer on top (*Microcoleus* sp. [20]). (B) Non-radiative charge recombination in *Microcoleus* PS2 due to changes in the redox potential of  $Q_A$  and  $Q_B$  sites (blue arrows: forward ET; green arrows: protective route) (Fig. taken from ref. 21); reactions generating singlet oxygen marked in red.

## Chapter 2

The major gap in efficiency occurs between light and dark reactions, and the major general reason is the fundamental difference in the kinetics of the reactions involved (see time range in Fig. 8).

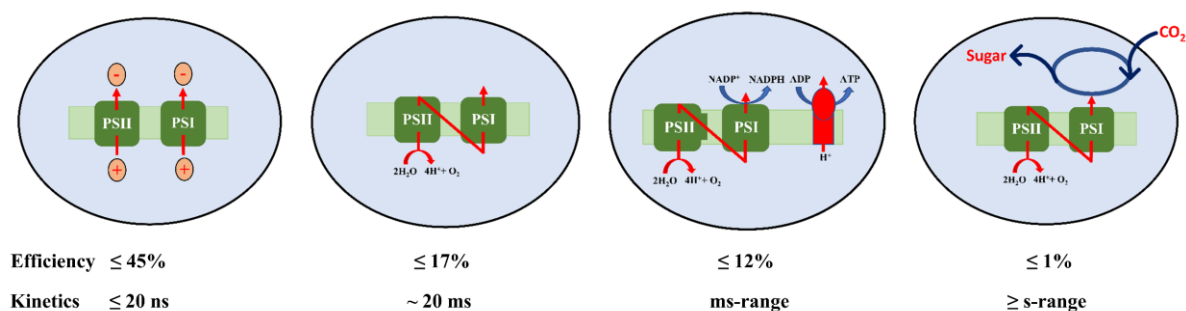


**Figure 8:** Efficiency of major steps in photosynthetic reactions starting from 100% incident sunlight: processes of the light reactions in the thylakoid membrane. <sup>[4]</sup>

While all light reactions occur in the pico- and (lower) ms range, the  $CO_2$ -fixation reaction catalyzed by ribulose-bisphosphate-carboxylase (Rubisco) in microalgae has a turnover of 0.3 per second, which is combined with a general inefficiency of the  $CO_2$ -fixing enzymes and pathways. This is the reason for the 99% loss of the harvested light energy. In consequence, using algae to produce biomass via photosynthesis is energetically an extreme waste of energy. Biotechnologically, the best gain of the harvested light energy would be to use the electrons directly from the acceptor sites of the two photosystems, that is, PS2 and PS1. Which portion of the available electrons can be harvested without seriously compromising downstream reactions relevant for the survival of the cell (C-fixation reactions, etc.). Efficiency measurements of whole cells under HL conditions show that a considerable amount of the harvested light energy under these conditions cannot be used due to a blockage of electron flow at the slow dark reactions. To prevent HL-induced damage via photo-oxidative effects, the cell releases this surplus energy as fluorescence and heat, which of course is also a considerable waste of energy. The energy released as heat and/or fluorescence can amount to about 70% of the absorbed radiation energy. Preliminary studies have shown that a considerable part of this energy may be used if an appropriate sink is available in the cells (see Fig. 9). There are also indications that more than two-thirds of the so-called carbon partitioning could be used to create other products. Examples are a more than 80% carbon partitioning rate into ethanol reported by Kopka et al. <sup>[24]</sup> and close to 70% by Savakis et al. <sup>[25]</sup>. However, optimization toward such goals normally requires various steps of metabolic engineering involving also approaches of synthetic biology.

## 2.2 Tuning of intrinsic PS parameters relevant for application

Figure 9 provides an overview on the possible targets for manipulating the ET on a cellular level. Most of these parameters have been experimentally tested and some of the results will be presented as examples in the following section.

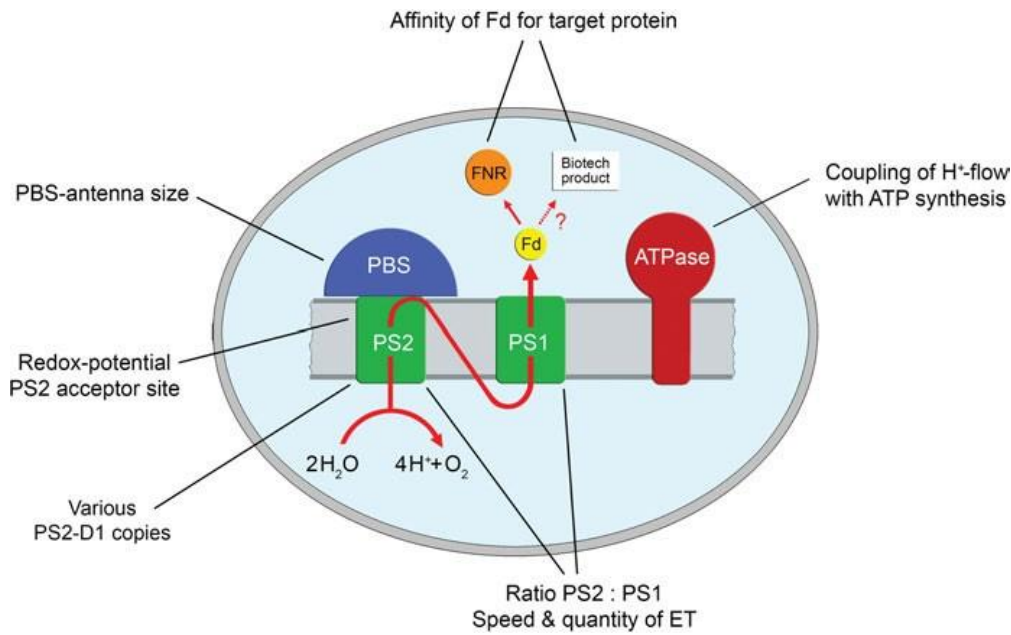


**Figure 9: Impact sites for manipulation of cellular photosynthetic electron transport (ET):** uncoupling ATPase yields a rate increase of ET by about a factor of 2<sup>[26]</sup>, switching to a different PS2-D1 copy yields stabilization<sup>[18]</sup>, truncation of PBS increases the ratio of PS2/PS1 with corresponding speeding up of ET<sup>[27]</sup> and engineering of Fd/FNR, for example, increases H<sub>2</sub> photoproduction yields by a factor of 18, while decreasing FNR activity.<sup>[28]</sup>

### 2.2.1 Manipulation of light harvesting

Reduction of the phycobilisome (PBS) antenna size promotes biotechnological application of photosynthesis in many ways:

- PBS constitute up to 63% <sup>[29, 30]</sup> of the soluble cellular proteins, that is, PBS reduction can save tremendous energy for the synthesis of other products.
- Reduction or even deletion of PBS increases the PS2/PS1 ratio of the cell from approximately 1:5 to up to 1:1 (F. Mamedov, pers.com.). As the PS2 content is the bottleneck for electron supply from the water-splitting reaction, this in parallel increases the linear ET up to a factor of 5.5 as can be shown by light-dependent oxygen evolution measurements.<sup>[31]</sup> This additional electron supply can be used for the generation of biotechnological products.
- A smaller PBS antenna size also enables to tolerate significantly higher light intensities such as direct exposure to bright sunlight which is relevant for biotechnological mass cultivation under extreme conditions as known from deserts <sup>[14]</sup>. Due to self-shading effects, reduction of PBS antenna size also enables higher cell densities, that is, more product formation, in mass cultures. <sup>[27]</sup>

However, the complete removal of PBS as in case of the PAL mutant (Fig. 10) apparently causes major metabolic problems as shown by quantitative proteomics. <sup>[14, 30]</sup> For this reason, a balance between positive and negative effects is crucial in optimizing a design cell for biotechnological applications. The olive mutant seems to represent the best compromise for this purpose. <sup>[31]</sup>

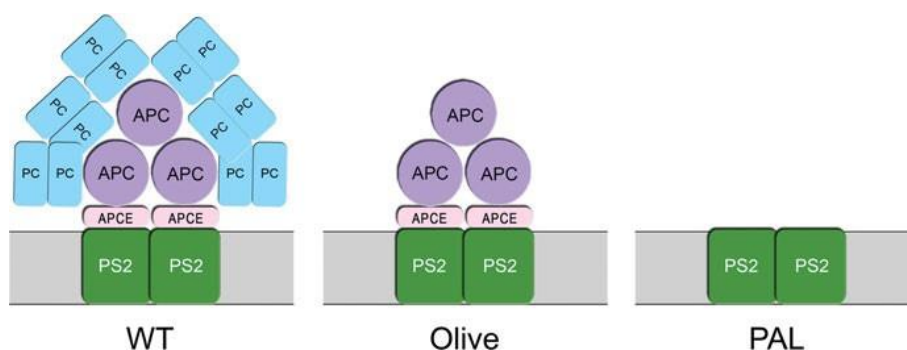


**Figure 10:** Phycobilisome antenna sizes of *Synechocystis* PCC 6803 wildtype (WT) cells and mutants Olive and PAL. The olive mutant lacks the PC (phycocyanin) subunits, while in the PAL mutant phycobilisomes are abolished entirely. <sup>[27]</sup>

Another approach to optimize light harvesting could be an antenna extension into the infrared (IR) range (Fig. 11). Such an antenna already exists in photosynthetic bacteria which contain only one photosystem (PS1 or PS2 precursor without water-splitting ability). If integrated into the oxygenic photosynthesis of cyanobacteria, such IR-ranged antenna could increase the



quantum efficiency by using a range of the sunlight spectrum up to now completely unused, especially if both photosystems would be equipped with different antennae. [33]

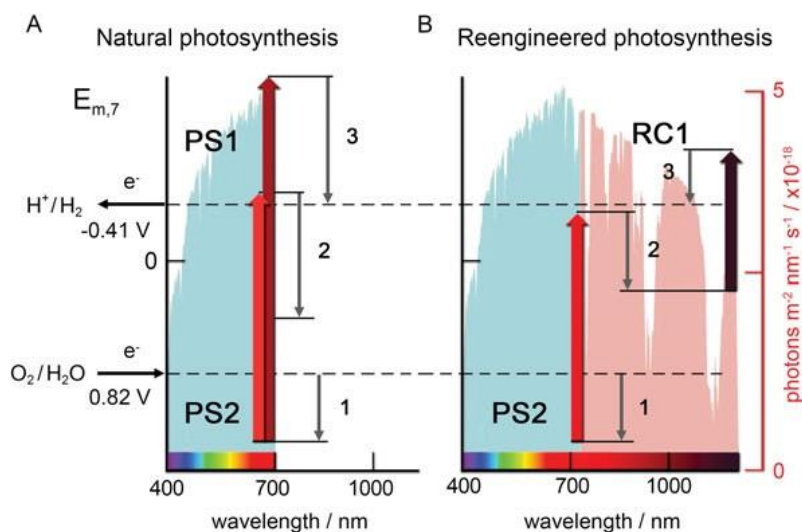


**Figure 11:** Photoelectrochemical energy capture diagram for natural (A) and engineered (B) photosynthesis, according to the thermodynamic principles for improved efficiency. In (B) PS1 is replaced by RC1, a new reaction center with farther-red-absorbing Chl pigments, which increases the photosynthetic efficiency by approximately doubling the solar photon capture. For further details, see [33] (figure acc. to ref. 33).

## 2.2.2 Product-oriented design of photosynthetic electron flow

Figure 12 shows potential sites to modify the photosynthetic electron flow for a biotechnological application. Branching off parts of these electrons at the level of the light reaction ensures a high quantum efficiency for the products that were estimated to range between 10% and 14% [33, 34], thus being about 10–20-fold higher than the quantum efficiency of “classical” photosynthesis with a sugar component as a product. As mentioned earlier, branching off electrons for the generation of a desired product should not endanger the “maintenance” of the cell, that is, the minimal required energy for a cell to maintain the most fundamental metabolic processes without dying. Of course, optimization does not only concern the design cell itself but also the respective environment, that is, growth management and so on (see below).

Especially for cyanobacteria, achieved values for C-partitioning seem to be very high for desired products, and for this reason these species are better suited for biotechnology than eukaryotic microalgae.

Potential sites for branching off electrons from the light reaction are P1 at PS2, P2 at PS1 (fusion with  $H_2ase$ , see [35, 36]), P3 at Fd [37] and P4 at NADPH (reduction of externally added components [38]). In reality, the situation is more complicated than shown in Fig. 12A, as PS1 via its electron acceptor ferredoxin (Fd) is an important switching point for the cellular metabolism, funnelling

photosynthetically mobilized electrons in many different biochemical pathways as shown in Fig. 12B. Practically, for each of these reactions, the affinity of Fd for the respective enzyme and the enzyme concentration within the cell have to be considered in order to predict the hierarchy of electron supply for all competing reactions. If this is done for a cyanobacterial cell, the significance of N-assimilation (NIR) and S-assimilation (SIR) is about one order of magnitude lower compared to C-fixation (FNR), that is, they can be neglected in a first approach and branching off electrons should mainly be done in competition with FNR. As an example, the affinity of Fd for FNR was decreased by site-directed mutagenesis (SDM) within the interacting surface areas of both Fd and FNR to redirect electrons to a target hydrogenase ( $H_2ase$ ). When combining such SDM variants of Fd and FNR in a competition assay between FNR and  $H_2ase$  for photosynthetically mobilized electrons, 73% of the photohydrogen evolution activity measured in the absence of FNR could be recovered, while  $H_2ase$  only reached 4% of this control activity when using wildtype proteins of Fd and FNR (see Fig. 13). This demonstrates the high potential of engineering metabolic pathways and cells for new products at the expense of photosynthetic electrons.<sup>[28, 39]</sup> An alternative approach has been published by Appel et al. by fusing hydrogenase directly to PS1.<sup>[35]</sup> In this case, there is a direct electron transfer from PS1 to hydrogenase which is presently only hampered by the fact that this hydrogenase is inhibited by the  $O_2$  molecules generated in the water-splitting reaction at PS2, that is, presently, in the living cell this reaction can only occur under anaerobic conditions. However, gaining a detailed understanding of the inactivation mechanisms occurring at the active centers of [NiFe] and [FeFe] hydrogenases and establishing effective molecular tolerance or resistance strategies will hopefully allow photohydrogen production to occur under oxygenic conditions which will assure a high quantum yield.<sup>[40]</sup> Considering most of the possible improvements by cellular design outlined above, model calculations for a potential  $H_2$  production rate by cyanobacteria predict an approximately 100-fold increase in comparison with typical production yields by green algae.<sup>[32]</sup>

Another example is the use of photosynthetic electrons originating from water splitting to provide NADPH for recombinant oxidoreductases.<sup>[38]</sup> It could be shown that small hydrophobic substrates can be taken up by the cell from the surrounding medium; reduction in the cell is followed by product excretion into the environment. This facilitates harvesting of the desired product considerably.<sup>[38]</sup> These selected examples show that directed re-routing of electrons in specially designed cells is possible. However, it should also be considered that reactions in the test tube with selected reaction partners are different from conditions in the living cell. For instance, comparison with selected mutants of Fd, FNR and  $H_2ase$  under test tube and physiological conditions shows severe differences. In case of *Synechocystis*, experiments have shown that cells do not survive with FNR mutants.



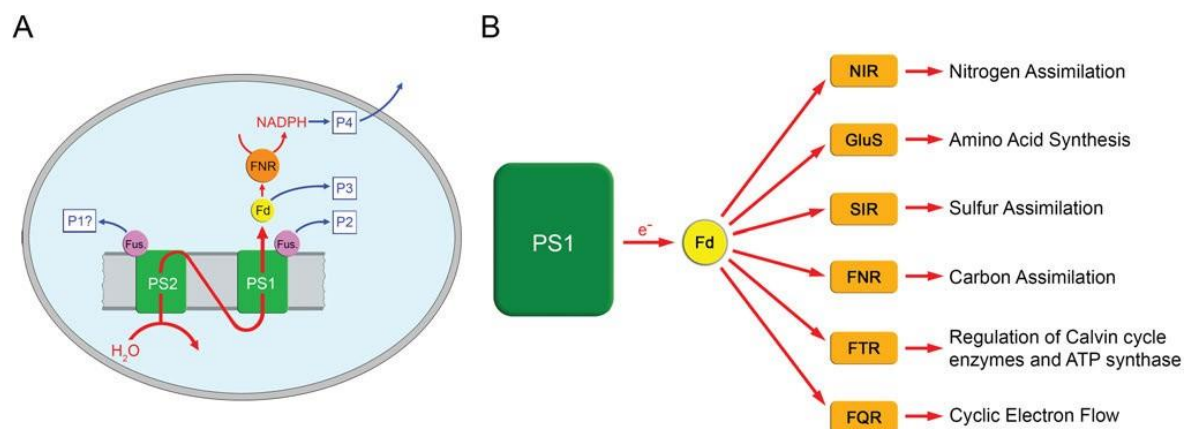


**Figure 12:** Potential sites for branching off photosynthetic electrons for biotechnological product generation (A) and significance of PS1/Fd branching point for electron distribution in the cyanobacterial cellular metabolism (B); for detailed explanations, see text.

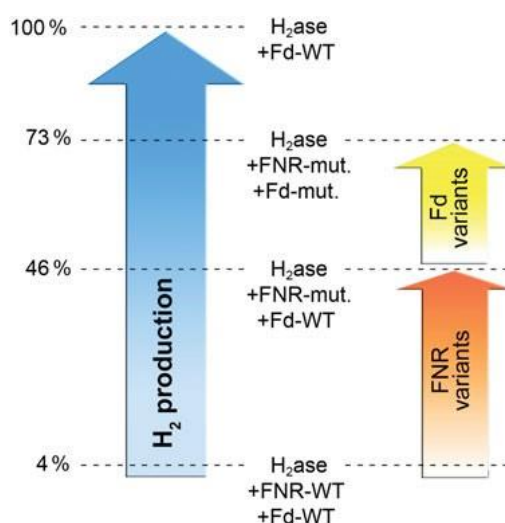


**Figure 13:** Competition of FNR and H<sub>2</sub>ase for photosynthetic electrons from Fd: comparison of H<sub>2</sub> generation in the test tube after mixing isolated H<sub>2</sub>ase with ferredoxin (Fd) (left) and H<sub>2</sub>ase with Fd in competition with FNR (wild type and mutants of Fd and FNR) (right).<sup>[28]</sup>

being severely affected with their affinity for Fd, thus preventing a transfer of the most impactful combination of protein variants measured *in vitro* to the living cell.<sup>[39]</sup> However, in this mutant strain, a functional electron sink (i.e., an engineered hydrogenase) did not exist which may change the whole redox situation. This exemplifies that *in vitro* experiments are just an indication for the results that may be achieved *in vivo* with corresponding mutant strains and that for gradual improvements each individual mutant needs to be tested under *in vivo* conditions. Establishing reliable *in vitro* simulations of all cellular processes in a cyanobacterial cell is not yet possible.

## 2.3 Tuning of extrinsic PS parameters relevant for application

### 2.3.1 Artificial versus natural environment: which parameters can be optimized?

Microalgae have a relatively low cell density compared to other microbes. In most cases, light is limiting in their natural environment which requires a sophisticated arrangement of additional antennae PBS in case of cyanobacteria and LHC in case of green algae. In contrast, industrial conditions normally provide sufficient light which permits a considerable reduction of the native antenna size (see above). This in turn allows to reach much higher cell densities combined with correspondingly higher product yields in photobioreactors (PBR) as surface-exposed cells with a decreased antenna size show a much smaller shading effect for internal cells than wild-type cells<sup>[27]</sup> (see Fig. 14). Additionally, light intensity and light quality can now be adjusted tailor-made, and

even different sunlight conditions equivalent to region dependent variations can now be simulated due to advanced LED technology. Example: Reduction of the PBS antenna size can increase the dry cell weight per Liter culture to a factor of 1.57<sup>[41]</sup>, and — due to more cells with more PS2 the rate of linear photosynthetic ET from water splitting increases up to 5.5-fold.<sup>[31]</sup> However, this maximal performance only applies under conditions when cell density, illumination and nutrient supply are optimal. For this reason, all those parameters need to be maintained at a constant level, which can only be realized by a continuous cultivation system. This type of cultivation under turbidostatic process control eliminates the relation between cultural growth and cell density which is kept constant by controlled dilution with fresh growth media. If this approach is complemented by a detailed proteome analysis, bottlenecks of metabolism and stress conditions can be indicated and prevented. Upscaling of such a system is possible and has been shown in a 100 L flat plate reactor in cooperation with an industrial partner (for details, see Fig. 15).

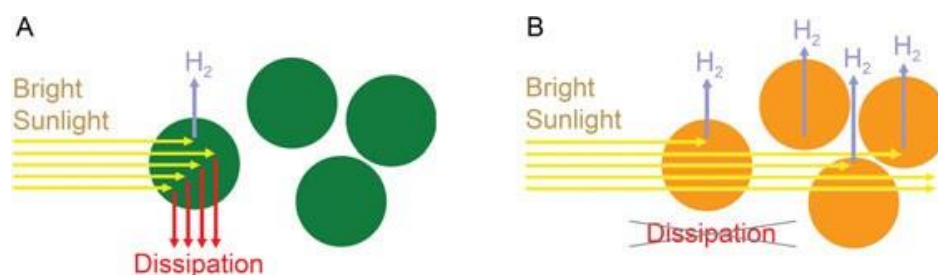


**Figure 14:** Impact of PBS size on self-shading effect in PBR with high cell densities. WT cell (A) and cells with truncated PBS antenna (B).<sup>[27]</sup>

### 2.3.2 Product-oriented design of the photosynthetic electron flow

The highly optimized photosynthetic ET chain of cyanobacteria can be used to drive redox biotransformations for the conversion of externally supplied substrates into desired products. Cyanobacteria are particularly interesting host organisms because their metabolism is “over-reduced” compared to heterotrophic bacteria. This surplus of photosynthetic redox power can be harnessed for biotechnological applications, particularly to supply oxidoreductases with NADPH.



**Figure 15:** A 100 L flat plate PBR as a pilot example for scaling up for future mass fermentation of cyanobacteria (coop. with KSD Co., Hattingen).<sup>[27]</sup>

Oxidoreductases play an important role for the industrial production of fine chemicals and pharmaceuticals. As redox enzymes, they rely on electron supply by redox cofactors, which are often more expensive than the product (e.g., NADPH). Therefore, co-factor regeneration systems were developed that depend on other organic co-substrates like glucose or isopropanol. Their application led to other problems like a poor atom efficiency of the process and the stoichiometric production of co-products like gluconic acid in case of glucose. An ideal system would regenerate the redox co-factor just from water, like photosynthesis does. However, photosynthetic co-factor regeneration is very complex and not fully understood in all details. At least two consecutive light-driven reactions, catalyzed by PS2 and PS1, are necessary to bridge the potential difference between  $\text{H}_2\text{O}$  and NADPH. Water oxidation releases oxygen as a byproduct, which is another advantage of the system, as many oxidoreductases (e.g., monooxygenases or dioxygenases) depend on oxygen. Cyanobacteria are the simplest organisms performing oxygenic photosynthesis and several model organisms like *Synechocystis* have been extensively studied. In principle, wild-type cyanobacteria can be employed for redox biotransformations, but the productivity and space-time yield of these native systems are fairly limited due to the low expression level of native oxidoreductases. However, the availability of various tools for the genetic manipulation of cyanobacteria enables the expression of recombinant oxidoreductases with optimized genetic elements (e.g., promoters, ribosome-binding sites and riboswitches) to increase productivity. In a proof-of-concept study, Königer et al. introduced the gene of the ene-reductase YqjM from *B. subtilis* under the control of the light-induced *psbA* promoter into *Synechocystis*.<sup>[38]</sup> With this system, several prochiral substrates were converted with a maximum

specific activity of more than 100 U per gram cell dry weight ( $U_{gcdw}^{-1}$ ) and optical purity (99% ee). The success of the concept of light-driven whole cell biotransformation was later verified with other oxidoreductases, for example, with a CYP450 monooxygenase from *Acidovorax* sp. CHX100 with a specific activity of  $39 U_{gcdw}^{-1}$ .<sup>[42]</sup> Further optimization of the YqjM system was achieved by exchanging the promotor  $P_{psbA2}$  to  $P_{cpc}$  (1.3-fold increase of activity) and especially by increasing the NADPH supply. Changes in the cellular NADPH pool were monitored by PAM fluorescence spectroscopy, which led to the conclusion that the photosynthetic supply of NADPH was not sufficient to compensate for the additional consumption by YqjM. Cyanobacteria features a very versatile electron transfer network that enables a quick adaptation to changing environmental conditions, particularly to changing light intensities, as overreduction of the photosynthetic electron transfer chain (imbalance of, e.g., NADPH production and consumption) leads to the generation of reactive oxygen species and damage of the photosynthetic apparatus. Therefore, additional electron sinks, like flavodiiron proteins (FLVs), are important to enable the efficient dissipation of excess energy in a so-called water–water cycle.<sup>[43]</sup> FLVs are essential for cyanobacteria to survive under natural conditions but they are expendable under controlled laboratory conditions. A knockout of Flv1 and Flv3 in the *Synechocystis* YqjM overexpression strain almost doubled the maximum product formation rate.<sup>[44]</sup> This example illustrates the potential of the general streamlining approach to increase productivities. Future strategies will include controlled inactivation of other competing electron sinks and particularly address the low space-time yield of cyanobacterial cultures. Usually, the volumetric production of heterotrophic bacteria can be easily optimized by increasing the cell density of the culture. This is currently not possible with cyanobacteria, as the maximum cell density and particularly the productivity of redox-driven biotransformations are limited by the ability of light to penetrate the culture. High-density cultures are usually not performing better, as the substrate and light becomes less available. Novel PBR designs and techniques of cell immobilization may help solve this fundamental problem (see below).

## 2.4 State of the art and future potential

### 2.4.1 Future design cells

Bioengineering of cyanobacterial cells for the generation of special products can now make use of the experiences gained from various mutants. Most importantly, all these effects are usually not additive, and the respective mutants have to be introduced step by step with detailed metabolic analysis. Simulation of such effects on the cellular level by metabolic programming would be highly interesting in the future. Especially the source–sink dynamics should be analyzed carefully and

## Chapter 2

individually for each product. If there is no balance between electrons generated by water splitting and electrons used for products, aggressive side products will be formed like oxygen radicals which limit the yield by destroying components of the ET chain.

The following is a toolbox for tentative approaches toward a design cell. They may be mixed/combined according to specific requirements:

- Individual mutants, some of which already introduced above, should be combined in one single design cell: they involve stabilization of PS2 (subunits from thermophiles or high light-resistant species), increasing the number of photosynthetic electrons (increasing PS2 concentration by PBS reduction), speeding up electrons (by partial ATPase uncoupling) and re-routing Fd-gated electrons (by Fd and FNR mutants).
- Introduction of light-regulated genes, which may switch on special product generation under HL, while cell maintenance could profit under normal/low light conditions, allowing cells to proliferate. This also could save energy under growth conditions.
- Designing fusion proteins with subunits at the acceptor side of the photosystems to minimize interfering reactions and optimize product yields. This has recently been shown for PS1 with hydrogenase. <sup>[35]</sup> Energetically superior would be the direct fusion or the wiring of the PS2 acceptor side with hydrogenase as shown in Fig. 16 possibly as proof of principle for other enzymes. Here, the challenge would be to divert the electrons from pheophytin despite the rapid kinetics of competitive redox reactions. In addition, due to the water-splitting reaction at PS2 an oxygen-tolerant hydrogenase is required. However, the combination of light-powered water-splitting and hydrogen production within a single engineered enzyme complex would be unique. As outlined in <sup>[12]</sup>, the capacity of such systems could be prechecked and optimized in electrode-based semiartificial devices before engineering them in living cells.

## Chapter 2

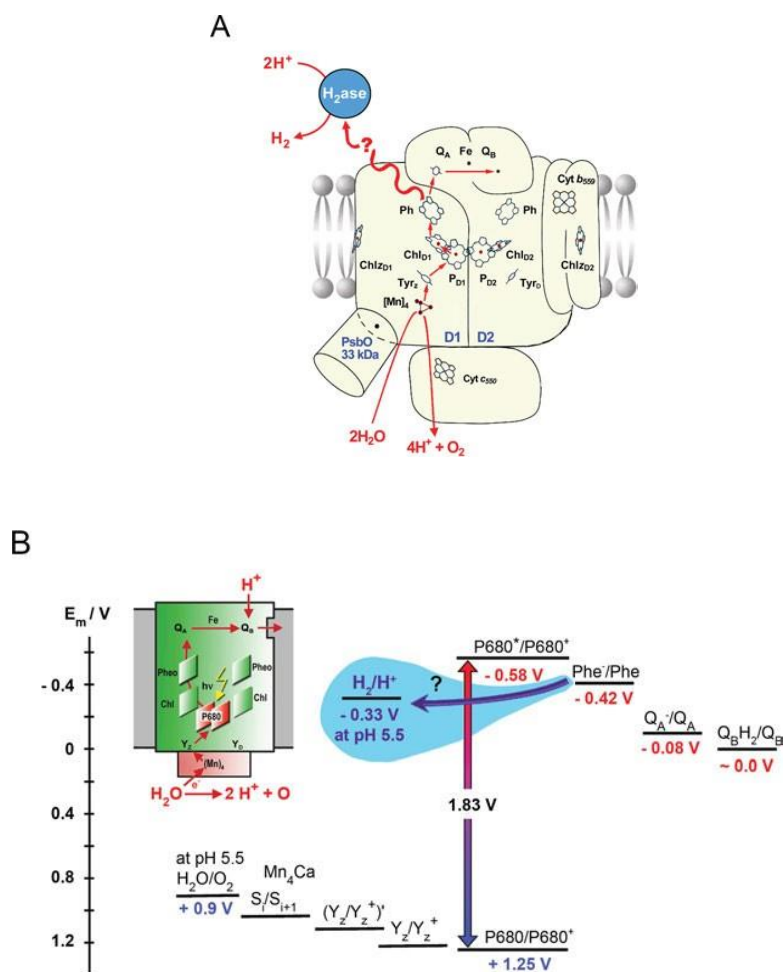


**Figure 16:** (A) Example for a fusion construct between PS2 and hydrogenase, which is thermodynamically favored but depends on the availability of an oxygen-tolerant enzyme, maybe in combination with oxygen-scavenging reactions. (B) Energetics of the coupling represented by the redox potential of the components, that is, PS2 and fusion partner hydrogenase.

### 2.4.2 Environmental design

The commercial production of biohydrogen, biomass and biomass-based products requires low cost and efficient production systems in case of microalgae especially efficient PBR. Key factors for the design of PBR are temperature, light and agitation.<sup>[45]</sup>

**Temperature:** Tolerance for light intensity and optimal behavior of metabolism in microalgae PBR compared to open ponds. This problem can be addressed by passive evaporative heating systems such as freshwater sprays or heat exchangers, but they require a large amount of water. Major problem is that 95% of the sunlight is outside of the PAR which involves heat dissipation and an increase in temperature.<sup>[46]</sup> This can be minimized by engineering the photonic spectrum and by use of IR spectrum filters in PBR.

**Light:** Light plays a crucial role in photosynthetic efficiency, especially as factors like atmospheric scattering and latitude change of the light source limit its availability. This spatiotemporal behavior of light which impacts the light capture can be optimized by proper positioning of the PBR — for instance by east–west orientation at latitude  $\geq 35^\circ\text{N}$  or north–south orientation for latitudes  $\leq 35^\circ\text{N}$ .<sup>[47]</sup> Additionally, synchronizing technologies help (1) automatic movement of the PBR with solar tracking devices and angling the reactor to the trajectory of the light angle<sup>[48]</sup>; (2) wireless light emitters for uniform light distribution and increase of overall light intensity; and (3) using wave-length shifters (quantum dots and fluorescent or phosphorescent compounds) to convert the spectral range of light with less photosynthetic significance, such as green gap, to a more photosynthetically efficient spectral range.<sup>[49]</sup> Also, the design of PBR depends on specific needs and the strain type.

**Production of lipids from microalgae:** Presently, a two-phase two-step system is most promising. In the first phase, microalgae are grown in closed PBR under controlled conditions (pH, light, cell density, no contaminations) to achieve higher growth rates in less time. In the second phase (lipid induction), microalgae are grown in open raceway ponds under nutrient deprivation or deliberate environmental stress or alternatives, for instance, for the production of astaxanthin.<sup>[50]</sup> Biohydrogen production from microalgae: hydrogen gas requires a closed PBR, which also helps in microbial cultivation.

**Biomass production from microalgae:** Although closed and open PBRs are used for biomass production of microalgae, open raceway ponds are frequently utilized.<sup>[51]</sup> Due to their high sunlight exposure throughout the year, tropical countries could be a strategic region for the large-scale production of algal-based products or biomass.<sup>[52]</sup> However, recently small-scale PBR have also extensively improved. The so-called high-density cultivation systems enabled a 10-fold increase in cell density by modifying both the dimension and the aeration of the system.<sup>[53]</sup> With this system, cell densities similar to those reached by *E. coli* cultures are within the reach.<sup>[54]</sup> An example for a successful application is the production of cyanophycin.<sup>[55]</sup>



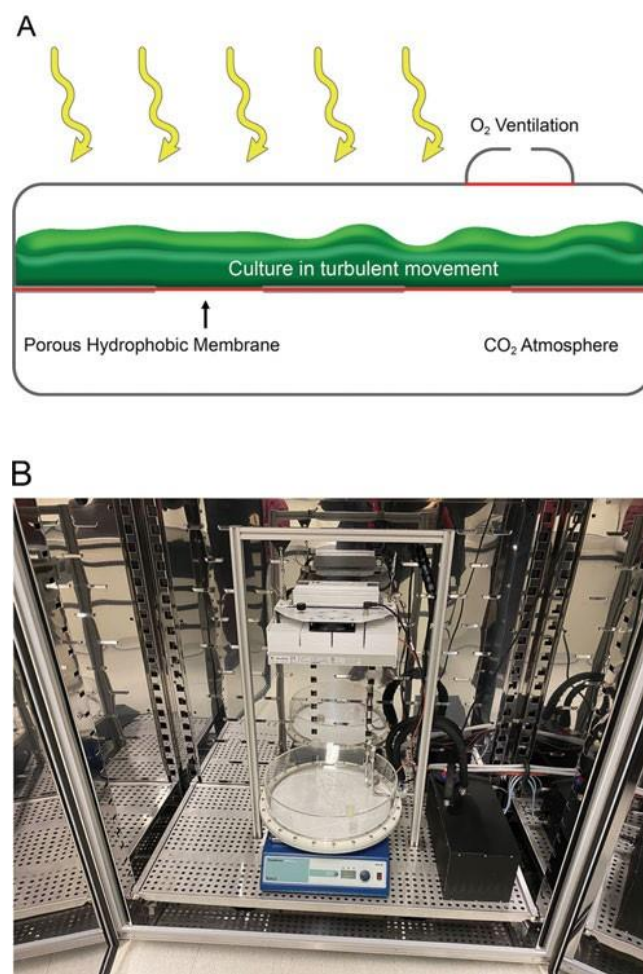


**Figure 17:** High-density cultures (HDC system, patent DE 10 2013 015 969 B4), based on a membrane which is impermeable for water and supplies CO<sub>2</sub> from below. This system achieves very high cell densities (up to 30 g DW/L for some strains) without negative effects due to photoinhibition even at very high light intensities (>2000  $\mu\text{E}/\text{m}^2/\text{s}$ ) (R. Steuer, HU Berlin, pers. com.).

### 2.4.3 Semi-artificial systems

While semiartificial systems involving PS2 always face the problem of lability due to the missing repair function, PS1 is much more stable especially if isolated from thermophilic strains.<sup>[56, 57]</sup> As even mesophilic complexes are quite stable and also easy to manipulate genetically, PS1 from *Synechocystis* PCC 6803 has been used as a light-powered electron pump as illustrated in Fig. 18. In this case, PS1–carbon nanotube conjugates in solution have been shown to transfer photoelectrons from PS1 to the carbon nanotube, generating directed photocurrents.<sup>[58]</sup> Such a principle may be very useful for an application in artificial photosynthesis, for instance, as a nano-optoelectronic device. Usage of ITO (Indium tin oxide) electrodes provide an opportunity to load high amounts of PS1 and PS2 on electrode surfaces which enables the use of biophotoelectrochemical devices for solar fuel production.<sup>[59]</sup>

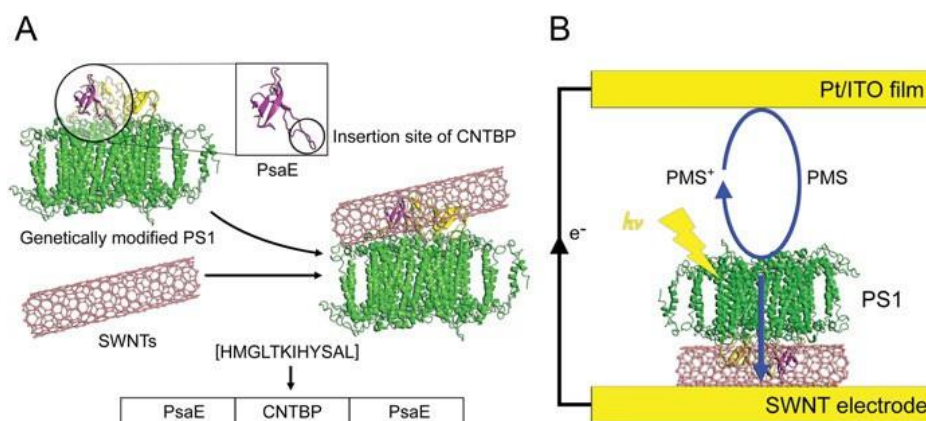


**Figure 18:** (A) PS1 complexes with engineered carbon nanotube binding peptide, conjugated on a single-walled carbon nanotube; (B) electron flow from PS1 to the carbon nanotube (SWNT) electrode as part of a device with PMS as a redox mediator, which generates current during photoirradiation; and (C) electron flow diagram representing the redox potential of each component. (Figures acc. to ref. 58 modified).

However, one of the major limitations in PS1-based electrochemical systems is their stability. In recent years, a significant improvement could for instance be achieved by encapsulating PS1 in organic microparticles: this retained the 100% activity of PS1 even after 10 days.<sup>[60]</sup> However, this system is incompatible with PS1 deposition on electrode surfaces. In future, the design of an electrode setup considering the stability will make the system even more efficient for large-scale applications.

Another example is the spatial organization and immobilization of algal/bacterial cell communities in dextran-in-PEG emulsion microdroplets.<sup>[61]</sup> Enclosing the photosynthetic cells with a shell of bacterial cells undergoing aerobic respiration enables photohydrogen production in daylight under air due to localized oxygen depletion (Fig. 19). This is also a proof of principle for utilizing aqueous two-phase separated droplets as vectors for controlling algal cell organization and photosynthesis in synthetic microspaces. Such photosynthetic microbial microreactors may generally be useful for multiple functionalities of photosynthesis in the future.

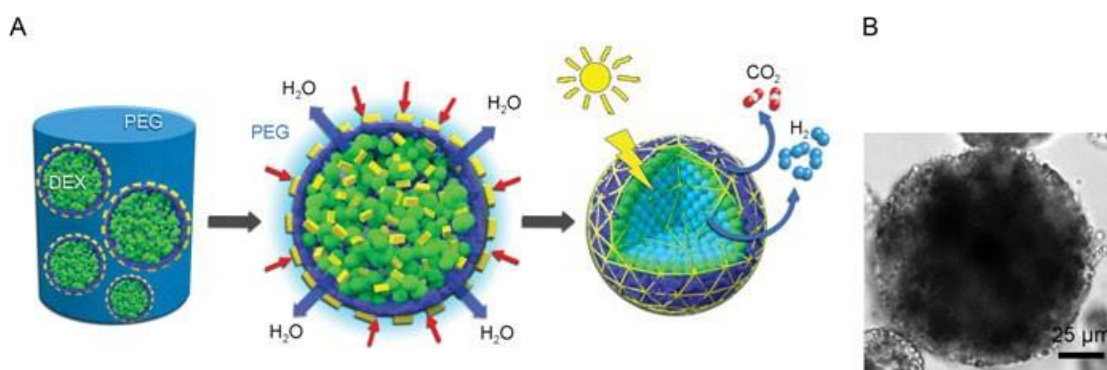


**Figure 19:** (A) Multicellular droplet-based living microreactors, based on algal/bacterial hybrid spheroids: droplets consist of mixtures of *Chlorella* cells (inside, green) and PEGylated *E. coli* cells (outside, blue), that is, the photosynthetic algal cells are enclosed by a thin oxygen-depleting layer of respiratory bacterial cells. Hyperosmotic compression results in consolidation and immobilization of the two cellular micro niches. Hydrogen production is enhanced by hypoxic photosynthesis in the core, consisting of a closely packed aggregate of algal cells immobilized in a dextran/BSA (yellow rectangles) hydrogel matrix. (B) Bright-field image of a single dextran-in-PEG emulsion droplet with captured algal and surface-adsorbed bacterial cells (Figures from ref. 61, modified).

## 2.4.4 Modelling

In future, modelling will help considerably in predicting and engineering of photosynthesis-based products.<sup>[62]</sup> As cyanobacteria are the most simple organisms performing oxygenic photosynthesis, and as thousands of characterized mutants are available – for instance, from *Synechocystis sp.* PCC 6803 – they could be ideal “simple” model organisms. The final aim is to optimize the metabolic engineering of cells to generate products by photosynthesis without compromising vital reactions that are the basis for survival (and reproduction) of the cell. This way, highest efficiency could be achieved without testing many mutants by “trial and error.”, although – on the whole cell level – this is still a future scenario and will require more knowledge about all the fundamental reactions in a cell, cyanobacteria may be the ideal choice due to their simplicity, the possibility of mass cultivation and genetic engineering. Such a modelling will also help optimally distribute the harvested light energy between basic cellular (“housekeeping”) and specific biotechnological reactions. Overall, the combination of modelling and synthetic biology will help overcome the natural limitations of photosynthetic cells.

## 2.5 Conclusions and outlook

Figure 20 summarizes the potential use of photosynthetic electrons for a selection of “solar” products. Strategies for a realization and an outlook on future perspectives of photosynthesis are as follows:

- Semiartificial systems (biophotovoltaic cells) can be extremely useful to develop and optimize new approaches for harnessing light energy with the help of photosynthesis. In comparison with “natural” photosynthesis they lack, however, dynamic adaptations such as the reversible mono-/trimerization of PS1 and the state transitions to optimize light harvesting or the repair function of PS2 (see below). Future will show whether advanced (semi-)artificial photosynthesis-based systems will be able to imitate such dynamics due to rational, energetic, ecological and economic reasons, electrons, have to come from water, which is available nearly everywhere worldwide. For this process, water splitting at PS2 is mandatory. However, PS2 is the weakest point of the whole photosynthetic ET chain and due to photooxidative damage has to be repaired every 20-30 min by a very sophisticated cellular repair system which (up to now) cannot be realized in a semiartificial system. For this reason, for the time being, most or all photosynthesis-based “applied” systems have to be modified/optimized cellular systems, that is, “design cells.”

Using photosynthesis for product generation is not primarily a problem of efficiency, but due to cost-free availability of sunlight will finally be decided by the price of this product. For this purpose, all parameters have to be considered, including the efficiency of the design cell, costs of PBR generation, its lifetime, its running costs and its disposal. Also, the amount of product generated per time is decisive. For this reason, a life cycle assessment of the environmental impacts and cumulative energy demand is mandatory before starting such a project, as is a comparison with competitive procedures.<sup>[63]</sup> The use of seawater versus fresh-water organisms could also be an important point to evaluate. Due to their robustness and versatility, cyanobacteria have recently been shown to be the basis for biological life support systems during Mars exploration programs.<sup>[64]</sup> Apparently, they can use N<sub>2</sub> and C from the atmosphere and mineral nutrients from the Martian regolith and also grow under low pressure as demonstrated with *Anabaena* PCC 7938 in a specifically designed low-pressure PBR. Via photosynthesis, they could regenerate atmospheric gases, especially O<sub>2</sub>, supporting the growth of other organisms and also feed secondary consumers like *E. coli*. In future, cyanobacteria may play an important role in such bioregenerative life support systems for spaceflight and planetary outposts.

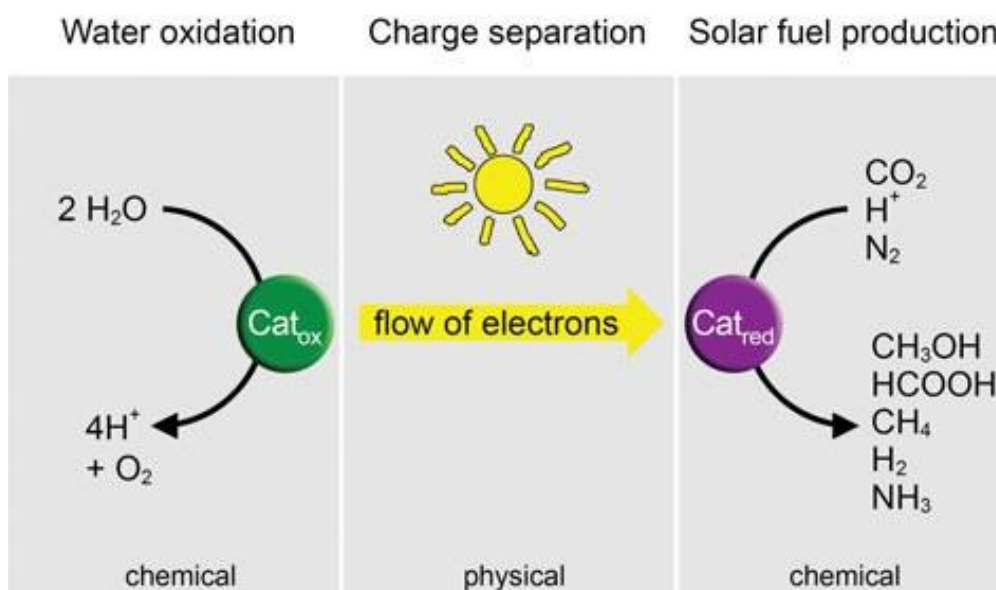


**Figure 20:** Summary of the potential use of photosynthetic electrons for “solar” products (selection). Solar energy has an outstanding potential as a cheap, clean and sustainable energy source but it has to be captured and transformed into chemical energy in the form of chemical bonds as in natural photosynthesis. One of the chemical products that can be synthesized by photosynthetic organisms from basic components and yet exhibits huge potential as a sustainable energy carrier is hydrogen gas. Its combustion produces water and allows to use  $\text{CO}_2$  as primary source for generating chemicals such as methanol and various acids, which could be used in manufacturing and processing industries.<sup>[65]</sup>

## 2.6 References

- [1] Acatech – National Academy of Science and Engineering, German National Academy of Sciences Leopoldina, Union of the German Academies of Sciences and Humanities (Eds.). Artificial Photosynthesis. Munich, 2018, 74.
- [2] Kim SK. Marine bioenergy production. In: Kim SK, ed. Essentials of Marine Biotechnology ed. Cham Switzerland, Springer, 2019, 297–341.
- [3] Rexroth S, Nowaczyk MM, Rögner M. Cyanobacterial photosynthesis: The light reactions. In: Hallenbeck P, ed. Modern Topics in Phototrophic Prokaryotes ed. Cham Switzerland, Springer, 2017, 163–91.
- [4] Ocean color and land vegetation data from SeaWiFS. Reveals the dynamic seasonal pattern of distribution of primary production (Accessed April 4, 2021, at [https://oceancolor.gsfc.nasa.gov/SeaWiFS/BACKGROUND/Gallery/biosphere\\_egg\\_caption.jpg](https://oceancolor.gsfc.nasa.gov/SeaWiFS/BACKGROUND/Gallery/biosphere_egg_caption.jpg)).
- [5] The SeaWiFS Project. NASA/Goddard Space Flight Center and Orbimage. (Accessed April 4, 2021 at [https://oceancolor.gsfc.nasa.gov/SeaWiFS/BACKGROUND/Gallery/biosphere\\_egg\\_caption.jpg](https://oceancolor.gsfc.nasa.gov/SeaWiFS/BACKGROUND/Gallery/biosphere_egg_caption.jpg)).
- [6] Umena Y, Kawakami K, Shen JR, Kamiya N. Crystal structure of oxygen-evolving photosystem II at a resolution of 1.9 Å. Nature 2011, 473, 55–60.
- [7] Kurisu G, Zhang H, Smith JL, Cramer WA. Structure of the cytochrome *b<sub>6</sub>f* Complex of oxygenic photosynthesis: Tuning the cavity. Science 2003, 302, 1009–14.
- [8] Fromme P, Jordan P, Witt HT, Klukas O, Saenger W, Krauss N. Three-dimensional structure of cyanobacterial photosystem I at 2.5 angstrom resolution. Nature 2001, 411, 909–17.
- [9] Baker NR, Harbinson J, Kramer DM. Determining the limitations and regulation of photosynthetic energy transduction in leaves. Plant Cell Environ 2007, 30, 1107–25.
- [10] Rögner M. Metabolic engineering of cyanobacteria for the production of hydrogen from water. Biochem Soc Trans 2013, 41, 1254–9.
- [11] Kothe T, Schuhmann W, Rögner M, Plumeré N. Semi-artificial photosynthetic Z-scheme for hydrogen production from water. Biohydrogen, De Gruyter, 2015, 189–210.
- [12] Kothe T, Pöller S, Zhao F, Fortgang P, Rögner M, Schuhmann W, et al. Engineered electron-transfer chain in photosystem 1 based photocathodes outperforms electron-transfer rates in natural photosynthesis. Chem – A Eur J 2014, 20, 11029–34.
- [13] Rexroth S, Wiegand K, Rögner M. Cyanobacterial design cell for the production of hydrogen from water. In: Rögner M, ed. Biohydrogen. Berlin, Germany, De Gruyter, 2015, 1–18.
- [14] Badura A, Kothe T, Schuhmann W, Rögner M. Wiring photosynthetic enzymes to electrodes. Energy Environ Sci 2011, 4, 3263–74.
- [15] Zabret J, Bohn S, Schuller SK, Arnolds O, Möller M, Meier-Credo J, et al. Structural insights into photosystem II assembly. Nat Plants 2020, 7, 524–38.
- [16] Sander J, Nowaczyk M, Buchta J, Dau H, Vass I, Deák Z, et al. Functional characterization and quantification of the alternative PsbA copies in *Thermosynechococcus elongatus* and their role in photoprotection. J Biol Chem 2010, 285, 29851–6.
- [17] Hartmann V, Ruff A, Schuhmann W, Rögner M, Nowaczyk MM. Analysis of photosystem II electron transfer with natural PsbA-variants by redox polymer/protein biophotoelectrochemistry. Photosynthetica 2018, 56, 229–35.
- [18] Sugiura M, Azami C, Koyama K, Rutherford AW, Rappaport F, Boussac A. Modification of the pheophytin redox potential in *Thermosynechococcus elongatus* Photosystem II with PsbA3 as D1. Biochim Biophys Acta – Bioenerg 2014, 1837, 139–48.



- [19] Ohad I, Nevo R, Brumfeld V, Reich Z, Tsur T, Yair M, et al. Inactivation of photosynthetic electron flow during desiccation of desert biological sand crusts and *Microcoleus* sp.-enriched isolates. *Photochem Photobiol Sci* 2005, 4, 977–82.
- [20] Ohad I, Berg A, Berkowicz SM, Kaplan A, Keren N. Photoinactivation of photosystem II: Is there more than one way to skin a cat? *Physiol Plant* 2011, 142, 79–86.
- [21] Chen M, Blankenship RE. Expanding the solar spectrum used by photosynthesis. *Trends Plant Sci* 2011, 16, 427–31.
- [22] Janssen M, Tramper J, Mur LR, Wijffels RH. Enclosed outdoor photobioreactors: Light regime, photosynthetic efficiency, scale-up, and future prospects. *Biotechnol Bioeng* 2003, 81, 193–210.
- [23] Kopka J, Schmidt S, Dethloff F, Pade N, Berendt S, Schottkowski M, et al. Systems analysis of ethanol production in the genetically engineered cyanobacterium *Synechococcus* sp PCC 7002. *Biotechnol Biofuels* 2017, 10, 1–21.
- [24] Savakis PE, Angermayr SA, Hellingwerf KJ. Synthesis of 2,3-butanediol by *Synechocystis* sp. PCC 6803 via heterologous expression of a catabolic pathway from lactic acid- and Enterobacteria. *Metab Eng* 2013, 20, 121–30.
- [25] Imashimizu M, Bernát G, Sunamura EI, Broekmans M, Konno H, Isato K, et al. Regulation of F<sub>0</sub>F<sub>1</sub>-ATPase from *Synechocystis* sp. PCC 6803 by  $\gamma$  and  $\epsilon$  subunits is significant for light/dark adaptation. *J Biol Chem* 2011, 286, 26595–602.
- [26] Nowaczyk M, Rexroth S, Rögner M. Biotechnological potential of cyanobacteria. *Biotechnology*. In: Rögner M, ed. *Biohydrogen*. Berlin, Germany, De Gruyter, 2015, 141–64.
- [27] Wiegand K, Winkler M, Rumpel S, Kannchen D, Rexroth S, Hase T, et al. Rational redesign of the ferredoxin-NADP<sup>+</sup>-oxidoreductase/ferredoxin-interaction for photosynthesis-dependent H<sub>2</sub>-production. *Biochim Biophys Acta – Bioenerg* 2018, 1859, 253–62.
- [28] Moal G, Lagoutte B. Photo-induced electron transfer from photosystem I to NADP<sup>+</sup>: Characterization and tentative simulation of the in vivo environment. *Biochim Biophys Acta – Bioenerg* 2012, 1817, 1635–45.
- [29] Liberton M, Chrisler WB, Nicora CD, Moore RJ, Smith RD, Koppelaar DW, et al. Phycobilisome truncation causes widespread proteome changes in *Synechocystis* sp. PCC 6803. *PLoS One* 2017, 12, 1–18.
- [30] Bernát G, Waschewski N, Rögner M. Towards efficient hydrogen production: The impact of antenna size and external factors on electron transport dynamics in *Synechocystis* PCC 6803. *Photosynth Res* 2009, 99, 205–16.
- [31] Waschewski N, Bernát G, Rögner M. Engineering photosynthesis for H<sub>2</sub> production from H<sub>2</sub>O: Cyanobacteria as design organisms. In: Vertes AA, Editor Nasib Qureshi (Co-Editor), Hideaki Yukawa (Co-Editor), Hans P. Blaschek (Co-Editor). *Biomass to Biofuels-Strategies for Global Industries*. Chichester, UK, John Wiley & Sons, 2010, 387–401.
- [32] Blankenship RE, Tiede DM, Barber J, Brudvig GW, Fleming G, Ghirardi M, et al. Comparing photosynthetic and photovoltaic efficiencies and recognizing the potential for improvement. *Science* 2011, 332, 805–9.
- [33] Dau H, Zaharieva I. Principles, efficiency, and blueprint character of solar-energy conversion in photosynthetic water oxidation. *Acc Chem Res* 2009, 42, 1861–70.
- [34] Appel J, Hueren V, Boehm M, Gutekunst K. Cyanobacterial in vivo solar hydrogen production using a photosystem I-hydrogenase (PsaD-HoxYH) fusion complex. *Nat Energy* 2020, 5, 458–67.
- [35] Kanygin A, Milrad Y, Thummala C, Reifschneider K, Baker P, Marco P, et al. Rewiring photosynthesis: A photosystem I-hydrogenase chimera that makes H<sub>2</sub>: In vivo. *Energy Environ Sci* 2020, 13, 2903–14.
- [36] Eilenberg H, Weiner I, Ben-Zvi O, Pundak C, Marmari A, Liran O, et al. The dual effect of a ferredoxin-hydrogenase fusion protein in vivo: Successful divergence of the photosynthetic

- electron flux towards hydrogen production and elevated oxygen tolerance. *Biotechnol Biofuels* 2016, 9, 1–10.
- [37] Köninger K, Gómez Baraibar Á, Mügge C, Paul CE, Hollmann F, Nowaczyk MM, et al. Recombinant cyanobacteria for the asymmetric reduction of C=C bonds fueled by the biocatalytic oxidation of water. *Angew Chemie – Int Ed* 2016, 55, 5582–5.
  - [38] Kannchen D, Zabret J, Oworah-Nkruma R, Dyczmons-Nowaczyk N, Wiegand K, Löbbert P, et al. Remodeling of photosynthetic electron transport in *Synechocystis* sp. PCC 6803 for future hydrogen production from water. *Biochim Biophys Acta – Bioenerg* 2020, 1861, 148208.
  - [39] Winkler M, Duan J, Rutz A, Felbek C, Scholtysek L, Lampret O, et al. A safety cap protects hydrogenase from oxygen attack. *Nat Commun* 2021, 12, 1–10.
  - [40] Kirst H, Formighieri C, Melis A. Maximizing photosynthetic efficiency and culture productivity in cyanobacteria upon minimizing the phycobilisome light-harvesting antenna size. *Biochim Biophys Acta – Bioenerg* 2014, 1837, 1653–64.
  - [41] Hoschek A, Toepel J, Hochkeppel A, Karande R, Bühler B, Schmid A. Light-dependent and aeration-independent gram-scale hydroxylation of cyclohexane to cyclohexanol by CYP450 harboring *Synechocystis* sp. PCC 6803. *Biotechnol J* 2019, 14, 1–10.
  - [42] Allahverdiyeva Y, Isojärvi J, Zhang P, Aro EM. Cyanobacterial oxygenic photosynthesis is protected by flavodiiron proteins. *Life* 2015, 5, 716–43.
  - [43] Assil-Companiononi L, Büchsenschütz HC, Solymosi D, Dyczmons-Nowaczyk NG, Bauer KKF, Wallner S, et al. Engineering of NADPH supply boosts photosynthesis-driven biotransformations. *ACS Catal* 2020, 10, 11864–77.
  - [44] Huang Q, Jiang F, Wang L, Yang C. Design of photobioreactors for mass cultivation of photosynthetic organisms. *Engineering* 2017, 3, 318–29.
  - [45] Nwoba EG, Parlevliet DA, Laird DW, Alameh K, Moheimani NR. Light management technologies for increasing algal photobioreactor efficiency. *Algal Res* 2019, 39, 101433.
  - [46] Sierra E, Acién FG, Fernández JM, García JL, González C, Molina E. Characterization of a flat plate photobioreactor for the production of microalgae. *Chem Eng J* 2008, 138, 136–47.
  - [47] Hindersin S, Leupold M, Kerner M, Hanelt D. Irradiance optimization of outdoor microalgal cultures using solar tracked photobioreactors. *Bioprocess Biosyst Eng* 2013, 36, 345–55.
  - [48] Delavari Amrei H, Nasernejad B, Ranjbar R, Rastegar S. Spectral shifting of UV-A wavelengths to blue light for enhancing growth rate of cyanobacteria. *J Appl Phycol* 2014, 26, 1493–500.
  - [49] Zhang BY, Geng YH, Li ZK, Hu HJ, Li YG. Production of astaxanthin from *Haematococcus* in open pond by two-stage growth one-step process. *Aquaculture* 2009, 295, 275–81.
  - [50] Acién FG, Molina E, Reis A, Torzillo G, Zittelli GC, Sepúlveda C et al. Photobioreactors for the production of microalgae. In: Gonzalez-Fernandez C, Muñoz R, ed. *Microalgae-Based Biofuels and Bioproducts*. Duxford, UK, Elsevier, 2017, 1–44.
  - [51] Ugwu CU, Aoyagi H, Uchiyama H. Photobioreactors for mass cultivation of algae. *Bioresour Technol* 2008, 99, 4021–8.
  - [52] Bähr L, Wüstenberg A, Ehwald R. Two-tier vessel for photoautotrophic high-density cultures. *J Appl Phycol* 2016, 28, 783–93.
  - [53] Dienst D, Wichmann J, Mantovani O, Rodrigues JS, Lindberg P. High density cultivation for efficient sesquiterpenoid biosynthesis in *Synechocystis* sp. PCC 6803. *Sci Rep* 2020, 10, 5932.
  - [54] Lippi L, Bähr L, Wüstenberg A, Wilde A, Steuer R. Exploring the potential of high-density cultivation of cyanobacteria for the production of cyanophycin. *Algal Res* 2018, 31, 363–6.
  - [55] Nguyen K, Bruce BD. Growing green electricity: Progress and strategies for use of Photosystem I for sustainable photovoltaic energy conversion. *Biochim Biophys Acta – Bioenerg* 2014, 1837, 1553–66.



- [56] Badura A, Guschin D, Kothe T, Kopczak MJ, Schuhmann W, Rögner M. Photocurrent generation by photosystem 1 integrated in crosslinked redox hydrogels. *Energy Environ Sci* 2011, 4, 2435–40.
- [57] Nii D, Miyachi M, Shimada Y, Nozawa Y, Ito M, Homma Y, et al. Conjugates between photosystem I and a carbon nanotube for a photoresponse device. *Photosynth Res* 2017, 133, 155–62.
- [58] Bobrowski T, Conzuelo F, Ruff A, Hartmann V, Frank A, Erichsen T, et al. Scalable fabrication of biophotoelectrodes by means of automated airbrush spray-coating. *ChemPlusChem* 2020, 85, 1396–400.
- [59] Cherubin A, Destefanis L, Bovi M, Perozeni F, Bargigia I, De La Cruz Valbuena G, et al. Encapsulation of Photosystem I in organic microparticles increases its photochemical activity and stability for Ex Vivo photocatalysis. *ACS Sustain Chem Eng* 2019, 7, 10435–44.
- [60] Xu Z, Wang S, Zhao C, Li S, Liu X, Wang L, et al. Photosynthetic hydrogen production by droplet- based microbial micro-reactors under aerobic conditions. *Nat Commun* 2020, 11, 1–10.
- [61] Zavřel T, Faizi M, Loureiro C, Poschmann G, Stühler K, Sinetova M, et al. Quantitative insight into the cyanobacterial cell economy. *Elife* 2019, 8, e42508.
- [62] Rosner V. Analysis and assessment of current photobioreactor systems for photobiological hydrogen production. In: Rögner M, ed. *Biohydrogen*. Berlin, Germany, De Gruyter, 2015, 19–40.
- [63] Verseux C, Heinicke C, Ramalho TP, Determann J, Duckhorn M, Smagin M, et al. A low-pressure, N<sub>2</sub>/CO<sub>2</sub> atmosphere is suitable for cyanobacterium-based life-support systems on Mars. *Front Microbiol* 2021, 12, 611798.
- [64] El-Khouly ME, El-Mohsnawy E, Fukuzumi S. Solar energy conversion: From natural to artificial photosynthesis. *J Photochem Photobiol C Photochem Rev* 2017, 31, 36–83.

## Chapter 3: Light-driven NADPH cofactor recycling by photosystem I for biocatalytic reactions

Hitesh Medipally, Alice Guarneri, Lars Pospisil, Maurice C. R. Franssen, Willem J. H. van Berkel, Caroline E. Paul, and Marc M. Nowaczyk

Publication 2

**ChemCatChem 2023, e202300821**

**<https://doi.org/10.1002/cctc.202300821>**

**Abstract:** Biocatalytic asymmetric reduction of C=C and C=O bonds is highly attractive to produce valuable (chiral) chemicals for the fine and pharmaceutical industry yet occurs at the expense of reduced nicotinamide adenine dinucleotide coenzyme NADPH that requires recycling. Established methods each have their challenges. Here we developed a light-driven approach based on photosystem I (PSI) by mimicking the natural electron transfer from PSI via ferredoxin (Fd) towards ferredoxin NADP<sup>+</sup> reductase (FNR) in vitro. Illumination with red light led to reduction of NADP<sup>+</sup> to NADPH with a turnover frequency of 2.55 s<sup>-1</sup> (> 9000 h<sup>-1</sup>) at pH 7.5. Light-driven NADPH regeneration by PSI-Fd-FNR was coupled with three oxidoreductases for asymmetric reduction of C=C and C=O bonds, reaching up to 99 % conversion with a turnover number of 3035, and retaining enantioselectivity. This study demonstrates the capacity of a PSI system to drive continuous NADPH-dependent biocatalytic conversions with light.

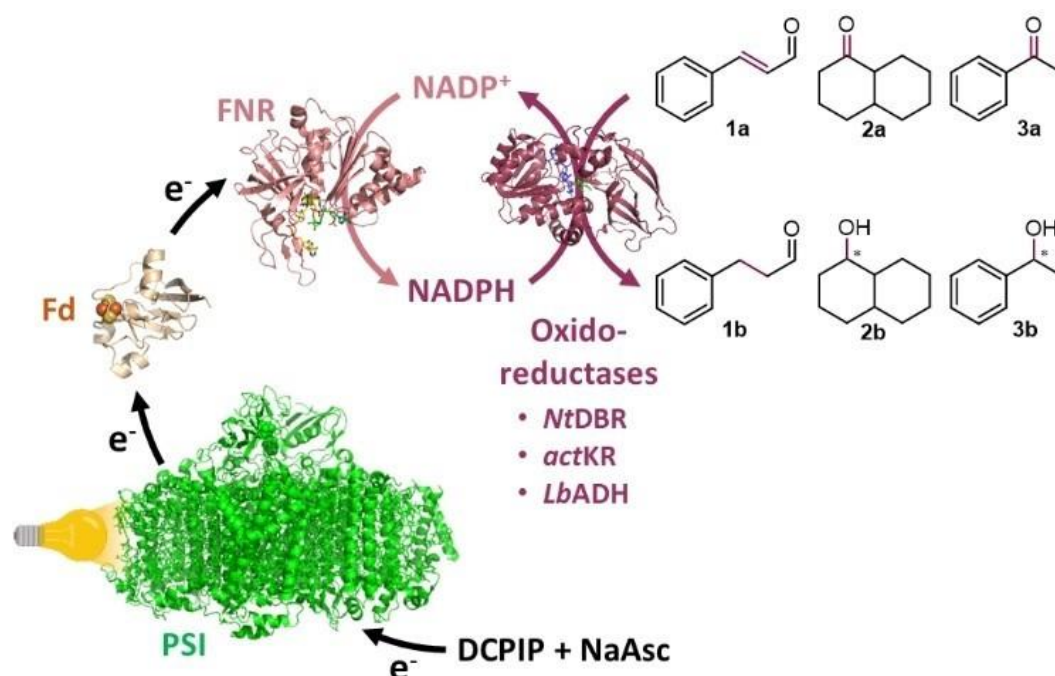


**Figure 1. Light-driven NADPH cofactor recycling by PSI-Fd-FNR for redox biocatalysis.** NaAsc: sodium ascorbate, DCPIP: dichlorophenolindophenol, PSI: photosystem I (PDB: 1JBO), Fd: ferredoxin (PDB: 5AUI), FNR: ferredoxin NADP<sup>+</sup> reductase (PDB: 1GJR), NADP<sup>+</sup>: nicotinamide adenine dinucleotide phosphate, *NtDBR*: *Nicotiana tabacum* double bond reductase, *actKR*: *actinorhodin* ketoreductase from *Streptomyces coelicor*, *LbADH*: *Lactobacillus brevis* alcohol dehydrogenase.

### 3.1 Introduction

Biocatalysts display exquisite efficiency, chemo-, enantio- and regioselectivity to synthesize a wide variety of chemicals under mild and economically sustainable conditions.<sup>[1]</sup> Oxidoreductases are one of the industrially most important classes of enzymes after hydrolases, and amount to approximately one-third of the reported enzymes in the BRAunschweig ENzyme DAtabase (BRENDA).<sup>[2]</sup> Many relevant in vitro oxidoreductase- catalyzed reactions require the continuous supply of nicotinamide adenine dinucleotide NAD(P)H as reductant and its recycling due to cost and stability.<sup>[3]</sup> Over the last decades enzymatic, electrochemical, and photochemical recycling systems have been developed,<sup>[4]</sup> with the enzymatic approach being favored. The most commonly used NAD(P)H recycling enzymes in laboratory or industrial scale include NAD- or NADP- dependent oxidoreductases such as glucose dehydrogenase (GDH), glucose-6-phosphate dehydrogenase (G6PDH), formate dehydrogenase (FDH), phosphite dehydrogenase (PTDH), alcohol dehydrogenase (ADH), and hydrogenase (Hyd). Some of these recycling systems have poor atom efficiency: GDH, G6PDH, or display low activity: FDH, PTDH, and Hyd.<sup>[5]</sup> Moreover, few enzymes are naturally NADP- dependent such as GDH, G6PDH and specific ADHs, limiting the pool of options for NADPH regeneration.

In contrast, the photosynthetic electron transport chain in cyanobacteria, algae and plants acts as an excellent platform for sustainable and efficient NADPH recycling, with water used as the primary electron donor.<sup>[6]</sup> Despite this advantage, its dependency on light for growth, a limited substrate scope due to the selective membrane barrier and low production rates make the in vivo photosynthetic system inefficient compared with other optimized heterotrophic production systems.<sup>[6b,7]</sup> In photosynthetic electron transfer, photosystem I (PSI) acts as a light-driven electron pump, which is reduced by plastocyanin (PC) or cytochrome *c*<sub>6</sub> (Cyt *c*<sub>6</sub>) and which provides electrons for NADPH recycling via ferredoxin (Fd) and ferredoxin NADP<sup>+</sup> reductase (FNR). The ultimate electron source for this process in the natural system is the water-splitting activity of photosystem II (PSII). Here, we developed the proof-of-concept for a light-driven in vitro system for NADPH recycling by coupling of isolated PSI,<sup>[8]</sup> Fd,<sup>[9]</sup> FNR,<sup>[10]</sup> with three different oxidoreductases (Figure 1).

Our recycling system was assembled by artificial reconstitution of the photosynthetic electron transport chain in vitro, thus mimicking the cathodic half-cell reaction of natural photosynthesis.<sup>[11]</sup> In the PSI-driven biocascade, the difference in reduction potentials (EM) of the used compounds provides a paradigm for sequential electron transfer (Figure 2a). NaAsc (EM: +0.078 V vs. a standard hydrogen electrode SHE) is used as a sacrificial electron donor, and DCPIP (EM: +0.228 V vs. SHE) acts as an electron mediator to PSI. Light-driven charge separation within PSI generates a strong

reducing potential (EM: -1.3 V vs. SHE), thus enabling electron transfer to Fd (EM: -0.43 V vs. SHE) via the terminal 4Fe-4S cluster (FB) of PSI. The single electron carrier Fd donates two electrons, one at each time to the FAD cofactor (EM: -0.38 V vs. SHE) of FNR, for the full reduction of  $\text{NADP}^+$  to NADPH.

Similar PSI-driven biocascade reactions have been reported previously as classical photoreduction assays for FDH,<sup>[11]</sup> FNR,<sup>[12]</sup> and Hyd.<sup>[13]</sup> Here we extended the scope of a PSI-biocascade and explored its ability as an NADPH recycling system. Three different oxidoreductases were coupled to demonstrate NADPH regeneration with PSI-Fd-FNR for asymmetric C=C and C=O reduction: i) *Nicotiana tabacum* double bond reductase (*Nt*DBR, EC 1.3.1.102), which reduces *trans*-cinnamaldehyde **1 a** to dihydrocinnamaldehyde **1 b**;<sup>[14]</sup> ii) *actinorhodin* ketoreductase from *Streptomyces coelicolor* (*act*KR, EC 1.1.1.184) that converts 1-decalone **2 a** to 1-decalol **2 b**;<sup>[15]</sup> and iii) alcohol dehydrogenase from *Lactobacillus brevis* (*Lb*ADH, EC 1.1.1.1)<sup>[16]</sup> to reduce acetophenone **3 a** to (*R*)-phenylethanol **3 b** (Figure 1).

## 3.2 Results and Discussion

In nature, PSI is embedded in the thylakoids, exposing one side of the complex to the basic stromal pH and the other end to the acidic luminal pH. The pH of the chloroplast lumen varies in the range of 5.8 to 6.5 under moderate light conditions. On the other hand, the stromal side pH is in the range of 7.8 to 8.0,<sup>[18]</sup> which makes it difficult to predict the optimal pH conditions for NADPH production in vitro. Therefore, we monitored the light-driven NADPH generation capacity of PSI-Fd-FNR at different pH conditions by measuring the concentration of NADPH at various time intervals over 6 h (Figures 2b, S3, S8 and S9). The reduction rate of  $\text{NADP}^+$  to NADPH at pH 7.0, 7.5 and 8.0 were determined to be 1.51, 1.73, and 1.17 mM/h, respectively, with the best turnover frequency (TOF) of  $2.55 \text{ s}^{-1}$  ( $9180 \text{ h}^{-1}$ ) at pH 7.5. A rapid increase in NADPH concentration was observed in the initial 30 min of the reaction, especially at pH 7.0 and 7.5, and slightly slower at pH 8.0. The small differences in the initial rates can be attributed to the different pH dependencies of the individual electron transfer steps in the cascade. The interaction of Fd with PSI is mainly entropy driven and therefore less affected by pH<sup>[19]</sup> whereas the interaction of PSI with its natural electron donors, PC, Cyt *c*<sub>6</sub> and, is driven by hydrophobic and electrostatic interactions with an optimum at acidic pH.<sup>[20]</sup> However, the artificial electron donors NaAsc and DCPIP behave differently in the in vitro cascade. DCPIP is in a reduced state (DCPIPH<sub>2</sub>) due to the presence of excess NaAsc (100 mM). The lack of net charge and the aromatic nature of DCPIPH<sub>2</sub> make it also a potential candidate for hydrophobic interaction with the donor site of PSI. NaAsc itself is known to donate electrons to the PSI donor site very slowly in its

deprotonated state.<sup>[17a]</sup> Thus, all electron transfer reactions in the system are mainly based on hydrophobic interactions, which explains the minor influence of the pH, with an optimum at pH 7.5 (see also Figures S1 and S2 for detailed information on electron transfer steps and protein-protein interactions within the biocascade).

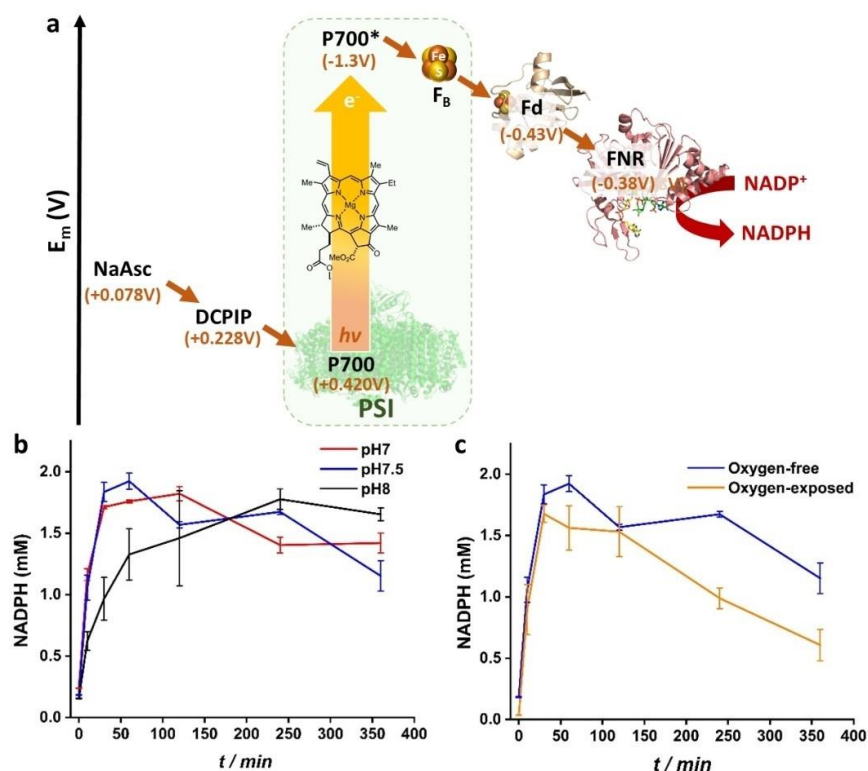


**Figure 2.** a) Schematic representation of electron transfer in the PSI-Fd-FNR cascade. Midpoint potential values are according to literature references vs. SHE; <sup>[12,17]</sup> b) pH-dependent production of NADPH by the PSI-Fd-FNR cascade. Conditions: 0.57  $\mu$ M PSI (50  $\mu$ g chlorophyll (Chl), 1  $\mu$ M FNR, 4  $\mu$ M Fd, 3 mM NADP<sup>+</sup>, 100 mM NaAsc, 0.8 mM DCPIP, buffer (black: 50 mM: MOPS-NaOH pH 7.0; red: 50 mM Tris-HCl pH 7.5; blue: 50 mM Tricine buffer pH 8.0 + 3.0 mM NaCl + 0.03 % n-dodecyl- $\beta$ -malto-side, red light ( $\lambda$ = 685 nm, 500  $\mu$ mol m<sup>-2</sup> s<sup>-1</sup>), 100 rpm, reaction volume 1 mL. c) Influence of molecular oxygen on NADPH production by the PSI-Fd-FNR cascade. NADPH production was monitored in aerobic (yellow line) and oxygen-free (blue line) conditions over time (0 to 6 h). Conditions: 0.57  $\mu$ M PSI (50  $\mu$ g Chl), 1  $\mu$ M FNR, 4  $\mu$ M Fd, 3 mM NADP<sup>+</sup>, 100 mM NaAsc, 0.8 mM DCPIP, Tris-HCl buffer pH 7.5, red light ( $\lambda$ = 685 nm, 500  $\mu$ mol m<sup>-2</sup> s<sup>-1</sup>), 100 rpm, reaction volume 1 mL, 25 °C. All experiments were performed in triplicate, error bars represent standard deviation.

Once the optimal pH was determined, we tested the influence of molecular oxygen on the PSI-Fd-FNR biocascade. Both the electron donor NaAsc and NADP<sup>+</sup> are relatively stable in the presence of O<sub>2</sub> but other components such as PSI,<sup>[17a]</sup> Fd,<sup>[21]</sup> and FNR,<sup>[22]</sup> are known to produce reactive oxygen species. To avoid these side reactions, all PSI-Fd-FNR bioconversions were performed in an O<sub>2</sub>-free

environment ( $< 10$  ppm) (Figure 2c). However, to investigate the effect of  $O_2$  on NADPH production, PSI-Fd-FNR was also exposed to air (pH 7.5, ordinary laboratory conditions) and the results were compared to a measurement in an  $O_2$ -free environment (Figure 2c). Interestingly, there was no significant difference in the initial rate of NADPH production in both reaction conditions. This indicates that the electron transfer between PSI, Fd, and FNR is highly streamlined due to the high concentration of  $O_2$  in the natural system, which is in agreement with previous results.<sup>[23]</sup>

The streamlined electron transfer can be explained by fast electron transfer within PSI,<sup>[24]</sup> a higher second-order rate constant of the interaction between PSI and Fd compared to  $O_2$ , which are  $3.5 \times 10^8 \text{ M}^{-1} \text{ s}^{-1}$  and  $7.5 \times 10^4 \text{ M}^{-1} \text{ s}^{-1}$ , respectively,<sup>[25]</sup> and a higher second-order rate constant of the interaction of Fd with FNR ( $6.2 \times 10^8 \text{ M}^{-1} \text{ s}^{-1}$ ),<sup>[12]</sup> which is faster than the reoxidation of Fd by dissolved  $O_2$ .<sup>[21]</sup> As a result, this streamlined electron transfer prevents interference by  $O_2$  in the presented PSI-Fd-FNR cascade. On the other hand, upon longer incubation under aerobic conditions, a faster decrease in NADPH concentration was observed than in the absence of  $O_2$  (Figure 2c). FNR is known to have a reversible function and can also oxidize NADPH in the presence of an electron acceptor.<sup>[22]</sup> In the PSI-Fd-FNR system,  $Fd_{ox}$ ,<sup>[26]</sup> DCPIP<sub>ox</sub>,<sup>[27]</sup> and  $O_2$  could play such a role, however DCPIP<sub>ox</sub> is short-lived due to the immediate reduction by NaAsc<sup>[28]</sup> and  $Fd_{ox}$  is expected to be rapidly reduced by PSI. Thus, the stronger decline in NADPH concentration under aerobic conditions might be related to the NADPH oxidase activity of FNR, which includes the reaction of  $O_2$  with the reduced flavin adenine dinucleotide (FAD) cofactor of FNR. Additionally, the decreases in NADPH concentration could be due to the decomposition of NADPH over time. The faster decline in NADPH concentration was observed at pH 7.0 and pH 7.5 compared with pH 8.0 (Figure 1b), indicating that the NADPH decomposition is pH dependent.<sup>[29]</sup> The comparison of PSI-Fd-FNR-mediated NADPH generation with other commonly used enzymes demonstrates the applicability of our approach (Table 1).

PSI-Fd-FNR outperformed the turnover number of FDH and PTDH by two to four-fold. Additionally, PSI-Fd-FNR clearly excelled over other light-driven NADPH recycling systems, which are based on FNR quantum dot fusions (FNR-QD),<sup>[33]</sup> and a graphene-based photocatalyst with a  $[Cp^*Rh(bpy)Cl]^+$  complex (Graphene photocat-Rh)<sup>[34]</sup> (Table 1). Also, the turnover number (TON) of PSI-Fd-FNR, calculated based on 1h time points, was determined to be 3035, indicating the robustness of the system. With a series of optimizations, the NADPH generation capacity of PSI-Fd-FNR could be further improved, e. g. by optimizing the stoichiometry of PSI, Fd and FNR, as well as by improving the rate of the individual electron transfer steps. The rate constant for DCPIPH<sub>2</sub> mediated reduction of the oxidized P700 reaction center of PSI under continuous illumination was reported to be  $1.9 \times$



$10^8 \text{ M}^{-1} \text{ s}^{-1}$  at pH 8.0 with methyl viologen as the final electron acceptor,<sup>[35]</sup> which is less than the rate constant of Fd reduction by PSI (as mentioned above) and clearly the rate-limiting step in electron transfer of the system. Additionally, the electron transfer rates of DCPIPH<sub>2</sub> and NaAsc are diffusion limited. Thus, isotropic immobilization of PSI on an electrode surface and efficient electronic coupling by redox-active hydrogels, as shown previously,<sup>[36]</sup> may also improve electron donation to the PSI-Fd-FNR cascade.

To further compare the different NADPH recycling systems, the performance of each system was evaluated based on additional parameters such as atom efficiency and simplicity of product isolation (Table 1). As a result, FDH and PTDH appear more promising compared to GDH, FNR-QD and PSI-Fd-FNR. In the case of FDH, CO<sub>2</sub> is formed as a byproduct and easily removed, whereas PTDH forms phosphate, which can also be easily separated via calcium precipitation. The by-products obtained in the case of graphene photocatalyst, GDH, FNR-QD and PSI-Fd-FNR are diethanolamine, gluconolactone/gluconic acid and dehydroascorbic acid, respectively, making these reactions atom inefficient. In addition, separation of the compounds from the reaction mixture is laborious and requires additional steps. Thus, the development of an electrode-based electron supply for PSI-Fd-FNR would also allow water oxidation to be coupled to the system as the ultimate electron source (e.g. by PSII<sup>[17d]</sup>) making it more sustainable and atom efficient. The biocatalytic potential of the PSI-Fd-FNR cofactor recycling system was evaluated by coupling it to three different oxidoreductases catalyzing the asymmetric reduction of C=C and C=O bonds. As a first proof-of-concept, *Nt*DBR was used for the chemoselective reduction of the C=C bond in *trans*-cinnamaldehyde **1a**, producing dihydrocinnamaldehyde **1b** (Figures 3 and S5).



## Chapter 3

**Table 1.** Comparison of PSI-Fd-FNR with other NADPH recycling catalysts, and relative comparison of performance.

NADPH generation catalyst	$k_{\text{cat}}$ (s <sup>-1</sup> )	$K_M$ (mM)	$k_{\text{cat}}/K_M$ (s <sup>-1</sup> mM <sup>-1</sup> )	TON <sup>[b]</sup>	pH	Organism	Electron transfer steps	Electron donor	$k_{\text{cat}}/K_M$ or TON (NADPH) <sup>[e]</sup>	Atom efficiency	Ease of work-up	Ref.
PSI-Fd-FNR	2.55 <sup>[a]</sup>	n.a.	n.a.	3035	7.5	<i>T. vestitus</i> BP1	4	sodium ascorbate	+	—	+	this study
GDH	260	0.027	9630	n.a.	6.5	<i>Bacillus megaterium</i>	1	glucose	+	—	+	[30]
FDH	1.07	3.5	0.31	n.a.	7.0	<i>Bacillus</i> sp. F1	1	sodium formate	+	+	+	[31]
PTDH	0.57	0.74	0.77	n.a.	7.25	<i>Pseudomonas stutzeri</i>	1	sodium phosphite	+	+	+	[32]
FNR-QD	0.40 <sup>[c]</sup>	n.a.	n.a.	1.48	7.0	<i>Chlamydomonas reinhardtii</i>	3	sodium ascorbate	+	—	+	[33]
Graphene photocat-Rh	0.004 <sup>[d]</sup>	n.a.	n.a.	n.a.	7.0	n.a.	2	triethanolamine	—	—	—	[34]

[a] TOF = ([substrate]/[catalyst])/time, based on 10 min time points (0.57  $\mu\text{M}$  PSI, 3 mM NADP<sup>+</sup>). [b] TON = [product]/[catalyst], based on 1 h time points. [c] TOF based on 2 h. [d] TOF based on 348 d<sup>-1</sup>. [e] Ranking order: + + +: Very good, + +: good, +: moderate, -: poor. n. a.: not available. Comparison adapted from reference<sup>[5]</sup> and this study.

We chose this double bond reductase over a flavin-dependent ene reductase (ER) to avoid cross reactivity with a flavin cofactor. *Nt*DBR is active with various  $\alpha,\beta$ -unsaturated activated alkenes, and its optimal pH range was determined to be pH 6.4–7.4.<sup>[14]</sup> *Nt*DBR-catalyzed reactions coupled to PSI-Fd-FNR were carried out at pH 7.0 and 8.0. We only observed a reduction product at pH 7.0, confirming the higher activity of *Nt*DBR at this pH value. After 4 h, the conversion of *trans*-cinnamaldehyde was 29.2 % (1.49 mM), reaching full conversion within 24 h. Therefore, coupling *Nt*DBR with PSI-Fd-FNR resulted in the steady-state consumption of NADPH, likely limiting the NADPH oxidase activity of FNR previously observed (Figure 2c).

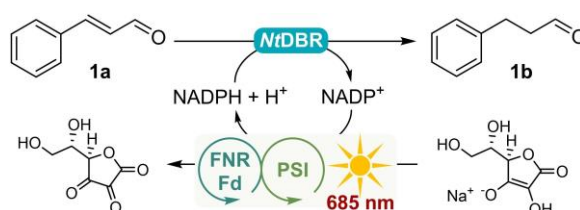


**Figure 3.** *Nt*DBR-catalyzed reduction of *trans*-cinnamaldehyde **1 a** to dihydrocinnamaldehyde **1 b** coupled to light-driven PSI-Fd-FNR NADPH recycling.

### Chapter 3

For the asymmetric reduction of a cyclic ketone, the actinorhodin ketoreductase *actKR* was chosen and coupled to PSI-Fd-FNR (Figure 4a). *actKR* selectively reduces *trans*-1-decalone **2a** to (*S*)-1-decalol **2b**,<sup>[15,37]</sup> however the substrate used in this reaction was a commercially available 65: 35 mixture of *trans*- and *cis*-isomers of 1-decalone, giving the theoretically two (*S*)-products with a maximum conversion of 65 % (Figure 4b). Running the reaction with PSI-Fd-FNR over 4 h, we observed two product peaks for 1-decalol **2b** (Figure S6), with 49 % conversion. The maximum 65 % conversion was reached over 24 h, leaving the *cis*-1-decalone unreacted due to the selectivity of *actKR*.

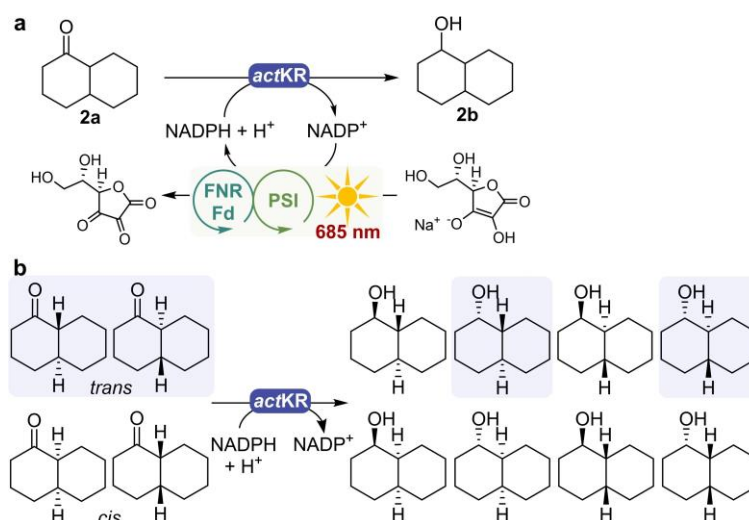


**Figure 4.** a) *actKR*-catalyzed reduction of 1-decalone **2a** to 1-decalol **2b** coupled to light-driven PSI-Fd-FNR NADPH recycling. b) Expected enantiomers highlighted in violet of (*S*)-1-decalol after *actKR*-catalyzed reduction of *trans*-1-decalone

The PSI-Fd-FNR cofactor recycling system was also coupled with *LbADH* for the asymmetric reduction of acetophenone **3a** (Figures 5, S4 and S7), obtaining 3.7 mM of (*R*)-1-phenylethanol **3b** in 4 h. A 24 h reaction afforded full conversion with a product yield of 4.0 mM (*R*)-1-phenylethanol **3b** and no acetophenone left due to evaporation under the current reaction set-up. Evaporation was confirmed in a control reaction without PSI, in which the acetophenone concentration displayed a loss of approximately 1 mM over 24 h of incubation under the reaction conditions (Table 2). Improvements to the reaction system would most likely address this issue and allow for a scale-up.

## Chapter 3

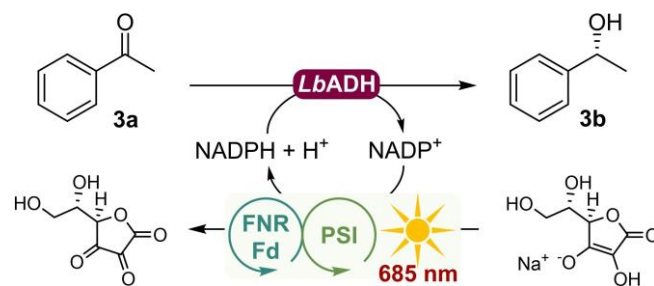


**Figure 5.** *LbADH*-catalyzed reduction of acetophenone **3a** to (*R*)-1-phenylethanol **3b** coupled to light-driven PSI-Fd-FNR NADPH recycling.

Table 2. Biocatalytic conversions of oxidoreductases coupled with the PSI-Fd-FNR cofactor recycling system. <sup>[a]</sup>			
Parameters	Biocatalytic reaction results		
Oxidoreductase	<i>Ni</i> DBR	<i>act</i> KR	<i>LbADH</i>
Substrate (5 mM)	<i>trans</i> -cinnamaldehyde <b>1 a</b>	<i>trans</i> -1-decalone <b>2 a</b>	acetophenone <b>3 a</b>
Product	dihydrocinnamaldehyde <b>1b</b>	decalol <b>2 b</b>	( <i>R</i> )-1-phenylethanol <b>3 b</b>
<b>4 h PSI-Fd-FNR recycling</b>			
Substrate conversion (%)	29.2 ± 4.6	49.5 ± 0.3	99.3 ± 9.0 <sup>[b]</sup>
Product yield (mM)	1.49 ± 0.24	2.47 ± 0.01	3.73 ± 0.08
<b>24 h PSI-Fd-FNR recycling</b>			
Substrate conversion (%)	> 99.9 ± 8.4	65.3 ± 0.9	93.7 ± 12.8 <sup>[b]</sup>
Product yield (mM)	4.97 ± 0.42	3.26 ± 0.04	3.98 ± 0.02
<b>24 h no PSI (control)</b>			
Substrate conversion (%)	< 0.1	< 0.1	< 0.1 (3.44 ± 0.02 mM acetophenone left) <sup>[b]</sup>
no product observed			

[a] Experiments performed in triplicate. [b] High substrate conversion yet incomplete yield observed due to evaporation of acetophenone over 24 h.

## 3.3 Conclusions

In conclusion, we successfully reconstituted the photosynthetic electron transport chain in vitro for the regeneration of NADPH. NADP<sup>+</sup> reduction by PSI-Fd-FNR was best at pH 7.5, reaching a turnover frequency of 2.55 s<sup>-1</sup> (> 9000 h<sup>-1</sup>). We observed no difference in the NADPH production rate under aerobic and anaerobic conditions. Instead, a faster decline of NADPH over time under aerobic conditions was ascribed to FNR oxidation activity and cofactor decomposition when unused. To prove applicability, PSI-Fd-FNR was coupled to *Ni*DBR, *act*KR, and *LbADH*, achieving full conversion without affecting enantioselectivity. The light-driven NADPH generation afforded a TON of 3050, thus, we demonstrated the capacity of PSI-Fd-FNR to drive continuous NADPH-dependent biocatalytic conversion.

### 3.4 Experimental Section

#### Enzymes purification

Enzymes were produced and purified as previously reported: PSI from *Thermosynechococcus vestitus* BP1 (formerly known as *T. elongatus* BP-1),<sup>[38]</sup> double bond reductase from *Nicotiana tabacum* (NtDBR),<sup>[14]</sup> actinorhodin ketoreductase from *Streptomyces coelicolor* (actKR),<sup>[37]</sup> alcohol dehydrogenase from *Lactobacillus brevis* (LbADH).<sup>[39]</sup> The genes of Fd and FNR from *T. vestitus* BP1 were recombinantly expressed in BL21  $\Delta$ iscR and BL21, respectively, and subsequently purified by affinity chromatography.<sup>[40]</sup>

#### Determination of NADPH production rate of PSI-Fd-FNR biocascade

Reaction conditions: 100 mM sodium ascorbate (NaAsc), 0.8 mM dichlorophenolindophenol (DCPIP), 50  $\mu$ g chlorophyll (Chl) equivalent photosystem I (PSI), 4  $\mu$ M ferredoxin (Fd), 1  $\mu$ M of ferredoxin NADP<sup>+</sup> reductase (FNR), 3 mM NADP<sup>+</sup>. Different pH and buffer conditions were used based on the type of biocatalytic reaction: 50 mM MOPS-NaOH pH 7.0, 50 mM Tris-HCl pH 7.5 or 50 mM Tricine buffer pH 8.0 with 30 mM NaCl and 0.03 % n-dodecyl- $\beta$ -maltoside in a reaction volume of 1 mL. Unless otherwise mentioned, all reactions were performed under anaerobic conditions at room temperature (25 °C to 31 °C), shaken at 100 rpm. NADP<sup>+</sup> reduction was initiated by illumination with red light ( $\lambda$ = 685 nm, 500  $\mu$ mol m<sup>-2</sup> s<sup>-1</sup>). For estimation of the produced NADPH, an aliquot of 30  $\mu$ L of the reaction medium was collected after 0, 10, 30 min, 1, 2, 4, and 6 h of incubation. The collected reaction medium was centrifuged with a 3 kDa Centricon<sup>TM</sup> filter to remove all protein components. The concentration step was performed until the volume was reduced to < 20  $\mu$ L. The flow-through was stored at -20 °C until future use.

The amount of NADPH was quantified by fluorescence spectroscopy (Edinburgh Instruments FLS900) using a quartz cuvette with 1 cm path length. 2  $\mu$ L of the above flow through was diluted to 2 mL, and then the measurement was performed. The sample was excited at 340 nm and emission spectra were recorded from 350 to 650 nm. The set parameters were dwell time 0.10 s, lamp Xe900, temperature 25 °C, scan slit: 1.9980, detector R928. The standard curve was established by serial dilution of NADPH (0 to 6  $\mu$ M). The standard curve with corresponding NADPH concentrations and fluorescence range are as shown (Figure S3). Based on the standard curve, the NADPH production rate of the PSI-Fd-FNR biocascade was estimated. Each subjected sample value represents the average of 5 scan repeats of 3 individual replicates.

### Determination of activity of the PSI-Fd-FNR biocascade

The NADP<sup>+</sup> reduction activity of the PSI-Fd-FNR biocascade was determined based on the NADPH concentration at 10 min time point of the reaction. The determined activity of PSI-Fd-FNR system was 0.092 U and 0.087 U at pH 7 and pH 7.5, respectively. The TOF and TON values were obtained by normalization of enzyme units of the PSI-Fd-FNR biocascade with respect to the time point and concentration of PSI.

### Coupling of PSI-Fd-FNR NADPH recycling system

Biotransformation reactions of *Nt*DBR, *act*KR, and *Lb*ADH were carried out with the PSI-Fd-FNR NADPH recycling system. Reaction conditions: 100 mM NaAsc, 0.8 mM DCPIP, 50 mg Chl equivalent PSI, 4  $\mu$ M Fd, 1  $\mu$ M FNR, 3 mM NADP<sup>+</sup>, 30 mM NaCl, 0.03 %  $\beta$ -DM, 5  $\mu$ M enzyme (Table 3), 5 mM substrate, buffer (Table 3), reaction volume: 1 mL, incubation time: 24 h, room temperature (25 °C to 31 °C), 100 rpm, inert atmosphere. Depending on the enzyme, the corresponding substrate and buffer were used (Table 3). To quench the biocatalytic reactions, the reaction medium was filtered through a 3 kDa cut-off filter until the protein volume reached < 50  $\mu$ L. The flow-through sample was extracted with 500  $\mu$ L ethyl acetate containing 5 mM dodecane (internal standard), and was vortexed and centrifuged (13,000 rpm, 10 °C, 4 min). The organic phase was separated, dried over anhydrous MgSO<sub>4</sub>, transferred to a GC vial and analyzed by GC-FID with calibration curves. Bioconversion was assessed at 4 and 24 h of reaction time (Table 2).

Table 3. Substrate concentration and buffers.		
Enzyme (5 $\mu$ M)	[Substrate] (5 mM)	Buffer
<i>act</i> KR	<i>cis/trans</i> -1-decalone	50 mM Tris-HCl pH 7.5
<i>Nt</i> DBR	<i>trans</i> -cinnamaldehyde	50 mM MOPS-NaOH pH 7.0
<i>Lb</i> ADH	acetophenone	50 mM Tris-HCl pH 7.5

## 3.5 References

- [1] a) S. K. Wu, R. Snajdrova, J. C. Moore, K. Baldenius, U. T. Bornscheuer. *Angew. Chem. Int. Ed.* **2021**, *60*, 88-119; b) C. K. Winkler, J. H. Schrittwieser, W. Kroutil. *ACS Cent. Sci.* **2021**, *7*, 55-71; c) U. Hanefeld, F. Hollmann, C. E. Paul. *Chem. Soc. Rev.* **2022**, *51*, 594-627.
- [2] L. Sellés Vidal, C. L. Kelly, P. M. Mordaka, J. T. Heap. *Biochim Biophys Acta Proteins Proteom* **2018**, *1866*, 327-347.
- [3] a) H. K. Chenault, G. M. Whitesides. *Appl. Biochem. Biotechnol.* **1987**, *14*, 147-197; b) A. Guarneri, W. J. H. van Berkel, C. E. Paul. *Curr. Opin. Biotechnol.* **2019**, *60*, 63-71.
- [4] S. Mordhorst, J. N. Andexer. *Nat. Prod. Rep.* **2020**, *37*, 1316-1333.
- [5] L. Lauterbach, O. Lenz, K. A. Vincent. *FEBS J.* **2013**, *280*, 3058-3068.
- [6] a) K. Köninger, Á. Gómez Baraibar, C. Mügge, C. E. Paul, F. Hollmann, M. M. Nowaczyk, R. Kourist. *Angew. Chem. Int. Ed.* **2016**, *55*, 5582-5585; b) L. Assil-Companiononi, H. C. Buchsensschutz, D. Solymosi, N. G. Dyczmons-Nowaczyk, K. K. F. Bauer, S. Wallner, P. Macheroux, Y. Allahverdiyeva, M. M. Nowaczyk, R. Kourist. *ACS Catal.* **2020**, *10*, 11864-11877; c) E. Erdem, L. Malihan-Yap, L. Assil-Companiononi, H. Grimm, G. D. Barone, C. Serveau-Avesque, A. Amouric, K. Duquesne, V. de Berardinis, Y. Allahverdiyeva, V. Alphan, R. Kourist. *ACS Catal.* **2022**, *12*, 66-72.
- [7] M. Hobisch, J. Spasic, L. Malihan-Yap, G. D. Barone, K. Castiglione, P. Tamagnini, S. Kara, R. Kourist. *ChemSusChem* **2021**, *14*, 3219-3225.
- [8] a) P. Jordan, P. Fromme, H. T. Witt, O. Klukas, W. Saenger, N. Krauss. *Nature* **2001**, *411*, 909-917; b) A. Badura, D. Guschin, T. Kothe, M. J. Kopczak, W. Schuhmann, M. Rogner. *Energy Environ. Sci.* **2011**, *4*, 2435-2440.
- [9] R. Mutoh, N. Muraki, K. Shinmura, H. Kubota-Kawai, Y. H. Lee, M. M. Nowaczyk, M. Rogner, T. Hase, T. Ikegami, G. Kurisu. *Biochemistry* **2015**, *54*, 6052-6061.
- [10] P. Liauw, T. Mashiba, M. Kopczak, K. Wiegand, N. Muraki, H. Kubota, Y. Kawano, M. Ikeuchi, T. Hase, M. Rogner, G. Kurisu. *Acta Crystallogr. Sect. F Struct. Biol. Cryst. Commun.* **2012**, *68*, 1048-1051.
- [11] M. Ihara, Y. Kawano, M. Urano, A. Okabe. *PLoS One* **2013**, *8*, e71581.
- [12] N. Cassan, B. Lagoutte, P. Setif. *J. Biol. Chem.* **2005**, *280*, 25960-25972.
- [13] C. E. Lubner, A. M. Applegate, P. Knorzer, A. Ganago, D. A. Bryant, T. Happe, J. H. Golbeck. *Proc. Natl. Acad. Sci.* **2011**, *108*, 20988-20991.
- [14] D. J. Mansell, H. S. Toogood, J. Waller, J. M. X. Hughes, C. W. Levy, J. M. Gardiner, N. S. Scrutton. *ACS Catal.* **2013**, *3*, 370-379.
- [15] P. Javidpour, J. Bruegger, S. Srithahan, T. P. Korman, M. P. Crump, J. Crosby, M. D. Burkart, S. C. Tsai. *Chem. Biol.* **2013**, *20*, 1225-1234.
- [16] S. Leuchs, L. Greiner. *Chem. Biochem. Eng. Q.* **2011**, *25*, 267-281.
- [17] a) A. Petrova, M. Mamedov, B. Ivanov, A. Semenov, M. Kozuleva. *Photosynth. Res.* **2018**, *137*, 421-429; b) D. Dvoranová, Z. Barbieriková, S. Dorotikova, M. Malcek, A. Brincko, L. Rispanová, L. Bucinsky, A. Stako, V. Brezová, P. Raptá. *J. Solid State Electrochem.* **2015**, *19*, 2633-2642; c) J. S. Fruton. *J. Biol. Chem.* **1934**, *105*, 79-85; d) T. Kothe, N. Plumeré, A. Badura, M. M. Nowaczyk, D. A. Guschin, M. Rogner, W. Schuhmann. *Angew. Chem. Int. Ed.* **2013**, *52*, 14233-14236; e) A. Badura, T. Kothe, W. Schuhmann, M. Rogner. *Energy Environ. Sci.* **2011**, *4*, 3263-3274.
- [18] a) D. M. Kramer, C. A. Sacksteder, J. A. Cruz. *Photosynth. Res.* **1999**, *60*, 151-163; b) M. D. L. Trinh, S. Masuda. *Front. Plant Sci.* **2022**, *13*, 919896.
- [19] a) P. Q. Y. Setif, H. Bottin. *Biochemistry* **1994**, *33*, 8495-8504; b) J. Li, N. Hamaoka, F. Makino, A. Kawamoto, Y. Lin, M. Rogner, M. M. Nowaczyk, Y. H. Lee, K. Namba, C. Gerle, G. Kurisu. *Commun Biol* **2022**, *5*, 951.

### Chapter 3

- [20] a) P. Fromme, A. Melkozernov, P. Jordan, N. Krauss. *FEBS Lett.* **2003**, 555, 40-44; b) T. Takabe, H. Ishikawa, S. Niwa, S. Itoh. *J Biochem* **1983**, 94, 1901-1911.
- [21] G. Wittenberg, W. Sheffler, D. Darchi, D. Baker, D. Noy. *Phys. Chem. Chem. Phys.* **2013**, 15, 19608-19614.
- [22] N. Carrillo, E. A. Ceccarelli. *Eur. J. Biochem.* **2003**, 270, 1900-1915.
- [23] K. Jensen, J. B. Johnston, P. R. O. de Montellano, B. L. Moller. *Biotechnol. Lett.* **2012**, 34, 239-245.
- [24] K. Nguyen, B. D. Bruce. *Biochim. Biophys. Acta Bioenerg.* **2014**, 1837, 1553-1566.
- [25] a) G. E. Milanovsky, A. A. Petrova, D. A. Cherepanov, A. Y. Semenov. *Photosynth. Res.* **2017**, 133, 185-199; b) P. Sétif. *Biochim. Biophys. Acta Bioenerg.* **2001**, 1507, 161-179.
- [26] M. Faro, S. Frago, T. Mayoral, J. A. Hermoso, J. Sanz-Aparicio, C. Gomez-Moreno, M. Medina. *Eur. J. Biochem.* **2002**, 269, 4938-4947.
- [27] R. Masaki, K. Wada, H. Matsubara. *J Biochem* **1979**, 86, 951-962.
- [28] M. I. Karayannis. *Talanta* **1976**, 23, 27-30.
- [29] J. T. Wu, L. H. Wu, J. A. Knight. *Clin. Chem.* **1986**, 32, 314-319.
- [30] T. Nagao, Y. Makino, K. Yamamoto, I. Urabe, H. Okada. *FEBS Lett.* **1989**, 253, 113-116.
- [31] H. T. Ding, D. F. Liu, Z. L. Li, Y. Q. Du, X. H. Xu, Y. H. Zhao. *J. Appl. Microbiol.* **2011**, 111, 1075-1085.
- [32] L. Zhang, E. King, W. B. Black, C. M. Heckmann, A. Wolder, Y. Cui, F. Nicklen, J. B. Siegel, R. Luo, C. E. Paul, H. Li. *Nat. Commun.* **2022**, 13, 5021.
- [33] K. A. Brown, M. B. Wilker, M. Boehm, H. Hamby, G. Dukovic, P. W. King. *ACS Catal.* **2016**, 6, 2201-2204.
- [34] S. Choudhury, J.-O. Baeg, N.-J. Park, R. K. Yadav. *Green Chem.* **2014**, 16, 4389-4400.
- [35] T. Fujii, E. Yokoyama, K. Inoue, H. Sakurai. *Biochim. Biophys. Acta* **1990**, 1015, 41-48.
- [36] P. Wang, A. Frank, F. Zhao, J. Szczesny, J. R. C. Junqueira, S. Zacarias, A. Ruff, M. M. Nowaczyk, I. A. C. Pereira, M. Rogner, F. Conzuelo, W. Schuhmann. *Angew. Chem. Int. Ed.* **2021**, 60, 2000-2006.
- [37] S. A. Serapian, M. W. van der Kamp. *ACS Catal.* **2019**, 9, 2381-2394.



## **Supplementary information**

### General information

Enzymes were produced and purified as previously reported: PSI from *Thermosynechococcus vestitus* BP1 (formerly also known as *T. elongatus* BP-1),<sup>[1]</sup> *Nicotiana tabacum* double bond reductase from *Nicotiana tabacum* (NtDBR),<sup>[2]</sup> actinorhodin ketoreductase from *Streptomyces coelicolor* (actKR),<sup>[3]</sup> alcohol dehydrogenase from *Lactobacillus brevis* (LbADH).<sup>[4]</sup> The genes of Fd and FNR from *Thermosynechococcus vestitus* BP1 were recombinantly expressed in BL21 *ΔiscR* and BL21, respectively and later purified by affinity chromatography.<sup>[5]</sup>

### Electron transfer and protein-protein interaction in PSI-Fd-FNR Biocascade

**Electron transfer in PSI-Fd-FNR biocascade:** Electron transfer in PSI-Fd-FNR biocascade depends on the paradigm of potential difference between individual components of the biocascade. However, here detailed electron transfer process of PSI-Fd-FNR biocascade is illustrated (Figure S1).

**Interaction of DCPIP with P700:** The small size and hydrophobic nature of DCPIPH<sub>2</sub> likely enables it to directly access the luminal side of PSI and reduce the oxidized P700 (chlorophyll *a*, molecular dimer). The hydrophobic patch on the luminal side of PSI may favor DCPIP over sodium ascorbate (NaAsc) due to the hydrophobic nature of DCPIP, which enables faster electron transfer. This hydrophobic patch is formed by some of the amino acids of PsaA and PsaB subunits of PSI, which were identified based on the Pc-PSI co-structure, as reported previously.<sup>[6]</sup>

**Interaction of Fd with PSI:** The cryo-EM co-structure of PSI-Fd as described in Li et.al 2022 revealed that Fd binds to the stromal side subunits of PSI, particularly PsaA, PsaC and PsaE.<sup>[7]</sup> In this study wide range of electrostatic and hydrophobic interactions was found to be crucial for the association of Fd and PSI. In Figure S2, we highlighted only the interaction surfaces of Fd with three subunits of PSI, PsaA (blue), PsaC (pink), and PsaE (green). These interactions placed the FeS cluster of Fd 8.2 Å away from the FeS cluster of the PsaC subunit of PSI, thus enabling direct electron transfer. Upon association of Fd with PSI, the dissociation of water molecules surrounding the interfaces of Fd and PSI energetically contributes to an increase in entropy which favors the complexation between Fd and PSI. Thus, the binding of Fd with PSI is entropy driven.<sup>[7]</sup>

**Interaction of Fd with FNR:** Crystallography and mutation studies have provided structural and biochemical insights into the interaction of maize leaf Fd and FNR.<sup>[8]</sup> Fd interacts at a concave region of the FAD domain of FNR. Interaction of Fd with the FAD domain, places the [2Fe-2S] cluster of Fd at close distance, almost 6 Å, from the isoalloxazine ring of FAD, such that direct electron transfer occurs between these two prosthetic groups. The interaction of Fd with FNR involves electrostatic interactions via salt bridges as well as hydrophobic interactions.<sup>[8]</sup> The amino acids involved in the interaction are highlighted, Fd (in red) and FNR (in blue), as indicated (Figure S2).

#### **NADPH production rate with the PSI-Fd-FNR biocascade**

Reaction conditions: 100 mM sodium ascorbate (NaAsc), 0.8 mM dichlorophenolindophenol (DCPIP), 50 µg chlorophyll (Chl) equivalent photosystem I (PSI), 4 µM ferredoxin (Fd), 1 µM of ferredoxin NADP<sup>+</sup> reductase (FNR), 3 mM NADP<sup>+</sup>. Different pH and buffer conditions were used based on the type of biocatalytic reaction: 50 mM MOPS-NaOH pH 7.0, 50 mM Tris-HCl pH 7.5, 50 mM Tricine buffer pH 8.0 +30 mM NaCl + 0.03% *n*-dodecyl-β-maltoside, reaction volume of 1 mL. Unless otherwise mentioned, all reactions were performed under anaerobic conditions at room temperature (25 °C to 31 °C), shaken at 100 rpm. NADP<sup>+</sup> reduction was initiated by switching on with red light (absorption maximum  $\lambda=685$  nm, 500 µmol m<sup>-2</sup> s<sup>-1</sup>). For estimation of produced NADPH, an aliquot of 30 µL of the reaction medium was collected after 0, 10, 30 min, 1, 2, 4, and 6 h of incubation. The collected reaction medium was centrifuged with a 3 kDa Centricon<sup>TM</sup> filter to remove all protein components. The concentration step was performed until the volume was reduced to <20 µL. The flow-through was stored at -20 °C until future use.

The amount of NADPH was quantified by fluorescence spectroscopy (Edinburgh Instruments FLS900) using a quartz cuvette with 1 cm path length. 2 µL of the above flow through was diluted to 2 mL, and then the measurement was performed. The sample was excited at 340 nm and emission spectra were recorded from 350 to 650 nm. The set parameters were dwell time 0.10 s, lamp Xe900, temperature 25 °C, scan slit: 1.9980, detector R928. The standard curve was established by serial dilution of NADPH (0 to 6 µM). The standard curve with corresponding NADPH concentrations and fluorescence range are as shown (Figure S3). Based on the standard curve, the NADPH production rate of the PSI-Fd-FNR biocascade was estimated. Each subjected sample value represents the average of 5 scan repeats of 3 individual replicates.

### Determination of activity of the PSI-Fd-FNR biocascade

The NADP<sup>+</sup> reduction activity of the PSI-Fd-FNR biocascade was determined based on the NADPH concentration at 10 min time point of the reaction. The determined activity of PSI-Fd-FNR system was 0.092 U and 0.087 U at pH 7 and pH 7.5, respectively. The TOF and TON values were obtained by normalization of enzyme units of the PSI-Fd-FNR biocascade with respect to the time point and concentration of PSI.

### Biotransformation reactions with *Nt*DBR, *act*KR, and *Lb*ADH

#### Coupled to the PSI-Fd-FNR NADPH recycling system

Biotransformation reactions of *Nt*DBR, *act*KR, and *Lb*ADH were carried out with the PSI-Fd-FNR NADPH recycling system. PSI-Fd-FNR biocascade reaction conditions: 100 mM NaAsc, 0.8 mM DCPIP, 50 mg Chl equivalent PSI, 4  $\mu$ M Fd, 1  $\mu$ M FNR and 3 mM NADP<sup>+</sup>, 30 mM NaCl, 0.03%  $\beta$ -DM. Reaction volume: 1 mL, incubation time: 24 h, room temperature (25 °C to 31 °C), 100 rpm. Depending on the enzyme, the corresponding substrate and buffer were used (Table S1). All oxidoreductases were added in an equal amount of 5  $\mu$ M. These biocatalytic reactions were performed under inert atmosphere.

Table S1. Substrate concentrations

Enzyme	Substrate	Conc. (mM)	Buffer
<i>act</i> KR	<i>trans</i> and <i>cis</i> -1-decalone	5	50 mM Tris-HCl pH 7.5
<i>Nt</i> DBR	<i>trans</i> -cinnamaldehyde	5	50 mM MOPS-NaOH pH 7.0
<i>Lb</i> ADH	acetophenone	5	50 mM Tris-HCl pH 7.5

To quench the biocatalytic reactions, the reaction medium was filtered through a 3 kDa cut-off filter until the protein volume reached <50  $\mu$ L. Then, the flow-through sample was subjected to extraction. For this, 500  $\mu$ L ethyl acetate with 5 mM dodecane (internal standard) was added, the sample was vortexed and centrifuged (13,000 rpm, 10 °C, 4 min) dried with anhydrous MgSO<sub>4</sub>, vortexed and centrifuged again, and the organic phase was decanted in GC vials to be analyzed by GC-FID with calibration curves. Bioconversion was assessed at 4 and 24 h of reaction (Table 2).

**With NADPH or coupled to GDH**

Biotransformation reactions of *NtDBR*, *actKR*, and *LbADH* were carried out using the substrates mentioned above (Table S1) with NADPH or coupled to GDH. Reaction conditions: 50 mM MOPS-NaOH pH 7.0, 30 mM NaCl for *NtDBR*, 50 mM Tris-HCl pH 7.5, 30 mM NaCl for *actKR*, *LbADH*, reaction volume: 1 mL, incubation time: 24 h, 25 °C, 500 rpm. In case of *NtDBR* and *actKR*, NADPH and substrate were added in an equimolar ratio of 5 mM with enzyme concentrations of 5  $\mu$ M, without red light. In case of *LbADH*, a glucose dehydrogenase (GDH) recycling system consisting of 10 U GDH from *Bacillus subtilis* (*BsGDH*), 3 mM NADP<sup>+</sup>, 100 mM glucose was used. Reactions were performed under aerobic conditions.

To quench the biocatalytic reactions, the reaction medium was filtered through a 3 kDa cut-off filter until the protein volume reached <50  $\mu$ L. Then, the flow-through sample was subjected to extraction. For this, 500  $\mu$ L ethyl acetate with 5 mM dodecane (internal standard) was added, the sample was vortexed and centrifuged (13,000 rpm, 10 °C, 4 min) dried with anhydrous MgSO<sub>4</sub>, vortexed and centrifuged again, and the organic phase was decanted in GC vials to be analyzed by GC-FID with calibration curves to obtain yields (Table S2).

**Table S2. Yield of biotransformation reactions with NADPH or GDH recycling**

Enzyme	Yield (%)
<i>NtDBR</i>	91.9 $\pm$ 4.0
<i>actKR</i>	62.2 $\pm$ 1.3
<i>LbADH</i>	81.7 $\pm$ 0.1

## Supplementary Figures

## Electron transfer with PSI-Fd-FNR biocascade

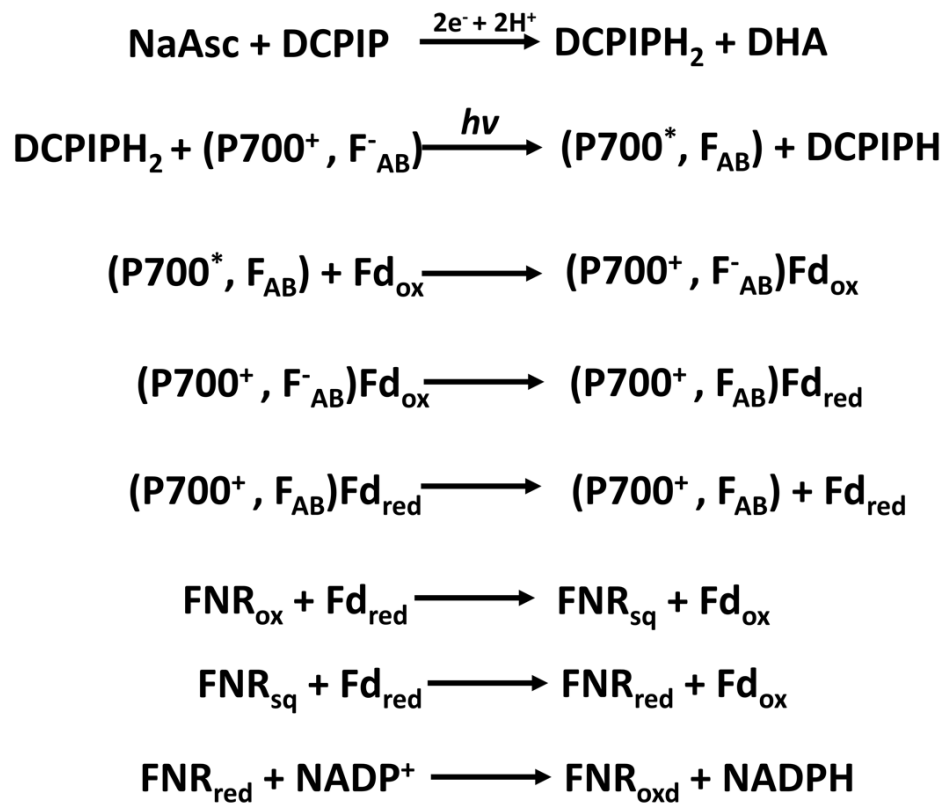


**Figure S1.** Series of electron transfer steps involved in the PSI-Fd-FNR biocascade. NaAsc: sodium ascorbate, DHA: dehydroascorbic acid, DCPIP: dichlorophenolindophenol, P700: chlorophyll *a*, molecular dimer, F<sub>AB</sub>: two iron-sulfur clusters present in PsaC subunit of PSI, Fd<sub>Red/Oxd</sub>: ferredoxin (oxidized or reduced), FNR<sub>Oxd/Sq/Red</sub>: ferredoxin NADP<sup>+</sup> oxidoreductase (oxidized or semi reduced/ reduced)

## Protein-protein interactions with PSI-Fd-FNR biocascade

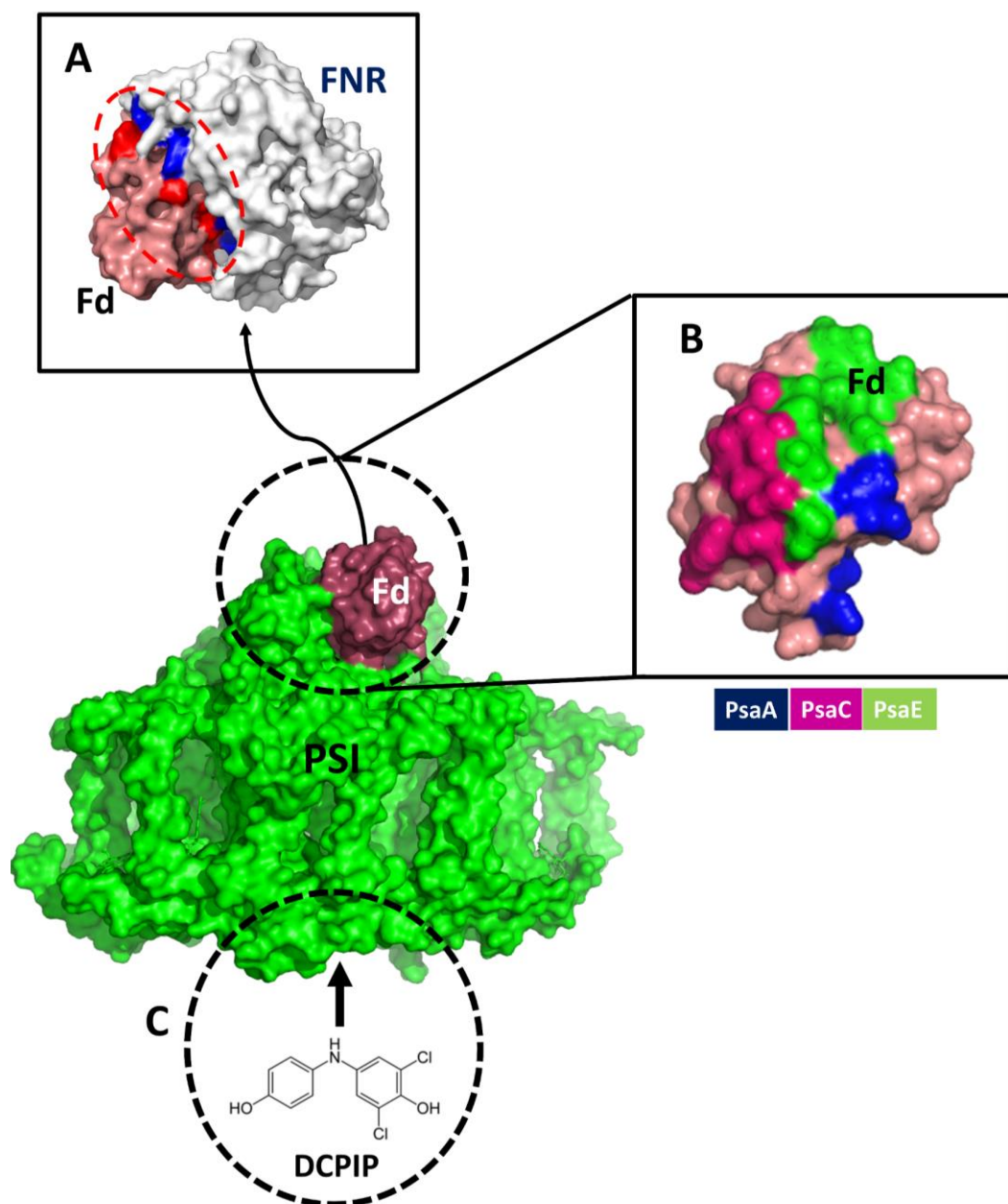


**Figure S2: Illustration of the protein-protein interaction within the PSI-Fd-FNR biocascade.** A) A co-crystal structure of Fd and FNR based on X-ray crystallography and their interactions (PDB: 1GAQ). Highlighted are the interacting surfaces of both proteins, Fd (red) and FNR (blue) are depicted as described previously. B) A co-structure of Fd and PSI based on cryo-electron microscopy and their interactions (PDB: 7FIX). Highlighted are the interacting surfaces of Fd participating in complex formation with 3 subunits of PSI, PsaA (blue), PsaC (pink), and PsaE (green) as described previously. C) Simplified schematic representation of the electron transfer from DCPIP to the luminal side of PSI. Unless otherwise mentioned, the protein structures used in this study were adapted using PyMOL.



## NADPH calibration curve

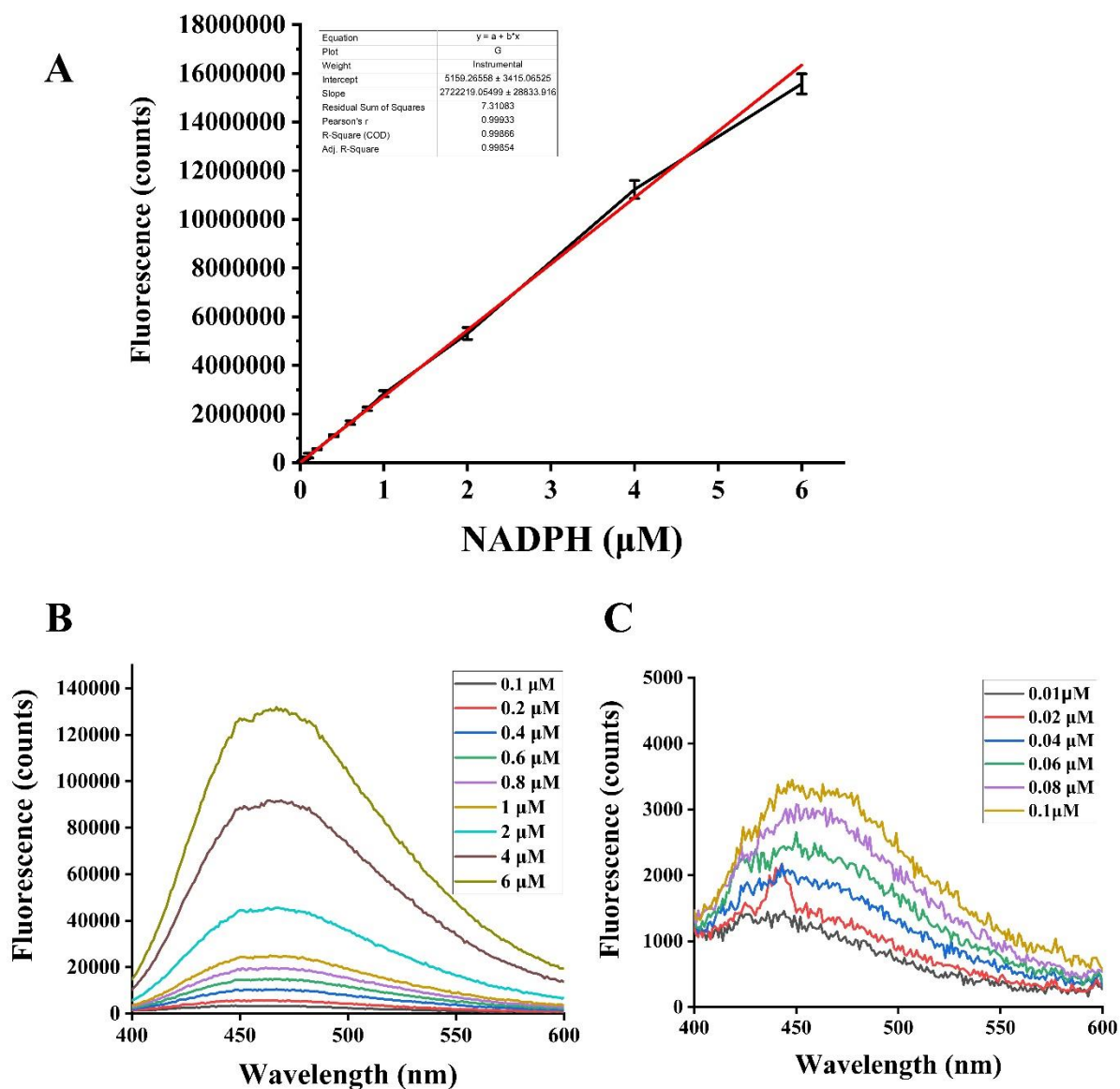


**Figure S3. Quantification of NADPH based on fluorescence.** **A)** Calibration curve of NADPH based on fluorescence area corresponding to concentration of NADPH (0.01 to 6  $\mu\text{M}$ ). **B)** Fluorescence area corresponding to NADPH concentration (0.1 to 6  $\mu\text{M}$ ). **C)** Fluorescence area corresponding to NADPH concentration (0.01 to 0.1  $\mu\text{M}$ ). Measurements were performed with an Edinburgh fluorescence spectrophotometer.

## Gas chromatography analyses

### Conversion of *trans*-cinnamaldehyde **1a**

Method: DB-5MS column, 70 °C hold 2 min, 10 °C/ min up to 120 °C and hold for 3 min, 5 °C/min up to 150 °C and hold for 5 min, 10 °C/ min up to 230 °C and hold for 2 min. Split ratio: 1:50, inlet at 220 °C. FID at 250 °C, Carrier gas H<sub>2</sub> at 19.41 psi, 2.0 mL/min. The standard curve of *trans*-dihydrocinnamaldehyde (0 to 5 mM) is depicted in **Figure S4**. The GC chromatogram of *trans*-cinnamaldehyde to dihydrocinnamaldehyde conversion is given in **Figure S5**.

Retention time (min)	Compound
5.4	dihydrocinnamaldehyde <b>1b</b>
6.0	dodecane (internal standard)
7.1	<i>trans</i> -cinnamaldehyde <b>1a</b>

### Conversion of 1-decalone **2a**

Method: DB-WAX column. 40 °C, hold 2 min, 10 °C/min to 230 °C, hold 3 min. Split ratio 1:10. Inlet at 220 °C. FID at 250 °C. Carrier gas at 19.41 psi, 2.0 mL/min. The standard curve of 65:35 mixture of *trans* and *cis*-1-decalone (0 to 5 mM) is depicted in **Figure S4**. The GC chromatogram of *trans* and *cis*-1-decalone to decalol conversion is depicted in **Figure S6**.

Retention time (min)	Compound
4.2	dodecane (internal standard)
11.3	<i>trans</i> and <i>cis</i> -1-decalone <b>2a</b>
12.1	Product 1 decalol <b>2b</b>
12.5	Product 2 decalol <b>2b</b>

ND: Not detected

### Conversion of acetophenone **3a**

Method: Chiraldex column, start at 100 °C, 5 °C/min up to 150 °C and hold for 0.5 min. Carrier gas: H<sub>2</sub>, split ratio: 1:50 inlet at 220°C, Carrier gas H<sub>2</sub>. The standard curve of (*R*)-1-phenylethanol (0 to 5 mM) is given in **Figure S4**. The GC chromatograms of the conversion of acetophenone to (*R*)-1-phenylethanol and (*S*)-phenyl-ethanol are depicted in **Figure S7**.

Retention time (min)	Compound
5.8	acetophenone <b>3a</b> (substrate)
6.5	dodecane (internal standard)
7.9	( <i>R</i> )-1-phenylethanol ( <i>R</i> )- <b>3b</b>
8.1	( <i>S</i> )-1-phenylethanol ( <i>S</i> )- <b>3b</b>

## GC calibration curves

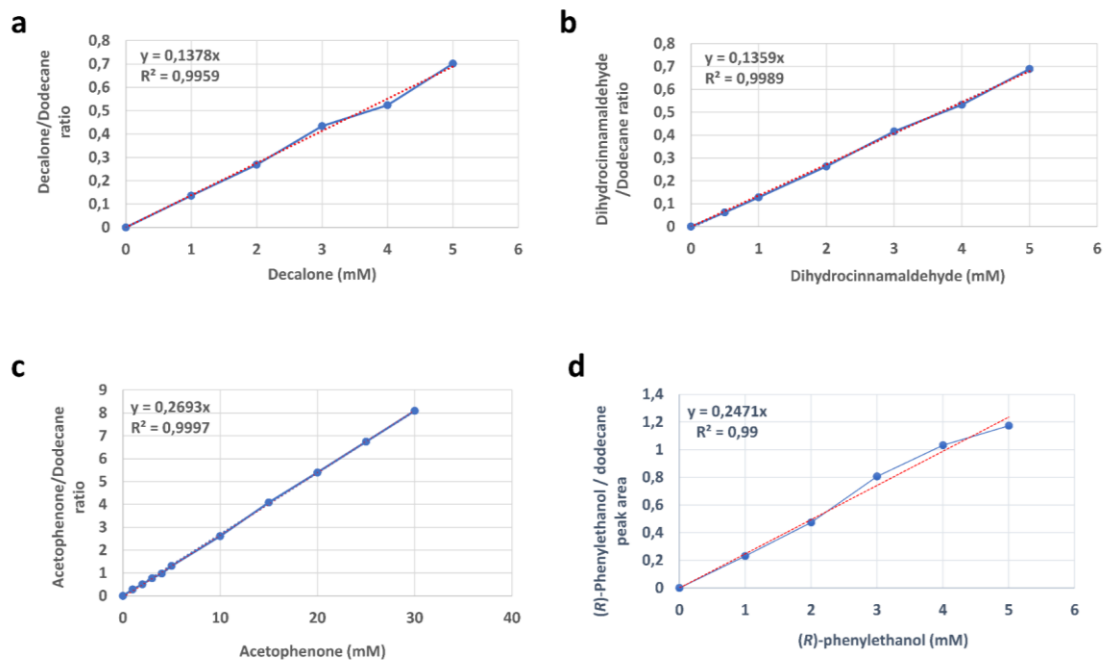


**Figure S4.** Calibration curves of compounds obtained based on GC measurements. **A)** Calibration curve of decalone. **B)** Calibration curve of dihydrocinnamaldehyde. **C)** Calibration curve of acetophenone. **D)** Calibration curve of (*R*)-1-phenylethanol.

## GC chromatograms

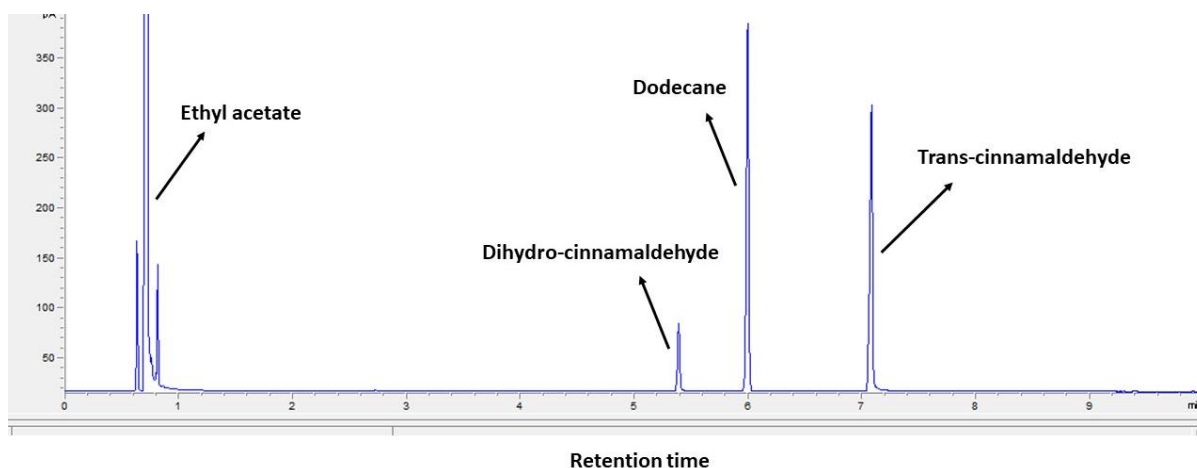


**Figure S5.** GC chromatogram of *NtDBR*-catalyzed *trans*-cinnamaldehyde **1a** reduction to dihydrocinnamaldehyde **1b** after a reaction time of 4 h.

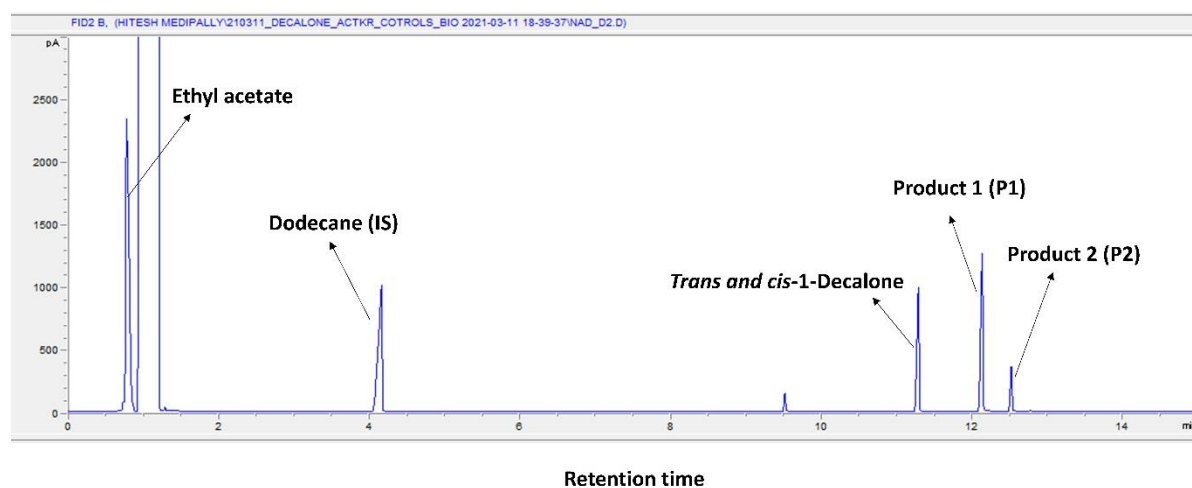


**Figure S6.** GC chromatogram of *actKR*-catalyzed *trans* and *cis*-1-decalone **2a** reduction after a reaction time of 24 h.

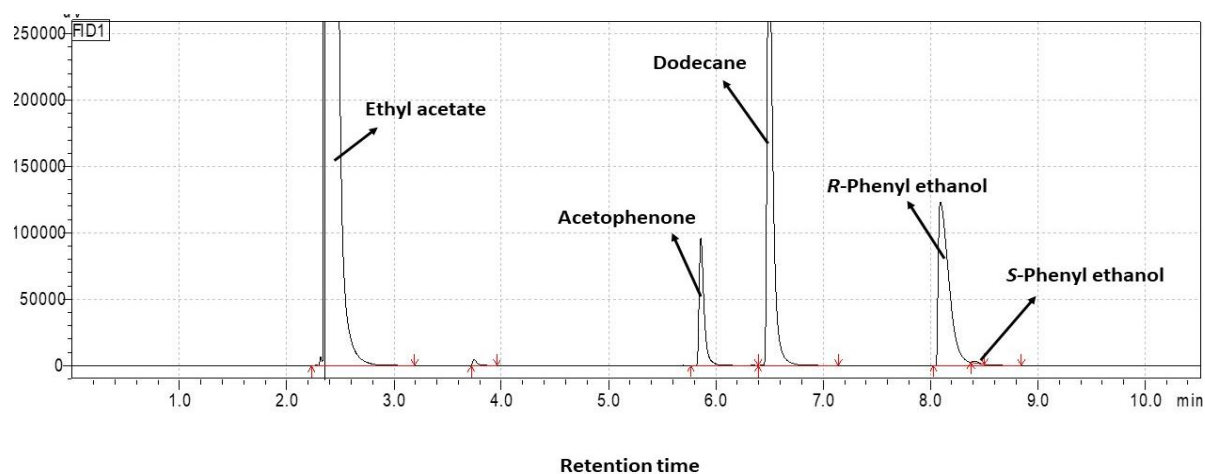


**Figure S7.** GC chromatogram of ADH-catalyzed acetophenone **3a** reduction after a reaction time of 4 h.

## Chapter 3

### Reaction setup and temperature of reaction overtime



**Figure S8.** Reaction setup with 1 mL reaction volume glass vials and red light at  $\lambda=685$  nm,  $500 \mu\text{mol m}^{-2} \text{s}^{-1}$ .

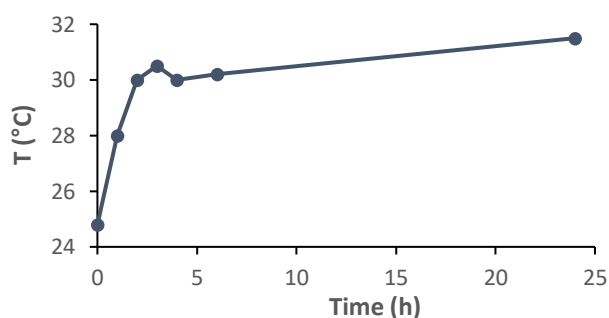


**Figure S9.** Change in temperature of the red light illuminated reaction medium over time (0 to 24 h).

## References

- [1] E. El-Mohsnawy, M. J. Kopczak, E. Schlodder, M. Nowaczyk, H. E. Meyer, B. Warscheid, N. v. Karapetyan, M. Rögner, *Biochemistry* **2010**, *49*, 4740–4751.
- [2] D. J. Mansell, H. S. Toogood, J. Waller, J. M. X. Hughes, C. W. Levy, J. M. Gardiner, N. S. Scrutton, *ACS Catal* **2013**, *3*, 370–379.
- [3] S. A. Serapian, M. W. van der Kamp, *ACS Catal* **2019**, *9*, 2381–2394.
- [4] N. Adebar, H. Gröger, *Bioengineering* **2019**, *6*, 1–26.
- [5] H. Medipally, M. Mann, C. Kötting, W. J. H. van Berkel, M. Nowaczyk, *ChemBioChem* **2023**, e202300025.
- [6] I. Caspy, A. Borovikova-Sheinker, D. Klaiman, Y. Shkolnisky, N. Nelson, *Nat Plants* **2020**, *6*, 1300–1305.
- [7] J. Li, N. Hamaoka, F. Makino, A. Kawamoto, Y. Lin, M. Rögner, M. M. Nowaczyk, Y.-H. Lee, K. Namba, C. Gerle, G. Kurisu, *Commun Biol* **2022**, *5*, 951.
- [8] G. Kurisu, M. Kusunoki, E. Katoh, T. Yamazaki, K. Teshima, Y. Onda, Y. Kimata-Arigo, T. He, *Nat Struct Biol* **200**

## Chapter 4: A clickable photosystem I, ferredoxin, and ferredoxin NADP<sup>+</sup> reductase Fusion system for light-driven NADPH regeneration

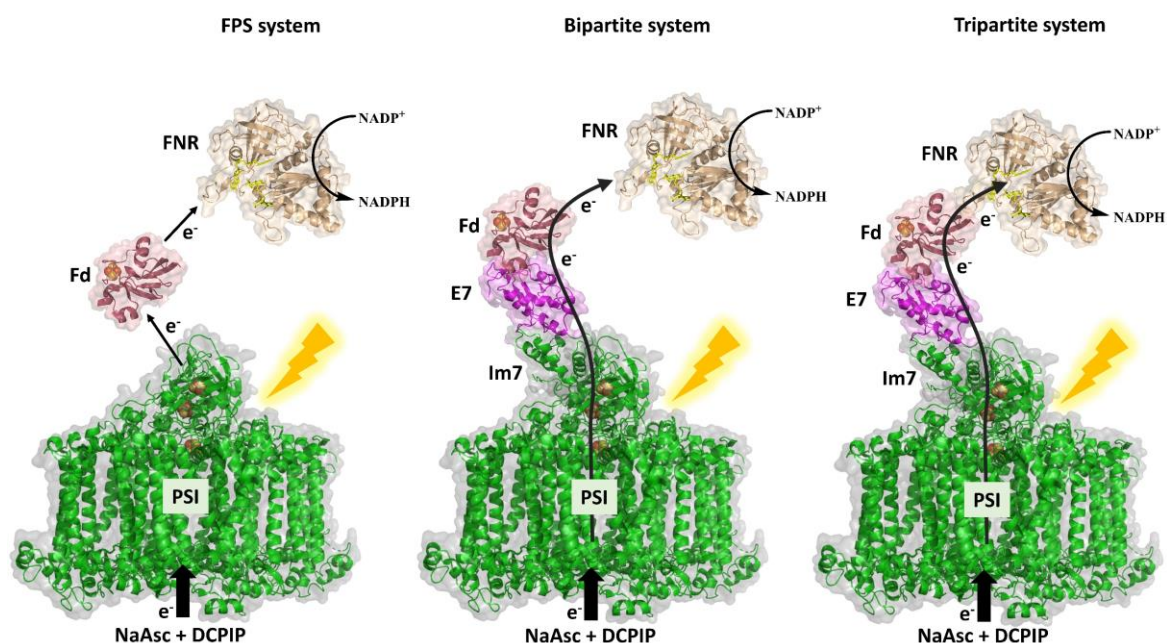
Hitesh Medipally, , Marvin Mann, Dr. Carsten Kötting, Prof. Dr. Willem J. H. van Berkel, Prof. Dr. Marc M. Nowaczyk

### Publication 3

**ChemBioChem 2023, e202300025**

**<https://doi.org/10.1002/cbic.202300025>**

**Abstract:** Photosynthetic organisms like plants, algae, and cyanobacteria use light for the regeneration of dihydronicotinamide dinucleotide phosphate (NADPH). The process starts with the light-driven oxidation of water by photosystem II (PSII) and the released electrons are transferred via the cytochrome  $b_6f$  complex towards photosystem I (PSI). This membrane protein complex is responsible for the light-driven reduction of the soluble electron mediator ferredoxin (Fd), which passes the electrons to ferredoxin NADP<sup>+</sup> reductase (FNR). Finally, NADPH is regenerated by FNR at the end of the electron transfer chain. In this study, we established a clickable fusion system for in vitro NADPH regeneration with PSI-Fd and PSI-Fd-FNR, respectively. For this, we fused immunity protein 7 (Im7) to the C-terminus of the PSI-PsaE subunit in the cyanobacterium *Synechocystis* sp. PCC 6803. Furthermore, colicin DNase E7 (E7) fusion chimeras of Fd and FNR with varying linker domains were expressed in *Escherichia coli*. Isolated Im7-PSI was coupled with the E7-Fd or E7-Fd-FNR fusion proteins through high-affinity binding of the E7/Im7 protein pair. The corresponding complexes were tested for NADPH regeneration capacity in comparison to the free protein systems demonstrating the general applicability of the strategy in vitro NADPH regeneration with PSI-Fd and PSI-Fd-FNR, respectively. For this, we fused immunity protein 7 (Im7) to the C-terminus of the PSI-PsaE subunit in the cyanobacterium *Synechocystis* sp. PCC 6803. Furthermore, colicin DNase E7 (E7) fusion chimeras of Fd and FNR with varying linker domains were expressed in *Escherichia coli*. Isolated Im7-PSI was coupled with the E7-Fd or E7-Fd-FNR fusion proteins through high-affinity binding of the E7/Im7 protein pair. The corresponding complexes were tested for NADPH regeneration capacity in comparison to the free protein systems demonstrating the general applicability of the strategy.



**Clickable PSI** - PSI-Im7 was used with free Fd and FNR (FPS system) or coupled to E7-Fd (bipartite system) and E7-Fd-FNR (tripartite system) via the E7-Im7 affinity system for continuous regeneration of NADP



## 4.1 Introduction

Photosystem I (PSI) is involved in light-driven electron transfer in photosynthetic organisms. It is regarded as one of the strongest biological reductants with high quantum efficiency and exceptional negative redox potential, which is sufficient to provide electrons to various intrinsic oxidoreductases involved in different metabolic processes of the cell, like carbon fixation or nitrogen assimilation.<sup>[1–3]</sup> Due to the natural abundance and stability of PSI, development of biohybrid solar devices using PSI for efficient conversion of solar energy into chemical energy is a promising strategy.<sup>[4–6]</sup> However, achieving direct electron transfer from PSI to a catalyst of interest is challenging due to its complex architecture and lack of cofactor exposure on the protein surface.<sup>[7]</sup> These features distinguish PSI from other single-molecule photosensitizers, which can act as direct reductants for enzymes.<sup>[8]</sup> The native and mobile redox mediator between PSI and many intrinsic oxidoreductases is ferredoxin (Fd)<sup>[1]</sup> Therefore, electron transfer is a diffusion dependent process and the rate of electron supply depends on the interaction frequency of three components (PSI, Fd, and the terminal oxidoreductase). A tailored redox interface can facilitate the exploitation of the high electron yield of PSI to drive specific oxidoreductases of interest. Several strategies were proposed to achieve direct electron transfer from PSI.<sup>[9–11]</sup> One of the most commonly used strategies is tethering the redox partner (Fd, oxidoreductase, or metal catalyst) onto the extrinsic subunits of PSI to achieve molecular confinement. This approach enables a rapid and direct electron transfer from PSI to the redox partner and helps in channelling electrons to the specific oxidoreductase of interest. For example, by tethering a thiol linker-containing hydrogenase on a PSI-Cyt *c*<sub>6</sub> fusion module, the electron transfer rate was two times higher compared to the natural system (105 vs. 45 e<sup>-</sup> PSI<sup>-1</sup> s<sup>-1</sup>).<sup>[9]</sup> Several types of other PSI-tethering strategies were proposed in recent years, such as reconstitution of Fd-PsaE-fusions to PSI complexes that were previously stripped and devoid of extrinsic stromal subunits,<sup>[12]</sup> recombination of the fusion to PsaE deletion mutants,<sup>[12]</sup> and site-directed assembly of Pt nanoparticles onto PSI.<sup>[13]</sup> Molecular tethering of redox partners was also reported previously by direct genetic fusion of a hydrogenase to the extrinsic subunits of PSI (PsaE, PsaD, PsaC)<sup>[10,14,15]</sup> as well as a direct genetic fusion of Fd with a hydrogenase.<sup>[16]</sup> All these models represent the combinations of bipartite fusions, i.e., either Fd or an oxidoreductase fused to PSI or Fd fused to the oxidoreductase.

We have developed a multipurpose PSI fusion system, which allows tethering of various mediators and catalytic modules such as Fd or Fd-FNR, aiming for tailored and efficient electron transfer from PSI to its redox partners. This fusion is based on the high-affinity interaction of the E7-Im7 system.

DNase E7 (E7) is a cytotoxic protein produced in *E. coli* and other Enterobacteriaceae strains as a stress response,<sup>[17,18]</sup> which degrades DNA unspecifically. To avoid degradation of its own genomic DNA, the host cell produces the counter “Immunity protein 7” (Im7), which strongly binds to E7 and inhibits its activity.<sup>[19,20]</sup> These two proteins associate with high affinity ( $K_D = 10^{-14}$  to  $10^{-17}$  M) and the protein couple can be used for highly efficient protein purification by affinity chromatography.<sup>[21]</sup> The cytotoxic activity of E7 can be suppressed by replacing a histidine residue at position 120 with alanine (H120A), allowing the safe recombinant expression of E7 in *E. coli* expression systems.<sup>[22]</sup>

In this study, Im7-modified PSI was generated and isolated from *Synechocystis* sp. PCC 6803 (hereafter *Synechocystis*) and combined with the recombinant chimeric protein constructs E7-Fd and E7-Fd-FNR as a proof of concept. Both model variants were tested based on light-induced NADPH formation and compared with the free protein system.

## 4.2 Results and Discussion

### Characterization of PSI-Im7-Histag

In this study, the N-terminus of Im7 was fused with the C-terminus of the PSI subunit PsaE. From a structural point of view, the PsaE subunit of PSI is exposed to the stroma and its C and N-terminus are freely accessible.<sup>[7]</sup> For this reason, and the fact that the least physiological consequences are exhibited by PSI lacking the PsaE subunit,<sup>[23]</sup> PsaE was chosen as the optimal subunit location for fusion with Im7. The fusion does not influence the growth rate of the PSI-Im7 mutant under provided growth conditions (Figure S1), indicating that this modification has no impact on the physiology of the strain. Blue Native (BN)-PAGE analysis revealed that the C-terminally His-tagged PSI-Im7 complex was successfully isolated using immobilized metal affinity chromatography (IMAC). In this way, we purified an equivalent of 3.2 mg chlorophyll (Chl) of PSI-Im7 from thylakoid membranes corresponding to the total Chl amount of 71 mg. The isolated PSI-Im7 was mostly present in the trimeric form (~ 1000 kDa; Figure 1A). The observed bands above 1000 kDa on BN-PAGE may correspond to larger PSI aggregates. SDS-PAGE subunit analysis (Figure 1B) of the PSI-Im7 complex was also performed, and individual subunits of PSI-Im7 were identified based on the previously determined masses of subunits. The following subunits of PSI-Im7 were identified: PsaA, PsaB, PsaC, PsaD, PsaE-Im7, PsaF. As expected, only IM7 modified PsaE was identified in PSI-Im7, indicating its successful integration into PSI. Identification of PsaC and PsaD further indicates that fusion of Im7 to PsaE did not influence the assembly of the other extrinsic subunits. Furthermore,

spectral analysis revealed no significant differences between the light-absorbing properties of PSI-Im7 and PSI-Wt (Figure S2A): both PSI complexes showed absorption maxima at 453 nm and 665 nm.<sup>[24]</sup>

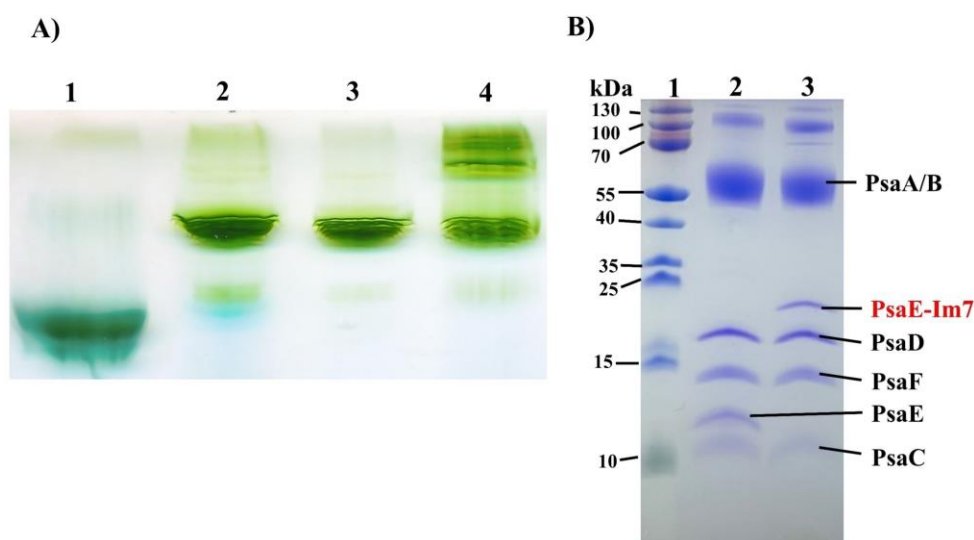


**Figure 1. Biochemical characterization of the PSI-Im7-Histag complex.** A) BN PAGE-based analysis of the oligomeric state of PSI Im7-Histag. 1: PSII monomer of *Thermosynechococcus vestitus* BP-1, 2: PSI Wt trimer of *T. vestitus* BP-1, 3: PSI-Wt trimer of *Synechocystis*, 4: PSI-Im7-Histag complex of *Synechocystis* after IMAC purification. Equivalents of 3.5  $\mu\text{g}$  Chl were loaded onto each gel lane. B) SDS-PAGE analysis of PSI-Im7: 1: Protein marker (PageRuler ThermoScientific™). 2: PSI-Wt of *Synechocystis*, 3: PSI-Im7-Histag of *Synechocystis*. Equivalents of 2.5  $\mu\text{g}$  Chl were loaded onto each gel lane.

The photoreduction rate of oxygen by isolated PSI-Im7 was comparable to that of PSI-Wt being  $1827 \pm 21 \mu\text{mol O}_2 \text{ mg Chl}^{-1} \text{ mL}^{-1} \text{ h}^{-1}$  for PSI-Wt and  $2038 \pm 24 \mu\text{mol O}_2 \text{ mg Chl}^{-1} \text{ mL}^{-1} \text{ h}^{-1}$  for PSI-Im7, respectively (Figure S2B). Thus, the PsaE-Im7 fusion does not influence PSI activity. The ability of PSI-Im7 to bind to DNase E7 and the photochemical activity of the complex was additionally verified by infrared difference spectroscopy. For this purpose, the Im7-tagged PSI was circulated over a chemically functionalized and E7-covered germanium internal reflection element (IRE). Figure S3 shows the binding of PSI-Im7 on this surface and the stability of the complex during the subsequent washing step. In the next step, the surface with the immobilized PSI-Im7 complex was used to investigate the light-induced conformational change of the protein. For comparison, the light-induced difference spectrum was also measured in a transmission measurement for PSI in solution. In both setups a similar difference spectrum was obtained, indicating native complex formation and immobilization of PSI (Figure S4). Due to the thickness of the transmission cuvette, total absorption by water occurred in the range between  $1680 \text{ cm}^{-1}$  and  $1600 \text{ cm}^{-1}$  in the transmission measurement, while the attenuated total reflection (ATR) measurement provided an evaluable difference spectrum in this spectral range. Both spectra agree with measurements of PSI-Wt in the literature.<sup>[25,26]</sup>

According to Hastings et al. 2015, the most prominent bands can be assigned as follows: The negative band at  $1700\text{ cm}^{-1}$ , as well as the positive band at  $1687\text{ cm}^{-1}$ , originate from the keto C=O vibration of the  $A_0$  state of chlorophyll a. The positive band at  $1755\text{ cm}^{-1}$  and the negative band at  $1749\text{ cm}^{-1}$  can be assigned to the ester C=O vibration of the  $A_0$  state of chlorophyll a. The negative band at  $1636\text{ cm}^{-1}$  corresponds to a C=C vibration of neutral phyloquinone (PhQ). The positive band at  $1687\text{ cm}^{-1}$  and the negative band at  $1670\text{ cm}^{-1}$  result from amide-I modes. In conclusion, the biochemical and spectroscopic analysis of PSI-Im7 did not reveal any major difference compared to PSI-Wt.

### Isolation and characterization of chimeric E7-Fd and E7-Fd-FNR fusion proteins

N-terminally His-tagged E7-Fd (EF) and E7-Fd-FNR (EFF) fusion proteins were produced in *E. coli* BL21 *ΔiscR* and purified by IMAC. The chimeric fusion proteins consist of a flexible amino acid (AA) linker of GGSG motifs between individual domains. The purity of each chimeric fusion protein was checked by SDS-PAGE (Figures S5 and S6) and successful cofactor assembly was demonstrated by UV-Vis absorption spectroscopy (Figure 2). The EF chimeras (linker length variations of 5, 10, and 15 AA) showed typical Fd absorption properties with spectral maxima at 330 and 420 nm (Figure 2A and 2C). The incorporation of the Fe-S cofactor was investigated by determining the ratio of 420/278 nm, which amounted to 0.59 for Fd and ~ 0.44 for EF (mean value of all variants), respectively. The former value was similar to the expected ratio of fully assembled Fd (0.56) reported previously,<sup>[2]</sup> while the reduced ratio observed for the EF fusion proteins can be explained by the presence of the additional E7 domain, which increases the absorption at 280 nm but not at 420 nm. For example, the calculated extinction coefficient of EF10 at 280 nm is  $24.32\text{ mM}^{-1}\text{ cm}^{-1}$  and that of the E7 domain alone is  $12.49\text{ mM}^{-1}\text{ cm}^{-1}$ . The absorption spectrum of FNR (Figure 2D) represented the typical pattern of a flavoprotein with absorption maxima at 394 nm and 459 nm, as well as a shoulder at 484 nm<sup>[27,28]</sup> and the typical absorption maxima of Fd were observed at 420 and 330 nm. In case of EFF chimeras (linker length variations between Fd and FNR of 5, 10, and 15 AA), the absorption maxima at 394 nm and 459 nm were observed (Figure 2D), indicating the assembly of the flavin adenine dinucleotide cofactor into the FNR domain of EFF. The 459/280 nm ratios for FNR and EFF were 0.29 and ~ 0.19 (mean value of all variants), respectively, which can be explained by the presence of the E7 and Fd domains in the fusion protein. Due to strong absorption of the EFF chimeras at 394 and 459 nm, the absorption peak at 420 nm related to the Fe-S cluster of the Fd domain was masked. However, at 330 nm, the absorption of the EFF chimeras was higher compared to FNR, consistent with the assembly of the Fe-S cluster into the Fd domains of EFF chimeras. To analyze the Fe-S cluster assembly in the EFF chimeras, the FNR spectrum was subtracted from the

spectra of the EFF chimeras (Figure S7). Distinct peaks at 330 and 420 nm clearly indicate the assembly of the Fe-S cluster.

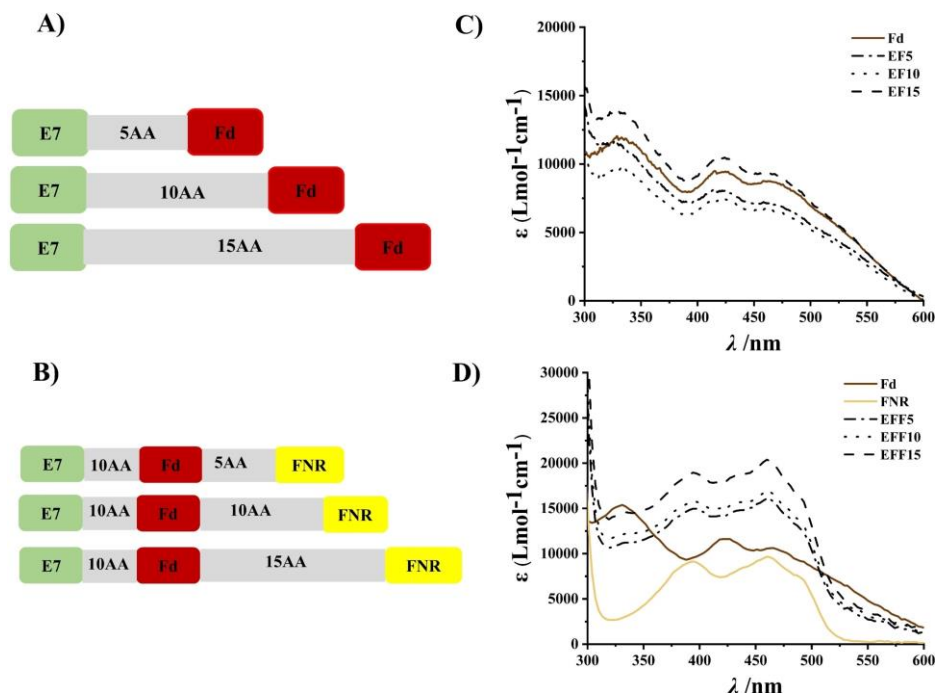


**Figure 2. Design and spectral characterization of E7-Fd (EF) and E7-Fd-FNR (EFF) chimeras.** A) Genetic design of E7-Fd chimeras with respective linker lengths of 5, 10, and 15 AA. B) Genetic design of E7-Fd-FNR with a constant linker length of 10 AA between E7 and Fd and varying linker lengths of 5, 10, and 15 AA between Fd and FNR. C) Absorption spectra of histag purified EF chimeras and strep-tag-purified Fd as reference. A protein concentration of 0.015 mM was used to determine the molar absorption coefficients ( $\epsilon$ ) using a UV-2450 spectrophotometer (Shimadzu) with a path length of 1 cm. D) Absorption spectra of histag purified EFF chimeras. Reference spectra of streptag purified Fd and histag purified FNR are also shown. A protein concentration of 0.4 mM was used to determine the molar absorption coefficients ( $\epsilon$ ) using a NanoDrop™ 2000 spectrophotometer (Thermofisher™) with 0.1 cm path length. Recombinant Fd and FNR are from *Thermosynechococcus vestitus* BP1. Experiments were conducted in triplicate and the data represent mean values

### Coupling of EF and EFF chimeras to PSI-Im7

The strong affinity of E7 for Im7 should promote the coupling of EF and EFF variants to PSI-Im7 even at very low concentrations, avoiding heterogeneity of the *in vitro* system. This feature will also provide an advantage in the case of *in vivo* implementation of the PSI fusions or in the establishment of other *in vivo* fusion systems. Nonetheless, to ensure that every protomer in trimeric PSI-Im7 binds chimeric EF/EFF variants, we used a 1: 8 molar ratio of PSI-Im7 (per protomer) and EF/EFF. The coupled complexes and excess of EF/EFF were separated by sucrose density gradient centrifugation (SDGC). The large differences in molecular weight between the coupled complexes (~ 1100 kDa)

and EF/EFF (< 100 kDa) chimeras allow easy separation via SDGC (Figure S8). The homogeneity and integrity of PSI chimeras after SDGC separation was confirmed by SDS-PAGE (Figure 3) and BN-PAGE analysis (Figures S9, S10).

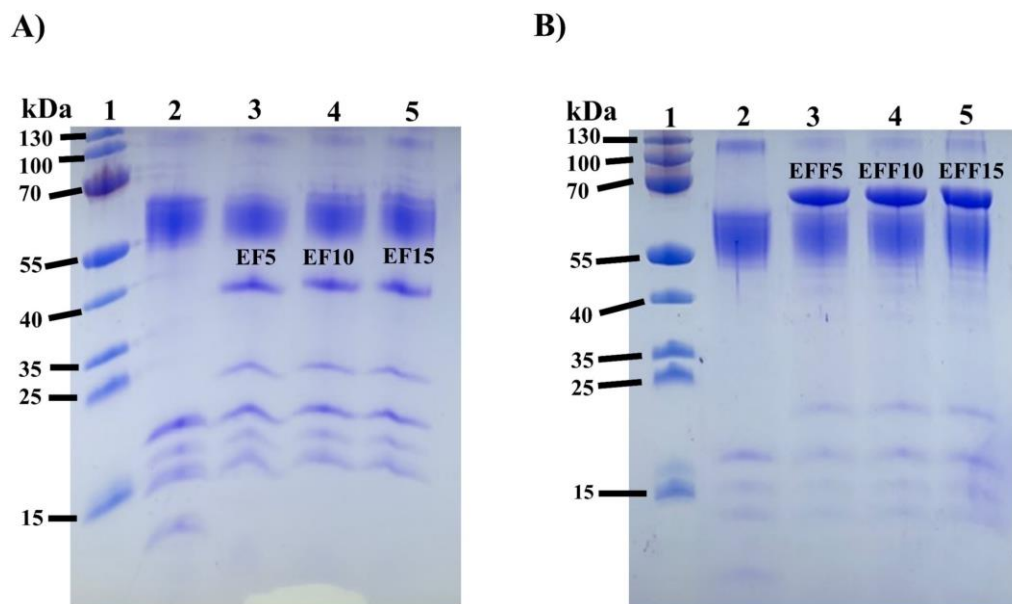


**Figure 3. SDS-PAGE analysis of PSI-Fd (PSI-EF) and PSI-Fd-FNR (PSI-EFF) chimeras after SDGC separation.** A) SDS-PAGE analysis of PSI EF chimeras. 1: Protein marker (PageRuler, ThermoScientific™) with masses of individual protein bands indicated on the left; 2: PSI Wt; 3: PSI EF5; 4: PSI EF10; 5: PSI EF15. B) SDS-PAGE analysis of PSI EFF chimeras. 1: Protein marker (PageRuler, ThermoScientific™) with masses of individual protein bands indicated on the left; 2: PSI Wt; 3: PSI EFF5; 4: PSI EFF10; 5: PSI EFF15. An equivalent of 2.5 µg Chl was loaded onto each gel lane.

### Light-induced $\text{NADP}^+$ reduction of PSI-Fd chimeras

In vitro light-induced electron transfer of PSI-Fd (PSI-EF) chimeras with variable linkers (PSI-EF5, PSI-EF10, PSI-EF15) was characterized by artificial reconstitution of the photosynthetic electron transport chain, including free FNR. Differences in the redox potentials between individual protein components allowed the successive electron transfer in a reconstituted cascade, i. e. from ascorbate to  $\text{NADP}^+$ . In this assay, light-induced electron transfer rates of PSI-EF5, PSI-EF10, PSI-EF15 chimeras, and the free protein system (FPS1) were determined to be  $2.05 \pm 0.22$ ,  $2.49 \pm 0.08$ ,  $1.51 \pm 0.20$  and  $2.02 \pm 0.29$   $\mu\text{M NADPH min}^{-1}$  (Figure 4). With PSI-EF10, the rate of light-induced  $\text{NADP}^+$  reduction compared most favorably with that of FPS1, strengthening the assumption that the optimal linker length between E7-Fd would be around 10 AA. Moal and coworkers reported that the  $\text{NADP}^+$  reduction rate of a PSI-PsaE-Fd coupled construct with a linker length of 10 AA between PSI-PsaE and Fd outperformed the FPS by 1.12-fold.<sup>[12]</sup> To avoid too strong association between PSI



and Fd, which resulted in the absence of catalytic activity, they substituted Arg39 of PsaE with Gln39.<sup>[12]</sup> In the case of PsaE-Im7, the strong association of Fd with PSI was not observed. This might be due to an extra distance or structural change created by the presence of E7-Im7. With a short linker (PSI-EF5), the initial rate of light-induced NADP<sup>+</sup> reduction was about equal to the rate obtained for the free protein system (Figure 4). However, in the case of PSI-EF15, the light-induced NADP<sup>+</sup> reduction was significantly less efficient than with FPS1 (Figure 4), suggesting that the long linker and additional space created by E7-Im7 made this fusion system sterically hindered. The results obtained are in agreement with those of Yacoby et al., who constructed a PSI-based electron transport chain with Fd-hydrogenase fusions for the anaerobic production of hydrogen gas.<sup>[29]</sup> The highest electron transfer rate of these Fd-hydrogenase fusions was achieved with a linker length of 25 AA. However, with 30 AA, the hydrogen production dropped significantly, which could be explained by diffusion-based constraints in the interaction of Fd with PSI and hydrogenase.

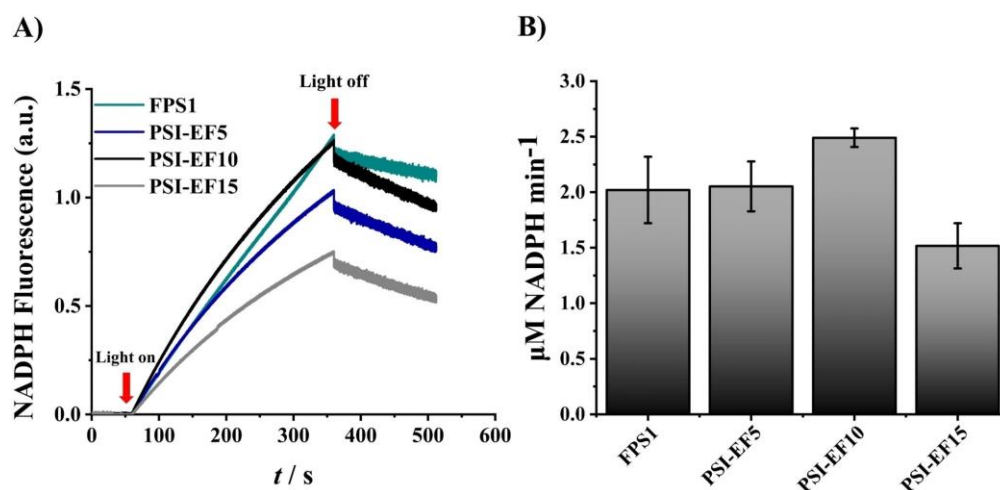


**Figure 4. Light-induced NADPH production by PSI Fd chimeras.** A) Light- induced NADPH formation of FPS1 (cyan), PSI EF5 (blue), PSI EF10 (black), and PSI EF15 (gray) was measured by NADPH fluorescence. The concentration of each fusion protein was 0.25 μM and the concentration of free FNR was 0.75 μM. FPS1 contained 0.25 μM PSI, 0.25 μM Fd, and 0.75 μM FNR. The total measuring time was 8 min with a dark (1 min)-light (5 min)-dark (2 min) cycle. All the experiments were performed in 1.5 mL reaction buffer (50 mM Tricine pH 8, 30 mM NaCl, 4 mM NaAsc, 100 μM DCPIP, 2.5 μM Cyt c<sub>6</sub>, 5 mM MgCl<sub>2</sub> (added only in the case of FPS1), 1 mM NADP<sup>+</sup>, 0.03 % DDM) by artificial reconstitution of the photosynthetic electron transport chain from ascorbate to NADP<sup>+</sup>. B) Initial rates of light-induced NADPH formation. The molar concentrations of PSI EFF fusion complexes were determined after ultracentrifugation based on the chlorophyll amount and considering that each PSI consists of 95 Chl molecules. Experiments were conducted in triplicates, and the data points represent the mean values with standard deviation.



### Light-induced NADP<sup>+</sup> reduction of PSI-Fd-FNR chimeras

The PSI-Fd-FNR (PSI-EFF) chimeras were also characterized by artificial reconstitution of the photosynthetic electron transport chain from ascorbate to NADP<sup>+</sup> and the NADP<sup>+</sup> photoreduction rates were compared with a free protein system (FPS2). The PSI-EFF linker variants (PSI-EFF5, PSI-EFF10, and PSI-EFF15) showed different electron transfer rates, as illustrated in Figure 5. The initial rates of NADP<sup>+</sup> photoreduction of FPS2, PSI-EFF5, PSI-EFF10, and PSI-EFF15 were  $5.30 \pm 0.62$ ,  $3.60 \pm 0.21$ ,  $1.63 \pm 0.15$ ,  $1.07 \pm 0.03$   $\mu\text{M NADPH min}^{-1}$ , respectively. In FPS2, a typical electron supply from PSI via Fd to FNR is expected, i. e. the simultaneous interchange of Fd<sub>ox</sub> with Fd<sub>red</sub> at the Fd-binding site of FNR for reduction of NADP<sup>+</sup> by FNR. [30] In case of the fusion constructs, two-sided tethering of Fd may have introduced steric hindrance in the electron transfer. Nevertheless, PSI-EFF5 activity was only slightly less compared to the activity of FPS2. With longer linker lengths, a decrease in NADP<sup>+</sup> photoreduction rate was observed. We speculate that the wide distance introduced by the linker may have created a lag in the interaction of Fd with FNR. As a result, PSI-EFF5 showed a higher NADP<sup>+</sup> photoreduction rate than PSI-EFF10 and PSI-EFF15, respectively. The functional behavior of each fusion complex might be explained more evidently in future work by building structural models and applying molecular dynamics simulations. [31] Furthermore, the NADPH formation rate of the tripartite system was observed to be faster compared to the bipartite system. The relatively faster NADPH formation rate in the tripartite system could be explained by the faster electron transfer rates between PSI, Fd, and FNR in the initial phase of the reaction (Figure 5). However, in the mid and final phase of the reaction, the higher NADPH fluorescence rate can be attributed to accumulated NADPH and its slow consumption by FNR. This is due to lower FNR concentration in the tripartite system sample (0.25  $\mu\text{M}$ ) compared to the bipartite system sample (0.75  $\mu\text{M}$ ), which is further confirmed by fast consumption of NADPH in the dark in case of the bipartite system (Figures 4 and 5).

### Light-induced electron transfer in various modified PSI fusion complexes

Several PSI fusion models proposed are tabulated below (Table 1). Although each PSI fusion model was developed in combination with different enzymes or mediators and assessed at different reaction conditions, they still can be compared based on electron transfer efficiency, i. e. number of electrons released out of light-excited PSI per second ( $\text{e}^- \text{PSI}^{-1} \text{s}^{-1}$ ). For this, the PSI amount was calculated by considering each PSI monomer consisting of 95 chlorophyll

molecules.<sup>[32]</sup> Among the various PSI fusion models, PSI was modified, particularly to drive hydrogen production *in vitro*, by using platinum or a hydrogen producing enzyme (FeFe or NiFe type hydrogenases) as a catalytic module. Greenbaum and coworkers pioneered the photocatalytic production of hydrogen by developing PSI-metal nanoparticles with direct precipitation of charged Pt ligands and colloidal Pt onto isolated PSI or chloroplasts, respectively.<sup>[33,34]</sup> These models are catalytically less active (Table 1), and deposition of Pt in proximity to the PSI active site was not regulated.

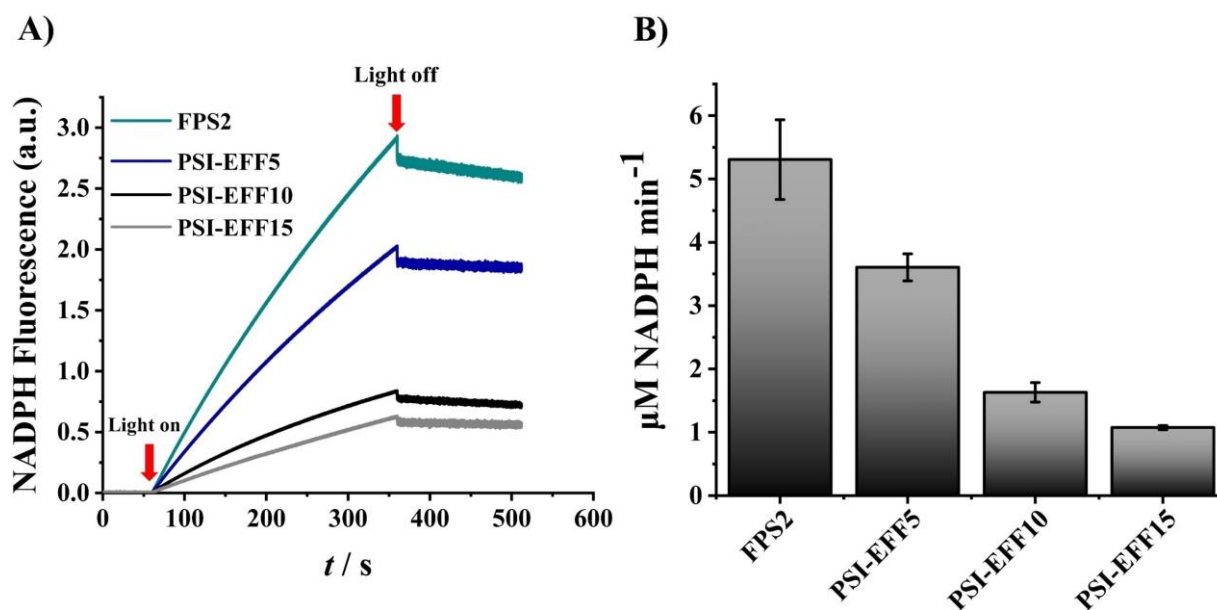


**Figure 5. Light-induced NADPH production by PSI-Fd-FNR chimeras.** A) Light-induced NADPH formation of FPS2 (cyan), PSI-EFF5 (blue), PSI-EFF10 (black), and PSI-EFF15 (gray) was measured by NADPH fluorescence. The concentration of each fusion protein was 0.25  $\mu\text{M}$ . FPS2 contained 0.25  $\mu\text{M}$  PSI, 0.25  $\mu\text{M}$  Fd, and 0.25  $\mu\text{M}$  FNR. The total measuring time was 8 min with a dark (1 min)-light (5 min)-dark (2 min) cycle. All the experiments were performed in 1.5 mL reaction buffer (50 mM Tricine pH 8, 30 mM NaCl, 4 mM NaAsc, 100  $\mu\text{M}$  DCPIP, 2.5  $\mu\text{M}$  Cyt  $c_6$ , 5 mM  $\text{MgCl}_2$  (added only in the case of FPS1), 1 mM  $\text{NADP}^+$ , 0.03 % DDM) by artificial reconstitution of the photosynthetic electron transport chain from ascorbate to  $\text{NADP}^+$ . B) Initial rates of light-induced NADPH formation. The molar concentrations of PSI-EF fusion complexes were determined after ultracentrifugation based on the chlorophyll amount and considering that each PSI consists of 95 Chl molecules. Experiments were conducted in triplicates, and the data represent the mean value with standard deviation.

Similarly, the nickel (II) diphosphine complex  $[\text{Ni}(\text{P}_2^{\text{Ph}}\text{N}_2^{\text{Ph}})_2](\text{BF}_4)_2$  was also deposited on PSI for hydrogen production.<sup>[35]</sup> Another approach was the development of a molecular wire, which connects the terminal  $\text{F}_\text{B}$  cluster of PSI with Pt or hydrogenase for direct electron transfer via a hexane-1,6-dithiol linker integrated into PSI by ligand rescue. In this procedure, recombinant PsaC in which

## Chapter 4

the cysteine residue at position 13 was replaced by glycine (C13G) was prepared from *E. coli* and reconstituted artificially with Fe-S clusters. This enabled the tethering of one end of the thiol linker to the terminal F<sub>B</sub> cluster and the other to the catalyst. Further, this artificially reconstituted PsaC subunit with the catalyst attached was later integrated into PSI.<sup>[9,36,37]</sup> With this approach, the catalyst was kept near the active site of PSI and the electron transfer rates obtained with this system were among the highest reported in the literature. However, this method, which employs synthetic thiol linkers, is not compatible with in vivo approaches because it cannot be applied to whole cells. An alternative approach is based on the in vitro reconstitution of a chimeric hydrogenase with PSI, which was isolated from a  $\Delta$ PsaE mutant.<sup>[15]</sup> In this approach, amino acid-based linkers were used to fuse the hydrogenase with PsaE, which enables in principle also in vivo applications. Indeed, it was shown that the photoautotrophic growth of the PSI- $\Delta$ PsaE mutant was not affected.<sup>[23]</sup> However, the direct electron transfer towards HydA1 coupled to PSI via PsaE was observed to have very low electron transfer rates (Table 1). Recently, Appel et al. and Kanygin et al. showed successful hydrogen production by in vivo PSI modification via direct electron transfer by genetic fusion of the hydrogenase to one of the extrinsic subunits (PsaC, PsaD) of PSI.<sup>[10,14]</sup> However, in both models, physiological constraints were noticed. For instance, in PSI-PsaD-Hox-YH-mutant from the cyanobacterium *Synechocystis*, binding of the PsaD-fusion displaces the PsaC subunit of PSI, and it is assumed that electrons are accepted from the Fx cluster.<sup>[14]</sup> Moreover, the PSI-PsaC-HydA fusion from the eukaryotic microalgae *Chlamydomonas reinhardtii* showed reduced Fd binding ability with PSI up to 50 %.<sup>[10]</sup> Therefore, modification of PsaC or PsaD with hydrogenase is considered a strong mutation leading to poor accumulation of hydrogenase-modified PSI in cells.<sup>[10]</sup> In case of PSI-Im7, the subunit composition and photoreduction activity of PSI are not affected. Also, within PSI-EFF chimeras, a decrease in linker length between Fd and FNR, proportionally increased the NADP<sup>+</sup> photoreduction rate of PSI-EFF chimeras. The electron transfer within PSI-EFF can be further improved by redesigning the linker between Fd and FNR and predicting and testing the suitable catalyst orientation and interaction frequency between PSI, Fd and catalyst might improve the photoreduction rates of the fusion complex.

## Chapter 4

**Table 1: Light-induced electron transfer rate in modified PSI complexes**

Type	$e^- \text{PSI}^-$ $^1\text{s}^{-1}$	Light intensity	pH of the reaction	Temperature of reaction	Literature
PSI-EF10	0.50	100 $\mu\text{E}$	8	25 °C	Present study Present study [15]
PSI-EFF5	0.73	100 $\mu\text{E}$	8	25 °C	
PSI-PsaE-HydA <sup>a</sup>	0.028	1150 $\mu\text{E}$	7.4	30 °C	
PSI-1,6 hexane dithiol- HydA-Cyt <sub>c</sub> crosslinked	73.40	996 $\mu\text{E}$	6.5	20 to 22 °C	[9]
PSI- 1,6 hexane dithiol- HydA <sup>a</sup>	1.44	459 $\mu\text{E}$	8.3	20 to 22 °C	[38]
PSI- 1,6 hexane dithiol-Pt	4.70	70 $\mu\text{E}$	8.3	20 to 23 °C	[11]
PSI-1,4-benzenedithiol-Pt	7.17	70 $\mu\text{E}$	8.3	20 to 23 °C	[11]
Platinized PSI complex	0.00119	2 × 16 $\mu\text{E}$	7	20 °C	[33]
Platinized PSI complex- PC crosslinked	0.0045	531 $\mu\text{E}$	7.1	25 °C	[39]

a)  $\text{W/m}^2$  was converted to  $\mu\text{E}$  based on online calculator (<https://www.skyeinstruments.com/unit-calculator/>)

### Application of PSI Im7 fusion model in development of next- generation photovoltaic cells

PSI has been extensively used as a photochemical module in the development of semi-artificial photosynthetic devices. [40–47] However, insulation of acceptor and donor side of PSI on the electrode surface to avoid charge recombination is challenging and was not realized in many of the PSI-electrode integration models. Due to the lack of insulation, reduced electron acceptors such as methyl viologen (MV) short-circuit the PSI electron input and output side. As a result, the photocurrent output of these models was compromised. In nature, PSI is incorporated into the thylakoid membrane in a defined orientation, preventing short-circuiting between the acceptor and donor side of PSI. In analogy with thylakoids, PSI was fabricated onto the electrode surface in an oriented manner via Langmuir Blodgett technology. [42] However, the dispersed and spatial distribution of PSI trimers achieved with Langmuir Blodgett technology on the electrode surface still contributes to short-circuiting effects. Recently, a significant improvement was made to reduce this by closing the gaps between the PSI trimers with PSI monomers to nullify the effect of spatial distribution. [48] On the other hand, to realize the complete potential of the electron transfer efficiency of PSI, a robust redox interface on both the donor and acceptor sides of PSI is essential. With lack of a proper electron acceptor, electrons from a photoexcited PSI- $\text{F}_\text{B}$  cluster back transfer to internal cofactors  $\text{F}_\text{A}$ ,  $\text{F}_\text{X}$ , and  $\text{A}_{1\text{A}}$ , successively, [49] resulting in charge recombination. Alternatively, the electrons are delivered to an immediately available electron acceptor. In photosynthetic cells, oxygen is such an example. Its reduction results in the formation of reactive oxygen species (ROS) that cause photodamage. Development of a semi-artificial photosynthetic device, which addresses the effect of charge recombination within PSI and short-circuiting within the system can be potentially created by integration of PSI-EFF fusion complexes on the electrode via Langmuir Blodgett technology. Due to

the built-in natural electron mediator within the PSI-EFF construct, the short-circuiting effect should be reduced, and the proximal presence of Fd near the PSI active site may avoid charge recombination within PSI. Another potential application of the PSI-EFF fusion model would be the establishment of rational partitioning of electrons from the photosynthetic electron transport chain to hydrogen production by creation and implementation of in vivo PSI-Im7-hydrogenase fusions.

### 4.4 Conclusions

In this study, we established and characterized Im7-E7 based bipartite (PSI-Fd) and tripartite (PSI-Fd-FNR) fusion systems for light-driven NADPH regeneration. In the bipartite PSI-Fd system, a 10 AA linker between E7 and Fd provided the highest electron transfer rate, most likely because this linker length allowed the required freedom and orientation between PSI-Fd and FNR. In the case of the tripartite PSI-Fd-FNR system, a 5 AA linker between Fd and FNR achieved the best electron transfer rate, which was somewhat lower than that of FPS, probably due to steric hindrance created by the two-sided tethering of Fd. Nevertheless, we believe that PSI fusions (either with or without Fd) based on the E7-Im7 system will have several advantages: i) it enables the fusion of single or multiple oxidoreductases, ii) it can be implemented both in vitro and in vivo, iii) in vivo, it would enable channeling of electrons to specific oxidoreductase of interest by exploiting electrons from the photosynthetic electron transport chain.

### 4.5 Experimental Section

#### Strain construction

A *Synechocystis* PSI PsaE Im7-Histag mutant was generated using the plasmid pRSET6a\_PsaE\_Im7\_Histag\_Kan<sup>R</sup> (Figure S11) via natural transformation. The PsaE gene together with flanking upstream and downstream regions (500 base pairs each) were amplified from the isolated genomic DNA of *Synechocystis* (primers 1&2, Table S1) and inserted into an empty pRSET6a vector via an KpnI restriction site. Later a kanamycin resistance cassette (Kan<sup>R</sup>) was amplified from an external plasmid by PCR (primers 3&4, Table S1) and inserted in the downstream region also via restriction sites XmnI and Eco47III. The C-terminus of the psaE gene was extended by molecular cloning with Im7 gene, which was amplified from an pRSET6a\_Im7\_sfGFP plasmid by PCR (primers 5&6, Table S1) and inserted via the restriction site of SfoI. The transformation was performed as described (SI). The transformed *Synechocystis* mutant was screened, selected by growing on agar plates with 100 µgmL<sup>-1</sup> kanamycin. The homogeneity of the mutant strain was

checked by PCR (primers 7&8, Table S1).

### **Cultivation of *Synechocystis* and membrane preparation**

*Synechocystis* cells were grown in a 25-L foil fermenter with BG11 medium at 30 °C and bubbled with 5 % (v/v) CO<sub>2</sub>-enriched air with a final volume of 20 L. The light intensity varied between 50–200 µE (white-light) depending on the cell density. Cells were harvested at OD<sub>680</sub>=2 after three to five days of cultivation. The harvested, culture was concentrated to a volume of 2 L with a DC10 LA hollow fiber system (Amicon) and the cells were pelleted by centrifugation (25 °C, 20 min at 3,500 g). The pellet was resuspended in 80 mL of storage buffer 1 (20 mM MES pH 6.5, 10 mM MgCl<sub>2</sub>, 10 mM CaCl<sub>2</sub>, 500 mM mannitol and 20 % (w/v) glycerol), and cells were snap-frozen in liquid nitrogen and eventually stored at -80 °C until further use. For membrane preparation, the cells were thawed, diluted with buffer A (20 mM MES pH 6.5, 10 mM MgCl<sub>2</sub>, 10 mM CaCl<sub>2</sub>), and pelleted (4 °C, 10 min at 21,000 g). Unless otherwise mentioned, all further steps were performed in the dark or under green light illumination. The cell pellet was resuspended in 5 mL of buffer A supplemented with 0.4 % (w/v) lysozyme per gram of fresh cell weight and incubated for 90 min at 37 °C. After centrifugation (4 °C, 15 min at 21,000 g), the pellet was resuspended in buffer A supplemented with 0.1 mg/mL of DNase (AppliChem) and 0.1 mM protease inhibitor (AEBSF Hydrochloride, AppliChem) and subjected to a French press for cell disruption (1 min at 14,000 psi, four cycles). The crude thylakoid membrane pellet was collected by ultracentrifugation (4 °C, 30 min at 140,000 g) and resuspended in buffer A. Until further use thylakoids were flash-frozen with liquid nitrogen and stored at -80 °C.

### **Purification of PSI-Im7**

Immobilized metal affinity chromatography was performed to isolate PSI Im7. For this, thylakoid membranes were thawed, resuspended in extraction buffer (20 mM MES pH 6.5, 10 mM CaCl<sub>2</sub>, 10 mM MgCl<sub>2</sub>, 1.2 % (w/v) DDM, 0.5 % (w/v) sodium cholate) with a final Chl concentration of 1 mg/mL, and incubated for 30 min at 20 °C.<sup>[50,51]</sup> After ultracentrifugation (4 °C, 1 h at 140,000 g), NaCl and imidazole were added to the supernatant with final concentrations of 300 mM and 20 mM, respectively. The supernatant was filtered through a 0.45 µm syringe filter (Sarstedt AG) and applied to a 5 mL Ni Sepharose His trap crude FF column (GE-Healthcare), which was equilibrated with buffer B (20 mM MES pH 6.5, 10 mM CaCl<sub>2</sub>, 10 mM MgCl<sub>2</sub>, 500 mM mannitol, 300 mM NaCl, 0.03 % (w/v) DDM and 20 mM imidazole). After washing the column with 50 mL of buffer B, bound PSI Im7 was eluted by buffer C (20 mM MES pH 6.5, 10 mM CaCl<sub>2</sub>, 10 mM MgCl<sub>2</sub>, 500 mM mannitol, 300 mM NaCl, 0.03 % (w/v) DDM and 500 mM imidazole). To concentrate the eluted



fractions and to remove excess of NaCl and imidazole, a buffer exchange was performed using spin concentrators (Amicon, Ultra-15, 100 kDa molecular weight cut off) with buffer D (20 mM MES pH 6.5, 10 mM CaCl<sub>2</sub>, 10 mM MgCl<sub>2</sub>, 500 mM mannitol, 0.03 % (w/v) DDM). The collected PSI-Im7 complexes were flash-frozen with liquid nitrogen and stored at -80 °C until further use.

### **SDS-PAGE-based characterization of PSI-Im7**

PSI Im7 subunit composition was analyzed by Tricine SDS-PAGE.<sup>[52]</sup> Denatured subunits were separated in a separating gel containing 40 % (w/v) polyacrylamide (acrylamide-bisacrylamide, 37.5:1) and 9.16 M urea, 4 % (w/v) glycerol. The separating gel was overlaid with stacking gel of 8.1 % polyacrylamide. PSI samples (equivalent to 2.5 µg Chl) were incubated in sample buffer for 30 min at 60 °C and loaded onto each lane. For all gel electrophoresis experiments, a PageRuler™ Prestained Protein Ladder (Thermofisher Scientific, product number 26616) was used. Electrophoresis was performed in Mini-PROTEAN System (BioRad) at 30 mA for 90 min with cathode buffer (0.1 M Tricine pH 8.25, 0.1 % (w/v) SDS) in the gel-plate cassette and anode buffer (0.1 M Tris pH 8.9) in the electrophoresis chamber. The gels were stained by Coomassie staining solution (0.2 % (w/v) Coomassie R250, 0.05 % (w/v) Coomassie G250, 2 % (v/v) ethanol, 5 % (v/v) methanol, 10 % (v/v) acetic acid. After 30 min of incubation in staining solution, gels were destained using destaining solution (7.5 % (v/v) acetic acid and 5 % (v/v) isopropanol).

### **Characterization of the oligomerization state of PSI-Im7 by BN-PAGE**

The oligomerization state of the isolated PSI-Im7 complex was analyzed by BN-PAGE.<sup>[53]</sup> Thereby, protein complexes were separated in a separating gel with a linear gradient of 3.2 to 16 % polyacrylamide (acrylamide-bis-acrylamide, 32:1). PSI samples (equivalent to 3.5 µg Chl) were mixed with BN PAGE loading buffer (50 mM Tricine, 15 mM Bis Tris pH 7.0 with 50 % glycine) and loaded into each lane in the stacking gel. Gel electrophoresis was performed with a Mini-PROTEAN system (BioRad). Initially, electrophoresis was performed at 30 mA for 90 min with blue cathode buffer (15 mM Bis Tris pH 7.0, 50 mM Tricine, and 0.02 % (w/v) Coomassie Brilliant blue 250). After 30 min, the gel chamber was exchanged with clear cathode buffer (15 mM Bis Tris pH 7.0, 50 mM Tricine) and electrophoresis was continued at 150 V for additional 90 min. Determination of concentration of PSI-Im7 and PSI-Im7 fusion chimeras (PSI complexes). The concentration of PSI complexes was determined based on the chlorophyll amount. For extraction of chlorophyll, 1–2 µL of PSI complexes were diluted in 1 mL methanol and the precipitated proteins of PSI were pelleted by centrifugation (5 min, 21000 g). The chlorophyll amount was estimated by measuring the



## Chapter 4

absorbance of the supernatant at 652, 665, and 750 nm and later subjected to equation <sup>[1]</sup> <sup>[54]</sup>. Afterwards, the chlorophyll amount was converted into molar concentration by considering that each PSI monomer consists of 95 chlorophyll molecules.<sup>[32]</sup>

$$[Chl.] = (16.29 * (A_{665} - A_{750}) - 8.54 * (A_{652} - A_{750})) * \left( \frac{\text{sample volume}}{\text{MeOH volume}} \right) * \frac{g}{ml}$$

### ATR-FTIR difference spectroscopy

The surface of the germanium IRE was functionalized as previously described.<sup>[26]</sup> Briefly, the surface was cleaned, oxidized with a mixture of oxalic acid and hydrogen peroxide and silanized using the triethoxy linker-Silane molecule (2,5-dioxopyrrolidin-1-yl 4-oxo-4-((3-(triethoxysilyl-propyl-amino-butanoate)). After silanization, the crystal surface was functionalized with E7 (10 µg/ml in 50 mM HEPES buffer pH 7.5) and the remaining surface was blocked with casein. Subsequently, PS1-Im7 (10 µg/ml in buffer D) was immobilized on the surface. The binding of PSI-Im7 was followed spectrally using its amide II absorption kinetics (Figure S3). The obtained absorbance of 10 mAU corresponds to a surface density of about 1 pmol/cm<sup>2</sup>. For the measurement of the light-induced difference spectrum of PSI-Im7, the sample compartment was darkened and a 250 W halogen lamp with a fiber optic light conductor and long pass filter (> 645 nm) was installed in front of the cuvette. Subsequently, the immobilized PSI-Im7 was measured for 10 minutes during continuous illumination, followed by equilibration without light for 2 minutes and measurement in darkness for 10 minutes. This measurement procedure was repeated ten times. For transmission measurement of PSI-Im7, 5 µg of protein in buffer D was added to an infrared cuvette with calcium fluoride windows (pathlength: 7 µm). The cuvette was then placed in the optical path of the spectrometer. The measurement procedure with its illumination and dark cycles was then performed analogously to the ATR experiment. In Figure S4, the bands facing upwards are bands from the light-adapted state, and those facing downwards are from the dark state. Bands that do not change upon irradiation are cancelled out in this difference spectrum.

### Creation of chimeric E7-Fd and E7-Fd-FNR fusion proteins

A synthetic genetic construct of E7-Fd-FNR was designed in silico by a sequential assembly of three gene segments of E7, Fd, and FNR with additional sequences coding for AA linkers between the segments. Unique restriction sites were added at the beginning and end of each segment of the genetic construct (Figure S12), enabling easy replacement of individual segments. The genetic construct E7-Fd was created by removing the FNR segment of E7-Fd-FNR via restriction digestion with BglII,

## Chapter 4

Eco109I. Additionally, a stop codon containing oligonucleotide (nucleotide sequences 9&10, Table S1) was re-introduced at the end of the Fd segment by sticky-end ligation. E7-Fd-FNR fusion chimeras were created by keeping linker lengths corresponding to 10 AA as non-variable between E7 and Fd segments, and linker length between Fd and FNR were varied by restriction digestion (BglII, XhoI) followed by sticky-end ligation with oligonucleotides (nucleotide sequences 11 to 14, Table S1) of respective linker length (5, 10, 15 AA). E7 Fd fusion chimeras were also created with variable linker lengths (5, 10, 15 AA) by restriction digestion (HindIII, NcoI) followed by sticky-end ligation with the corresponding oligonucleotides (nucleotide sequences 15 to 18, Table S1). All genetic constructs were cloned and expressed in a pASK-IBA7 expression vector.

### Expression of E7-Fd and E7-Fd-FNR variants

For a pre-culture, 2 to 3 colonies of *E. coli* BL21-*ΔiscR* transformed with pASK-IBA7-E7-Fd or pASK-IBA7-E7-Fd-FNR were picked under sterile conditions and inoculated in 50 mL LB media supplemented with ampicillin (120 µg/mL) and grown overnight. 1 to 5 % (v/v) of the starter culture was added to the main culture (LB media supplemented with 2 mM ferric ammonium citrate and 120 µg/mL of ampicillin) and incubated further at 37 °C under constant agitation at 130 rpm. As soon as the cultures reached an O.D<sub>600</sub> of 0.6, protein expression was induced by the addition of 0.2 µg/mL of anhydrotetracycline, and cultures were further incubated at 37 °C for 6 h. Then, cells were pelleted by centrifugation (4 °C, 20 min, 6842 g) and resuspended in TE buffer (10 mM Tris/HCl pH 8, 0.1 mM EDTA) to wash out the remnant growth medium.

### Isolation and purification of E7-Fd and E7-Fd-FNR variants

The harvested *E. coli* cells were suspended in equilibration buffer (100 mM Tris HCl pH 8.0, 500 mM NaCl, 20 mM imidazole (3 mL/g of cell pellet) and treated with lysozyme (10 mg/L cell culture), 0.1 % Triton X-100, 0.1 mM protease inhibitor (AEBSF Hydrochloride, AppliChem) for 30 min. Cells were then subjected to sonication (on ice, 5 × 30 s with 45–60 s break between each pulse, 70 % duty cycle, output 4–5). After sonication, lysed cells were centrifuged (4 °C, 30 min, 76800 g) to remove insoluble particles and cell debris. The protein-containing supernatant was collected and filtered through a 0.45 µm size cut-off filter and applied onto a 5 mL His Trap™ crude FF column (GE Healthcare), running in equilibration buffer. The purification process was monitored and controlled by the ÄKTA FPLC-system. After washing with 30 ml of equilibration buffer, the His-tagged chimeric proteins were eluted by application of elution buffer (100 mM Tris HCl pH 8, 500 mM NaCl, 500 mM imidazole). To concentrate the eluted fractions and to remove imidazole, a buffer

exchange was performed using spin concentrators (Amicon, Ultra-15, 30 kDa molecular weight cut off) with storage buffer 2 (100 mM Tris HCl pH 8.0, 300 mM NaCl). Purified fusion proteins EF and EFF were also stored in storage buffer 2 at 80 °C. The expression and isolation protocols of other proteins used in this study, such as Fd, FNR, and Cyt *c*<sub>6</sub> are mentioned in the supporting information (SI).

### UV-Vis spectra of E7-Fd and E7-Fd-FNR variants

UV-Vis absorption spectra of E7 Fd and E7 Fd FNR fusion proteins were measured using a UV-2450 spectrophotometer (Shimadzu) and NanoDrop™ 2000 spectrophotometer (ThermoFisher™), respectively. An equivalent of 15 µM of chimeric E7 Fd fusion and Fd protein was used for spectral determination with a final volume of 1 mL in storage buffer 2. In the case of E7 Fd FNR, to observe distinct peaks, E7 Fd FNR chimeras, free Fd and free FNR were used at a concentration of 0.4 mM in a final volume of 2 µL in storage buffer 2. The concentrations of free Fd and FNR were determined based on the absorbances at 422 nm and 459 nm, using molar absorption coefficients of 9.8 mM<sup>-1</sup> cm<sup>-1</sup> <sup>[55]</sup> and 10.00 mM<sup>-1</sup> cm<sup>-1</sup>, <sup>[56]</sup> respectively.

### Light-induced NADP<sup>+</sup> reduction

The reaction buffer used for the photoreduction of NADP<sup>+</sup> in both bipartite and tripartite systems was similar and adapted from previous literature.<sup>[12]</sup> The reaction buffer was the following: 50 mM Tricine pH 8, 30 mM NaCl, 4 mM NaAsc, 100 µM DCPIP, 2.5 µM, Cyt *c*<sub>6</sub> 5 mM MgCl<sub>2</sub> (added only in the case of FPS1 or FPS2) and 1 mM NADP<sup>+</sup>. For the bipartite system 0.25 µM PSI EF (5, 10, 15) chimeras and 0.75 µM free FNR were added to the reaction buffer. In case of FPS1 0.25 µM PSI, 0.25 µM Fd, and 0.75 µM FNR were added to the reaction buffer. For the tripartite system 0.25 µM PSI EFF (5, 10, 15) chimeras were added to the reaction buffer. In case of FPS2: PSI, Fd, and FNR were added in an equimolar ratio of 0.25 µM to the reaction buffer. The measurements were performed in a total volume of 1.5 mL at 25 °C. NADPH formation rates were analyzed by fluorescence spectroscopy (Dual-PAM-100, Walz Germany). The fluorescence was converted into NADPH quantity (µmol) based on the NADPH-fluorescence correlation curve (Figure S13). The total reaction time amounted to 8 min, whereby 1 min of pre-incubation in the dark was followed by a 5 min illumination with an actinic red light (100 µE) and a subsequent dark incubation for 2 min. The initial rate of NADP<sup>+</sup> reduction was analyzed based on the slope obtained during the first min of illumination.

## Chapter 4

### **Statistics and Software**

All the experiments were performed in replicates to ensure the consistency and reproducibility of the data. Unless otherwise mentioned, all the data and graphs were processed and prepared with the software Origin 2019b.

## 4.6 References

- [1] J. Mondal, B. D. Bruce, *Photosynthetica* **2018**, 56, 279–293.
- [2] G. Wittenberg, W. Sheffler, D. Darchi, D. Baker, D. Noy, *Phys. Chem. Chem. Phys* **2013**, 15, 19608–19614.
- [3] K. Nguyen, B. D. Bruce, *Biochim Biophys Acta Bioenerg* **2014**, 1837, 1553–1566.
- [4] E. Musazade, R. Voloshin, N. Brady, J. Mondal, S. Atashova, S.K. Zharmukhamdov, Huseynova, S. Ramakrishna, M. M. Najafpour, J. R. Shen, B. D. Bruce, S. I. Allakhverdiev, *J. Photochem. Photobiol.* **2018**, 35, 134–156.
- [5] A. H. Teodor, B. D. Bruce, *Trends Biotechnol* **2020**, 38, 1329–1342.
- [6] P. Wang, F. Zhao, A. Frank, S. Zerria, A. Lielpetere, A. Ruff, M. M. Nowaczyk, W. Schuhmann, F. Conzuelo, *Adv Energy Mater* **2021**, 11, 2102858.
- [7] P. Jordan, P. Fromme, H. T. Witt, O. Klukas, W. Saenger, N. Krauß, *Nature* **2001**, 411, 909–917.
- [8] F. F. Özgen, M. E. Runda, S. Schmidt, *ChemBioChem* **2021**, 22, 790–806.
- [9] C. E. Lubner, A. M. Applegate, P. Knörzner, A. Ganago, D. A. Bryant, T. Happe, J. H. Golbeck, *Proc Natl Acad Sci U S A*, **2011**, 108, 20988–20991.
- [10] A. Kanygin, Y. Milrad, C. Thummala, K. Reifschneider, P. Baker, P. Marco, Yacoby, K. E. Redding, *Energy Environ Sci* **2020**, 13, 2903–2914.
- [11] R. A. Grimme, C. E. Lubner, J. H. Golbeck, *Dalton Trans* **2009**, 10106.
- [12] G. Moal, B. Lagoutte, *Biochim Biophys Acta Bioenerg* **2012**, 1817, 1635–1645.
- [13] F. Zhao, F. Conzuelo, V. Hartmann, H. Li, M. M. Nowaczyk, N. P. Plumeré, M. Rögner, W. Schuhmann, *J. Phys Chem B* **2015**, 114, 13726–13731.
- [14] J. Appel, V. Hueren, M. Boehm, K. Gutekunst, *Nat Energy* **2020**, 5, 458–467.
- [15] M. Ihara, H. Nishihara, K.-S. Yoon, O. Lenz, B. Friedrich, H. Nakamoto, K. Kojima, D. Honma, T. Kamachi, I. Okura, *Photochem Photobiol* **2006**, 82, 676–682.
- [16] H. Eilenberg, I. Weiner, O. Ben-Zvi, C. Pundak, A. Marmari, O. Liran, M. S. Wecker, Y. Milrad, I. Yacoby, *Biotechnol Biofuels* **2016**, 9, 1–10.
- [17] M. A. Riley, J. E. Wertz, *Annu Rev Microbiol* **2002**, 56, 117–137.
- [18] M. Feldgarden, M. A. Riley, *Evolution* **1998**, 52, 1270–1276.
- [19] O. O. Kolade, S. B. Carr, U. C. Kühlmann, A. Pommer, C. Kleanthous, C. A. Bouchinsky, A. M. Hemmings, *Biochimie* **2002**, 84, 439–446.
- [20] T.P. Ko, C.C. Liao, W.Y. Ku, K.F. Chak, H. S. Yuan, *Structure* **1999**, 7, 91–102.
- [21] M. N. Vassilyeva, S. Klyuyev, A. D. Vassilyev, H. Wesson, Z. Zhang, M. B. Renfrow, H. Wang, N. P. Higgins, L. T. Chow, D. G. Vassilyev, *Proc Natl Acad Sci U S A* **2017**, 114, E5138–E5147.
- [22] D. C. Walker, Theonie Georgiou, A. J. Pommer, D. Walker, G. R. Moore, *Nucleic Acids Res* **2002**, 30, 3225–3234.
- [23] R. Jeanjean, A. Latifi, H. C. P. Matthijs, M. Havaux, *Biochim Biophys Acta Bioenerg* **2008**, 1777, 308–316.
- [24] Y. Li, N. Vella, M. Chen, *Photosynthetica* **2018**, 56, 306–315.
- [25] G. Hastings, *Biochim Biophys Acta Bioenerg* **2015**, 1847, 55–68.
- [26] J. Schartner, J. Güldenhaupt, B. Mei, M. Rögner, M. Muhler, K. Gerwert, C. Kötting, *J Am Chem Soc* **2013**, 135, 4079–4087.
- [27] Z. Deng, A. Aliverti, G. Zanetti, A. K. Arakaki, J. Ottado, E. G. Orellano, N. B. Calcaterra, E. A. Ceccarelli, N. Carrillo, P. A. Karplus, *Nat Struct Biol* **1999**, 6, 847–853.
- [28] D. L. Catalano-Dupuy, M. A. Musumeci, A. López-Rivero, E. A. Ceccarelli, *PLoS One* **2011**, 6, e26736.

- [29] I. Yacoby, S. Pochekaïlov, H. Toporik, M. L. Ghirardi, P. W. King, S. Zhang, *Proc Natl Acad Sci U S A* **2011**, *108*, 9396–9401.
- [30] N. Carrillo, E. A. Ceccarelli, *Eur J Biochem* **2003**, *270*, 1900–1915.
- [31] B. J. Harris, X. Cheng, P. Frymier, *J. Phys. Chem.* **2016**, *120*, 599–609.
- [32] T. Malavath, I. Caspy, S. Y. Netzer-El, D. Klaiman, N. Nelson, *Biochim Biophys Acta Bioenerg* **2018**, *1859*, 645–654.
- [33] J. W. Lee, C. V Tevault, S. L. Blankinship, R. T. Collins, E. Greenbaum, *Energy fuels* **1994**, *8*, 770–773.
- [34] E. Greenbaum, *Science* **1985**, *230*, 1373–1375.
- [35] S. C. Silver, J. Niklas, P. Du, O. G. Poluektov, D. M. Tiede, L. M. Utschig, *J Am Chem Soc* **2013**, *135*, 13246–13249.
- [36] M. L. Antonkine, E. M. Maes, R. S. Czernuszewicz, C. Breitenstein, E. Bill, C. J. Falzone, R. Balasubramanian, C. Lubner, D. A. Bryant, J. H. Golbeck, *Biochim Biophys Acta Bioenerg* **2007**, *1767*, 712–724.
- [37] C. E. Lubner, R. Grimme, D. A. Bryant, J. H. Golbeck, *Biochemistry* **2010**, *49*, 404–414.
- [38] C. E. Lubner, P. Knörzer, P. J. N. Silva, K. A. Vincent, T. Happe, D. A. Bryant, J. H. Golbeck, *Biochemistry* **2010**, *49*, 10264–10266.
- [39] B. R. Evans, H. M. O’Neill, S. A. Hutchens, B. D. Bruce, E. Greenbaum, *Nano Letter* **2004**, *4*, 1815–1819.
- [40] D. Mukherjee, M. Vaughn, B. Khomami, B. D. Bruce, *Colloids Surf. B* **2011**, *88*, 181–190.
- [41] D. Ciornii, A. Kölsch, A. Zouni, F. Lisdat, *Nanoscale* **2019**, *11*, 15862–15870.
- [42] F. Zhao, P. Wang, A. Ruff, V. Hartmann, S. Zacarias, I. A. C Pereira, M. M. Nowaczyk, M. Rögner, F. Conzuelo, W. Schuhmann, *Energy Environ. Sci* **2019**, *12*, 3133–3143.
- [43] T. Kothe, N. Plumeré, A. Badura, M. M. Nowaczyk, D. A. Guschin, M. Rögner, W. Schuhmann, *Angew. Chem. Int. Ed* **2013**, *52*, 14233–14236.
- [44] S. C. Feifel, H. Lokstein, M. Hejazi, A. Zouni, F. Lisdat, *Langmuir ACS* **2015**, *31*, 10590–10598.
- [45] S. C. Feifel, K. R. Stieger, H. Lokstein, H. Lux, F. Lisdat, *J Mater Chem A Mater* **2015**, *3*, 12188–12196.
- [46] C. J. Faulkner, S. Lees, P. N. Ciesielski, D. E. Cliffel, G. K. Jennings, *Langmuir ACS* **2008**, *24*, 8409–8412.
- [47] R. F. Simmerman, T. Zhu, D. R. Baker, L. Wang, S. R. Mishra, C. A. Lundgren, B. D. Bruce, *Bioconj Chem* **2015**, *26*, 2097–2105.
- [48] P. Wang, A. Frank, F. Zhao, J. Szczesny, J. R. C. Junqueira, S. Zacarias, A. Ruff, M. M. Nowaczyk, C. Pereira, M. Rögner, F. Conzuelo, W. Schuhmann, *Angew Chem Int. Ed* **2021**, *60*, 2000–2006.
- [49] G. Milanovsky, O. Gupta, A. Petrova, M. Mamedov, M. Gorka, D. Cherepanov, J. H. Golbeck, Semenov, *Biochim Biophys Acta Bioenerg* **2019**, *1860*, 601–610.
- [50] H. Kuhl, J. Kruip, A. Seidler, A. Krieger-Liszkay, M. Bünker, D. Bald, A. J. Scheidig, M. Rögner, *J. Biol. Chem.* **2000**, *275*, 20652–20659.
- [51] J. Zabret, S. Bohn, S. K. Schuller, O. Arnolds, M. Möller, J. Meier-Credo, P. Liauw, A. Chan, E. Tajkhorshid, J. D. Langer, R. Stoll, A. Krieger-Liszkay, B. D. Engel, T Rudack, J. M. Schuller, M. M. Nowaczyk, *Nat Plants* **2021**, *7*, 524–538.
- [52] H. Schägger, G. von Jagow, *Anal Biochem* **1987**, *166*, 368–379.
- [53] D. Neff, N. A. Dencher, *Biochem Biophys Res Commun* **1999**, *259*, 569–575.
- [54] C. Benitez, *Biochim Biophys Acta* **1989**, *975*, 143–196.
- [55] R. Mutoh, N. Muraki, K. Shinmura, H. Kubota-Kawai, Y. H. Lee, M. M. Nowaczyk, M. Rögner, T. Hase, T. Ikegami, G. Kurisu, *Biochemistry* **2015**, *54*, 6052–6061.

## Chapter 4

- [56] J. J. Van Thor, K. J. Hellingwerf, H. C. P. Matthijs, *Plant Mol Biol* **1998**, 36, 353–363.
- [57] E. El-Mohsnawy, M. J. Kopczak, E. Schlodder, M. Nowaczyk, H. E. Meyer, B. Warscheid, N. V. Karapetyan, M. Rögner, *Biochemistry* **2010**, 49, 4740–4751.
- [58] F. Zhao, S. Hardt, V. Hartmann, H. Zhang, M. M. Nowaczyk, M. Rögner, N. Plumeré, W. Schuhmann, F. Conzuelo, *Nat Commun* **2018**, 9, 1-9.
- [59] J. G. K. Williams, *Methods Enzymol*, **1988**, 167, 766–778.
- [60] M. K. Akhtar, P. R. Jones, *Appl Microbiol Biotechnol* **2008**, 78, 853-862.



# Supporting Information

### Supplementary Text

#### Light-induced oxygen reduction with PSI-Im7 and PSI-Wt

The light-induced oxygen reduction of PSI was performed as described previously with slight adaptations.<sup>[1]</sup> The activity of PSI was measured based on light-induced Mehler reaction.<sup>[2]</sup> The oxygen reduction rate was monitored as a function of time as a functional parameter and measured by an optic oxygen sensor (FiBOX3, PreSens<sup>TM</sup>). A PSI equivalent of 5  $\mu\text{g}$  of chlorophyll (Chl) was diluted with PSI activity buffer (30 mM HEPES pH 7.5, 50 mM KCl, 3 mM  $\text{MgCl}_2$ , 330 mM mannitol, 0.3 % (w/v)  $\beta$  DDM, 5 mM sodium ascorbate, 0.5 mM methyl viologen, 0.8 mM DCPIP). Measurements were performed at 30 °C. After an initial 1min dark incubation, PSI complexes were illuminated with red light ( $\lambda > 665 \text{ nm}$ ,  $4000 \mu\text{mol m}^{-2} \text{ s}^{-1}$ ) for 4 min. The PSI-dependent oxygen reduction rate was calculated based on the slope of the light-induced reaction phase and specified as  $\mu\text{mol O}_2 \text{ mg Chl}^{-1} \text{ mL}^{-1} \text{ h}^{-1}$ .

#### UV-vis spectrum of PSI-Im7 and PSI-Wt

Light absorption properties of isolated PSI-Wt and PSI-Im7 complexes were monitored by UV-Vis absorption spectra. Measurements were performed using a UV-2450 spectrophotometer (Shimadzu). PSI equivalent of 10  $\mu\text{g}$  Chl was dissolved in 1 mL of buffer D (20 mM MES, pH 6.5, 10 mM  $\text{CaCl}_2$ , 10 mM  $\text{MgCl}_2$ , 500 mM mannitol, 0.03 % (w/v)  $\beta$ -DDM). Absorbance spectra were normalized at 680 nm.

#### Analyzing photoautotrophic growth of *Synechocystis* Wt and PSI-Im7

Photoautotrophic growth of *Synechocystis* sp. PCC 6803 (*Synechocystis* Wt) and the *Synechocystis* sp. PCC 6803 PasE-Im7 mutant (*Synechocystis* Im7) was monitored without antibiotics for 10 days under continuous light of  $30 \mu\text{mol m}^{-2} \text{ s}^{-1}$  at 30 °C and 150 rpm. The initial volume of cell cultures was 200 mL with an initial optical density at 750 nm ( $\text{OD}_{750}$ ) of 0.1. The OD was measured periodically every second day for 10 days ( $n=4$ ).

#### Sucrose density gradient-based separation of excess E7-Fd and E7-Fd-FNR chimeras from PSI-Fd or PSI-Fd-FNR coupled complexes.

For the preparation of the continuous sucrose gradient, 30 ml of a sucrose solution (50 mM HEPES pH 7.5, 10 mM  $\text{CaCl}_2$ , 10 mM  $\text{MgCl}_2$ , 0.03 % (w/v)  $\beta$ -DDM, 20 % (w/v) sucrose) was filled into SW-28 (Beckmann coulter) centrifuge tubes and incubated overnight at -20 °C. Later, the sucrose gradient was developed by thawing the solution for 2 h at room temperature. A 1:8 molar ratio of PSI-Im7 and fusion chimeras (EF, EFF) were mixed together and dark-incubated

## Chapter 4

on ice for 30 min. Subsequently, a fusion mixture (~150 µg Chl) was applied on top of the gradient and subjected to ultracentrifugation (4 °C, 18 h, 140000 g). The initial acceleration and deceleration speed of ultracentrifugation was adjusted to a low rotation speed (100 g). After ultracentrifugation, three distinct bands were observed: B1: EF or EFF fusion chimeras, B2: monomeric PSI coupled complex, and B3: Trimeric PSI coupled complex, as shown in Figure S7. B3 was collected carefully and washed with buffer D and flash-frozen with liquid N<sub>2</sub> and stored at -80 °C until further use.

### Genetic transformation of *Synechocystis* Wt

50 mL of *Synechocystis* Wt were grown at 30 °C until OD<sub>750</sub>: 0.5-1. The cells were harvested by centrifugation (15 min, 2900-3800 g) and resuspended in BG-11 medium up to a final cell concentration of OD<sub>750</sub>: 2.0. 2.5 µg of plasmid DNA (pRSET6a\_PsaE\_Im7\_Histag\_Kan<sup>R</sup>) were mixed with 0.4 mL of equivalent cell suspension by gentle shaking. Further, the cell culture was incubated under 50 µE standard light at 30 °C for 24 hours. Later, the cells were grown on a selective agar medium with a gradual increase in kanamycin concentration from initially 40 µg/mL to the final concentration of 100 µg/mL. This method was adapted from Williams, 1988.<sup>[3]</sup>

### Fluorescence-based NADPH standard curve

NADPH fluorescence was correlated to the concentration of NADPH. The calibration curve was created by adding the required NADPH in a stepwise manner. 1.4 mL of reaction buffer (50 mM Tricine pH 8, 30 mM NaCl, 5 mM MgCl<sub>2</sub>) was added to a quartz cuvette and 5 µL of 284.03 µM NADPH stock solution was added in subsequent steps so that concentrations from 0 to 20 µM NADPH were achieved. The mixture was stirred briefly with a magnetic stirrer and allowed to settle for 1 min. Subsequently, the fluorescence of the corresponding NADPH concentration was measured for 30 s. The measurement was performed in triplicates for each concentration. The mean fluorescence value corresponding to each NADPH concentration was graphically represented, and the slope was calculated in Origin19b. The calculated slope was 0.137 arbitrary units (a.u.) / µM NADPH.

### Nucleotide sequences for linker variation

The nucleotide sequences for linker variation were created using oligonucleotides of respective lengths. Oligonucleotides were designed in Clone Manager 9 and were ordered from Sigma-Aldrich Ltd. Two complementary sequences of individual linker lengths (Table S1) were annealed by exposing sticky ends. For annealing, two complementary oligonucleotides (4.5

## Chapter 4

$\mu\text{M}$  forward and  $4.5 \mu\text{M}$  reverse oligonucleotides of respective linker lengths (5, 10, 15 amino acids), were mixed with 1x Taq buffer (Thermoscientific Ltd.) with a final concentration of 180 mM NaCl. The total volume was set to  $30 \mu\text{L}$  with  $\text{H}_2\text{O}$ . Subsequently, the oligonucleotide mixture was incubated at  $100^\circ\text{C}$  for 5 min and allowed to cool down slowly to room temperature. Later, excess Taq buffer and NaCl was removed from the annealed oligonucleotides via alcohol precipitation. Finally, precipitated oligonucleotides were resolved in TE buffer (10 mM Tris-HCl, pH 8.0, 1 mM EDTA) and stored at  $-20^\circ\text{C}$  until further use.

### Heterologous recombinant expression of Fd (PetF)

2 to 3 colonies of *E. coli* BL21  $\Delta\text{iscR}$  cells,<sup>[4]</sup> transformed with pASK-IBA7-PetF-streptag (PetF sequence from *T. vestitus* BP1), were grown on an agar plate supplemented with  $120 \mu\text{g/mL}$  ampicillin and were picked under sterile conditions to inoculate 50 mL LB media supplemented with antibiotics ( $120 \mu\text{g/mL}$  ampicillin) as preculture. 15 mL of preculture was added to the 1 L main culture (LB media and 2 mM ferric ammonium citrate) supplemented with antibiotics. Culture growth was monitored by absorbance at  $\text{OD}_{600}$ . After reaching an  $\text{OD}_{600}$  of 0.4-0.6, the culture was induced for protein expression with  $0.2 \mu\text{g/mL}$  of anhydrotetracycline. After incubation of the culture for 6 h at  $37^\circ\text{C}$ , cells were pelleted by centrifugation ( $4^\circ\text{C}$ , 20 min, 6900 g) and washed with TE buffer (10 mM Tris-HCl pH 8.0, 1 mM EDTA) for the removal of growth medium residues.

### Isolation and purification of Fd (PetF)

The harvested *E. coli* cells were suspended in streptag equilibration buffer (100 mM Tris-HCl pH 8.0, 3 mL/g of cell pellet) and treated with lysozyme (10 mg/L cell culture), 0.1 % (v/v) Triton X-100, 0.1 mg/mL of DNase (AppliChem), and 0.1 mM protease inhibitor (AEBSF Hydrochloride, AppliChem) for 30 min. Further, the sample was subjected to sonication (on ice,  $5 \times 30$  s with 45-60 s break between each pulse, 70 % duty cycle, and output between 4-5). After sonication, the sample was centrifuged ( $4^\circ\text{C}$ , 30 min, 21000 g) to remove insoluble particles and the collected supernatant was filtered through a  $0.45 \mu\text{m}$  cut-off filter. Later, the supernatant was applied on to a 5 mL Strep-tag column (GE Healthcare) pre-equilibrated with streptag equilibration buffer for purification of Fd. The Strep-tag column bound Fd was eluted by streptag elution buffer (100 mM Tris-HCl pH 8.0, 4 mM desthiobiotin). The purification process was monitored and controlled by the ÄKTA FPLC<sup>TM</sup> system. To concentrate the eluted fractions and to remove desthiobiotin, a buffer exchange was performed using spin concentrators (Amicon, Ultra-15, 3 kDa molecular weight cut off) with storage buffer 2 (100 mM Tris-HCl pH 8.0, 300 mM NaCl) and purified Fd was stored in storage buffer 2 at  $-20^\circ\text{C}$ . Protein

## Chapter 4

concentration of Fd was calculated via absorbance at 422 nm using the molar absorption coefficient  $\epsilon = 9.8 \text{ mM}^{-1} \text{ cm}^{-1}$ .

### Heterologous recombinant expression and purification of FNR (PetH)

2 to 3 colonies of *E. coli* BL21 transformed cells with pASK-IBA37<sup>+</sup>-PetH-Histag (PetH sequence from *T. vestitus* BP-1) picked under sterile conditions to inoculate 50 mL LB media supplemented with antibiotics (120  $\mu\text{g/mL}$  ampicillin) as preculture. 15 mL of preculture was added to the 1 L main culture (LB media) supplemented with antibiotics. After reaching an  $\text{OD}_{600}$  of 0.4-0.6, the culture was induced for protein expression with 0.2  $\mu\text{g/mL}$  of anhydrotetracycline and further incubated for 6 h at 37 °C. Later, the cells were pelleted by centrifugation (4 °C, 20 min, 6900 g) and washed with TE buffer (10 mM Tris-HCl pH 8.0, 1 mM EDTA) for the removal of growth medium residues. For purification, the cells were suspended in equilibration buffer (100 mM Tris-HCl pH 8.0, 500 mM NaCl, 20 mM Imidazole (3 mL/g of cell pellet). The suspended cells were treated with lysozyme (10 mg/L of cell culture), 0.1 % Triton X-100, 0.1 mM protease inhibitor (AEBSF Hydrochloride, AppliChem) for 30 min. Cells were then subjected to sonication on ice (5×30 s with 45-60 s break between each pulse, 70 % duty cycle, and output between 4-5). After sonication, the sample was centrifuged (4 °C, 30 min, 21000 g) to remove insoluble particles and the collected supernatant was filtered through a 0.45  $\mu\text{m}$  cut-off filter. Later, the protein-containing supernatant was collected and filtered through a 0.45  $\mu\text{m}$  size cut-off filter and applied onto 5 mL His Trap<sup>TM</sup> crude FF column (GE Healthcare) for the purification. The His-tagged chimeric proteins were eluted by application of elution buffer (100 mM Tris-HCl pH 8, 500 mM NaCl, 500 mM imidazole) in a gradient manner onto the column. The purification process was monitored and controlled by the ÄKTA FPLC<sup>TM</sup>-system. To concentrate the eluted fractions and to remove imidazole, a buffer exchange was performed using spin concentrators (Amicon, Ultra-15, 30 kDa molecular weight cut off) with storage buffer 2 and purified FNR was stored in storage buffer 2 at -20 °C. Protein concentration of FNR was calculated via absorbance at 459 nm using the molar absorption coefficient  $\epsilon = 10.00 \text{ mM}^{-1} \text{ cm}^{-1}$ .

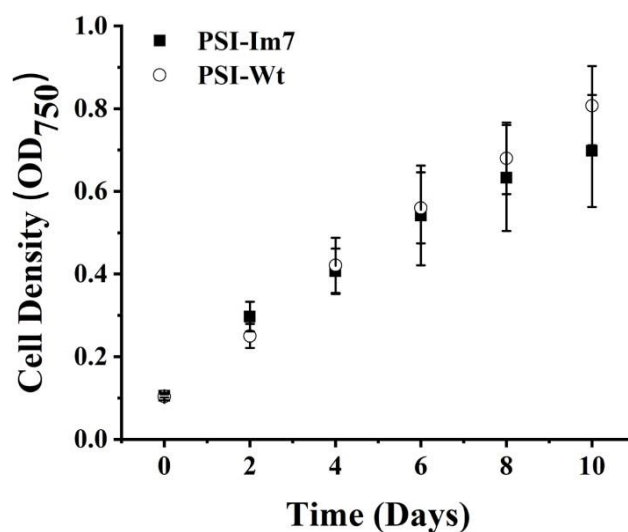
### Heterologous expression and purification of Cyt c<sub>6</sub> (PetJ)

pASK-IBA4-PetJ (PetJ sequence from *T. vestitus* BP-1) transformed *E. coli* BL21-PEC86 cells were grown on an agar plate supplemented with 120  $\mu\text{g/mL}$  ampicillin and 30  $\mu\text{g/mL}$  chloramphenicol. For the preparation of a preculture, 2-3 transformed colonies were picked under sterile conditions and inoculated in 50 mL LB media supplemented with 120  $\mu\text{g/mL}$

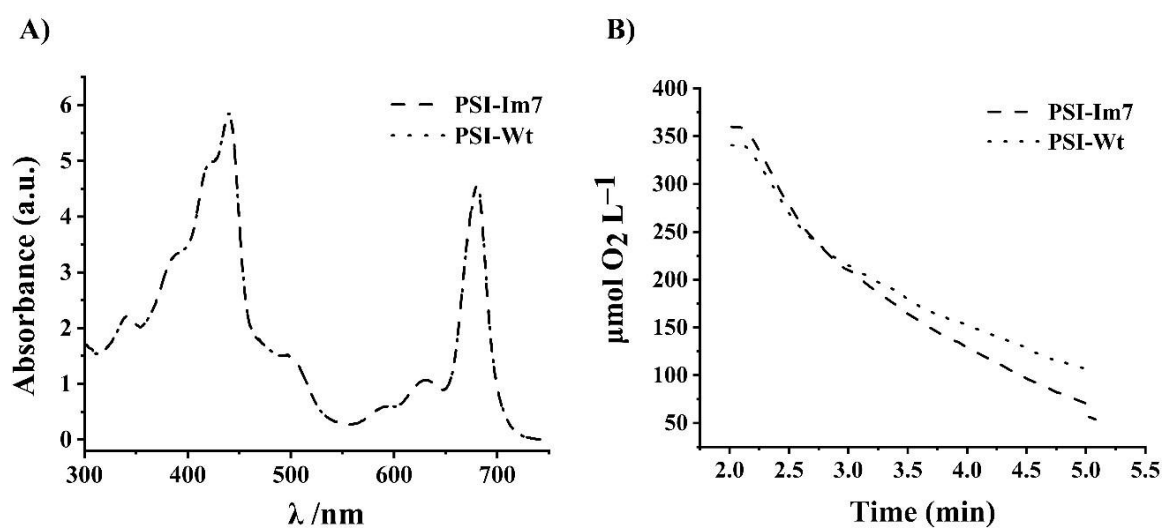
## Chapter 4

ampicillin, 30  $\mu\text{g/mL}$  chloramphenicol. A 15 mL aliquot of the preculture was added to 1 L of the main culture (TB media). After reaching an  $\text{OD}_{600}$  of 0.8, the culture was induced for protein expression with 0.2  $\mu\text{g/mL}$  of anhydrotetracycline and transferred into screw neck laboratory glass bottles to achieve microaerobic conditions for high yield expression of Cyt  $c_6$ . The culture was incubated under microaerobic condition for 12 h at 25 °C with continuous agitation at 100 rpm. After incubation, the cells were harvested and stored as mentioned above in Fd and FNR recombinant expression procedure. Unless otherwise specified, the purification of Cyt  $c_6$  was performed as described for FNR. To concentrate the eluted fractions and to remove imidazole, a buffer exchange was performed using spinconcentrators (Amicon, Ultra-15, 3 kDa molecular weight cut off) with storage buffer 2 and purified was Cyt  $c_6$  stored in storage buffer 2 at -20 °C. The concentration of the Cyt  $c_6$ -Histag was estimated via absorption at 552 nm using the molar absorption coefficient  $\epsilon=24.4 \text{ mM}^{-1} \text{ cm}^{-1}$ .

## Supplementary Figures



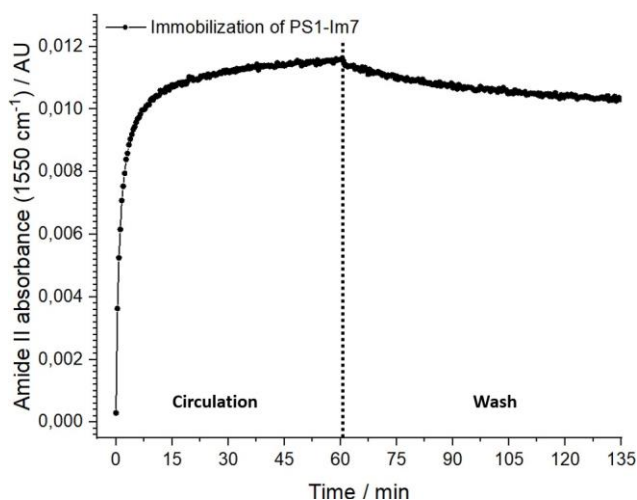
**Supplementary Figure 1: Photoautotrophic growth of *Synechocystis* Wt (open circle) and *Synechocystis* PSI-Im7 mutant (dark square).** The photoautotrophic growth was monitored by measuring optical density at 750 nm. Data represent the mean values and errors bars indicate the standard deviation of independent biological replicates (n=4).



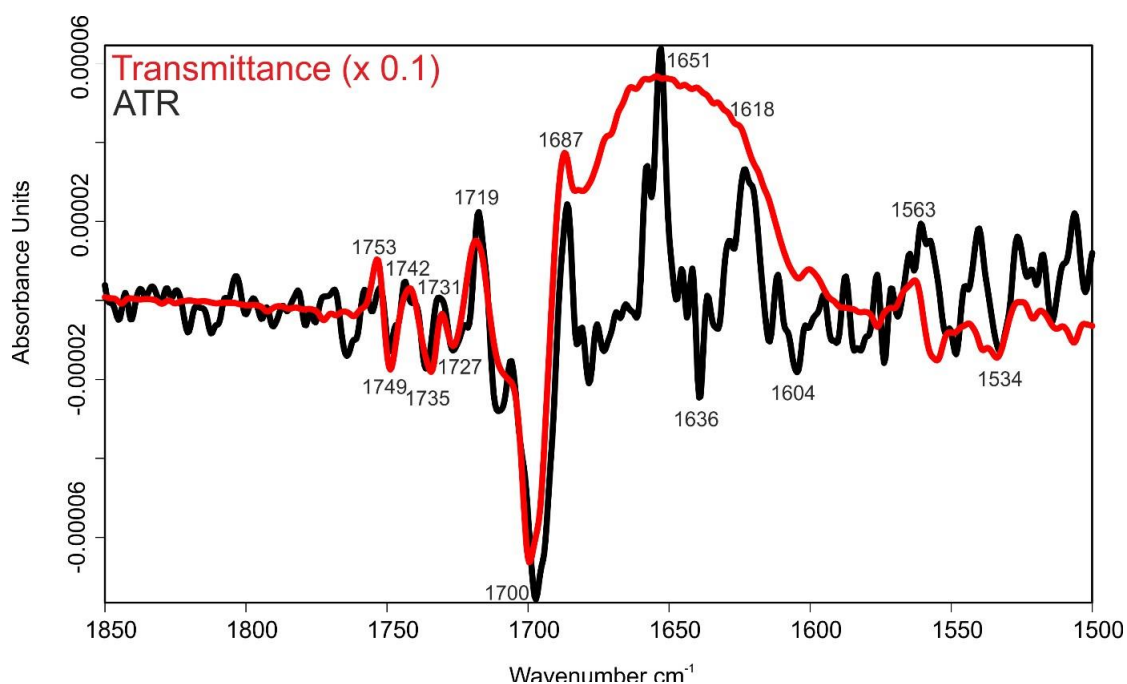
**Supplementary Figure 2. Oxygen reduction rate and UV-Vis spectral characterization of PSI-Im7 (Dashed line) & PSI-Wt (Dotted line).** A) UV-Vis absorption spectra of isolated PSI-Im7 and PSI-Wt. The spectral range was set to 300 to 750 nm and the data was normalized to the absorbance at 680 nm. Measurements were carried out in triplicates and the data represent the mean value. B) The oxygen reduction rate is normalized to the chl *a* concentration. The total measurement time was 5 min with a dark (1 min)- light (4 min) cycle. Measurements were carried out in triplicates and the mean value is shown for each data point.



## Chapter 4

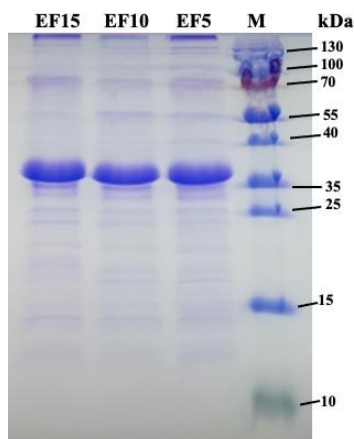


**Supplementary Figure 3: Kinetic profile of the PSI-Im7 immobilization on the E7-modified germanium surface.** Shown is the time course of amide II absorption at  $1550\text{ cm}^{-1}$ . The dashed line highlights the switch from the circulation step with PS1-Im7 to the washing step with buffer D.

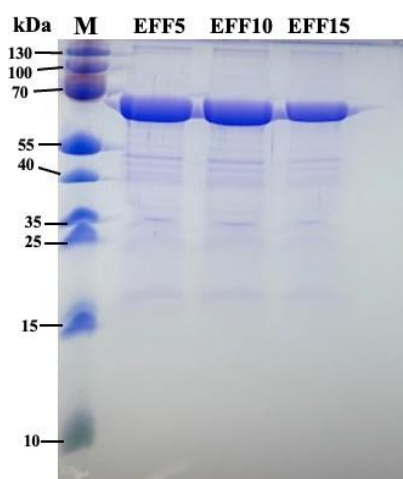


**Supplementary Figure 4: IR-difference spectra of the light-induced response of PSI-Im7.** The black spectrum results from the ATR measurement of immobilized PS1-Im7 on the E7-modified germanium crystal. The red spectrum was obtained by a transmission measurement. The latter one is obscured in the range between  $1680\text{ cm}^{-1}$  and  $1600\text{ cm}^{-1}$  due to the total absorption of water.

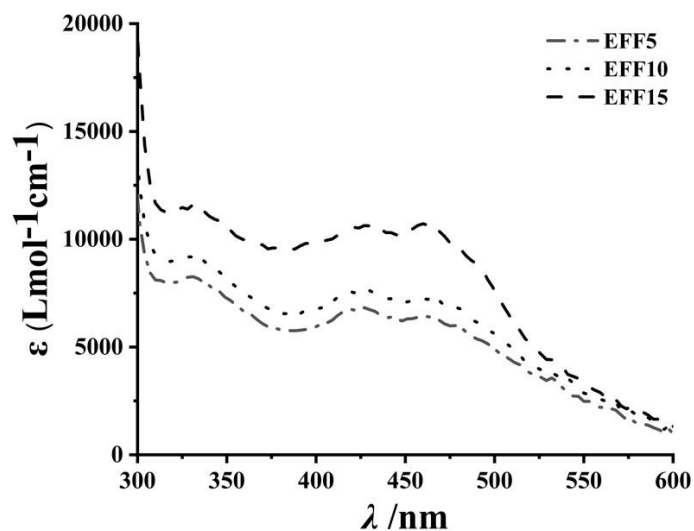
## Chapter 4



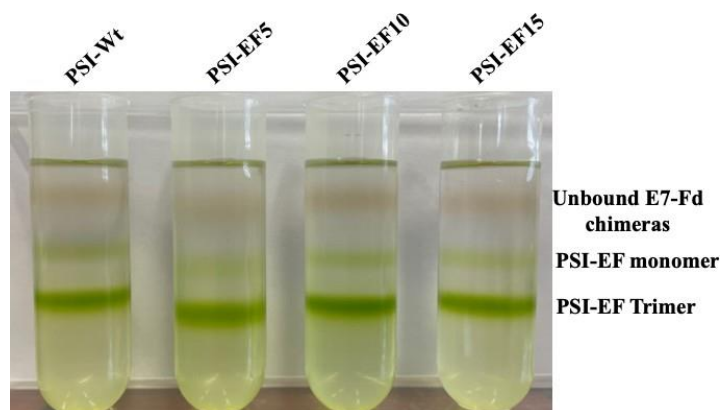
**Supplementary Figure 5. SDS-PAGE-based analysis of E7-Fd (EF) chimeras purified by His-tag affinity chromatography.** From left to right: Lanes 1 to 3: EF chimeras, with amino acid linker lengths of 5, 10, and 15 amino acids, respectively. Lane 4: Protein marker (PageRuler, ThermoScientific™). An equivalent of 10  $\mu$ g protein was loaded onto each lane.



**Supplementary Figure 6. SDS-PAGE analysis of E7-Fd-FNR (EFF) chimeras purified by His-tag affinity chromatography.** From left to right: Lane 1: Protein marker (PageRuler, ThermoScientific™). Lanes 2 to 4: EFF chimeras, with linker length variations of 5, 10, 15 amino acids between Fd and FNR, respectively. An equivalent of 10  $\mu$ g protein was loaded onto each lane.

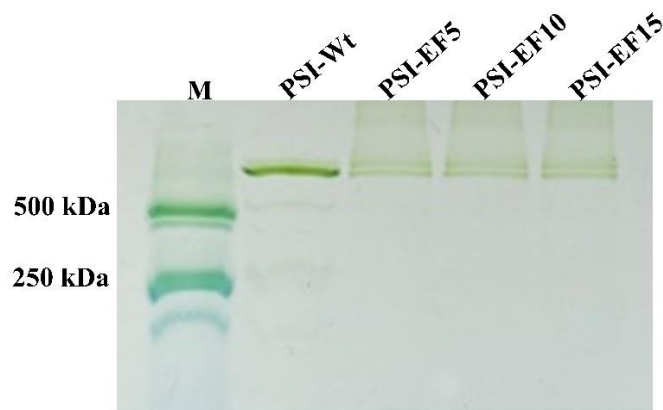


**Supplementary Figure 7. Absorption difference spectra between of EFF chimeras and free FNR.** All EFF spectra were subtracted with the spectrum of free FNR. The absorbance maxima of EFF chimeras after subtraction with FNR spectrum was at 330 nm and slight at 420 nm. For experimental details see Fig. 2D in the main manuscript.

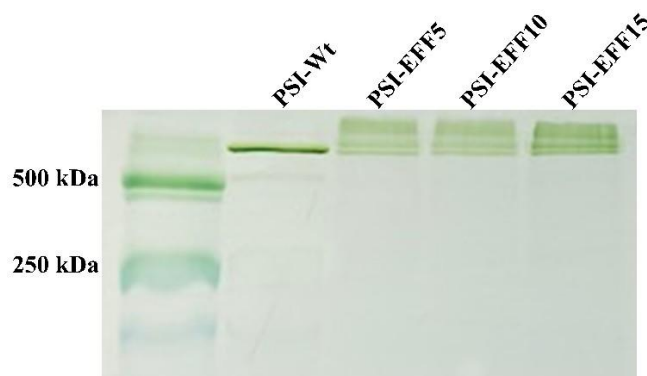


**Supplementary Figure 8. Continuous sucrose density gradient centrifugation PSI-EF chimeras.** Separation of unbound EF chimeric from PSI-Im7-coupled E7-Fd chimeras on a linear 0-20 % (w/v) sucrose density gradient. A mixture equivalent to 150  $\mu$ g Chl and corresponding molar concentrations of EF were loaded onto each centrifugation tube.

## Chapter 4



**Supplementary Figure 9. BN-PAGE-based analysis of PSI-Fd (PSI-EF) chimeras.** From Left to right: Lane 1: Photosystem II (PSII) dimer (500 kDa) and monomer (250 kDa) from *T. vestitus* BP-1, Lane 2: PSI-Wt from *Synechocystis* (trimeric) after incubation with EFF5, Lane 3 to 5: PSI-Im7 (trimeric) after coupling with EF chimeras (5 to 15), respectively. Equivalents of 1  $\mu$ g Chl PSI fusion complexes were loaded onto each lane.

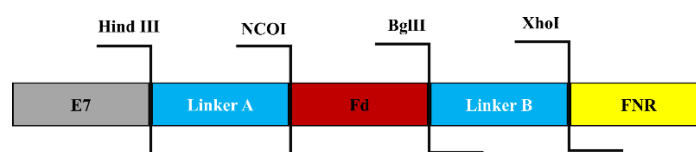


**Supplementary Figure 10. BN-PAGE of PSI-Fd-FNR (PSI-EFF) chimeras.** Lane 1: PSII dimer (500 kDa) and monomer (250 kDa) from *T. vestitus* BP-1, Lane 2: PSI-Wt from *Synechocystis* (trimeric) after coupling with EFF5, Lane 3 to 5: PSI-Im7 (trimeric) after coupling with EFF chimeras (5 to 15, respectively). PSI equivalents of 1  $\mu$ g Chl were loaded onto each lane.

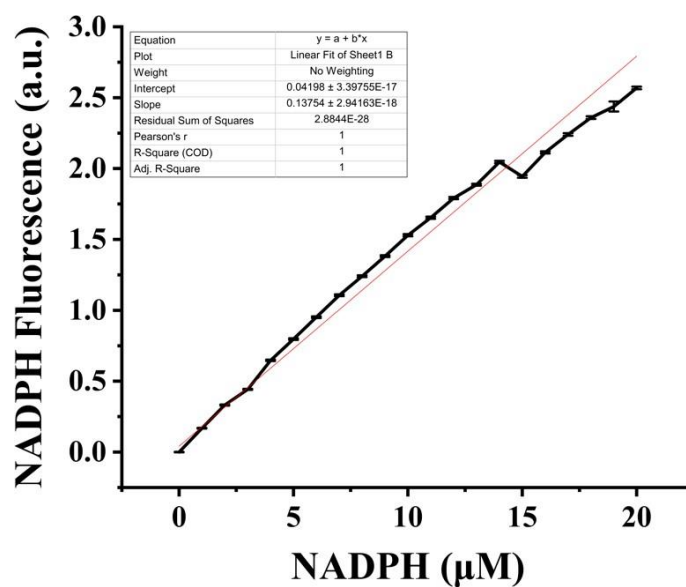


**Supplementary Figure 11. Schematic representation of the genetic construct of plasmid pRSET6a\_PsaE\_Im7-Histag\_KAN<sup>R</sup> used for the creation of the *Synechocystis* PSI-Im7 mutant.**

## Chapter 4



**Supplementary Figure 12. Schematic representation of synthetic genetic construct of E7-Fd-FNR fusion protein.** Each gene segment is separated with a nucleotide sequence corresponding to the amino acid linker. The end of each gene segment consists of a unique restriction site.



**Supplementary Figure 13. Fluorescence-based NADPH calibration curve.** The fluorescence of the corresponding NADPH concentration from 0 to 20  $\mu\text{M}$  was measured. The data represents the mean values of fluorescence corresponding to each NADPH concentration and the standard deviation is represented with error bars ( $n=3$ ).

## Supplementary Table

Supplementary Table 1: Oligonucleotides and primer used to create plasmid constructs (pASK-IBA7-E7-Fd-(FNR), PRSET6a-PsaE_Im7_Histag_Kan <sup>R</sup> ).			
No	Name of Linker	DNA sequence of linker 5'→3'	Purpose
1	PsaE-CT-forward	CAAGTTTTTGGGAGTAGGGGAGC	Used for amplification of PsaE along with upstream and downstream sequence from isolated <i>Synechocystis</i> Wt genome
2	PsaE-CT-reverse	GGGCATTTTTTAAAGGGCGGCG	Used for amplification of PsaE along with upstream and downstream sequence from isolated <i>Synechocystis</i> Wt genome
3	KanR-forward	CCGCTCATGAATTAATTCTTAGAAAACTCATCG	Used for amplification of Kanamycin resistance cassette from plasmid PRSF-Duet1
4	KanR-reverse	GAGCGCTGCATGCCTATTTG	Used for amplification of Kanamycin resistance cassette from plasmid PRSF-Duet1
5	Im7-forward	GGTGGGTCTGGTGAAGTAAAAATAGTATT AGTGATTACACAGAGGC	Used for amplification of Im7 gene from pRSET6a_Im7_sfGFP plasmid
6	Im7-reverse	TTAATGGTGATGGTGATGGTGATGGTGATG GTGAGCGCCTCCGCTGCCGCC	Used for amplification of Im7 gene from pRSET6a_Im7_sfGFP plasmid
7	PsaE-Im7-forward	GATATCGCCCGCTCATGAATTAATTCTTAG	Used for segregation check of PSI_Im7 mutant
8	PsaE-Im7-reverse	TTTTGCCGCGCTTG	Used for segregation check of PSI_Im7 mutant
9	Fd-stop reverse	GATCTTAGCTCGAGTGGCGGTGG	For the creation of E7-Fd construct from E7-Fd-FNR, a stop codon was reintroduced at the end of Fd with this oligonucleotide
10	Fd-stop forward	GCCCCACCGCCACTCGAGCTAA	For the creation of E7-Fd construct from E7-Fd-FNR, a stop codon was reintroduced at the end of Fd with this oligonucleotide
11	B5 reverse	TCGAGACTACCACTACCGCCA	Linker exchange to 5 AA between Fd and FNR
12	B5 forward	GATCTGGCGGTAGTGGTAGTC	Linker exchange to 5 AA between Fd and FNR
13	B15 reverse	TCGAGACTACCGCCACTCCCGCCACTGCCT CCGCTACCTCCGCTCCCACCA	Linker exchange to 15 AA between Fd and FNR
14	B15 forward	GATCTGGTGGGAGCGGAGGTAGCGGAGGC AGTGGCGGGAGTGGCGGTAGTC	Linker exchange to 15 AA between Fd and FNR

## Chapter 4

15	A5 reverse	CATGGACTACCACTCCCGCCA	Linker exchange to 5 AAbetween E7 and Fd
16	A5 forward	AGCTTGGCGGGAGTGGTAGTC	Linker exchange to 5 AAbetween E7 and Fd
17	A15 reverse	CATGGACTACCGCCACTCCCGCCACTGCCT CCGCTACCTCCGCTCCCACCA	Linker exchange to 15 AAbetween E7 and Fd
18	A15 forward	AGCTTGGTGGGAGCGGAGGTAGCGGAGGC AGTGGCGGGAGTGGCGGTAGTC	Linker exchange to 15 AAbetween E7 and Fd



## Chapter 4

### Protein sequences of E7-Fd, E7-Fd-FNR, PsaE-Im7-Histag

#### Protein sequences of EF

MHHHHHHASESKENKPGKATGDGDPVNNKWLNNAGEDLGSPVPDRIANDLRCEEFDSDDFR  
KKFWEEVSKDPELSKQFSRNNNDRMKVGKAPKTRTQDVSGKRTSFELHAEKPISQNGGVYDM  
DNISVVTPKRHIDIHRGKKLGGSGSGSGSPWATYKVTLVPRPDGSETTIDVPEDEYILDVAEEQ  
LDLPFSCRAGACSTCAGKLLEGEVDQSDQSFLDDDQIEKGFVLTCVAYPRSDCKILTQEEELY  
RS

Linker 5 amino acids	GGSGG
Linker 10 amino acids	GGSGSGSGSG
Linker 15 amino acids	GGSGSGSGSGSGSGG

#### Protein sequence of EFF

MHHHHHHASESKENKPGKATGDGDPVNNKWLNNAGEDLGSPVPDRIANDLRCEEFDSDDFR  
KKFWEEVSKDPELSKQFSRNNNDRMKVGKAPKTRTQDVSGKRTSFELHAEKPISQNGGVYDM  
DNISVVTPKRHIDIHRGKKLGGSGSGSGSPWATYKVTLVPRPDGSETTIDVPEDEYILDVAEEQ  
GLDLPFSCRAGACSTCAGKLLEGEVDQSDQSFLDDDQIEKGFVLTCVAYPRSDCKILTQEEEL  
YRSGGSGSGSGSLEYNATNSRSMFRYEVVGLRQTAETKTNIAIRNSGSQFFNVPYDRMNQ  
FMQQITRWGGKIVSIQPLNGTVAPLAATTEPAANNGAAPVKEKKVDIPVNIYRPNNPCIGKVISN  
EELVREGGEGTVKHIFDISGTELRYLEGQSIGIIPAGTDANGKPHKLRLYSIASTRHGDFQDDKT  
VSLCVRRLLEYKDKETGETIYGVCSSYLNQLQPGDEVKITGPVGKEMLLSDDPEATIIMLATGTGI  
APFRAFLWRMFKENNPDYQFKGLAWLFFGVAYTANILYKDELEAIQAQYPDHFRLTYAISREQ  
KTPDGGKMYIQGRIAEHADEIWQLLQKKNTHVYMCGLRGMEPGIDEAMTAAAKNGADWQE  
FLKGTLKKEGRWHV ETY

Linker 5 amino acids	GGSGG
Linker 10 amino acids	GGSGSGSGSG
Linker 15 amino acids	GGSGSGSGSG GGSGG

#### Protein sequence of PSaE-Im7-Histag

MALNRGDKVRIKRTESYWYGDVGTVASVEKSGILYPVIVRFDRVNYNGFSGSASGVNTNMF  
AENELELVQAAAKGGSGELKNSISDYTEAEFVQLLKEIEKENVAATDDVLDVLLEHFVKITE  
HPDGTDLIYYPSDNRRDSSPEGIVKEIKEWRAANGKPGFKQGGSGGAHHHHHHHHHH

### References

- [1] E. El-Mohsnawy, M. J. Kopczak, E. Schlodder, M. Nowaczyk, H. E. Meyer, B. Warscheid, N. v. Karapetyan, M. Rögner, *Biochemistry* **2010**, 49, 4740–4751.
- [2] F. Zhao, S. Hardt, V. Hartmann, H. Zhang, M. M. Nowaczyk, M. Rögner, N. Plumeré, W. Schuhmann, F. Conzuelo, *Nat Commun* **2018**, 9, 1-9.
- [3] J. G. K. Williams, *Methods Enzymol*, **1988**, 167, 766–778.
- [4] M. K. Akhtar, P. R. Jones, *Appl Microbiol Biotechnol* **2008**, 78, 853-862

## Chapter 5: Photosynthesis re-wired on the pico-second timescale

Tomi K. Baikie, Laura T. Wey, Joshua M. Lawrence, Hitesh Medipally, Erwin Reisner, Marc M. Nowaczyk, Richard H. Friend, Christopher J. Howe, Christoph Schnedermann, Akshay Rao & Jenny Z. Zhang

**Publication 4,**

**Nature 2023, 615, 836–840**

**<https://doi.org/10.1038/s41586-023-05763-9>**

**Abstract:** Photosystems II and I (PSII, PSI) are the reaction centre-containing complexes driving the light reactions of photosynthesis; PSII performs light-driven water oxidation and PSI further photo-energizes harvested electrons. The impressive efficiencies of the photosystems have motivated extensive biological, artificial and biohybrid approaches to ‘re-wire’ photosynthesis for higher biomass-conversion efficiencies and new reaction pathways, such as H<sub>2</sub> evolution or CO<sub>2</sub> fixation.<sup>[1,2]</sup> Previous approaches focused on charge extraction at terminal electron acceptors of the photosystems.<sup>[3]</sup> Electron extraction at earlier steps, perhaps immediately from photoexcited reaction centres, would enable greater thermodynamic gains; however, this was believed impossible with reaction centres buried at least 4 nm within the photosystems.<sup>[4,5]</sup> Here, we demonstrate, using in vivo ultrafast transient absorption (TA) spectroscopy, extraction of electrons directly from photoexcited PSI and PSII at early points (several picoseconds post-photo-excitation) with live cyanobacterial cells or isolated photosystems, and exogenous electron mediators such as 2,6-dichloro-1,4-benzoquinone (DCBQ) and methyl viologen. We postulate that these mediators oxidize peripheral chlorophyll pigments participating in highly delocalized charge-transfer states after initial photoexcitation. Our results challenge previous models that the photoexcited reaction centres are insulated within the photosystem protein scaffold, opening new avenues to study and rewire photosynthesis for biotechnologies and semi-artificial photosynthesis.

## 5.1 Main text

The photodynamics of Photosystems I and II have been extensively studied in vitro using ultrafast TA spectroscopy.<sup>[6]</sup> In this technique, the sample’s absorbance spectrum is measured by a broadband probe laser after photo-excitation by a pump laser (that is, pump-probe spectroscopy), with access to photodynamics occurring on the subpico-second timescale. Previously, it has been challenging to apply ultrafast TA spectroscopy on the photosystems in vivo, with plant or algal cells (typically 10 µm in size)<sup>[7]</sup> being highly scattering. Recently, ultrafast TA spectroscopy was successfully applied to *Nannochloropsis* sp. algal cells (2–5 µm in size)<sup>[8]</sup>, whose small size lessened these scattering effects.<sup>[9]</sup> Here, we studied *Synechocystis* sp. PCC 6803 (hereafter *Synechocystis*) cyanobacterial cells (Fig. 1a–c), which is a model organism for studying photosynthesis because of the endosymbiotic origin of the chloroplast in eukaryotic plants and algae.<sup>[10]</sup> The smaller size of *Synechocystis* cells (less than 2 µm)<sup>11</sup> further reduced the scattering, and the photodynamics of the photosystems in vivo could be resolved using ultrafast TA spectroscopy. Photo-excitation of *Synechocystis* cells with a 200 fs pump pulse centred at 450 nm revealed rich initial transient spectral features in the visible (550–800 nm). We identified a prominent negative feature at 685 nm (Fig. 1d), which decayed within

roughly 20 ps to 10% of its initial value. We attribute this feature to the ground-state bleaching of the photoactive reaction centres of PSI and PSII. A lower-energy feature at 715 nm grew within roughly 2 ps after photoexcitation and subsequently decayed on a longer pico-second timescale, indicating rapid excited state relaxation processes. Similarly, we observed higher-energy positive transient features (less than 680 nm), which we assign to contributions from the photo-induced absorption of phycobilisomes (PBSs) and carotenoids, as these features resemble those of in vitro steady state absorption measurements<sup>[12,13]</sup> and are absent from isolated photosystems (Supplementary Fig. 7). We verified that the photosystems remained intact without photodamage, consistent over several biological replicates, and were in a closed state through-out these measurements (Supplementary Figs. 1–4). We confirmed that the key spectral features arise from fully assembled photosystems (Supplementary Information section 1.5.4.).

To probe the effect of exogenous electron mediators on the photodynamics of cyanobacterial cells, we repeated the same measurements with the addition of DCBQ. As shown in Fig. 1e, we found that addition of DCBQ led to accelerated decay dynamics of the negative feature at 685 nm. Simultaneously, the signal rise observed at 715 nm was suppressed, with a noticeable effect evident in just 600 fs after photo-excitation. The effect was also observed when pumping at the band edge of the reaction centres (Supplementary Figs. 5 and 6). These observations demonstrate that DCBQ can alter the excited state decay pathways of the photosynthetic reaction centres in *Synechocystis* cells on a subpico-second timescale. Previously, DCBQ has been thought to extract electrons only from the terminal electron acceptor site of PSII, the QB pocket (Fig. 1c). However, we note that the mid-point potential of DCBQ (+0.315 V versus standard hydrogen electrode (SHE) at pH 7)<sup>[14]</sup> makes it suitable for extracting electrons from both PSI ( $P700^*/P700^+ = -1.290$  V,  $FB/FA^- = -0.590$  V)<sup>[15]</sup> and PSII ( $P680^*/P680^+ = -0.660$  V).<sup>[16]</sup> To rule out energy transfer from the reaction centres to DCBQ as the mechanism resulting in the observations shown in Fig. 1e, we characterized the optical properties of suspensions of cells in the presence of DCBQ. As reported in Fig. 2b, the absorption spectrum of cells includes prominent absorption bands at 450, 680 and 700 nm corresponding primarily to the chlorophylls in the cell's PSII and PSI complexes, whereas DCBQ absorbs below 300 nm. The lack of overlap in the absorption spectra of DCBQ before reduction and fluorescence of the intact cells indicates that energy transfer mechanisms in the form of Förster resonances are not active.<sup>[9]</sup> After considering possible quenching mechanisms, we conclude that the effect caused by DCBQ must stem from an electron transfer mechanism (more detail in Supplementary Information section 1.5.5.).

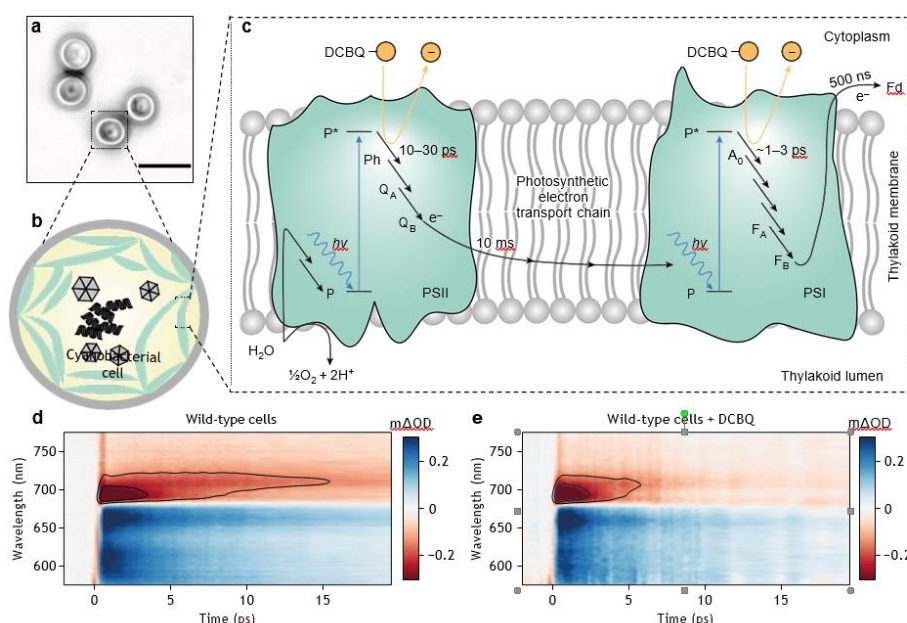


**Fig. 1 | Exogenous electron mediator acts on the pico-second timescale in living cells.** **a**, Bright field microscopy of *Synechocystis* sp. PCC 6803 cells. Scale bar, 5 µm. **b**, Schematic of a cell showing intracellular thylakoid membranes (green). **c**, Schematic of a simplified photosynthetic electron transport chain. The chain starts with PSII, in which a special pair of chlorophylls known as P680 is photoexcited to P680\* directly or by energy transfer from other chlorophylls. An initial charge separated state with the primary electron acceptor pheophytin (Ph) [P680<sup>+</sup>–Ph<sup>–</sup>] is formed with a lifetime of 10–30 ps (ref.<sup>34</sup>) driving water oxidation. The extracted electrons exit PSII through terminal plastoquinones Q<sub>A</sub> and Q<sub>B</sub>. The electrons are shuttled along the chain, with the first diffusion step at roughly 10 ms (ref.<sup>35</sup>). The electrons are received by PSI and with further input of light, the P700 is photoexcited to P700\* and an initial charge separated state with the primary electron acceptor chlorophyll A<sub>0</sub> [P700<sup>+</sup>–A<sub>0</sub><sup>–</sup>] is formed with a lifetime of roughly 1–3 ps (ref.<sup>36</sup>). The electrons exit PSI through the terminal iron-sulfur clusters F<sub>A</sub> and F<sub>B</sub>. The electrons are shuttled through ferredoxin (Fd) that takes around 500 ns (ref.<sup>37</sup>) and then onto various pathways, including the Calvin–Benson cycle. On the addition of the electron mediator DCBQ (orange circle), a new electron transfer pathway forms (orange arrow). **d,e**, Ultrafast TA spectroscopy map of wild-type cells (**d**) and cells with DCBQ (**e**) (5 mM) between –2 and 20 ps photo-excited at 450 nm in units of differential absorption (mΔOD). Two contours have been drawn at the same signal intensity to highlight the reduced lifetime of the 685 nm feature and suppression of the 715 nm rise on the addition of DCBQ. Maps are one sample, representative of several biological replicates (cells, n = 8, + DCBQ, n = 5).

It is known that all chlorophylls embedded within PSII and PSI are energetically degenerate at room temperature. Photo-excitation thus results in a highly delocalized excited state shared across several chlorophylls.<sup>[17,18]</sup> Previous studies on isolated reaction centres from the photosynthetic purple non-sulfur bacterium *Rhodobacter sphaeroides* at 77 K showed that the initially excited state shows charge-transfer character and can form intermediate charge-transfer states within 200 fs (ref.<sup>19</sup>). Similarly, recent femtosecond crystallography results of the photosynthetic reaction

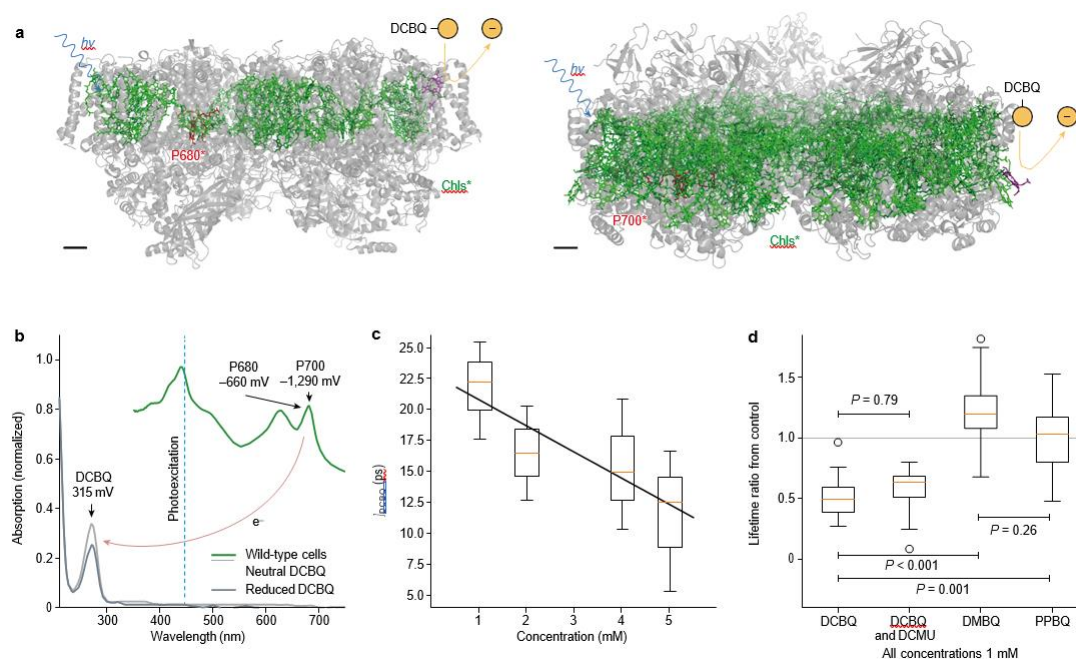


**Fig. 2 | Action of quinone electron mediators on wild-type cells.** **a**, Schematic representation of the proposed mechanism of early DCBQ reduction by PSII and PSI. The chlorophylls are photoexcited (Chls\*, green), including the special pairs of chlorophylls (P680\* and P700\*, red in the left most monomer), in a delocalized excited state. The initial charge separated states are formed and rapidly delocalized across the chlorophylls. DCBQ (orange circle) is reduced through a peripheral chlorophyll (purple) that protrudes from the protein scaffold into the thylakoid membrane. PSII crystal structure by Young et al. (Protein Data Bank ID 5TIS)<sup>[38]</sup>; PSI crystal structure by Jordan et al. (Protein Data Bank ID 1JB0).<sup>[4]</sup> Scale bar, 10 Å. **b**, Absorption spectra of *Synechocystis* cells (green), and reduced and neutral DCBQ (greys). **c**, Retrieved electron transfer lifetimes to DCBQ ( $\tau_{\text{DCBQ}}$ ). Detail of the model in Supplementary Information section 1.5.2. The black line is a linear fit to the medians. **d**, Lifetime change on the addition of DCBQ, DMBQ, PPBQ, and DCMU with DCBQ, detail of the model in Supplementary Fig. 14. Presented are the ratios of the additive lifetimes from samples in which no quinone was added (control). A ratio of 1 (grey line) indicates no effect. Student's *t*-test comparisons are overlaid. In **c** and **d**, the box extends from the lower to upper quartile values of the data, the whiskers extend from the box to show the range of the biological replicates ( $n = 4$ , except DCBQ  $n = 5$ , and the orange line represents the median).

centre of another purple non-sulfur bacterium *Blastochloris viridis* (formerly known as *Rhodopseudomonas viridis*) demonstrated electron transfer reactivity within 3 ps (ref. <sup>20</sup>). In the light of these observations, we postulate that photoexcitation of the chlorophyll pigments within the photosystems of *Synechocystis* at room temperature can also form highly delocalized intermediate charge-transfer states within the time resolution of our measurement (200 fs), followed by electron transfer kinetics. Given that the cell absorption spectra for all DCBQ concentrations remained unchanged (Supplementary Fig. 22), we conclude that DCBQ does not



tightly bind to the chlorophylls at the core of the reaction centre. Instead, DCBQ most likely interacts with peripheral chlorophyll pigments protruding from the protein scaffold of the photosystems, thereby interacting with the highly delocalized charge-transfer state formed after the initial photoexcitation (Fig. 2a, also see Supplementary Information for in-depth discussion).

On the basis of this assessment, we constructed a simple kinetic model (Supplementary Fig. 14) and applied global analysis techniques to time-resolved TA data from cells to extract the relevant lifetimes. We then used this model to determine how efficiently DCBQ diverts electrons away from the native electron transfer chain (Supplementary Information section 1.5.3.). As highlighted in Fig. 2c, our analysis yielded declining electron transfer lifetimes for increased DCBQ concentration. On the basis of our model and these values, we can estimate that 1 mM DCBQ diverts  $17 \pm 6\%$  of the initial photoexcited reaction centre population in wild-type *Synechocystis* cells. Critically, this electron transfer occurs as early as 600 fs (Fig. 1d,e), which is consistent with our hypothesis that electrons can be extracted from rapidly formed, delocalized chlorophyll charge-transfer states. Further support for this mechanistic picture stems from further control experiments with 3-(3,4-dichlorophenyl)-1,1-dimethylurea (DCMU), which binds to the  $Q_B$  pocket in PSII (ref. <sup>21</sup>), competing against DCBQ docking and reduction thereafter. Here, the TA measurements with DCBQ and DCMU yielded similar effects to those with only DCBQ, indicating that DCBQ acts at the initial stages of the photosynthetic pathway, rather than only at the  $Q_B$  site (Fig. 2d and Supplementary Fig. 15). This trend is also supported by analogous photo-electrochemistry measurements, in which DCBQ was observed to extract electrons at a site that is alternative to the  $Q_B$  site (roughly 30% of the photocurrent, Supplementary Fig. 26).

The ability of DCBQ to interact with the photosynthetic electron transport chain at longer timescales was also probed. Photoluminescence decay measurements revealed a reduction in luminescence lifetime with increasing DCBQ concentration, consistent with pulse amplitude modulation fluorometry studies of eukaryotic algal cells in the presence of benzoquinones (Supplementary Fig. 28).<sup>[3,14,22]</sup> This is consistent with DCBQ interfering with the photosynthetic electron transport chain beyond the pico-second timescales explored in TA. Oxygen evolution measurements confirmed that PSII continues to perform oxidation of water *in vivo* in the presence of DCBQ at all concentrations tested in the TA experiments, suggesting the pathway for holes generated by photo-excitation remains active on the addition of DCBQ (Supplementary Fig. 30). However, a long-term cytotoxicity assay revealed that all concentrations of DCBQ greater than 200  $\mu\text{M}$  are cytotoxic to the cells after 12 h, but there was no correlation between the cytotoxicity

of benzoquinones and their ability to re-direct electrons from the electron transport chain (Supplementary Fig. 31). We tested two other common benzoquinone mediators, phenyl-1,4-quinone (PPBQ) and 2,6-dimethyl-1,4-benzoquinone (DMBQ), which have comparable mid-point potentials to DCBQ.<sup>[14,23]</sup> Figure 2d outlines that the early onset decay in the TA spectrum found for DCBQ was not observed in PPBQ- and DMBQ-treated cells (Supplementary Information section 1.6., Supplementary Fig. 15). Similarly, complementary photo-electrochemistry experiments highlighted that DCBQ was the only benzoquinone screened that was reduced earlier than  $Q_B$  in PSII *in vivo*, as it mediated electron transfer to electrodes in the presence of DCMU (Supplementary Fig. 26). The observation that PPBQ and DMBQ did not demonstrate early interactions with the reaction centres may originate from poor protein-molecule association effects or their lower solubilities in aqueous solutions, which may lead to the quinones being sequestered in intracellular membranes and precipitating in aqueous compartments as they entered the cell.<sup>[14]</sup>

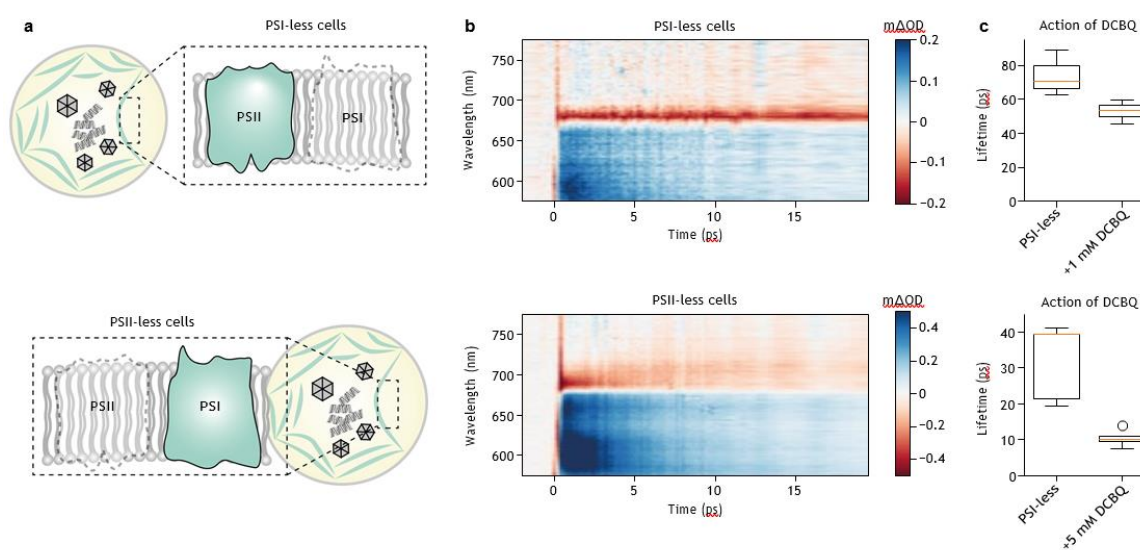


**Fig. 3 | Action of DCBQ on cells genetically modified to have only one type of photosystem. a,** Schematic representation of photosystem-less mutants analyzed (top, PSI-less and bottom, PSII-less). **b,** TA spectra between  $-2$  and  $20$  ps of cell mutants excited at  $450$  nm under the same conditions as wild-type cells in their TA spectrum in Fig. 1d (top, PSI-less; bottom, PSII-less). The PSII-less spectrum (bottom) closely resembles that of the wild-type cells. Maps are of one sample, representative of several biological replicates (PSI-less,  $n = 4$ ; PSII-less,  $n = 5$ ). **c,** Lifetimes determined from global analysis in the photosystem-less cells and with the addition of DCBQ (top, PSI-less; bottom, PSII-less). The box extends from the lower to upper quartile values of the data, the whiskers extend from the box to show the range of the biological replicates (PSI-less + DCBQ,  $n = 4$ ; PSII-less + DCBQ,  $n = 3$ ) and the orange line represents the median.

Next, we set out to explain the action of DCBQ electron extraction from different stages of the photosynthetic electron transport chain. To this end, we carried out ultrafast TA spectroscopy on the photosystems in vivo with genetically engineered *Synechocystis* lacking either PSI or PSII intact protein complexes (Fig. 3a). These measurements were further complemented in vitro with isolated photosystems, with and without DCBQ. The full analysis of the data is presented in Supplementary Information. Briefly, the transient response of isolated photosystems shows good agreement with previous reports with PSII dominated by a prominent bleach at 680 nm that decays on the nanosecond timescale<sup>[6,24–26]</sup>, whereas PSI shows a bleach signal at 690 nm and a lower-energy stimulated emission growing in and subsequently decaying on the pico-second timescale between 705 and 720 nm (refs.<sup>27–30</sup>). This latter feature originates from low-energy chlorophylls (so-called ‘red forms’), which are present in cyanobacterial PSI cores, albeit their exact spectral position can vary largely in different species.<sup>[27]</sup> We can therefore confidently assign the transient response to photo-excitation of P680 and P700 in PSII and PSI, respectively.

Whereas the mutant cells and isolated photosystems allow us to deconvolute the spectral features of the reaction centres, the changes in the lifetimes highlight the importance of observing the photodynamics of wild-type cells to obtain accurate insights into the photosynthetic electron transport chain. Following photo-excitation at 450 nm, the PSI-less mutant cells showed spectral features that were markedly different from wild-type cells (Fig. 3b, top panel). The PSI-less cells showed a long-lived bleach at its absorption maximum at 680 nm, lasting longer than a nanosecond. This spectral feature is well matched to that of isolated PSII but shows a slower decay. This extended ground-state bleach probably arises as the natural charge-extraction pathways were blocked, or not fully functional, due to the absence of functional PSI. By contrast, the PSII-less cells showed more similar dynamics to wild-type cells, with the familiar low-energy spectral feature more than 690 nm also found in isolated PSI (Fig. 3b). We then studied the effect of DCBQ addition on these mutant cells, as they most closely resemble our in vivo studies (full details in Supplementary Information section 1.7.). On the addition of 1 mM DCBQ to the PSI-less cells, we found a reduction from 74 to 53 ps in the lifetime of the short component of the signal (Fig. 3c, top panel). This suggests that electron extraction by DCBQ treatment from PSII in PSI-less cells occur over a much longer timescale than the sub-20 ps quenching dynamics observed in the wild-type cells. By contrast, on the addition of 1 mM DCBQ to PSII-less cells, we found a reduction in the lifetimes that closely resembled the behaviour in wild-type cells. Measurements of living cells are advantageous compared to the those of in vitro systems due to the robustness of the cells and the ability to

study altered pathways produced by means of genetic engineering. However, *in vitro* measurements are useful in identifying spectral features due to their relative simplicity. Measurements of isolated PSI and PSII showed similar spectral features (Supplementary Information section 1.7.) and lifetime reductions compared to mutant cells on the addition of DCBQ, further supporting our assignments and proposed mechanism. Considering the *in vitro* and *in vivo* measurements together, we conclude that in the experimental arrangement described here, we primarily resolve electron transfer from PSI to DCBQ. This is in line with the more accessible nature of PSI compared to PSII. Although PSII is also weakly accessible to DCBQ in the PSI-less cells, no corresponding long-lived signal is observed in the wild-type cells that can be directly assigned to PSII with sufficient statistical certainty. Whereas the fast kinetics of DCBQ reduction by PSI *in vivo* is desirable, the positive mid-point potentials of benzoquinones limit the power densities they can generate or redox reactions they can catalyze in semi-artificial photosynthesis<sup>[31]</sup>. To test whether alternative classes of mediators can also extract charge through this non-classical pathway, methyl viologen ( $MV^{2+}/MV^{\cdot+} = -0.325$  V versus SHE at pH 7)<sup>[32]</sup> was investigated. Methyl viologen is the most common synthetic mediator used in reductive catalysis and could unlock greater energy densities compared to DCBQ while bridging the gap between natural and artificial photosynthesis. Our results are consistent with methyl viologen also being able to extract charge from PSI chlorophylls at the pico-second timescale in isolated PSI (Supplementary Fig. 20). This demonstrates that ultrafast electron extraction from photosystems is not limited to any one class of mediator molecules and opens new opportunities in mediator design and chemical generation.

### 5.3 Conclusion and outlook

Taken together, our results show that *in vivo* electron transfer from photosynthesis to various exogenous electron mediators is possible directly from the initially photoexcited states of the photosystems, that is, from the earliest possible step in the photosynthetic electron transport chain. This opens new possibilities for re-wiring biological photosynthesis and creates a link between biological and artificial photosynthesis. For example, manipulation of this non-classical pathway could mitigate the losses associated with light stress in biotechnological and agricultural applications or help to channel charges out for alternative uses in power and chemical generation. Furthermore, these results call for a re-examination of mediated electron transfer strategies, which have long been used to study photosynthesis as well as for enhancing the performance of bioelectrochemical devices such as biophotovoltaics<sup>[33]</sup>. We also show that

## Chapter 5

the pico-second charge-extraction pathway is not limited to one class of mediators, suggesting that the bioengineering of endogenous mediators, cascades and other biohybrid approaches could be used in the future to expand on and optimize this pathway.

These results also yield new insights into photosynthesis. Contrary to the current understanding that the excited reaction centres are insulated within the photosystem protein scaffold, the action of DCBQ and methyl viologen demonstrate that the scaffold is leaky. This is a potentially significant route in the cell for loss of electrons that might otherwise be used for photosynthesis and may have a role in photo-protection or be a key cause of cell damage from production of reactive oxygen species. More generally, our work highlights that in vivo ultrafast TA spectroscopic measurements are feasible and shows rich information on photoexcited dynamics of living systems. This could be a powerful new tool for understanding photosynthesis bioenergetics and its regulation, especially under conditions of light stress.

## 5.4 References

- [1] Grattieri, M., Beaver, K., Gaffney, E. M., Dong, F. & Minteer, S. D. Advancing the fundamental understanding and practical applications of photo-bioelectrocatalysis. *Chem. Commun.* **56**, 8553–8568 (2020).
- [2] Zhang, J. Z. & Reisner, E. Advancing photosystem II photoelectrochemistry for semi-artificial photosynthesis. *Nat. Rev. Chem.* **4**, 6–21 (2020).
- [3] Fu, H.-Y. et al. Redesigning the QA binding site of Photosystem II allows reduction of exogenous quinones. *Nat. Commun.* **8**, 15274 (2017).
- [4] Jordan, P. et al. Three-dimensional structure of cyanobacterial photosystem I at 2.5 Å resolution. *Nature* **411**, 909–917 (2001).
- [5] Shen, G., Boussiba, S. & Vermaas, W. F. J. *Synechocystis* sp. PCC 6803 strains lacking photosystem I and phycobilisome function. *Plant Cell* **5**, 1853 (2007).
- [6] Berera, R., van Grondelle, R. & Kennis, J. T. M. Ultrafast transient absorption spectroscopy: principles and application to photosynthetic systems. *Photosynth. Res.* **101**, 105–118 (2009).
- [7] Harris, E. H. *Chlamydomonas* as a model organism. *Annu. Rev. Plant Physiol. Plant Mol. Biol.* **52**, 363–406 (2001).
- [8] Suda, S. et al. Taxonomic characterization of a marine *Nannochloropsis* species, *N. oceanica* sp. nov. (Eustigmatophyceae). *Phycologia* **41**, 273–279 (2019).
- [9] Park, S. et al. Chlorophyll–carotenoid excitation energy transfer and charge transfer in *Nannochloropsis oceanica* for the regulation of photosynthesis. *Proc. Natl Acad. Sci. USA* **116**, 3385–3390 (2019).
- [10] Howe, C. J., Barbrook, A. C., Nisbet, R. E. R., Lockhart, P. J. & Larkum, A. W. D. The origin of plastids. *Philos. Trans. R. Soc. B: Biol. Sci.* **363**, 2675–2685 (2008).
- [11] Lea-Smith, D. J. et al. Hydrocarbons are essential for optimal cell size, division, and growth of cyanobacteria. *Plant Physiol.* **172**, 1928–1940 (2016).
- [12] Fălămas, A., Porav, S. A. & Tosa, V. Investigations of the energy transfer in the phycobilisome antenna of *Arthrospira platensis* using femtosecond spectroscopy. *Appl. Sci.* **10**, 4045 (2020).
- [13] Kopczynski, M. et al. Ultrafast transient lens spectroscopy of various C40 carotenoids: lycopene,  $\beta$ -carotene, (3R,3' R)-zeaxanthin, (3R,3' R,6' R)-lutein, echinenone, canthaxanthin, and astaxanthin. *Phys. Chem. Chem. Phys.* **7**, 2793–2803 (2005).
- [14] Longatte, G. et al. Investigation of photocurrents resulting from a living unicellular algae suspension with quinones over time. *Chem. Sci.* **9**, 8271–8281 (2018).
- [15] Evans, M. C. W. & Heathcote, P. Effects of glycerol on the redox properties of the electron acceptor complex in spinach Photosystem I particles. *Biochim. Biophys. Acta Bioenerg.* **590**, 89–96 (1980).
- [16] De Causmaecker, S., Douglass, J. S., Fantuzzi, A., Nitschke, W. & Rutherford, A. W. Energetics of the exchangeable quinone, Q<sub>B</sub>, in Photosystem II. *Proc. Natl Acad. Sci. USA* **116**, 19458–19463 (2019).
- [17] Stirbet, A. Excitonic connectivity between photosystem II units: what is it, and how to measure it? *Photosynth. Res.* **116**, 189–214 (2013).
- [18] Mirkovic, T. et al. Light absorption and energy transfer in the antenna complexes of photosynthetic organisms. *Chem. Rev.* **117**, 249–293 (2017).
- [19] Ma, F., Romero, E., Jones, M. R., Novoderezhkin, V. I. & van Grondelle, R. Both electronic and vibrational coherences are involved in primary electron transfer in bacterial reaction center. *Nat. Commun.* **10**, 933 (2019).
- [20] Dods, R. et al. Ultrafast structural changes within a photosynthetic reaction centre. *Nature* **589**, 310–314 (2021).
- [21] Trebst, A. The three-dimensional structure of the herbicide binding niche on the reaction center polypeptides of photosystem II. *Z. Naturforsch. C J. Biosci.* **42**, 742–750 (1987).



- [22] Longatte, G. et al. Evaluation of photosynthetic electrons derivation by exogenous redox mediators. *Biophys. Chem.* **205**, 1–8 (2015).
- [23] O'Reilly, J. E. Oxidation-reduction potential of the ferro-ferricyanide system in buffer solutions. *Biochim. Biophys. Acta Bioenerg.* **292**, 509–515 (1973).
- [24] Durrant, J. R. et al. Subpicosecond equilibration of excitation energy in isolated photosystem II reaction centers. *Proc. Natl Acad. Sci. USA* **89**, 11632–11636 (1992).
- [25] Groot, M. L. et al. Initial electron donor and acceptor in isolated Photosystem II reaction centers identified with femtosecond mid-IR spectroscopy. *Proc. Natl Acad. Sci. USA* **102**, 13087–13092 (2005).
- [26] Klug, D. R., Durrant, J. R. & Barber, J. The entanglement of excitation energy transfer and electron transfer in the reaction centre of photosystem II. *Philos. Trans. R. Soc. London, Ser. A* **356**, 449–464 (1998).
- [27] Russo, M., Casazza, A. P., Cerullo, G., Santabarbara, S. & Maiuri, M. Ultrafast excited state dynamics in the monomeric and trimeric photosystem I core complex of *Spirulina platensis* probed by two-dimensional electronic spectroscopy. *J. Chem. Phys.* **156**, 164202 (2022).
- [28] Slavov, C., Ballottari, M., Morosinotto, T., Bassi, R. & Holzwarth, A. R. Trap-limited charge separation kinetics in higher plant photosystem I complexes. *Biophys. J.* **94**, 3601–3612 (2008).
- [29] Lee, Y., Gorka, M., Golbeck, J. H. & Anna, J. M. Ultrafast energy transfer involving the red chlorophylls of cyanobacterial photosystem I probed through two-dimensional electronic spectroscopy. *J. Am. Chem. Soc.* **140**, 11631–11638 (2018).
- [30] Shelaev, I. V. et al. Femtosecond primary charge separation in *Synechocystis* sp. PCC 6803 photosystem I. *Biochim. Biophys. Acta Bioenerg.* **1797**, 1410–1420 (2010).
- [31] Weliwatte, N. S., Grattieri, M. & Minteer, S. D. Rational design of artificial redox-mediating systems toward upgrading photobioelectrocatalysis. *Photochem. Photobiol. Sci.* **20**, 1333–1356 (2021).
- [32] Bennett, T. et al. Elucidating the role of methyl viologen as a scavenger of photoactivated electrons from photosystem I under aerobic and anaerobic conditions. *Phys. Chem. Chem. Phys.* **18**, 8512–8521 (2016).
- [33] Wey, L. T. et al. The development of biophotovoltaic systems for power generation and biological analysis. *Chem. Electro. Chem.* **6**, 5375–5386 (2019).
- [34] Kato, M., Zhang, J. Z., Paul, N. & Reisner, E. Protein film photoelectrochemistry of the water oxidation enzyme photosystem II. *Chem. Soc. Rev.* **43**, 6485–6497 (2014).
- [35] Lea-Smith, D. J., Bombelli, P., Vasudevan, R. & Howe, C. J. Photosynthetic, respiratory and extracellular electron transport pathways in cyanobacteria. *Biochim. Biophys. Acta, Bioenerg.* **1857**, 247–255 (2016).
- [36] Kurashov, V. et al. Critical evaluation of electron transfer kinetics in P700–FA/FB, P700–FX, and P700–A<sub>1</sub> Photosystem I core complexes in liquid and in trehalose glass. *Biochim. Biophys. Acta Bioenerg.* **1859**, 1288–1301 (2018).
- [37] Setif, P. Q. Y. & Bottin, H. Laser flash absorption spectroscopy study of ferredoxin reduction by photosystem I: spectral and kinetic evidence for the existence of several photosystem I-ferredoxin complexes. *Biochemistry* **34**, 9059–9070 (1995).
- [38] Young, I. D. et al. Structure of photosystem II and substrate binding at room temperature. *Nature* **540**, 453–457 (2016).



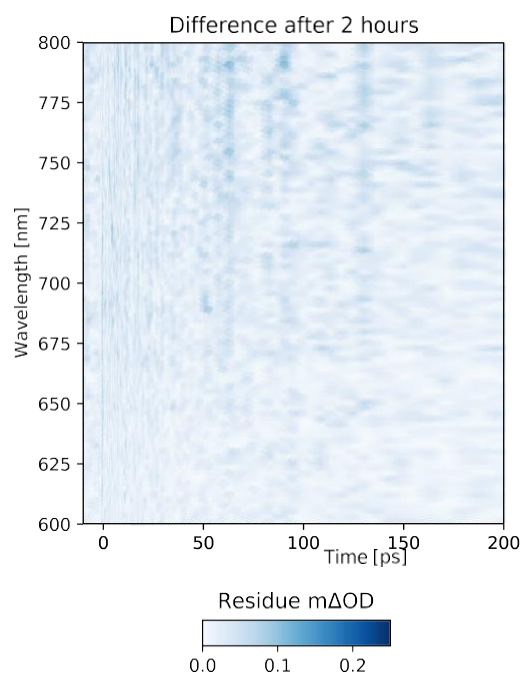
## **Supplementary information**

# 1 Ultrafast Transient Absorption Spectroscopy

## 1.1 TA controls on wild-type cells

### 1.1.1 Samples not damaged over long laser illumination

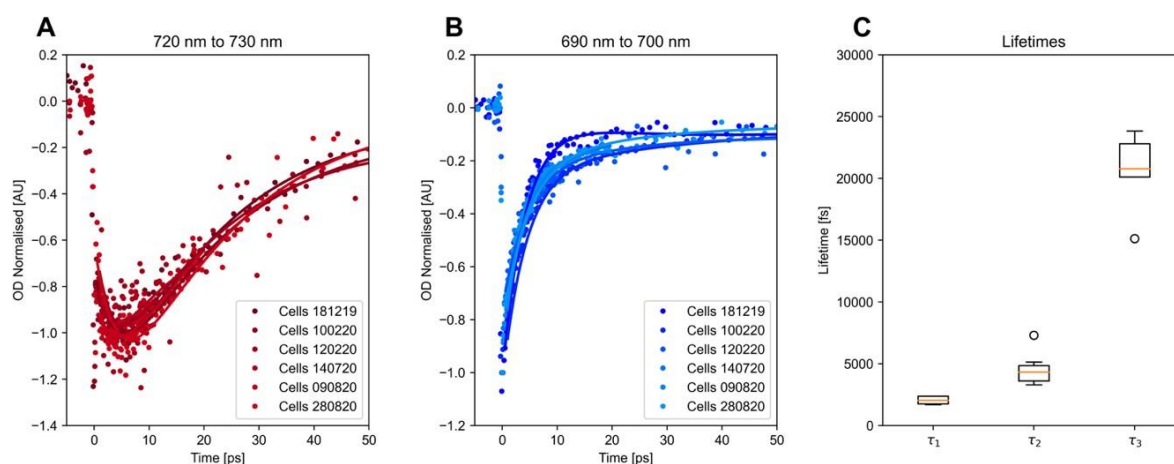
Measurements were made over 15 min on average (maximum 17 min) and a fresh biological sample was loaded into the cuvette for each measurement. To check whether the photosystem reaction centres were degrading under the laser during these measurements, additional measurements were made whereby wild-type *Synechocystis* cells in solution were exposed to the laser continuously for 2 h. This is an 8-fold increase in duration compared to the typical measurement time for experiments reported throughout. We compared the 2 hour measurement with a 15 minute measurement and found them to be no different beyond measurement uncertainty (**SI Figure 1**). As the samples were not stirred during measurements, these results also suggest that thermally driven Brownian motion continuously moved cells outside the laser focus point, preventing any measurable burn of the sample over the 2 h tested. Addition of DCBQ (any concentration) resulted in an initial equilibration period (15 min), after which no difference could be detected in the transient absorption signal within 2 h.



**SI Figure 1 - Cell lifetime under laser illumination:** Difference between the ultrafast TA spectra from wild-type *Synechocystis* cells after a 15 minute measurement and after being exposed to the laser continuously for 2 h. No difference was observed, indicating that cells remained photoactive without appreciable changes in TA spectra. Difference map is of one biological sample, representative of multiple replicates ( $n = 3$ ).

### 1.1.2 Agreement between biological replicates

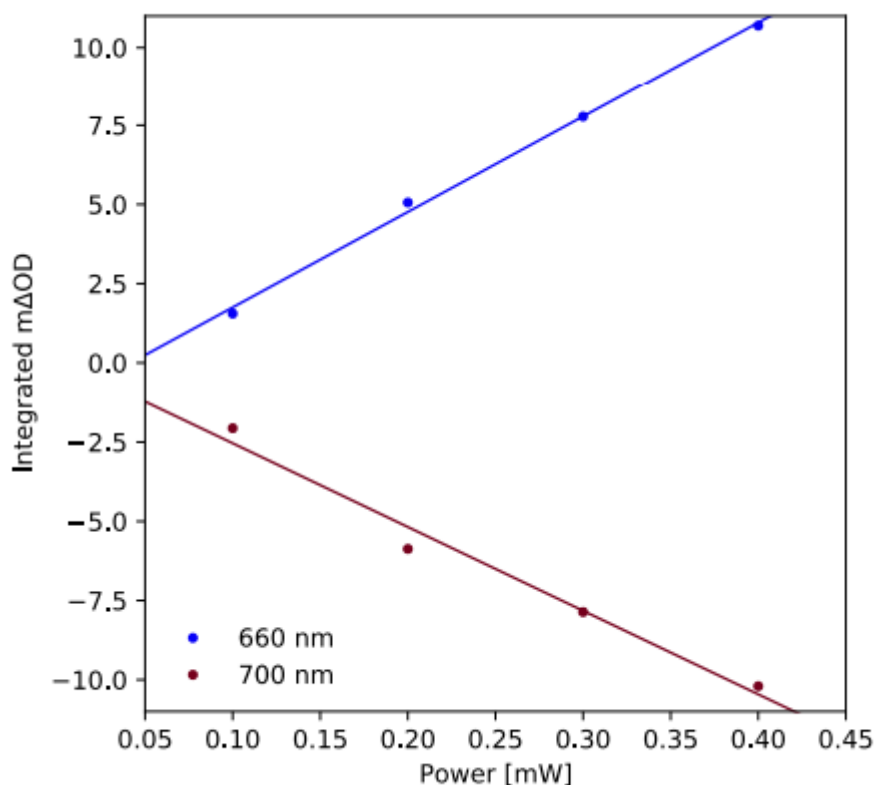
For all TA experiments, biological replicates were collected for each biological sample. The number of biological replicates for each biological sample is specified in **SI Tables 3-12**. The spectral features of different biological replicates were in good agreement (**SI Figure 2**). A fit was completed using the global analysis method described below in **SI Section 1.4**. This gave us the confidence to present TA spectra from one biological sample representative of multiple biological replicates (e.g. **Figure 1D-E**, **Figure 3B**), and further quantitative analysis used multiple biological replicates as specified (e.g. **Figure 2C-D**, **Figure 3C**).



**SI Figure 2 - Cell replicates.** **A)** The normalized averaged absorption signal between 720 nm and 730 nm, normalized at the peak of the rise at 8 ps, for six biological replicates of wild-type *Synechocystis* cells, with the date of the experiment over a period of 8 months. **B)** The averaged spectra between 690 nm and 700 nm normalized at 400 fs, avoiding the coherent artefact. Overlaid to the data points is the solid line fit based on the global fitting method. **C)** Lifetimes determined from the fit, revealing that the cells from different replicate cultures display remarkable consistency in the decay constant.

### 1.1.3 No damage or sub populations measured with increasing laser power

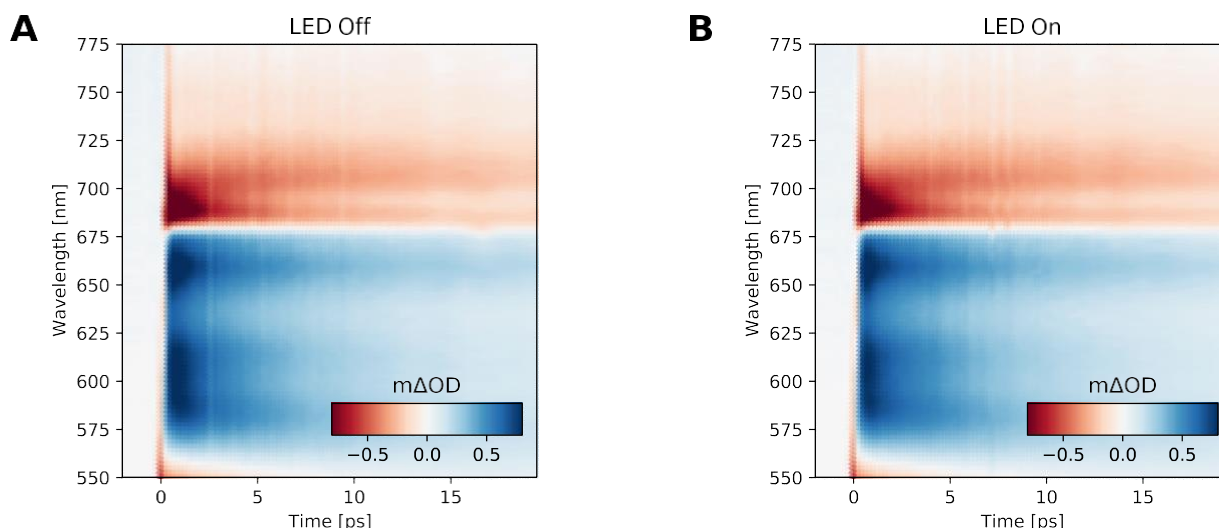
We investigated whether the transient absorbance signal exhibited linear or non-linear effects with respect to the laser (pump) power. Non-linear behaviour could indicate damage to the photosystems or some population dependent process. Spectra of wild-type *Synechocystis* cells were measured over different laser powers between 0.25 - 0.40 mW at 450 nm (laser beam diameter  $280 \times 240 \mu\text{m} = 6.27 \times 10^{-8} \text{ m}^2$ ,  $370 - 600 \text{ mW cm}^{-2}$ ,  $14000 - 22000 \mu\text{mol photons m}^{-2} \text{ s}^{-1}$ ). Spectra at 660 nm and 700 nm were extracted and integrated in time. As the power was varied from low energy to high energy, the dependence of the integrated transient absorption signal at 660 nm and 700 nm was shown to be linear, suggesting little degradation at these measurement powers and timescales (**SI Figure 3**).



**SI Figure 3 - Power dependence.** The integrated transient absorption signal against pump power at 450 nm. The brown line gives the integrated absorption at 700 nm, whereas the blue line gives the integrated absorption at 660 nm, which correlate to two wavelengths of opposing signal sign. In both the high energy and low energy datasets, the power dependence is linear against integrated mΔOD. This suggests a linear relationship between photon and RC interaction at time ranges >200 ps. All measurements reported elsewhere throughout this paper were made at 0.25 mW.

#### 1.1.4 Determination that reactions centres are in a closed state during TA Spectroscopy

Reaction centres can be considered in an open or closed state. For instance, in PSII an open reaction centre has the primary quinone QA oxidized and ready to undergo stable charge separation, whereas a closed reaction centre has QA reduced to QA<sup>-</sup> and charge separation will be followed by fast charge recombination.<sup>1</sup> To characterize whether the reaction centres were in an open or closed state under the TA set-up, the spectra of wild-type *Synechocystis* cells were measured with and without constant illumination with a backlight intended to close the reaction centres. The spectra without and with the backlight were compared and found to be no different beyond measurement uncertainty (**SI Figure 4**). This indicated that the reaction centres were in a closed state during our measurements.



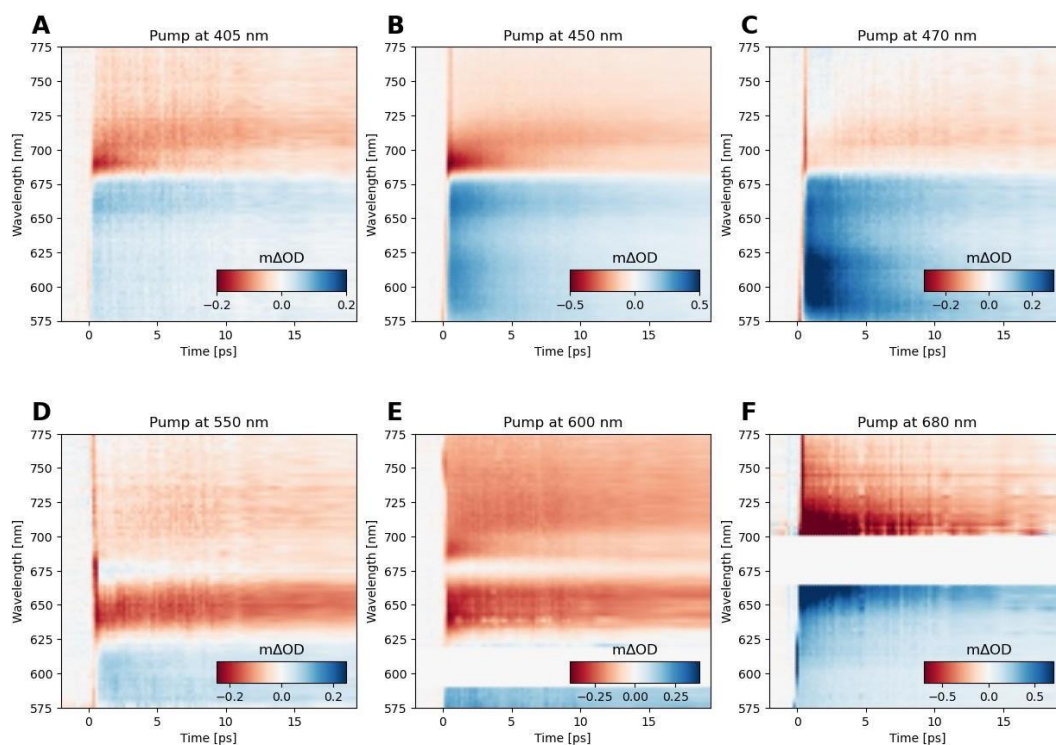
**SI Figure 4 – Reaction centres within wild-type *Synechocystis* cells are closed during TA measurements.**

Ultrafast transient absorbance measurements were performed as previously reported.<sup>2</sup> The pump pulse was set to 450 nm. The sample solutions were placed in 1 mm path length cuvettes (Hellma). The pump and probe beams were focused to a size of  $280 \times 240 \mu\text{m}$  and  $55 \times 67 \mu\text{m}$ , respectively **A**) with no continuous illumination, and **B**) with a  $1500 \mu\text{mol photons m}^{-2} \text{s}^{-1}$  white (520 - 900 nm) light LED pointing towards the sample and 10 cm from the laser overlap point during measurements. Maps are of one biological sample, representative of multiple replicates ( $n = 3$ ).

### 1.1.5 Wavelength dependence

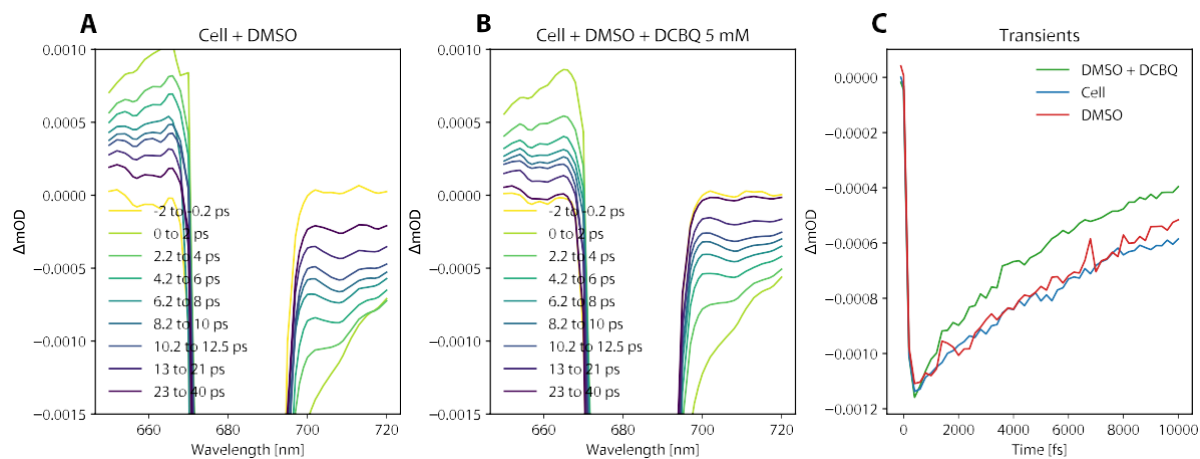
To investigate the behaviour of the spectral features, the wavelength of the pump pulse was varied. The first spectral feature of note centred around 680 nm that formed within 200 fs of photoexcitation, which we assigned to a highly delocalized intermediate charge-transfer (CT) state. This feature was present in the spectra measured from photoexcitation of wild-type *Synechocystis* cells with a 200-fs pump pulse centred at 405 nm, 450 nm and 470 nm (**SI Figure 5A-C**). The feature centred around 680 nm was not as readily observed in the spectra measured with a pump pulse centred at 550 nm, which corresponds to the lack of absorption features in the steady state absorption spectra at 550 nm (**SI Figure 5D**) and was obscured with the pump pulse centred at 600 nm and 680, over which a white overlay has been applied (**SI Figure 5E-F**). Another spectral feature, centred around 715 nm, grows in within  $\sim 2$  ps after photoexcitation and subsequently decays on a longer ps timescale, which we assigned to rapid excited state relaxation processes within the reaction centres. This feature was present in the spectra measured with a pump pulse centred at 405 nm, 450 nm, 470 nm, 550 nm and 680 nm (**SI Figure 5A-D & F**). For all other measurements, a pump pulse centred at 450 nm was chosen, because of its high absorbance by the sample, and clarity in the 525-725 nm region. With the 680 nm pump we also added 5 mM DCBQ to the cell sample (**SI Figure 6C**), to evidence that DCBQ mediated electron transfer need not invoke higher excited states beyond band edge excitation.

## Chapter 5



**SI Figure 5 - Wavelength dependence in transient absorbance experiments.**

Ultrafast transient absorption spectra of wild-type *Synechocystis* cells with different wavelengths of the pump pulse. One sample is shown for each pump pulse wavelength, representative of three biological replicates measured.



**SI Figure 6 - TA spectra and DCBQ mediated accelerated decay dynamics at 680 nm pump experiments. A** Spectra from cells and DMSO (5%) excited at 680 nm. **B** Spectra from cells, DCBQ (5 mM) in DMSO (5%) excited at 680 nm. The suppressed rise at 710 nm is visible. **C** Cell (in blue), plus DMSO (in red) and DMSO and DCBQ (in green) transients, averaged between 708 and 715 nm, plotted as a function of time, highlighting the DCBQ induced accelerated decay.



## 1.2 Introducing the different biological samples and their TA spectra

To help assign the transient spectral features of wild-type *Synechocystis* cells to the different components in the PETC, different biological samples were tested: isolated PSII dimers,<sup>3</sup> isolated PSI monomers,<sup>4</sup> mutant *Synechocystis* cells lacking intact PSI complexes but with intact PSII complexes (PSI-less cells),<sup>5</sup> mutant *Synechocystis* cells lacking intact PSII complexes but with intact PSI complexes (PSII-less cells),<sup>6</sup> and the Olive mutant which has no phycocyanin (PC) discs but still has the allophycocyanin (APC) core of the phycobilisome (PBS).<sup>7</sup> Each biological sample was loaded into the cuvette at a final concentration of 5 nmolChl ml<sup>-1</sup>, and excited with a 200 fs pump pulse centred at 450 nm.

The spectra of PSII-less cells (**SI Figure 7 B**) appeared closer to that of wild-type cells (**Figure 1D**, **SI Figure 7A**), with the familiar low-energy spectral feature >690 nm and a zero-signal crossing at 682 nm at 400 fs. The spectra of isolated PSI (**SI Figure 7E**) was consistent with previous studies and contained the low-energy spectral feature >690 nm.<sup>8</sup>

In contrast, the spectra of PSI-less cells (**SI Figure 7C**) showed a wealth of spectral features that were markedly different from wild-type cells and similar to the spectra of isolated PSII (**SI Figure 7F**). The transient absorption spectra of isolated PSII were consistent with previous studies.<sup>8</sup> Notably, in the spectra of PSI-less cells and isolated PSII there was a very long-lived positive signal (i.e. less absorption) at its absorption maximum at 680 nm that lasted longer than a nanosecond.

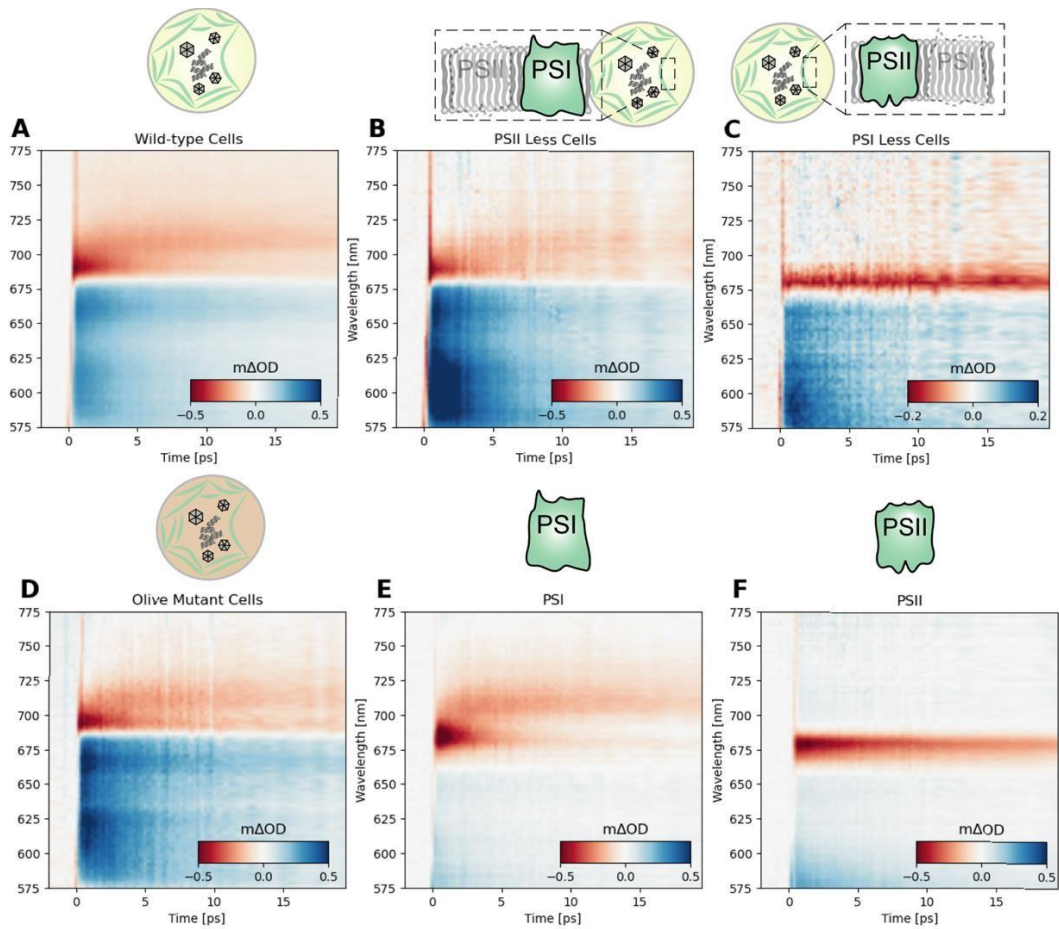
TA spectrum of Olive mutant cells was similar to wild-type cells, indicating that the PC discs in the PBS were not responsible for the features in the visible range when illuminated at 450 nm (**SI Figure 7D**). A mutant with the entire PBS removed including the APC core could be investigated in future studies to further probe the nature of the AC core on the high energy (< 650 nm) bleach signal. Part of the bleach at < 650 nm may be attributed to non-photosystem photoactive components of cells, such as complete PBS containing the AC core and carotenoids. Therefore, in our analysis of the photodynamics of the photosystems, we focus on the lower energy features around 685 and 715 nm, which assign to different components in the PETC and are supported by isolated reaction centre studies (**SI Figure 7E-F**).

From the results of all these different biological samples, the transient spectral features of wild-type *Synechocystis* cells could be assigned to the different components in the PETC. The feature centred around 715 nm was present only in the spectra of wild-type and PSII-less cells, hence we conclude that PSI action is responsible for this feature, which we show is readily quenched by the action of DCBQ. Long-lived features were present in the spectra of isolated PSII and the PSI-less cells, so were assigned to PSII action. We note that the 685 feature is a combination of PSI and PSII signals in the cells and any system with both PSI and PSII, rendering unambiguous assignment difficult

The wild-type cells' initial transient spectral features were dominated by signatures from PSI, as might be expected based on a PSI trimer having approximately 4-fold higher chlorophyll count compared to a PSII dimer and an assumption that there existed an equal number of PSII dimers to PSI trimers per complete PETC in wild-type cells.<sup>9</sup> Similarly, the PSI-less cells had a lower signal intensity and signal to noise ratio with lower chlorophyll content for similar cell size (scattering), making it a challenging

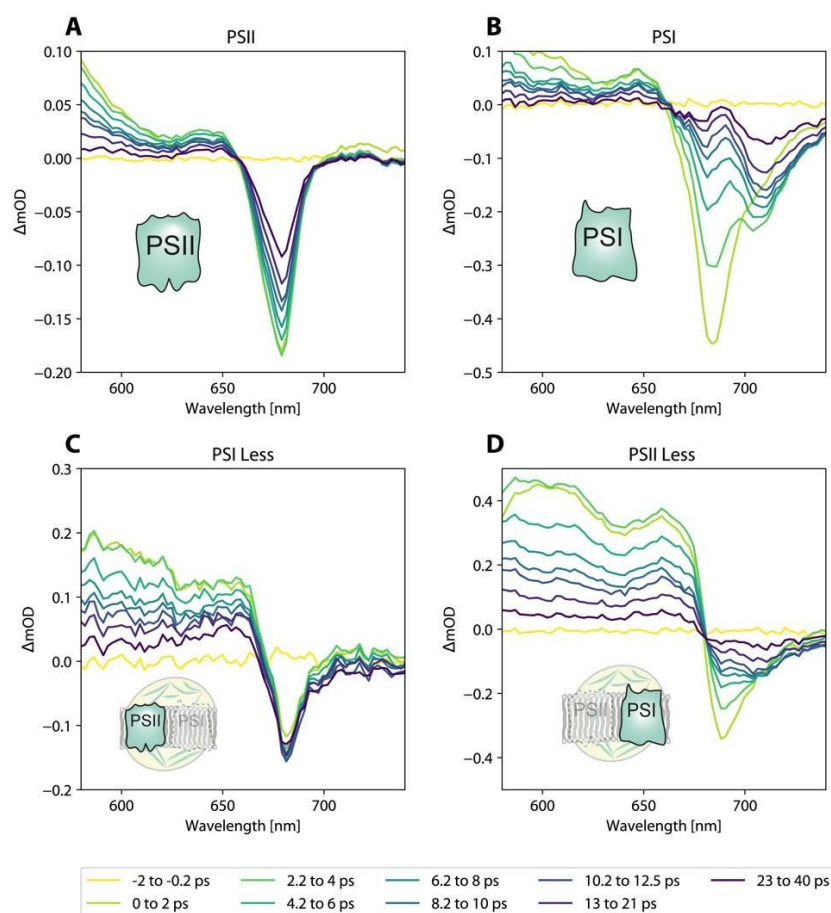


sample for absorbance spectroscopy.



**SI Figure 7 - TA comparison between biological samples**

Ultrafast transient absorption spectra of different biological samples. **A)** *Synechocystis* cells wild-type, **B)** photosystem I (PSI)-less mutant cells with only photosystem II (PSII), **C)** PSII-less mutant cells with only PSI; **D)** Olive mutant cells with no phycocyanin (PC) discs but still with the allophycocyanin (APC) core of the phycobilisomes (PBS) and **E)** Isolated PSI, and **F)** Isolated PSII. All biological samples were excited at 450 nm. One biological replicate shown for each sample, representative of three to six biological replicates measured.



**SI Figure 8 - TA spectral comparison between biological samples**

Ultrafast transient absorption spectra at selected times of different biological samples. **A)** Isolated PSI, and **B)** Isolated PSII **C)** photosystem I (PSI)-less mutant cells with only photosystem II (PSII), **D)** PSII-less mutant cells with only PSI. All biological samples were excited at 450 nm. One biological replicate shown for each sample, representative of three to six biological replicates measured. Cell spectra with and without the presence of DMSO and DCBQ is given **SI Figure 13** – TA of wild-type *Synechocystis* cells in the presence of DCBQ and DMSO.

### 1.3 PSI in previous studies

Although the spectral dynamics of isolated PSI in previous studies resemble our isolated PSI measurement, some differences remain in terms of the clarity and exact energy of the observed features. This would be expected given that PSI protein super complexes differ in different photosynthetic organisms (summarized in next paragraph) in terms of their light harvesting components, types of chlorophylls and absorption of different chlorophyll *a* pigments. Further, studies on isolated systems also involve different purification processes e.g. in membrane or particles, trimer or monomer, whole super complex or core. For these reasons we compare our whole cell wild-type and mutant spectra to our isolated PS spectra (all cyanobacterial systems, and all with the photosystems in their final complex form e.g. we use an isolated PSII dimer, PSI trimers).

In plants and algae, PSI is in a super complex of a core and a light-harvesting component (PSI-LHCI). In cyanobacteria, the phycobilisomes (PBS) are mainly an antennae for PSII but also for PSI during state transitions. Plant and algal PSI and associated light harvesting complexes also contain chlorophyll *b*, whereas cyanobacteria only contain chlorophyll *a*. There are other cyanobacterial species that contain far red chlorophylls in their PSII like chlorophyll *d* and *f*,<sup>10</sup> but not in *Synechocystis*. Within the chlorophyll *a* pigments, there are “red forms”, which absorb at lower energy than the reaction centre chlorophylls at wavelengths longer than 700 nm (more background and reviewed by Karapetyan et al., 2006<sup>11</sup>). Red chlorophylls differ in number, position and absorption in PSI in different photosynthetic organisms. The number of red chlorophylls is very species dependent. 5-10% of the chlorophylls are far red in different cyanobacteria.<sup>12</sup> The red chlorophylls in plants are largely located in the peripheral LHCI complexes away from the P700.<sup>13</sup> However, in cyanobacteria these red chlorophylls are located in the core of PSI. In cyanobacteria, the most red forms are created in the edges of the monomers coming together in the PSI trimer.<sup>14</sup> In plants, the red chlorophylls absorb in the 710–730 nm window.<sup>15</sup> In cyanobacteria, the red chlorophylls are more diverse and absorb in the 705-740 nm region. In *Synechocystis* PSI (our whole cell species), the red Chls absorb in the 707-715 nm window.<sup>16</sup> In *Thermo elongatus* PSI trimers (our isolated PS species), the red Chls absorb in 708 and 719 nm.<sup>14</sup> *Spirulina platensis* has the most red shifted chlorophyll known with an absorption centred at 740 nm.<sup>16</sup>

## Chapter 5

Table 1 PSI and PSII literature comparison Description of biological sample	Cyanobacteria or Algae/Plant	TA Pump Wavelength	Reference
Partial (subunits A–E, K, and M) monomeric PSI complex from <i>Synechocystis</i> sp. PCC 6803	Cyanobacteria	680 nm	Akhtar et al., 2021 <sup>17</sup>
Trimeric PSI complexes from <i>Synechocystis</i> sp. PCC 6803	Cyanobacteria	720 nm	Shelaev et al., 2010 <sup>18</sup>
PSI trimers from <i>Synechocystis</i> sp. PCC 6803	Cyanobacteria	720 – 760 nm	Cherepanov et al., 2017 <sup>19</sup>
PSI in intact membranes, PSI in detergent-isolated particles from PSII-less <i>Synechocystis</i> sp. PCC 6803	Cyanobacteria	590 nm	Hastings et al., 1995 <sup>20</sup>
PSI complexes isolated from <i>Synechococcus</i> sp. PCC 7002 and <i>Synechocystis</i> sp. PCC 6803	Cyanobacteria	700 nm	Lee et al., 2018 <sup>21</sup>
Trimeric PSI of <i>Thermosynechococcus elongatus</i>	Cyanobacteria	675 nm	Anna et al., 2012 <sup>22</sup>
PSI core of <i>Spirulina platensis</i>	Cyanobacteria	680 nm	Russo et al., 2022 <sup>16</sup>
core PSI particles of <i>Chlamydomonas reinhardtii</i>	Algae/Plant	670 & 700 nm	Muller et al., 2003 <sup>23</sup>
detergent-isolated PSI core particles from <i>Chlamydomonas reinhardtii</i> (wild-type and with HN(B656) mutation in PSI)	Algae/Plant	590 nm	Melkozernov et al., 1997 <sup>24</sup>
isolated PSI-Light-Harvesting Complex I (PSI-LHCI) super complex and in the isolated PSI core complex of <i>Spinacia oleracea</i>	Algae/Plant	480 – 650 nm	Russo et al. 2020 <sup>25</sup>
PSI-LHCI super complex isolated from <i>Spinacia oleracea</i>	Algae/Plant	490 & 620 nm	Molotokaite et al., 2017 <sup>15</sup>
isolated core and intact PSI particles and stroma membranes from <i>Arabidopsis thaliana</i>	Algae/Plant	663 nm	Slavov et al., 2008 <sup>26</sup>
PSI-LHCI and PSI-LHCI-LHCII super complexes isolated from <i>Arabidopsis thaliana</i>	Algae/Plant	N/A (TCSPC)	Santabarbara et al., 2017 <sup>27</sup>
Proteoliposomes with native plant thylakoid membrane lipids and different stoichiometric ratios of LHCII:PSI(LHCI) from <i>Pisum sativum</i>	Algae/Plant	N/A (TCSPC)	Akhtar et al., 2016 <sup>28</sup>

## 1.4 Global analysis of TA spectra

### 1.4.1 Background to global fitting

A transient absorption dataset can be thought of as a matrix with each point assigned a spectral value and a time value<sup>29</sup>. This time value is the delay of the probe pulse relative to the pump pulse. This may be negative if the probe pulse arrives before pump. The spectral value is the magnitude of the signal at some wavelength resolution. In some circumstances, it is permissible to assume that the wavelength components decay with some rate, i.e. their magnitude of the spectra changes in time. This is to say that the data is separable into wavelength spectra with a corresponding time dependent decay.

The data can also be made simpler, or more properly defined as “reducing the dimensions of the data”. Instead of dealing with every timepoint and every wavelength datapoint, we attempt to simplify the data into fewer dimensions. Dimensionality reduction is a treatment common in many forms of data analysis, for instance in image compression. A common way of doing so is singular value decomposition (SVD), which is a method of drawing out the major components of the data. We retain the components of the data which describe the vast majority of the data. We now more rigorously define our data treatment below.

Global analyses are well established techniques to identify components of transient spectral data.<sup>29</sup> We provide a brief overview of the techniques utilized here. Supposing the spectral components behave independently, and the response of the detector is linear with intensity, Beer's law states that the noise-free, time-resolved absorption spectrum is a superposition of component's absorption spectrum weighted by their concentration. Thus, the absorption spectrum,  $\psi(t, \lambda)$  can be written as a superposition of the contributions of the  $n$  different bases:

$$\psi(t, \lambda) = \sum_{l=1}^n c_l(t) \varepsilon_l(\lambda)$$

**Equation 1**

where  $c_l(t)$  and  $\varepsilon_l(\lambda)$  denote, respectively, the concentration and spectrum of a component. Practically, our transient data is recorded as a regular array  $w \times t$  matrix,  $[D]$ , where  $w$  is the number of wavelengths in each spectrum and  $t$  is the number of time delays at which spectra are obtained. Beer's law can then be simply expressed in matrix form as by the product of two matrices:

$$[D] = [A][C]$$

**Equation 2**

where  $[A]$  is a  $w \times n$  matrix containing the spectra of the  $n$  individual components in its columns, while  $[C]$  is an  $n \times t$  matrix containing the time behaviour of the excited-state concentrations of the components in its rows. Using singular value decomposition (SVD) it is possible to reduce the dimensionality of the problem as well as fitting to a noise-reduced subset of matrix  $D$ . If  $D$  is an  $m \times n$  real matrix with  $m > n$ , then  $D$  can be written in the form:

$$D = USV^T$$

**Equation 3**

We follow the notation used by the Mathematica language, where  $U$  has dimensions of  $m \times m$ ,  $S$  has  $m \times n$ , and  $V$  has  $n \times n$ . In both systems,  $U$  and  $V$  are unitary, so that  $U^T U = I$  and  $V^T V = I$  (where

the two identity matrices may have different dimensions).  $S$  has entries only along the diagonal, known as singular values. The weighted left singular vectors (wLSV) are given by  $US$ . Assuming separability, as in Equation 2, decomposing the transient data in this way has a physical interpretation:  $U$  is the unitary matrix of left singular vectors giving the temporal dependence of the signal,  $V^T$  is the unitary matrix giving the spectral dependence of the signal. However, the spectra themselves cannot be directly assigned to a specific photoactive component.

Retaining the number of wLSVs whose corresponding singular values are significantly larger than the rest is a good approximation for a sufficient number of bases to retain.<sup>30</sup> The number of bases chosen gives only an estimate of the number of orthogonal components appropriate to represent the data. The choice in basis makes no estimation of any underlying reaction scheme. In global analysis, we conduct a simultaneous analysis of multiple kinetic traces at different wavelengths to model our dataset, or a noise-reduced subset of the dataset described by the basis choice from SVD. The reduced data facilitates the interpretation of observed dynamics by reducing the dimensionality of the problem. In this type of analysis we have no *a priori* knowledge for a detailed kinetic model, so we target a minimally descriptive model lessening the risk of identification problems due to over parameterization. However, in this case, the results from our analysis likely leads to an oversimplification of the data as we resolve the minimum number of physical processes required to describe the dataset. We assume a model of the sum of weighted exponentials:

$$\psi(t, \lambda) = \sum_i A_i(\lambda) e^{-t/c_i}$$

Equation 4

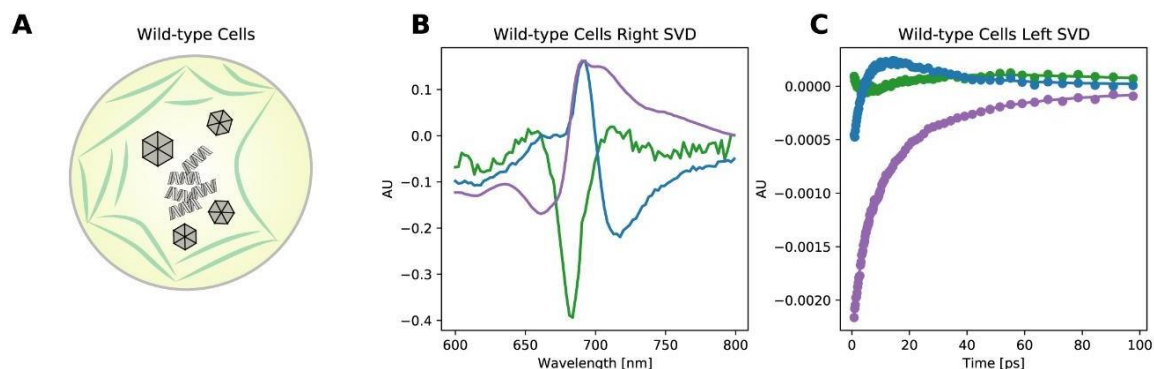
where  $i$  corresponds to the size of the basis expansion used to describe the data,  $A_i(\lambda)$  denotes the coefficient related to each wavelength and  $r_i$  is the lifetime associated with each exponential decay.

### 1.4.2 Singular value decomposition of different biological samples

To analyze the features of the transient absorbance spectra of the photosystems *in vitro* and *in vivo*, the spectra of the different biological samples with varying photosystems (described in **SI Section 1.2**, not including the Olive mutant) were deconvoluted by Singular Value Decomposition (SVD) as described above in **SI Section 1.4.2**. The transient data were decomposed into two vector sets: vectors giving the spectral dependence of the dataset and vectors giving the temporal dependence of the dataset. The number of wLSVs whose corresponding singular values were significantly larger than the rest was retained for each: three vectors were retained for wild-type cells (**SI Figure 9**) and PSII-less cells (**SI Figure 10A-C**), and two vectors were retained for isolated PSI (**SI Figure 10D-F**), isolated PSII (**SI Figure 11D-F**) and PSI-less mutant cells (**SI Figure 11A-C**). Although these choices of vectors in the SVD decomposition do not estimate the underlying reaction scheme or necessarily correspond to individual photoactive machineries, they give a lower bound to the number of observed physical processes. Corresponding components, similar both in the spectral and temporal decomposition, were observed in the SVD of the PS-less cells and the isolated photosystems. Comparing isolated PSI and PSII-less cells (**SI Figure 10**), and distinctly, isolated PSII and PSI-less cells (**SI Figure 11**) the component spectra (Left SVD – panels **B & E** in **SI Figure 10 & 9**) and component concentrations (Right SVD – panels **C & F** in **SI Figure 10 & 9**) have similar features in



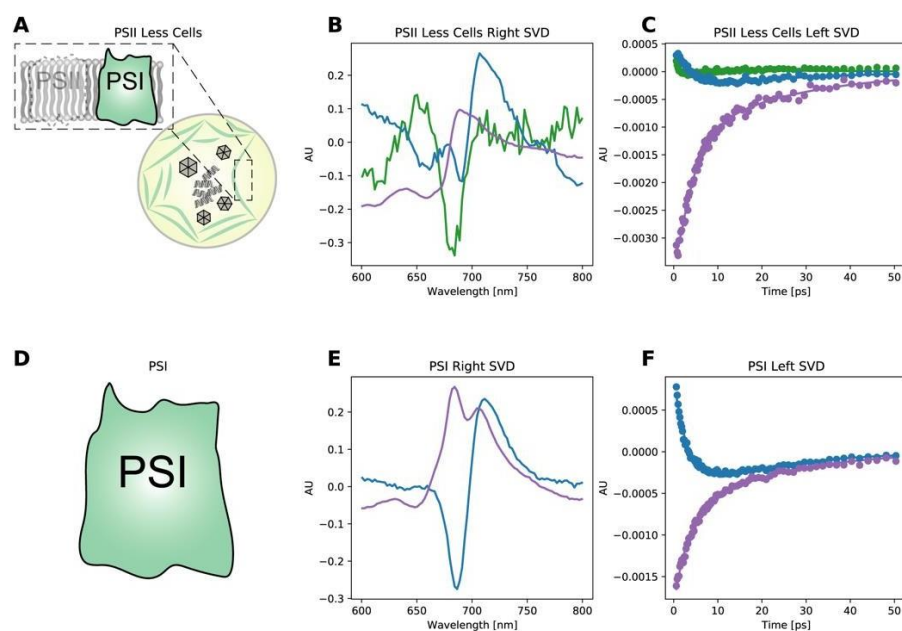
the region of interest (650 – 750nm) as well similar component decays in each case. This further reaffirms our supposition that in the cell systems we directly resolve the reaction centres *in vivo*. To evidence the validity of the basis in the SVD decomposition, the vectors described in **SI Figure 9**, **SI Figure 10** and **SI Figure 11** were combined to reform spectra and compared to the original data (**SI Figure 12**).



**SI Figure 9 – Singular value decomposition (SVD) of the wild-type *Synechocystis* cells.**

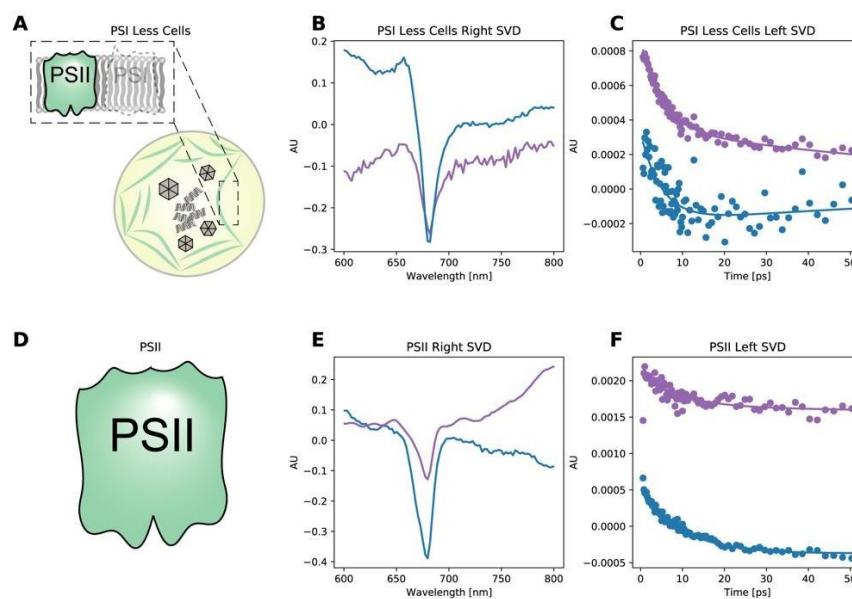
A) Cartoon of wild-type cells. B) Spectral dependence of the wild-type cells' TA data from SVD. SVD is an established method to decompose TA data, assuming the data is separable into spectral and wavelength components.<sup>31</sup> C) Corresponding temporal decay for spectral components from panel B. The SVD decomposition is given by solid round markers, and the global fit is the solid line in the corresponding color. We roughly assign the green components to the bleach from PSII, whereas the blue and purple components are more difficult to allocate directly to a single reaction centre, however, they both include components from PSI. Data from one sample presented, which was representative of three biological replicates.





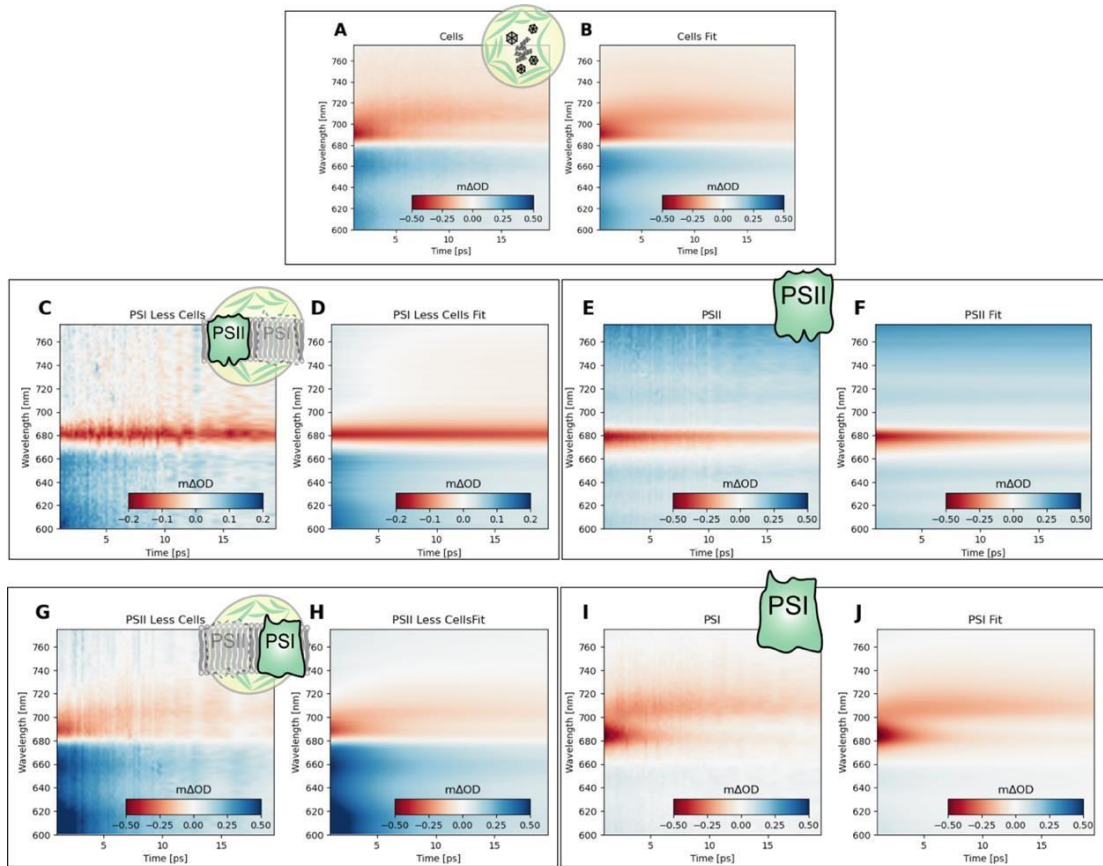
**SI Figure 10 - Singular value decomposition (SVD) of mutant PSII-less cells and isolated PSI.**

**A)** Cartoon of PSI-less cells. **B)** Spectral dependence of the PSI-less cells' TA data from SVD where 3 components were retained. SVD is an established method to decompose TA data, assuming the data is separable into spectral and wavelength components<sup>31</sup>. **C)** Corresponding temporal decay for spectral components from panel B. The SVD decomposition is given by solid round markers, and the global fit is the solid line in the corresponding color. **D)** Cartoon of isolated PSI. **E)** Spectral dependence of the isolated PSI TA data from SVD where 2 components were retained. **F)** Corresponding temporal decay for spectral components from panel E. The SVD decomposition is given by solid round markers, and the global fit is the solid line in the corresponding color. Data from one sample presented, which was representative of three biological replicates.



**SI Figure 11 - Singular value decomposition (SVD) of mutant PSI-less cells and isolated PSII**

**A)** Cartoon of PSII-less cells. **B)** Spectral dependence of the PSII-less cells' TA data from SVD with two components retained. SVD is an established method to decompose TA data, assuming the data is separable into spectral and wavelength components.<sup>31</sup> **C)** Corresponding temporal decay for spectral components from panel B. The SVD decomposition is given by solid round markers, and the global fit is the solid line in the corresponding color. **D)** Cartoon of isolated PSII. **E)** Spectral dependence of the isolated PSII TA data from SVD with two components retained. **F)** Corresponding temporal decay for spectral components from panel E. The SVD decomposition is given by solid round markers, and the global fit is the solid line in the corresponding color. Data from one sample presented, which was representative of three biological replicates.

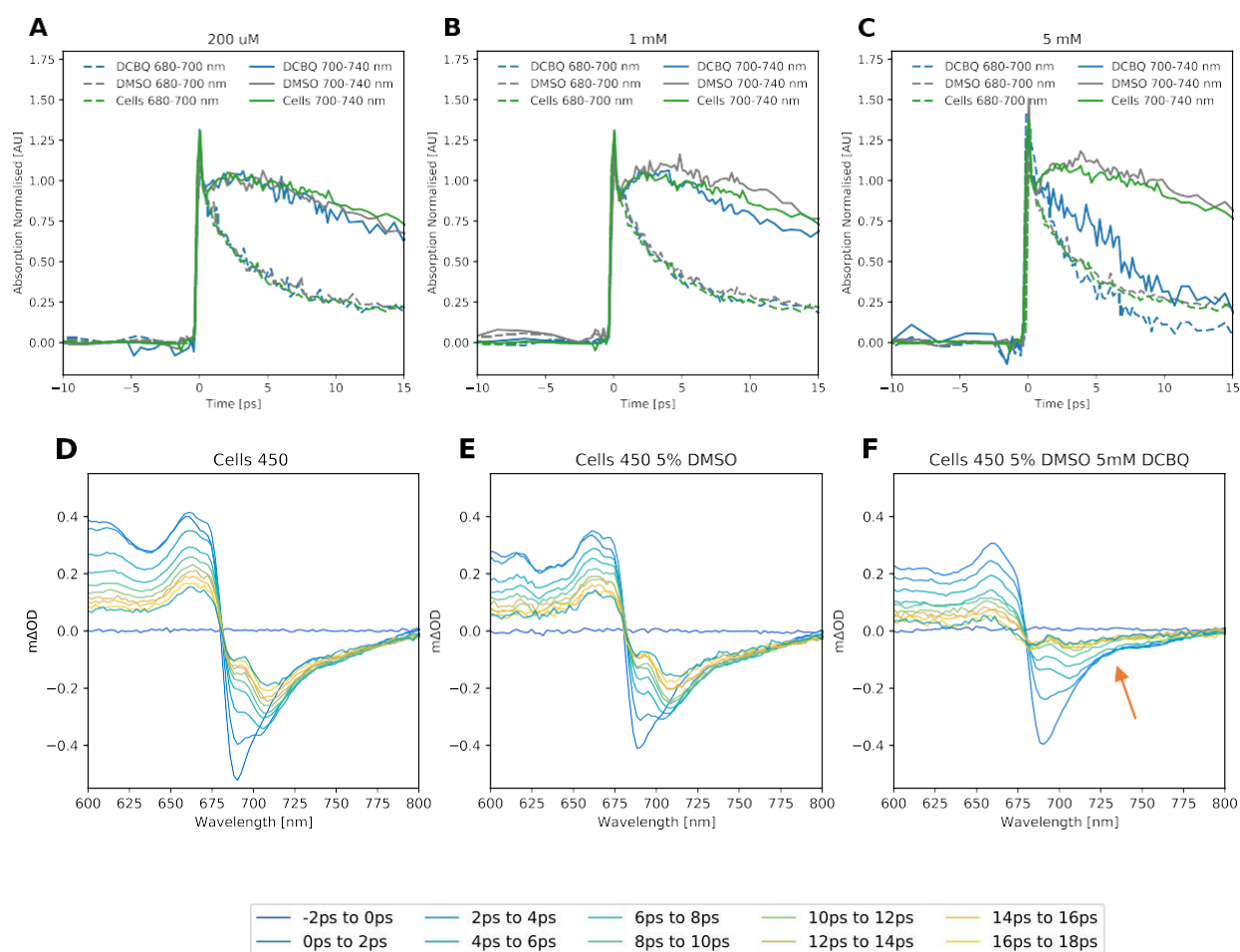


**SI Figure 12 - Singular value decomposition summary.**

Ultrafast TA spectra of different biological samples with varying photosystems: **A & B)** Wild-type cells, **C & D)** PSI-less cells, **E & F)** Isolated PSII, **G & H)** PSII-less cells and **I & J)** Isolated PSI. For each pairing, the spectra from TA measurements is given on the left, and the spectra reconstructed from the retained SVD components in SI Figure 9, SI Figure 10 and SI Figure 11 is given on the right. Data from one sample presented, which was representative of three biological replicates.

## 1.5 Addition of DCBQ to wild-type cells

### 1.5.1 TA spectral features of wild-type cells with DCBQ added



**SI Figure 13 – TA of wild-type *Synechocystis* cells in the presence of DCBQ and DMSO**

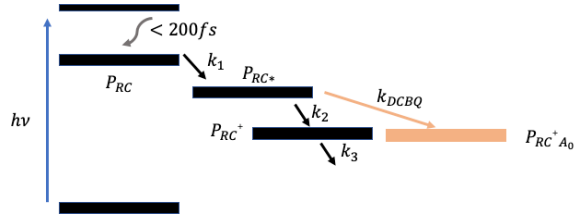
Wild-type cells (in green) have had an increasing volume of DMSO (in grey) and concentration of DCBQ + DMSO (blue) added, **A**) has 200 uM DCBQ added, which corresponds to 0.2% DMSO, **B**) has 1 mM DCBQ added, which corresponds to 1% DMSO, **C**) has 5 mM DCBQ added which corresponds to 5% DMSO. DMSO is the solvent by which DCBQ is solubilized, and so the effect of the DMSO can be determined. The effect of DMSO is small, even at high concentrations. Upon the addition of DCBQ, there is a dramatic decay in the 700 nm to 740 nm curve, which corresponds to the 715 nm feature in **D**, **E** and **F** and missing, as highlighted by the red arrow in **F**.

### 1.5.2 Model of DCBQ reduction by the reaction centre

Modelling the photosynthetic electron transport chain has been a subject of significant study.<sup>29,32</sup> For example, Müller *et al.* use nine distinct kinetic rates to describe the early electron transfer steps in isolated PSI.<sup>33</sup> Further, as experiments reported here were carried out at room temperature, the characteristic absorption spectra within the PETC broaden, which complicates the association of spectral features to specific elements in the PETC. In this study we cannot easily deconvolute these pathways, hence the use of the phenomenological model guided by the SVD component analysis in the preceding sections (**SI Section 1.4**). However, the global fitting method reported in **SI Section 1.4**

is unable to describe branched models.

Based on our assessment described in the main text of the mechanism of DCBQ reduction by the highly delocalized CT state formed after the initial photoexcitation, we constructed a simple branched kinetic model (SI Figure 12), and use 3 distinct sequential states, which broadly correspond to the photoexcited reaction centres and electron acceptors (A0 is the primary electron acceptor chlorophyll in PSI, pheophytin is the primary electron acceptor in PSII).



**SI Figure 14 – Branched kinetic model of DCBQ reduction by the highly delocalized CT state formed after initial photoexcitation.**  $P_{RC}$  is the initially excited reaction centre (P680 in PSII or P700 in PSI),  $P_{RC}^*$  is a sequential state of the photoexcited reaction centre,  $P_{RC}^+DCBQ^-$  is created upon reduction of DCBQ and  $P_{RC}^+$  is the natural decay pathway.  $k_1$  (2 ps),  $k_2$  (4.5 ps) and  $k_3$  (20.8 ps) (see SI Figure 2 - Cell replicates.) are the rate coefficients for the wild type cells.

Our branched kinetic model is defined by Equations 5 through 7,

$$\frac{dP_{RC}}{dt} = -k_1P_{RC}$$

Equat

$$\frac{dP_{RC}^*}{dt} = k_1P_{RC} - k_2P_{RC}^* - k_{DCBQ}P_{RC}^*$$

Equat

$$\frac{dP_{RC^+A_0^-}}{dt} = k_2P_{RC}^* - k_3P_{RC^+A_0^-}$$

Equat

where  $P_{RC}$  is the photoexcited reaction centre (P680 in PSII or P700 in PSI),  $P_{RC}^*$  is a later photoexcited reaction centre (100% conversion efficiency from  $P_{RC}$ ),  $P_{RC}^+$  is the final charge separate state and  $t$  is time. Attempts to globally fit the data with fewer rates did not yield satisfactory results.

### 1.5.3 Electron extraction efficiency as a function of DCBQ concentration

We utilize a compartmental model<sup>29</sup> to apply the proposed scheme in SI Section 1.5.2 to the measured TA spectra. We carry out the analysis on a wild-type cell sample without DCBQ, where  $k_{DCBQ} = k_{ET}\eta_{DCBQ} = 0$ . Here,  $k_{ET}$  is the electron transfer rate, and  $\eta_{DCBQ}$  the concentration of DCBQ. We then measured a TA concentration series by the incremental addition of DCBQ to aliquots of wild-type cells from the same cell culture. These measurements were performed under

identical conditions immediately after one another. We fix  $k_1$ ,  $k_2$  and  $k_3$  from the wild-type cells without DCBQ, and then determine  $k_{DCBQ}$  as a function of DCBQ concentration from the samples with the addition of DCBQ.

Given our model, we can estimate the proportion of the CT states which decay through the DCBQ pathway through the quantum yield of DCBQ mediated electron transfer:

$$\phi_{ET} = \frac{k_{ET} \eta_{DCBQ}}{k_2 + k_{ET} \eta_{DCBQ}},$$

Equation 8

Based on our knowledge of  $k_{ET} \eta_{DCBQ}$  and the individually obtained rate constants for the cell ( $k_2$ ), we can then determine the extraction for each specific concentration,  $\phi_{1mM} = 17\%$ ,  $\phi_{2mM} = 20\%$ ,  $\phi_{4mM} = 25\%$ ,  $\phi_{5mM} = 27\%$ .

Equation 9

Uncertainty in the cell (without artificial quinone) lifetime is  $\tau_{SE} = \frac{s}{\sqrt{n}} = 0.657$  ps, where  $s$  is the standard deviation and  $n$  is the number of biological replicates, in this case 5. The standard error in  $k_{ET} = 2.4 \times 10^{-6} \text{mM}^{-1}$ . We assume no error in the concentration of DCBQ. This gives the associated error in extraction efficiency as:

$$\delta\phi_{1mM} = 17\% \sqrt{\left(\frac{2.4 \times 10^{-6}}{8.5 \times 10^{-6}}\right)^2 + 2 \left(\frac{0.657}{5.112}\right)^2} = \pm 5.7\%$$

Equation 10

### 1.5.4 DCBQ acts upon photosystems in living cells that are fully assembled and intact

DCBQ is reduced by the early CT state of fully assembled and intact photosystems where the P680 or P700 is embedded  $> 2$  nm from the periphery of the protein scaffold. We have observed DCBQ to act on the early CT state of the photosystems both *in vitro* and *in vivo*. The isolated photosystem preparations are of high purity and homogeneity as dimers of PSII and trimers of PSI because during preparation we control for this through chromatography.<sup>3,34,35</sup>

However, the photosystems in cells are assembled in intermediate stages, some of these so-called ‘assembly intermediates’ could expose the P680 and P700  $< 2$  nm from DCBQ and need to be considered.<sup>36</sup> We conclude that the TA would not be sensitive to assembly intermediates which have a different bleach to the intact photosystems. There is evidence from steady-state absorption measurements suggesting that Chl *a* pigments retain a differing bleach signal based on their protein scaffold environment.<sup>37</sup> However, in the worst case, assuming that both populations of photosystems (i.e. assembly intermediates and fully assembled photosystems) absorb identically, would suggest in wild-type cells that the TA signal is comprised of a mixture of assembly intermediates and fully assembled photosystems. For example, if the assembly intermediates were 10% of the total population, this would suggest approximately -0.04 mΔOD of the signal may be attributed to assembly intermediates.



However, the addition of DCBQ affects the dynamics we observe significantly. Supposing again, in a worst- case scenario, where DCBQ only quenches disconnected chlorophylls and assembly intermediates, this suggests that 90% of the transient signal must remain unchanged, whereas 10% of the initial signal would decay over the timescale we have identified. This is not observed in the data.

Reviewing **SI Figure 13** – TA of wild-type *Synechocystis* cells in the presence of DCBQ and DMSO, the 710 nm feature is suppressed much further than would be expected if it were coming from a subpopulation of intermediates. The relative ratio of the 685 nm peak and the 710 nm feature, which in **SI Figure 13** – TA of wild-type *Synechocystis* cells in the presence of DCBQ and DMSO **D** is close to 1:2, where it is 1:1 with DCBQ addition (see green trace). This is a significant change, and >30% in terms of the kinetic model, but in terms of signal intensities, it is greater than a 50% signal reduction of the 715 nm peak relative to the 685 nm peak. This cannot be explained with impurities or assembly intermediates.

Further, photosystems in cells were found not to degrade significantly during TA measurements (**SI Figure 1**, which might expose the internal cofactors, including P680 and P700, to DCBQ.

In any case, as the extraction efficiency for DCBQ is so great, specifically  $17 \pm 5\%$  at 1 mM DCBQ and as high as 27% for 5 mM DCBQ, even if DCBQ is reduced by subpopulations of photosystems in their assembly intermediate states, DCBQ must also be reduced by the main population of fully assembled photosystems

### 1.5.5 DCBQ quenching mechanism

If the DCBQ-photosystems interaction that results in the observed ps time scale quenching phenomena relies on energy transfer, spectral overlap between the donor and acceptor has to exist. These may be resolved from absorption and photoluminescence measurements. From our measurements it becomes apparent that DCBQ does not have required accessible states, in particular spectral overlap for energy transfer. We therefore discount energy transfer in the DCBQ case. We note that Dexter energy transfer also only proceeds if the spectral overlap is non-zero, as encoded through the spectral overlap integral.

If the interaction is based on electron transfer, while it must be short ranged, it does not require spectral overlap, and it would scale with concentration. Our experimental results are consistent with these requirements. The mid-point potential of DCBQ (+0.315 V vs SHE at pH 7) makes it suitable to extract electrons from PSI also ( $P700^*/P700^+ = -1.290$  V,  $F_B/F_B^- = -0.590$  V) and PSII ( $P680^*/P680^+ = -0.660$  V). Structural modelling (see below) suggests there exist sites where DCBQ may bind to peripheral chlorophyll pigments. Upon illumination and the formation of the delocalized charge, electron transfer from the peripheral chlorophyll to the mediator will be possible as understood from Marcus theory.

Among the other mechanisms, neither exciplex formation, collisional quenching or static quenching are sufficient to explain our results of an ultrafast accelerated decay in P680/P700. We have tabulated the various mechanisms Table 2



Table 2 Quenching mechanisms	Physical Description	Relevance to our System	References
<b>Dynamic Quenching</b>			
<b>FRET</b>	An RC, in its electronic excited state, may transfer energy to an acceptor through nonradiative dipole–dipole coupling.	No overlap between non-reduced DCBQ absorption and PL of RCs. No accessible states.	38, 39, 40
<b>Dexter</b>	Bilateral exchange of electrons.	No overlap between non-reduced DCBQ absorption and PL of RCs. No accessible states.	41
<b>Excimer Formation</b>	Short molecule formed from two species, which would not bond if in ground state.	Exciplex formation should be a shallow state, with broad features, which we donot observe.	42, 43
<b>Static Quenching</b>			
<b>Static Quenching</b>	Ground state complex formed before excitation.	1- Would result in no change in excitedstate lifetime, contrary to our results 2 – Cell and DCBQ absorption spectrumdo not change from cell spectrum.	44
<b>Other Mechanisms</b>			
<b>DCBQ Induced Vibrational Relaxation</b>	Changes in structure result in increased thermalization rate to the ground state.	Invokes the generation of new phonons mediated by DCBQ, unlikely given structure of RCs.	
<b>Diffusion</b>	Excited RC encounters atom that facilitates non-radiative decays	Too slow to act on fs timescale when understood through kinetic theory.	45
<b>Electron Transfer</b>	Electron moves from electron donor to electron acceptor.	Short range and requires suitable energetics and binding sites, which we have identified.	42, 46

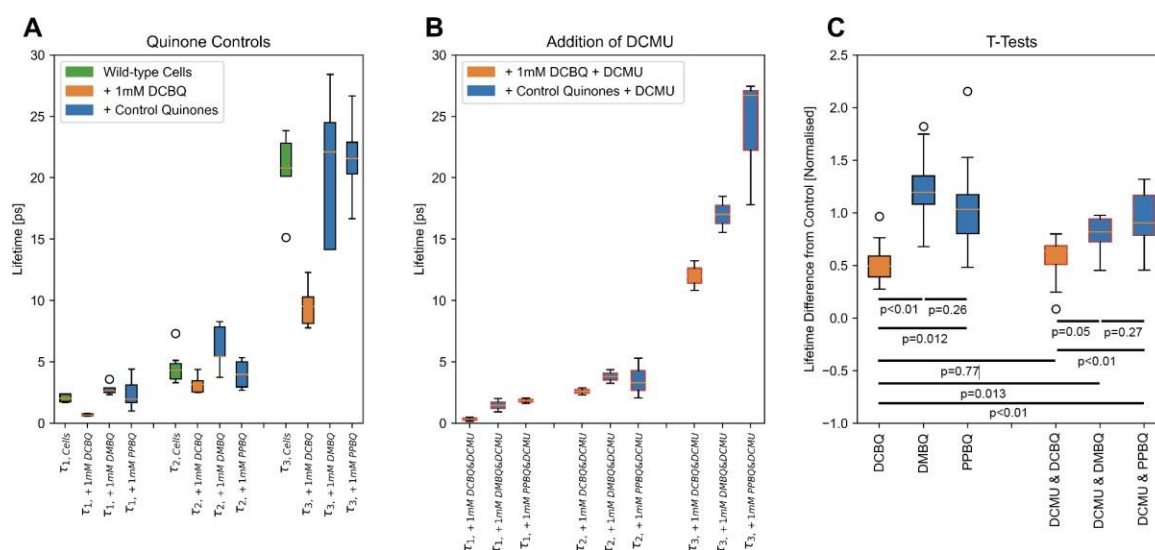
## 1.6 Addition of DCMU along with DCBQ (or other screened benzoquinones) to wild-type cells

To compare the effect of different benzoquinones we carried out TA experiments on wild-type *Synechocystis* cells, with and without different benzoquinones along with their associated solvents (DMSO, ethanol, SDS). DMBQ and PPBQ are benzoquinones that have been shown in previous studies to enhance photocurrent output from eukaryotic algae but not as efficiently as DCBQ,<sup>47–50</sup> which we confirmed in cyanobacteria (see **SI Section 4**). SDS is a detergent used to aid solubilization of DMBQ and PPBQ in ethanol as they are otherwise insoluble in aqueous BG11 medium.

Neither 1 mM DMBQ or 1 mM PPBQ, or equivalent control experiments with only solvent added, demonstrated quenching (**SI Figure 15A** - compare  $r_1$ ,  $r_2$ ,  $r_3$  lifetimes of cells in green with cells + control quinones in blue). As already demonstrated in **Figure 1D-E**, DCBQ addition demonstrated a decrease in lifetimes compared to that of cells with no additives (**SI Figure 15A** - compare  $r_3$

lifetimes of cells in green with cells + 1 mM DCBQ in orange).

To compare the timing of action of DCBQ relative to the QB pocket in PSII we carried out TA experiments with DCBQ in conjunction with 3-(3,4-dichlorophenyl)-1,1-dimethylurea (DCMU). DCMU is known to bind to the QB pocket in PSII,<sup>51</sup> competing against benzoquinone docking there and reduction thereafter. We also tested DMBQ & DCMU and PPBQ & DCMU as controls. However, comparison of the raw lifetimes is more challenging here (**SI Figure 15B**) and needs further analysis. In the global fitting, each spectral component decays independently, so we cannot directly assign a specific component and hence a lifetime to quenching by DCBQ. Instead, each lifetime ( $r_1$ ,  $r_2$ ,  $r_3$ ) is weighted equally. The ratio of the lifetimes upon addition of DCBQ to that of wild-type cell sample with no benzoquinone addition is determined and plotted in **SI Figure 15C** (select samples also in **Figure 2d**). Samples which showed no difference in lifetimes would therefore have a mean ratio of 1. Only the difference in lifetimes after addition of DCBQ significantly deviated from 1 to approximately 0.5 (orange bar, first entry). Further, student t-tests comparisons between sample sets reveal that only the sample with DCBQ & DCMU (orange bar, fourth entry) had a meaningful change in lifetimes when compared to PPBQ, DMBQ, PPBQ & DCMU, and DMBQ & DCMU (all approximately 1). Therefore, upon the co-addition of DCMU, only the benzoquinone DCBQ demonstrated a statistically significant decrease in lifetimes ( $p < 0.01$ ); this means we can determine that the action of DCBQ can be assigned to electron transfer steps before.



**SI Figure 15 – Lifetimes with different benzoquinones and DCMU combinations**

**A & B) Lifetimes.** **A)** Benzoquinones DCBQ, PPBQ or DMBQ each 1 mM added to wild-type *Synechocystis* cells. Neither DMBQ or PPBQ (blue) show a measurable change the transients in the early timescale compared to cells with no additives (green) as DCBQ (orange) does. Data from three biological replicates. **B)** Benzoquinones DCBQ, PPBQ or DMBQ each 1 mM added to wild-type *Synechocystis* cells along with DCMU (1 mM). Data from two biological replicates. **C)** Ratio of lifetimes ( $r_{WT}/r_{Additive}$ ) of cells with no additives, and cells treated with benzoquinones (panel A) and DCMU combinations (panel B)

## 1.7 Addition of DCBQ to the different biological samples

To determine the location of early time DCBQ mediated electron extraction within the cell, we carried out TA experiments with and without DCBQ on the different biological samples with varying photosystems (described in **SI Section 1.2**, not including the Olive mutant). TA spectra of the different biological samples without DCBQ added is presented in **SI Figure 7**. Singular Value Decomposition of the TA spectra of the different biological samples with DCBQ added is presented in **SI Figure 10** and **SI Figure 11**. This section presents the TA data from experiments with DCBQ, and comparisons of that data with TA data from experiments without DCBQ.

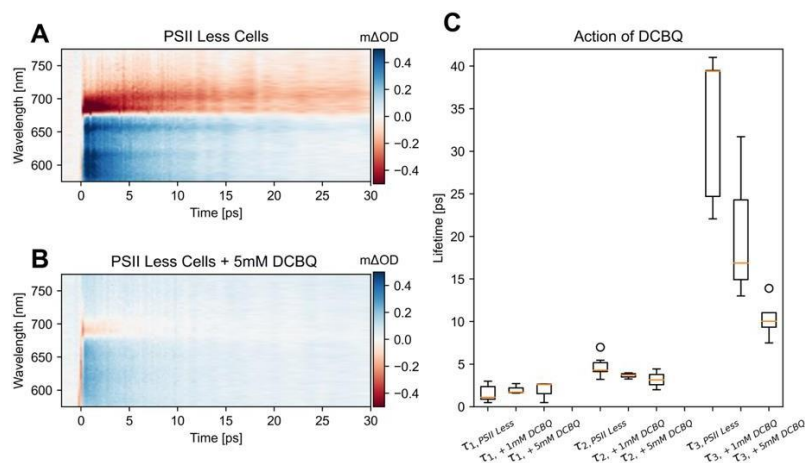
Biological samples that contain functional PSI, which includes PSII-less cells (**SI Figure 16**) and isolated PSI (**SI Figure 17**), exhibited similar lifetimes for the long component. As described in **SI Section 1.4.2** (**SI Figure 10**), three components were retained in the PSII-less cells and two components for isolated PSI. The reduction in the lifetime of these components as a function of DCBQ concentration is more extreme in the isolated system (isolated PSI) compared to *in vivo* (PSII-less cells). PSII-less cells exhibited a reduction in  $\tau_2$  upon addition of DCBQ, whereas this is not observed in short lifetime component of isolated PSI.

Biological samples that contain functional PSII only, which includes PSI-less cells (**SI Figure 18**) and isolated PSII (**SI Figure 19**) show markedly different spectral features from those observed in the wild-type cells (previously described in **SI Section 1.2** (**SI Figure 7**)). The long component ( $\sim 1$  ns) is two orders of magnitude greater than that observed in biological samples that contain functional PSI including wild-type cells ( $\sim 30$  ps). This long component does not meaningfully change upon the addition of DCBQ in biological samples that contain functional PSII. However, the shorter lifetime in biological samples that contain functional PSII exhibits a DCBQ mediated decay. The short lifetime decrease is otherwise difficult to deconvolute from the combined PSI and PSII signals in this region in wild-type cells. This is because the spectral features have significant overlap, as well as the lifetimes being similar in magnitude. PSI-less cells also have a smaller transient signal magnitude, likely arising from the fact that PSI has a 4-fold higher chlorophyll count compared to PSII. We were unable to increase the concentration of the cells in the TA experiments to get greater signal, as scattering overwhelmed the probe signal.

Although we have shown that electron extraction may occur from both PSI and PSII, both in cells and in isolation, it is difficult to determine with certainty the portion of charge extracted from PSI and, separately, from PSII in the wild-type cells. However, the similarity in the magnitude of lifetime reduction upon the addition of DCBQ, tends to suggest we are most sensitive to the CT state in PSI in the TA experiments described here.

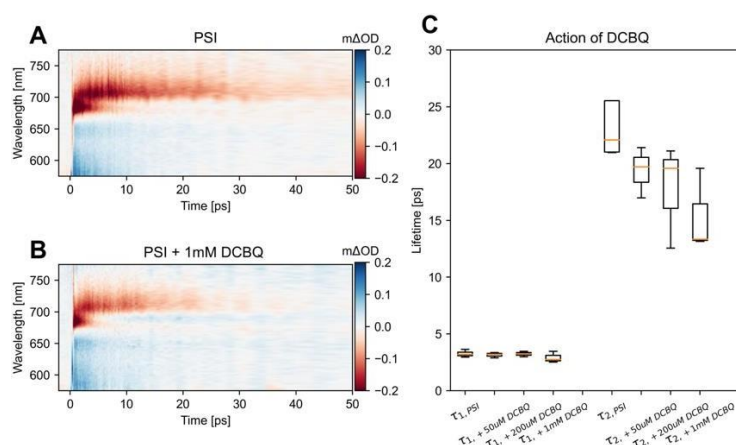
Calculated lifetimes from all TA experiments are reported in **SI Tables 1-9**.

## Chapter 5



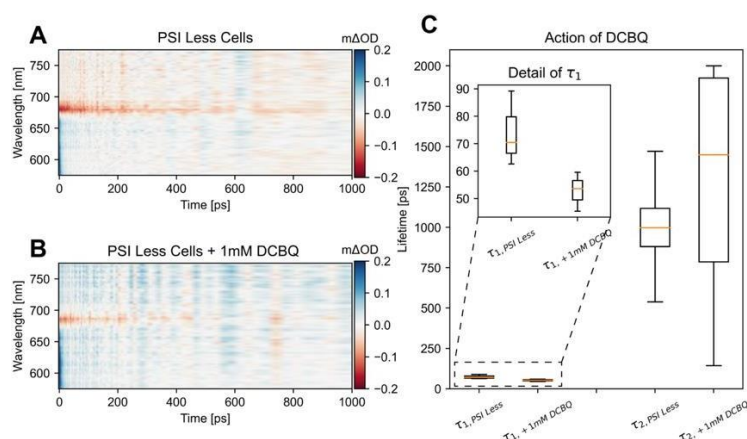
**SI Figure 16 – Analysis of PSII-less cells in the presence of DCBQ**

**A)** TA map of PSII-less cells before the addition of DCBQ. **B)** TA map of PSII-less cells with 5% DMSO and 5 mM DCBQ. Neither map is normalized, and both were measured under the same experimental configuration. **C)** As outlined in SI Figure 10, three components of the PSII-less mutants were retained, and three associated lifetimes were determined from the global fit. The lifetimes closely match that of the wild-type cells. Data in panel C is from 3 to 5 biological replicates and maps in panels A and B are from one sample representative of replicates.



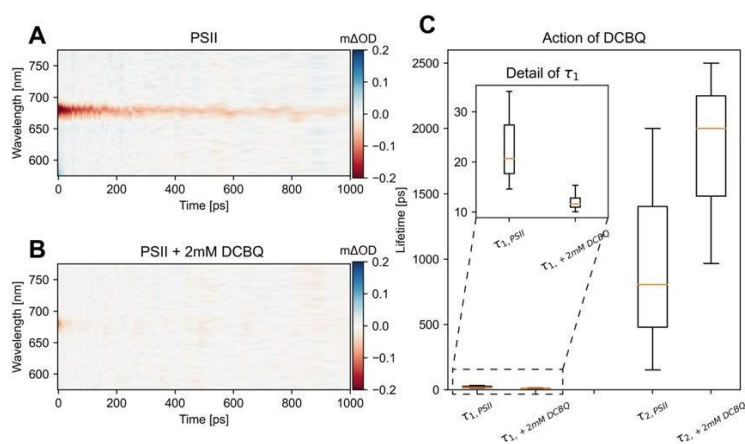
**SI Figure 17 - Analysis of isolated PSI proteins in the presence of DCBQ.**

**A)** TA map of isolated PSI before the addition of DCBQ. **B)** TA map of isolated PSI with 1% DMSO and 1 mM DCBQ. Neither map is normalized, and both were measured under the same experimental configuration. **C)** As outlined in SI Figure 10, two components from isolated PSI were retained and two associated lifetimes were determined from the global fit. The lifetimes closely match that of the wild-type cells. Data in panel C is from 3 to 5 biological replicates and maps in panels A and B are from one sample representative of replicates.



**SI Figure 18 - Analysis of PSI-Less cells in the presence of DCBQ.**

**A)** TA map of PSI-less cells before the addition of DCBQ. **B)** TA map of PSI-less cells with 1% DMSO and 1 mM DCBQ. Neither map is normalized, and both were measured under the same experimental configuration. **C)** As outlined in SI Figure 11, two components from PSI-less cells were retained, and two associated lifetimes were determined from the global fit. Data in panel C is from 3 to 5 biological replicates and maps in panels A and B are from one sample representative of replicates. The longer lifetime, on the order of 1 ns does not significantly change upon the addition of DCBQ, it is also difficult to compute with accuracy due to the reduction in signal from the sample with addition of DCBQ at long times. The shorter lifetime, plotted in detail in the inset, does show a reduction upon the addition of DCBQ.



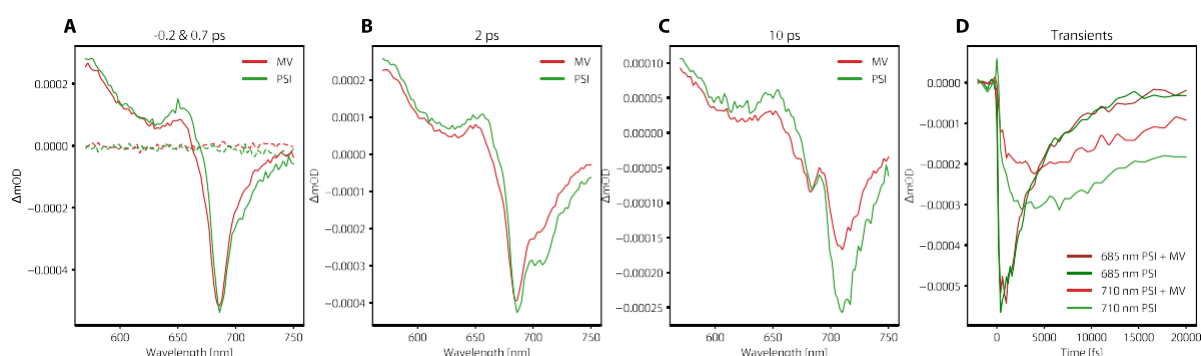
**SI Figure 19 - Analysis of isolated PSII in the presence of DCBQ.**

**A)** TA map of isolated PSII before the addition of DCBQ. **B)** TA map of isolated PSII with 2% DMSO and 2 mM DCBQ. Neither map is normalized, and both were measured under the same experimental configuration. **C)** As outlined in SI Figure 11, two components from of isolated PSII were retained, and two associated lifetimes were determined from the global fit. Data in panel C is from 3 to 5 biological replicates and maps in panels A and B are from one sample representative of replicates. The longer lifetime, on the order of 1 ns does not meaningfully change upon the addition of DCBQ and has significant uncertainty due to the reduction in signal from the DCBQ sample. The shorter lifetime, plotted in detail in the inset, does show a reduction upon the addition of DCBQ and is shorter than of the PSI-less cells.

## 1.8 Addition of methyl viologen to the PSI

Methyl viologen ( $MV^{2+}$ ) is the most common electron mediator in artificial photosynthesis for electrocatalysis to facilitate chemical transformations (e.g. hydrogenases for hydrogen evolution). To demonstrate that higher-energy electrons can be extracted from photoexcited reaction centres by this class of mediators, TA experiments were performed on isolated PSI with and without  $MV^{2+}$  ( $-0.325$  V vs SHE for the  $MV^{2+}/MV^{\bullet+}$  redox couple at pH 7)<sup>52</sup>. The spectral components of isolated PSI exhibited diminished lifetimes in the presence of  $MV^{2+}$  (**SI Figure 20**), comparable to those seen in the presence of DCBQ. The extinction coefficient and population of the reduced species limit observable rise in the red to below the signal to noise limit of our system. Nevertheless, these results suggest  $MV^{2+}$  can also oxidize peripheral chlorophyll pigments of PSI.

We found that  $MV^{2+}$  had no effect when added to cell suspensions (cell results not shown here).  $MV^{2+}$  has been documented to be impermeable when oxidized and very weakly permeable when reduced in *E. coli* cells.<sup>53,54</sup> Furthermore, *in vivo* use of  $MV^{2+}$  as an electron mediator is limited by its high toxicity, which is attributed to its PSI oxidation and generation of reactive oxygen species. Trade-offs between the mid-point potential, photocurrent generation and toxicity of electron mediators has been explored in previous studies<sup>55</sup>. Future research can utilize TA to guide the design and synthesis of electron mediators with fast kinetics, favorable energetics, and low cytotoxicity.



**SI Figure 20 - Analysis of isolated PSI in the presence of  $MV^{2+}$ .**

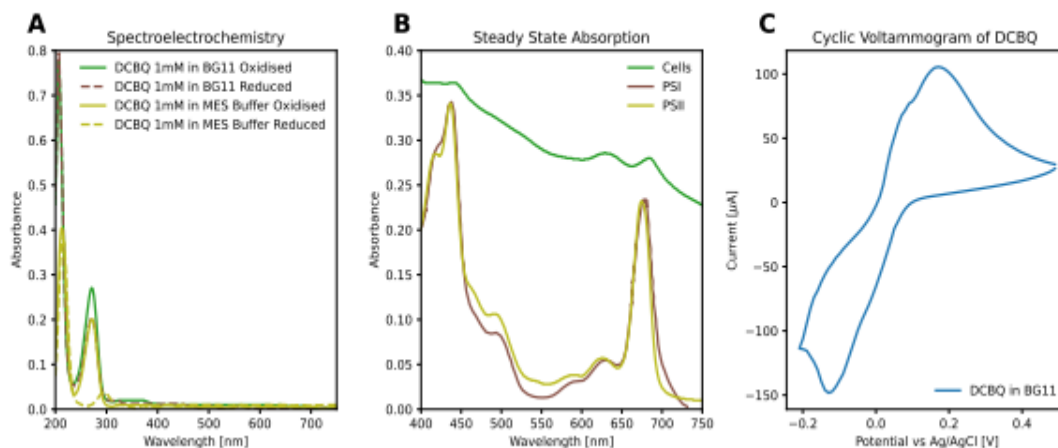
**A)** TA spectra of isolated PSI with and without  $MV^{2+}$ . Dashed line is at  $-0.2$  ps. **B & C)** – TA spectra at  $2$  and  $10$  ps. **D)** TA transients at  $685$  nm and  $710$  nm, highlighting the suppressed rise of the  $710$  nm feature and accelerated decay dynamics.  $MV^{2+}$  sample has been rescaled to match PSI bleach at  $200$  fs. Plotted data are of one sample, representative of 4 biological replicates.

## 2 UV-Visible Steady State Absorption and Spectroelectrochemistry

To determine whether DCBQ could participate in energy transfer mechanisms in the form of Dexter or Förster resonances from PSII *in vivo* or *in vitro*, the optical properties of separate solutions of the biological samples and DCBQ were characterized. The absorption spectrum of cells was dominated by broad scattering background, which was less present in isolated PSII (SI Figure 21). Prominent absorption bands at  $450$ ,  $680$  and  $700$  nm correspond to the chlorophylls in the PSII and PSI complexes in cells. The absorption band at  $622$  nm corresponds to the phycobilisomes in cells. The absorption spectra of DCBQ in its neutral and reduced forms in BG11 medium and MES buffer displayed peaks at less than  $300$  nm (SI Figure 21). The lack of overlap in the absorption spectra between DCBQ before reduction and the photosystems fluorescence *in vivo*



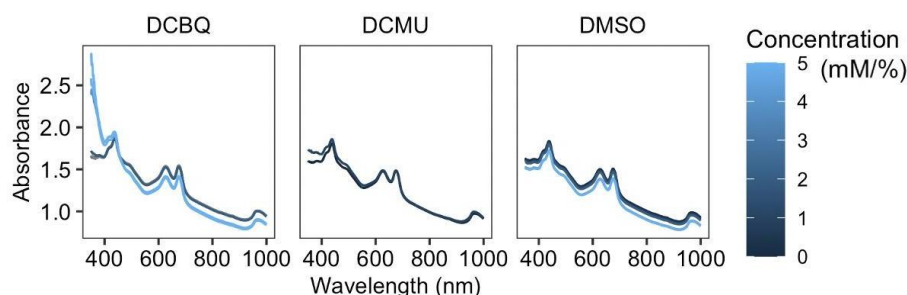
indicates that energy transfer mechanisms, such as Förster resonances, could not be active in DCBQ-mediated quenching.<sup>56</sup> DCBQ must hence act with an electron transfer mechanism when extracting charge from photoexcited photosystem.



**SI Figure 21 – Spectro-electrochemical characterizations of DCBQ and UV-vis absorption of biological samples** **A)** DCBQ in neutral (without applied potential) and partially reduced ( $-0.1$  V vs Ag/AgCl for 30 min, without stirring) forms in BG11 medium used for cells and MES buffer used for isolated photosystems. **B)** Biological samples wild-type *Synechocystis* cells and isolated photosystem I & II. **C)** Cyclic voltammogram of DCBQ (1mM) in BG11 medium, under atmospheric conditions with applied potential 0.5 V to  $-0.2$  V,  $0.01$  V steps,  $0.05$  V  $s^{-1}$  at pH 8.5 at  $25^{\circ}C$ .

To investigate if DCBQ was binding to the photosystems *in vivo* and *in vitro* and that it was changing its optical properties, the optical properties of solutions of the biological samples mixed with DCBQ were measured. Absorption spectra were measured 5 min after each addition. A final reading at the maximum concentration of DCBQ tested (5 mM) was repeated after an additional 20 min (exceeding the maximal length of a transient absorption spectroscopy run). The peaks in the absorption spectra for all cell and DCBQ solutions did not shift (**SI Figure 22**). We conclude that DCBQ is not tightly binding to the reaction centre chlorophylls. Controls DMSO solvent (0.2 – 5 %) and DCMU (1 mM) were also tested and found not shift the absorption spectra.





**SI Figure 22 - Absorption spectra of *Synechocystis* cells mixed with spectroscopy additives.**

Wild-type *Synechocystis* cells were mixed with 0.2 – 5 mM DCBQ (in 0.2-5% DMSO), 1 mM DCMU (in 1% DMSO) or 0.2-5% DMSO. Concentration in the key in mM for DCBQ and DCMU or % for DMSO. Absorption spectra was measured 5 min after each addition. A final reading at the maximum concentration of DCBQ tested (5 mM) was repeated after an additional 20 min (approximate length of a transient absorption spectroscopy run)

### 3. Structural studies

#### 3.1 Location of primary electron donors within the photosystem protein complexes

Marcus theory describes how electrons may tunnel between cofactors when they are separated by approximately 2 nm (20 Å) or less.<sup>57</sup> Therefore, for electron transfer to occur from the early photoexcited state of photosynthetic reaction centres to DCBQ, the primary electron donors (P680/P700) and DCBQ would need to be within 2 nm of each other. Using PyMOL, we measured the distances between the primary electron donors and the edge of the protein scaffold of the photosystem protein complexes. The distance between the primary electron donors and any known binding pockets/docking sites within the protein scaffold were also determined.

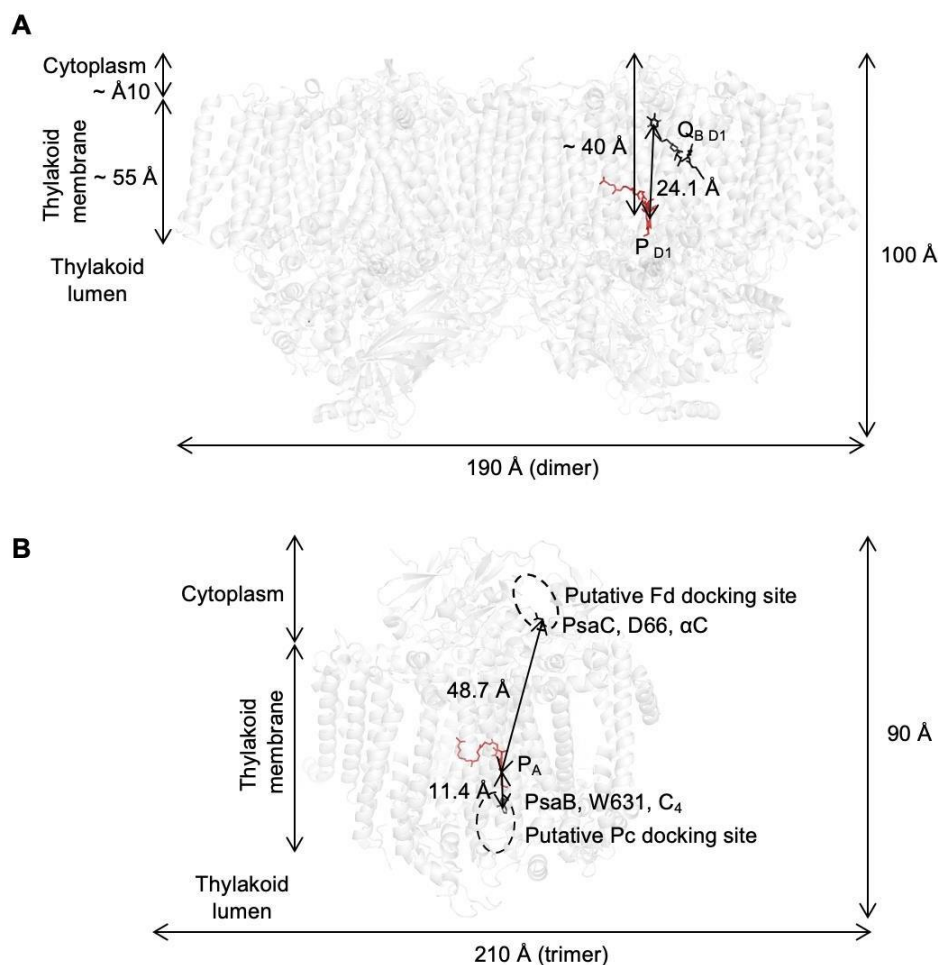
PSII exists as a dimer in oxygenic photosynthetic organisms, although monomers have also been isolated from cells.<sup>58</sup> The structure of a PSII dimer from *T. elongatus* under room temperature, two-flash illumination and ‘damage-free’ conditions (using an X-ray free electron laser) at 2.25 Å resolution by Young *et al.* (2016) (Protein Data Bank ID: 5TIS) was analysed.<sup>59</sup> In each monomer in the PSII dimer, the primary electron donor associated with the D1 (PsbA) protein subunit (PD1, one of the chlorophyll molecules in the P680) was measured to be ~40 Å from the cytoplasmic side of the protein scaffold and 24.1 Å from QB in the QB binding pocket (**SI Figure 23A**), both greater than 2 nm for fast electron transfer to occur.

In most cyanobacteria, PSI exists as a trimer under optimal conditions although is also present as a monomer as a small fraction of the total amount of PSI.<sup>60</sup> Under different growth conditions, such as iron limitations or high temperatures the ratio of monomers to trimers shifts toward the monomeric form.<sup>61,62</sup> It is generally accepted that in plants and algae PSI is monomeric.<sup>63–66</sup> The X-ray crystal structure of a PSI monomer from the cyanobacterium *Synechococcus elongatus* at 2.5 Å resolution by Jordan *et al.* (2001) (Protein Data Bank ID: 1JB0) was analysed.<sup>67,68</sup> While in PSI there is no established intraprotein binding pocket like the QB binding pocket in PSII, there are putative docking

sites for ferredoxin (Fd) (or flavodoxin under iron limitation) at the cytoplasmic side (or stromal side in eukaryotic oxygenic photosynthetic organisms) and for plastocyanin (Pc) (or Cyt  $c_6$  under copper limitation) at the luminal side.

While the exact locations of these docking sites have not been established, the docking site for Fd is hypothesized to be in a pocket formed by protein subunits PsaC, PsaD and PsaE,<sup>67</sup> the location of which for distance measurements was approximated as the central C atom of the aspartic acid residue at position 66 in the PsaC protein subunit. In the PSI monomer, the primary electron donor associated with the PsaA protein subunit in the A-branch (P<sub>A</sub>, one of the chlorophyll molecules in the P700) were measured to be 48.7 Å from the putative Fd docking site (also the cytoplasmic side of the protein scaffold) (**SI Figure 23B**).

The docking site for Pc is hypothesized to be a hollow close to the pseudo-C2 axis formed by  $\alpha$ -helices of the PsaA and PsaB protein subunits.<sup>67,69</sup> Tryptophan residues from PsaA and PsaB protrude into the hollow and are hypothesized to engaged in interaction with and/or electron transfer from Pc to the oxidized primary electron donor P700<sup>+</sup>.<sup>67,69</sup> The location of the putative Pc docking site was approximated for distance measurements as the C4 atom of the indole group of the tryptophan residue at position 631 in the PsaB protein subunit. P<sub>A</sub> was measured to be 11.4 Å from the putative Pc-docking site, which was less than the 2 nm maximum for electron transfer to be permissible under the limits imposed by Marcus theory.

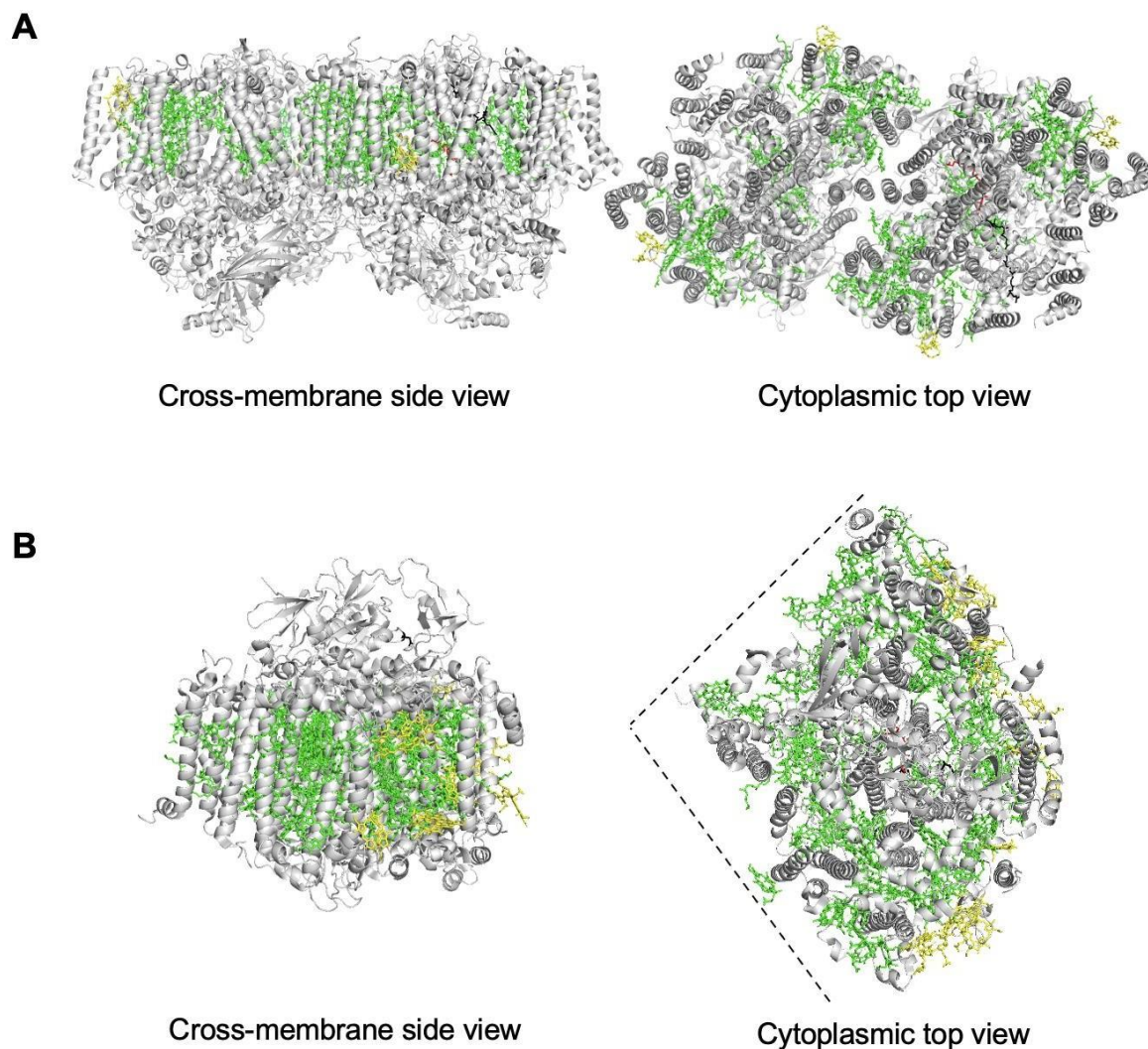


**SI Figure 23 - Location of the primary electron donors within the photosystem protein complexes. A)** Structure of the photosystem II (PSII) dimer (grey transparent ribbons) showing the locations and distances between the primary electron donor (PD1, red) and the terminal quinone (QB D1, black) in the QB pocket and the edges of the protein scaffold. Ring-to-ring distance between PD1 and QB D1 24.1 Å, distance between PD1 and the cytoplasmic side of the protein scaffold ~40 Å, both greater than 2 nm for electron transfer, calculated using PyMOL. Structure rendered in PyMOL from the crystal structure by Young et al. (2016) (Protein Data Bank ID: 5TIS).<sup>59</sup> **B)** Structure of the photosystem I (PSI) monomer (grey transparent ribbons) showing the locations and distances between the primary electron donor (P<sub>A</sub>, red) and the putative ferredoxin (Fd) and pyocyanin (Pc) docking sites (dashed ovals), amino acids in the putative docking sites as a proxy for their location (black) and the edges of the protein scaffold. Distance between P<sub>A</sub> and the central C atom of the aspartic acid residue at position 66 in the PsaC protein subunit (PsaC, D66, αC) 48.7 Å, greater than 2 nm for electron transfer. Distance between P<sub>A</sub> and the C<sub>4</sub> atom of the indole group of the tryptophan residue at position 631 in the PsaB protein subunit (PsaB, W631, C<sub>4</sub>) 11.4 Å, less than 2 nm for electron transfer. Distances calculated using PyMOL. Structure rendered in PyMOL from the crystal structure by Jordan et al. (2001) (Protein Data Bank ID: 1JB0).<sup>67</sup>

### 3.2 Location of chlorophylls within the photosystem protein complexes

However, all chlorophylls embedded within the reaction centres are energetically degenerate at room temperature.<sup>70,71</sup> Photoexcitation thus results in a highly delocalized excited state shared across several chlorophylls (described by the Lake Model of photoexcitation).<sup>70,71</sup> At the sub-picosecond timescale, the reaction centres are in a delocalized charge-transfer state capable of charge transfer.<sup>72,73</sup> Indeed, there are chlorophylls less than 2 nm inside from the edge of the protein scaffold, including four that protrude from the PSII dimer (**SI Figure 24A**, in yellow) and 14 that protrude from the PSI monomer on sides not against another PSI monomer in the trimer (**SI Figure 24B**, in yellow). Most of these protruding chlorophylls are in the sections of the photosystem protein complexes within the thylakoid membrane. Only the top ~10 Å of PSII is exposed in the cytoplasm of cyanobacterial cells (or stroma of chloroplasts in plants and algae) and ~55 Å of PSII is located within the thylakoid membrane,<sup>74</sup> and so only the PsaC, PsaD and PsaE subunits of PSI are not in the thylakoid membrane. Notably, DCBQ is soluble in phospholipid bilayers so it may access to structures within in the thylakoid membrane, including the peripheral chlorophylls in the photosystems.

We conclude that upon photoexcitation of the photosynthetic reaction centres, the charge-transfer (CT) state extends to periphery chlorophylls within < 200 fs. Favored at high concentrations, DCBQ was reduced by a periphery chlorophyll into the semiquinone radical (DCSQ<sup>•-</sup>), with potentially a second electron transfer to the fully reduced form (example for PSII and PSI illustrated in **Figure 2A** in the main text).



**SI Figure 24 - Location of chlorophylls in the photosystem protein complexes**

**A)** Structure of the photosystem II (PSII) dimer (grey ribbons), primary electron donor (PD1, red), the terminal quinone (QB D1, black) in the QB pocket, chlorophylls (green), and some chlorophylls that protrude from the protein scaffold (yellow) that would enable DCBQ to associate at a distance less than 2 nm for electron transfer. Structure rendered in PyMOL from the crystal structure by Young et al. (2016) (Protein Data Bank ID: 5TIS).<sup>59</sup>

**B)** Structure of the photosystem I monomer (grey ribbons), primary electron donor (PA, red), amino acids in the putative Fd and Pc docking sites as a proxy for their location (black), chlorophylls (green), and some chlorophylls that protrude from the protein scaffold (yellow) that would enable DCBQ to associate at a distance less than 2 nm for electron transfer. Dashed line indicates the sides of the monomer that link to other monomers in the trimer. Structure rendered in PyMOL from the crystal structure by Jordan et al. (2001) (Protein Data Bank ID: 1JB0).<sup>67</sup>

## 4. Photoelectrochemistry

The ability of a candidate benzoquinone molecule to enhance photocurrents stemming from *Synechocystis* cells and isolated PSII complexes was determined using photoelectrochemistry. In these experiments, the biological components were immobilized onto IO-ITO working electrodes of appropriate dimensions and the photocurrent profiles were measured using chronoamperometry under



light/dark cycles without and then with benzoquinones (and DCMU). Chronoamperometry was performed at an applied potential of 0.5 V vs SHE for maximal mediation by benzoquinones (as derived from previous stepped chronoamperometry and based on their mid-point potentials).<sup>9,47,75</sup> The photocurrent was measured as the difference between the steady-state current outputs in the light and dark periods. Photocurrent magnitudes with benzoquinone and DCMU were calculated relative to the neat sample with zero benzoquinone or DCMU as 1 arbitrary unit (a. u.). The extent of increased photocurrent output in the presence of the benzoquinone relative to the photocurrent output without the exogenous mediators indicate the ability of the benzoquinone to serve as a mediator between the PETC and the electrode.<sup>76</sup>

First, different benzoquinones were screened: DCBQ, phenyl-1,4-quinone (PPBQ) and 2,6-dimethyl-1,4-benzoquinone (DMBQ). Based on the concentration of benzoquinone tested in previous studies, 1 mM was chosen as the concentration of the different benzoquinones to test.<sup>9</sup> DCBQ (1 mM) increased the photocurrent of *Synechocystis* cells on IO-ITO electrodes approximately 50-fold (**SI Figure 25**). PPBQ (1 mM) and DMBQ (1 mM) each mediated less efficiently than DCBQ (1 mM), giving approximately 40-fold and 10- fold increases in photocurrent, respectively.

The effects of PPBQ and DMBQ on cells were greater with SDS detergent (8.2 mM final concentration), added to aid their solubilization (**SI Figure 27**). This suggested that different solubility of benzoquinones in the aqueous BG11 medium (and also the aqueous cytosol of the cell) may account for differences in their ability to mediate. Indeed, it has been suggested before that benzoquinones can be sequestered in intracellular membranes and precipitate in aqueous compartments of the cell.<sup>48</sup> Nevertheless, there was some mediation without SDS with PPBQ and DMBQ (10% EtOH) giving approximately 20-fold and 5-fold increase in photocurrent, respectively, so the ultrafast transient absorption spectroscopy studies were able to be performed without SDS.

For isolated PSII on IO-ITO electrodes, DCBQ and PPBQ mediated similarly efficiently, increasing the photocurrent approximately 2-fold (**SI Figure 26**). This was consistent with the limited ability of PPBQ to efficiently mediate electrons *in vivo* being caused by its reduced ability to access PSII from the cytoplasm.

To determine the relationship between concentration of DCBQ and electron mediation efficiency, different concentrations of DCBQ were tested. For cells, the minimum concentration tested was 200  $\mu$ M, which was the maximum concentration of DCBQ that was not cytotoxic to the cells over 12 h (**SI Figure 31**),<sup>75</sup> and the maximum concentration tested was 5 mM, which was the concentration that yielded a clearly observable difference in the transient absorption spectra. This concentration range included 1 mM, which was the concentration of benzoquinone tested in previous studies.<sup>9</sup> A minimum concentration of 50  $\mu$ M was tested for isolated PSII. The maximal increase in photocurrent of *Synechocystis* cells on DCBQ treatment was approximately 50-fold at a concentration of 1 mM, and the increase dropped to 20-fold at 5 mM DCBQ (**SI Figure 26**). As with whole cells, the maximum mediation of photocurrent from isolated PSII was not seen at the highest concentration of DCBQ tested. The maximal increase in photocurrent of isolated PSII on DCBQ treatment was approximately 8-fold at a concentration of 200  $\mu$ M, and only 2-fold at 1 mM DCBQ (**SI Figure 26**).

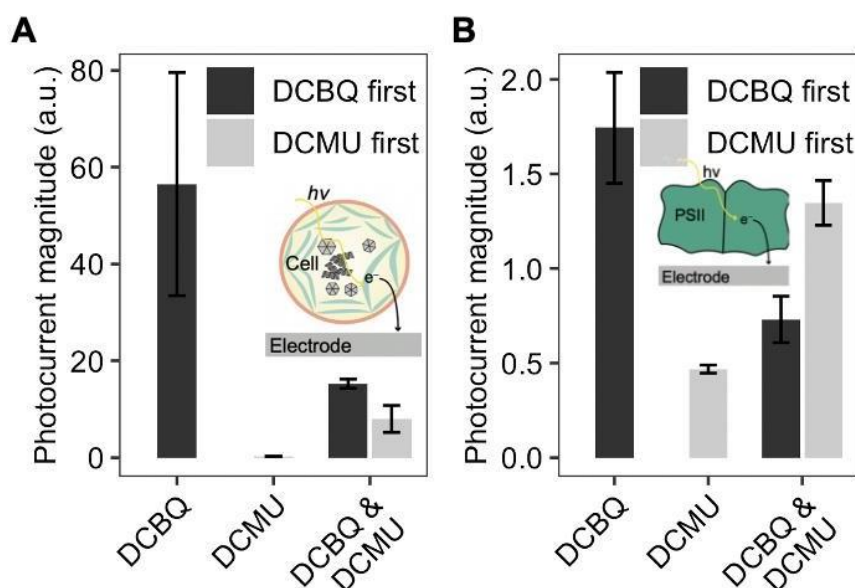
The fact that addition of DCBQ resulted in a bigger increase in photocurrent output for cells (50-fold) than for isolated PSII (8-fold) indicates that the isolated PSII were inherently more efficiently wired to the electrodes than whole cells, due to their participation in direct electron transfer to IO-ITO electrodes,<sup>77</sup> whereas cells participate in indirect electron transfer via an endogenous electron mediator.<sup>9,78,79</sup> The effect of solvents used in the above experiments was tested. The increase of photocurrent output by exogenous benzoquinones was not due to the solvents/detergents in which they were dissolved. In fact, the solvents/detergents reduced the photocurrent output slightly (**SI Figure 27B**). However, none of the photocurrents of samples with solvents was statistically different from those without solvent.

To examine benzoquinone electron mediation upstream and downstream of QB, DCMU was tested in combination with the benzoquinones. First, the effect of the order of addition of the benzoquinone and DCMU to the cells or isolated PSII was tested with DCBQ (**SI Figure 25**). The order affected the photocurrent magnitude but not the trend: DCBQ and DCMU yielded higher photocurrents than DCMU only. Cells with DCBQ added before DCMU gave higher photocurrent than cells with DCMU added first, which was most likely due to cell death from the herbicide action. Isolated PSII with DCMU added before also adding DCBQ gave higher photocurrent than DCBQ added first, which was some evidence that the QB binding pocket was not the only site of mediation in PSII by DCBQ. For subsequent experiments DCMU was added after any benzoquinones.

It has been demonstrated that QA can participate in direct electron transfer from isolated PSII to the electrode as there is photocurrent from isolated PSII treated with DCMU but with no natural or exogenous electron mediators present.<sup>80</sup> Conversely, *Synechocystis* cells treated with DCMU yield no photocurrent. Therefore, QA cannot transfer electrons to the electrode when inside of cells.

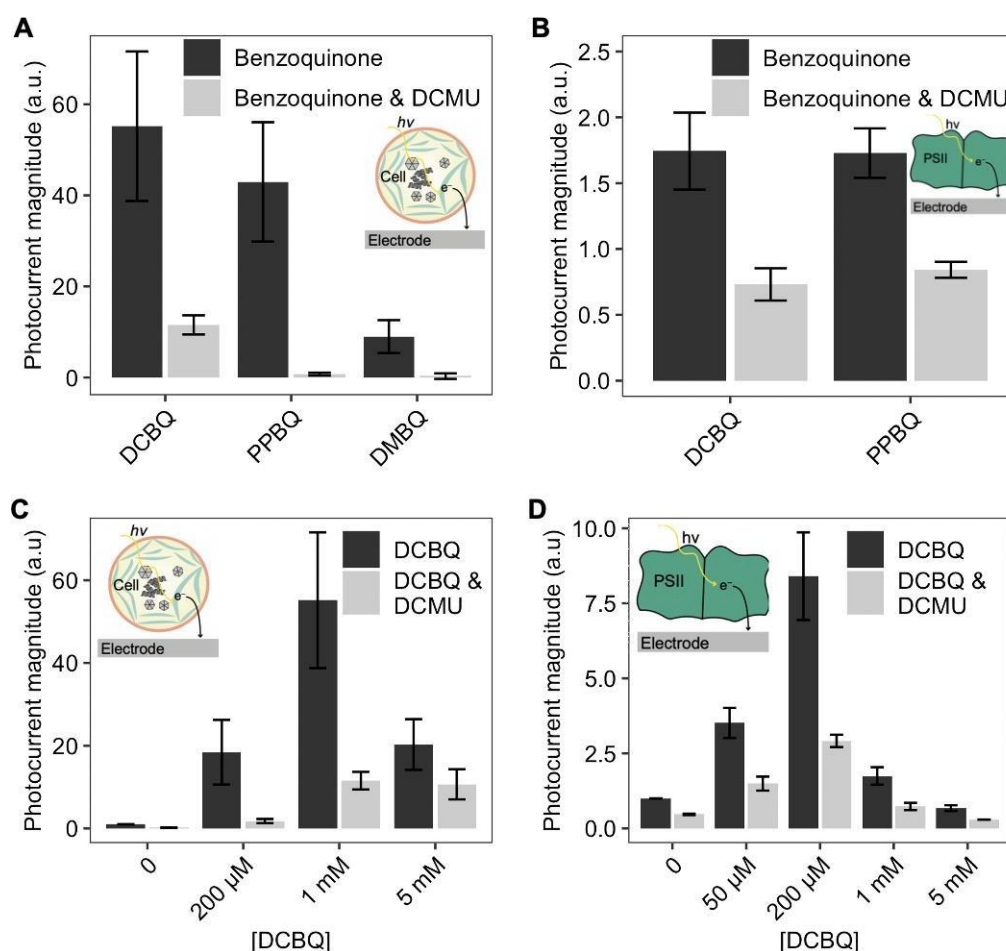
It has also been demonstrated that small cationic molecules can interact with PSII near QA to extract electrons; with DCBQ being a poor molecular acceptor for sites near QA.<sup>81,82</sup> The photocurrent from *Synechocystis* cells in the presence of equimolar concentrations of DCBQ and DCMU was approximately one third of that without the herbicide present (**SI Figure 26**). The one third is what DCBQ mediates from PSII before QA, some of which we measured using TA; the missing two thirds must be mediation by DCBQ from QB and further downstream in the PETC, including from early in PSI. PPBQ and DMBQ did not mediate at all in the presence of DCMU. For isolated PSII, again, approximately one-third of photocurrent was yielded in the presence of equimolar DCMU and DCBQ, and PPBQ performed similarly to DCBQ (**SI Figure 26**). This is consistent with the cell membrane being a barrier for both PPBQ and DMBQ as mediators. Therefore, DCBQ was the only benzoquinone electron mediator screened that appeared to extract electrons at a point that is earlier than QB in PSII *in vivo*, which is consistent with the TA results.





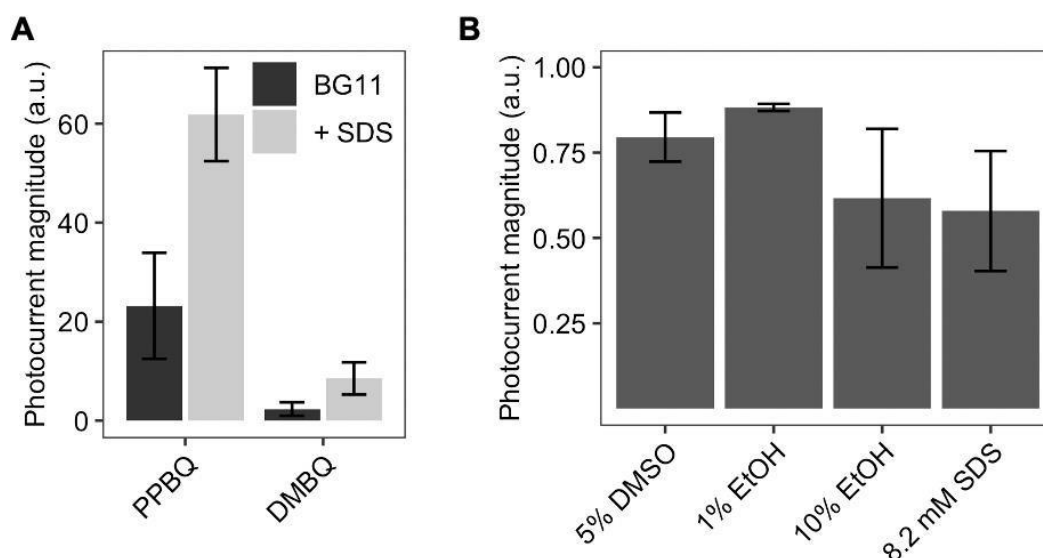
**SI Figure 25 - Effect of the order of addition of DCBQ and DCMU on photocurrent enhancement by exogenous electron mediators.**

**A)** *Synechocystis* cells, and **B)** isolated PSII. Photocurrent outputs with DCBQ (1 mM) and DCMU (1 mM) added in different orders. Photocurrent magnitudes calculated from the difference in steady state current density in the light and the dark. Photocurrent magnitudes with benzoquinone and DCMU were calculated relative to the neat sample with zero benzoquinone or DCMU as 1 arbitrary unit (a. u.). Photoelectrochemistry parameters include: 0.5 V vs SHE and an Ag/AgCl reference electrode and a Pt-meshelectrode, 25°C, atmospheric conditions, BG11 medium (pH 8.5) electrolyte for cells and MES buffer (pH 6.5) electrolyte for PSII, 60 s/90 s light/dark cycles for cells and 15 s/15 s light/dark cycles for PSII, 50  $\mu\text{mol photons m}^{-2} \text{s}^{-1}$  680 nm light. Data presented as the average of three biological replicates  $\pm$  standard error of the mean



**SI Figure 26 - Photocurrent enhancements from exogenous addition of benzoquinones**

**A) & C)** *Synechocystis* cells, and **B) & D)** isolated PSII. **A) & B)** Photocurrent outputs with different benzoquinones (1 mM) added: 2,6-dichloro-1,4-benzoquinone (DCBQ), phenyl-1,4-quinone (PPBQ) and 2,6-dimethyl-1,4-benzoquinone (DMBQ). In the absence and presence of DCMU (1 mM). **C) & D)** Photocurrent outputs with different concentrations of DCBQ and DCMU (1 mM) added. Photocurrent magnitudes calculated from the difference in steady state current density in the light and the dark. Photocurrent magnitudes with benzoquinone and DCMU were calculated relative to the neat sample with zero benzoquinone or DCMU as 1 arbitrary unit (a. u.). Photoelectrochemistry parameters as in SI Figure 25. Data presented as the average of three biological replicates  $\pm$  standard error of the mean.

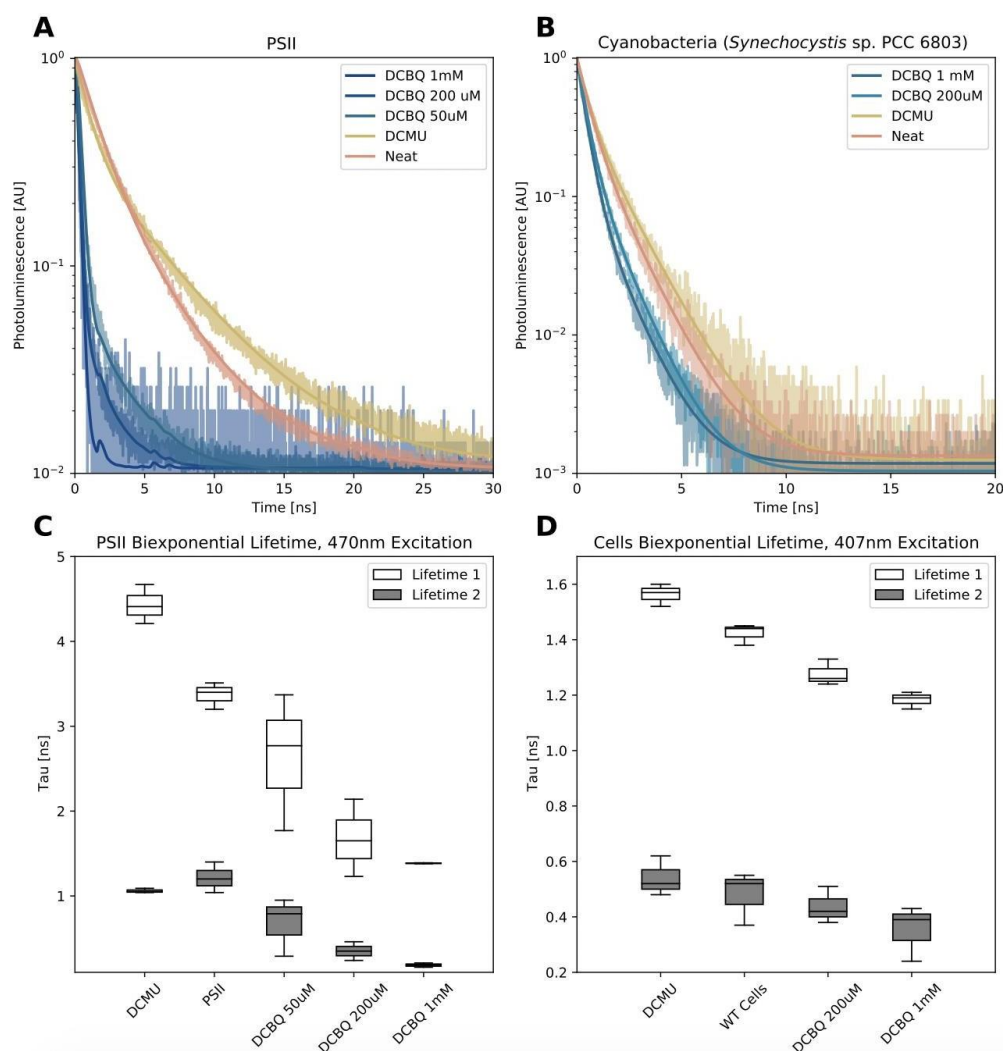


**SI Figure 27 - Change in photocurrent of *Synechocystis* cells in the presence of solvents.** **A)** Photocurrent outputs with PPBQ and DMBQ with and without SDS to aid solubilization in aqueous BG11 medium used as the electrolyte. **B)** Change in photocurrent of *Synechocystis* cells in the presence of solvents. Photocurrent magnitudes calculated from the difference in steady state current density in the light and the dark. Photocurrent magnitudes with solvents were calculated relative to the neat sample in BG11 with zero solvent as 1 arbitrary unit (a. u.). Photoelectrochemistry parameters as in SI Figure 25. Data presented as the average of three biological replicates  $\pm$  standard error of the mean. For panel B, raw photocurrent outputs were statistically non-significant.

## 5. Time-Correlated Single-Photon Counting Measurements

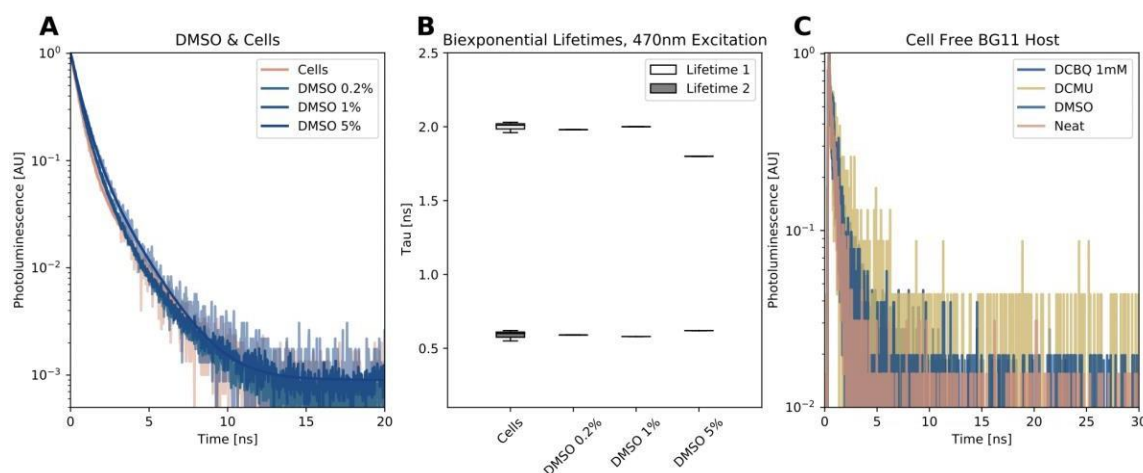
Previously, PSII has been studied *in vivo* in photosynthetic microorganisms via nano-second time-correlated single-photon counting (TCSPC).<sup>83-86</sup> To record the time-resolved photoluminescence decay of the samples, TCSPC was performed on isolated PSII and wild-type *Synechocystis* cells with DCBQ. The PSII reaction centres can be considered to be in an open or closed state. An open reaction centre has the primary quinone QA oxidized and ready to undergo stable charge separation, whereas a closed reaction centre has QA reduced to Q<sup>-</sup>. In a closed reaction centre charge separation will be followed by fast charge recombination and enhanced chlorophyll fluorescence yield owing to the larger probability of decay via the chlorophyll excited state.<sup>1</sup>

Both PSII and PSII with DCMU (1 mM) displayed the long-lived chlorophyll emission indicative of closed reaction centres (**SI Figure 28-A,C**). PSII with DCBQ (1 mM) displayed a much shorter-lived emission, which is indicative of open reaction centres. The cells had much longer-lived emissions than the isolated PSII and displayed the same effects of DCMU and DCBQ (**SI Figure 28-B, D**). Upon increasing the concentration of DCBQ, we observed a linear reduction in both lifetimes with concentration, reaching  $1.2 \text{ ns} \pm 0.4 \text{ ns}$  at the highest concentration of DCBQ tested in TCSPC (1 mM) for isolated PSII and cells, respectively. DMSO solvent did not measurably change the photoluminescence decays of cells (**SI Figure 29A-B**). BG11 medium controls assured us that the sample was the only emitting species at the pump wavelength (**SI Figure 29C**). These results indicated that DCBQ acted on PSII *in vivo* and *in vitro* within nanoseconds after photoexcitation. Calculated lifetimes from TCSPC are reported in **SI Tables 10-12**.



**SI Figure 28 - TCSPC analysis of biological samples treated with DCBQ or DCMU.**

**A & C)** isolated PSII treated with DCBQ or DCMU. **B & D)** Wild-type *Synechocystis* cells treated with DCBQ or DCMU. **A-B)** Time-resolved radiative decay dynamics. Wild-type cells exhibit radiative decay dynamics well described by a bi-exponential decay (solid line). **C-D)** Lifetimes.



SI Figure 29 - TCSPC controls.

**A & C)** Time-resolved radiative decay dynamics. Wild type cells exhibit radiative decay dynamics well described by a bi-exponential decay (solid line) in panel A. **B)** Lifetimes of panel A. **A-B)** Wild-type *Synechocystis* cells treated with different volumes of DMSO solvent. **C)** BG11 medium with no cells with DCBQ, DCMU or DMSO added.

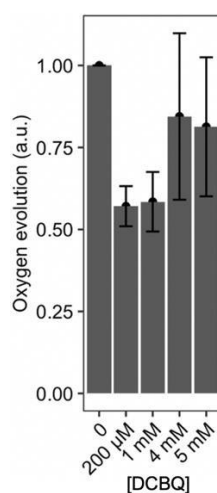
## 6. Oxygen Evolution

To confirm that PSII was performing photolysis of water *in vivo* in the presence of the difference concentrations of DCBQ, we measured oxygen evolution. Cells without DCBQ treatment showed healthy PSII activity for cells in early stationary phase of  $23 \pm 4 \mu\text{mol}(\text{O}_2) \text{mg}^{-1} \text{h}^{-1}$ . In parallel, the cells were treated with different concentrations of DCBQ for 15 min prior to measuring oxygen evolution. The oxygen evolution of cells treated with DCBQ was normalized to that without DCBQ as 1 arbitrary unit (a.u.) (**SI Figure 30**). Cells treated with lower concentrations of DCBQ ( $\leq 1 \text{ mM}$ ) showed approximately half the PSII activity of untreated cells. Cells treated with higher concentrations of DCBQ (up to 5 mM) showed similar PSII activity to that of untreated cells, although with high variability between biological replicates. These results confirmed that PSII was performing photolysis of water *in vivo* in the presence of DCBQ even up to the highest concentrations and exposure times tested in the TA. The cause of the reduction of PSII activity *in vivo* after DCBQ treatment is the scope of future studies, although we did follow up with cytotoxicity assays that showed that high concentration DCBQ exposure for hours kills the cells (see **Section 7**). Further, even though cells were found to generate approximately half the number of electrons from water lysis in the presence of 1 mM DCBQ, they yielded 50-fold higher extracellular electron transfer to an electrode under illumination than untreated cells (see **SI Section 4**). This indicated that the dominant action of DCBQ is to compete with the downstream natural electron transfer pathways rather than increasing water oxidation rates by PSII.

Note that oxygen evolution was measured on the time scale of seconds after illumination like the photoelectrochemistry experiments, whereas the TA measurements probed events on the sub-picosecond timescale after photoexcitation. Oxygen evolution occurs by the  $\text{Mn}_4\text{Ca}$  cluster in PSII's oxygen evolving complex (OEC) completing the photo-induced Kok cycle, the final step of which takes 1 ms.<sup>87</sup> This is also the 4<sup>th</sup> step within PSII after photo-excitation of the P680, with the hole that formed by the 1<sup>st</sup> step (formation of the initial charge separated state with the primary electron

acceptor pheophytin (Ph) [ $\text{P680}^{+\bullet}\text{-Ph}^-$ ] that has a lifetime of 10-30 ps) migrating to the OEC to be filled by the electrons produced by photolysis of water. Therefore, the OEC is the kinetic bottleneck during the re-wiring of electron transfer from the reaction centre in the presence of DCBQ.

The electrons produced from water oxidation by the OEC are shuttled via the electron transport chain to PSI through the plastoquinone (PQ) pool to the cytochrome *b6f* complex (Cyt *b6f*) and then through a plastocyanin (Pc) pool.<sup>88</sup> The bottleneck in re-wiring electron transfer from the P700 early after photoexcitation is diffusion of plastoquinone from the QB pocket in PSII to the cytochrome *b6f* complex which takes approximately 10 ms.<sup>88</sup> However, before photoexcitation, the Pc pool is somewhat reduced<sup>89</sup> and is a short-term source of electrons for PSI before it is refilled by PSII action. This may account for why we found that the sub-picosecond reduction of DCBQ was dominated by PSI.



**SI Figure 30 - Oxygen evolution of wild-type *Synechocystis* cells with DCBQ.**

Measurement using  $1500 \mu\text{mol photons m}^{-2} \text{ s}^{-1}$  light at 627 nm. The electrolyte was BG11 medium (pH 8.5). Data presented as the mean of five biological replicates, error bars are standard error of the mean.

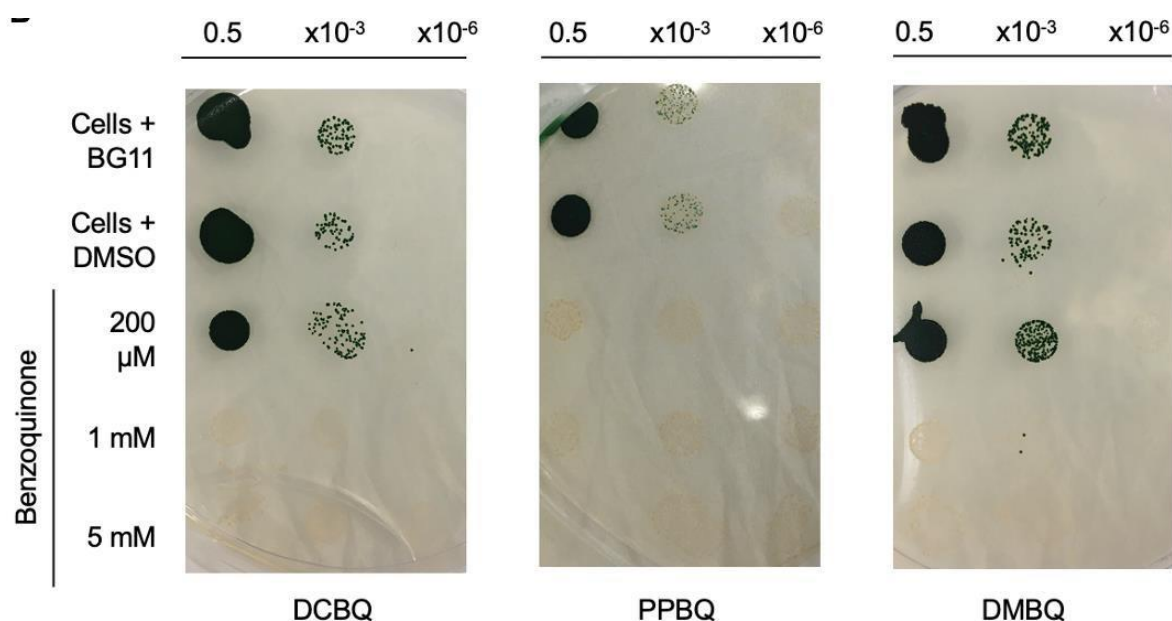
## 7. Cytotoxicity

In addition to assessing the health of the cells following laser irradiation experimental conditions (**SI Figure 1**), we also explored the longer-term effects of the benzoquinones on cells growth. Spot assays were performed. Equivalent amounts of wild-type *Synechocystis* cells to those that adhered to the IO-ITO electrodes after photoelectrochemical experiments (5 nmol Chl *a*) were incubated with concentration ranges of up to 5 mM for DCBQ, PPBQ and DMBQ for 1 day under constant light ( $50 \mu\text{mol photons m}^{-2} \text{ s}^{-1}$  white light used for culturing). Three control conditions were also assayed: cells in BG11 (no mediator), and cells in BG11 with 5% (v/v) DMSO (the highest concentration of DMSO solvent for benzoquinone addition). After exposure to the mediators, the *Synechocystis* cells were re-suspended in fresh BG11 medium, spotted onto BG11 agar plates, and incubated for 1 week. The highest concentration of exogenous mediator at which the cells could still grow after 24 h exposure was identified (**SI Figure 31**). These results suggest that cytotoxicity artefacts are not the cause of the effect on the early CT state as PPBQ is more cytotoxic than DCBQ, however, only DCBQ showed a



significant change on the early picosecond timescale.

Exogenously added DCBQ and DMBQ were non-toxic at concentrations  $\leq 200 \mu\text{M}$ . However, even  $200 \mu\text{M}$  PPBQ was toxic to the cells, with no growth observed. These results indicated that DCBQ ( $200 \mu\text{M}$ ) was not cytotoxic when the sub-picosecond after photoexcitation was measured to a small degree (**Figure 2C**). There was not a correlation between the cytotoxicity of the different benzoquinones or the concentration of DCBQ that killed cells (**SI Figure 31**) and their ability to re-direct electrons from the electron transport chain and enhance extracellular electron transfer to an electrode (see **SI Section 4**). There was also not a correlation between the concentration of DCBQ that killed cells (**SI Figure 31**) and the PSII activity (**SI Figure 30**).

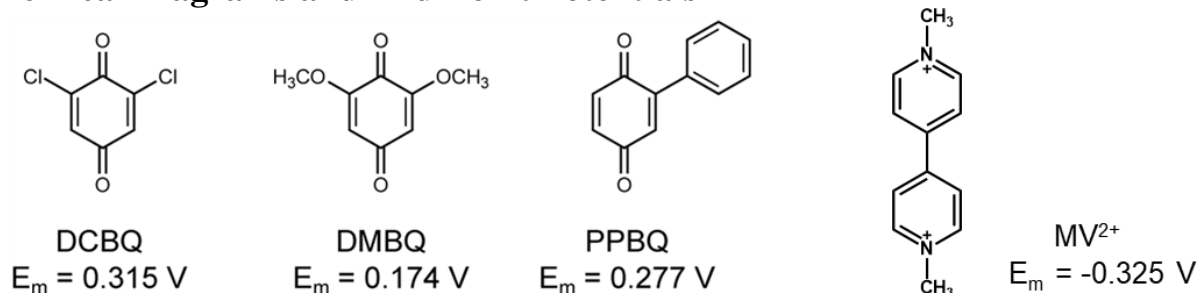


**SI Figure 31 - Cytotoxicity spot assays.**

Cytotoxicity spot assays to determine the effect of addition of exogenous electron mediators on the growth of wild-type *Synechocystis* cells. Benzoquinones tested: 2,6-dichloro-p-benzoquinone (DCBQ), phenyl-1,4-quinone (PPBQ), 2,6-dimethyl-p-benzoquinone (DMBQ). Cells ( $5 \text{ nmol Chl } a$ ) were incubated with the mediators at different concentrations for 24 h under  $50 \mu\text{mol photons m}^{-2} \text{ s}^{-1}$  white light. The cells were resuspended in BG11, and their concentration standardized to an OD750 of 0.5. Serial dilutions were prepared, spotted on agar and incubated for 1 week. Cytotoxicity spot assay controls: Cells in BG11 (no mediator), and cells in BG11 with 5 % (v/v) DMSO (no mediator). All data shown was from a single representative plate from 3 biological replicates.



## 8. Chemical Diagrams and Mid-Point Potentials



SI Figure 32 – Chemical Structures.

Chemical structures and mid-point potentials of electron mediators used in this study Mediators: 2,6- dichloro-1,4-benzoquinone (DCBQ), phenyl-1,4-quinone (PPBQ), 2,6-dimethyl-p-benzoquinone (DMBQ), and methyl viologen (MV<sup>2+</sup>). Mid-point potentials ( $E_m$ ) from the literature versus SHE and at pH 7.<sup>90,91</sup>

### Tabulated Lifetimes

Table 3 TA lifetimes ( $\tau$ ) of multiple biological replicates (n = 8) of wild-type cells (SI Figure 2 - Cell replicates.)

Value	$r_1$ [fs]	$r_2$ [fs]	$r_3$ [fs]
Mean	2047.95	4547.56	20803.8
Median	2040.65	4328.63	20783.1
Standard Deviation	327.149	1296.16	2700.56

Table 4 TA lifetimes ( $\tau$  in fs) of wild-type cells with different concentrations of DCBQ added (n = 5)(Figure 2C)

Value	Concentration of DCBQ added (mM)			
	1	2	4	5
Mean	21903.9	16613.7	15510.8	11603.7
Median	22369.9	16630.9	15046.5	12600.7
Standard Deviation	3934.5	3813.82	5258.37	5730.34

Table 5 TA lifetimes ( $\tau$ ) of PSI-less cells and PSI-less cells with 1 mM DCBQ added (SI Figure 18 - Analysis of PSI-Less cells in the presence of DCBQ.)

Additive	n	Value	$r_1$ [ps]	$r_2$ [ps]
-	4	Mean	74.1037	1001.57
		Median	70.4831	997.921
		Standard Deviation	13.6584	381.003
DMBQ 1 mM	4	Mean	52.8946	1260.84
		Median	53.6296	1452
		Standard Deviation	7.10907	870.196

Table 6 TA lifetimes ( $\tau$ ) of isolated PSI and PSI with different concentrations of DCBQ added (SI Figure 17 - Analysis of isolated PSI proteins in the presence of DCBQ.)

## Chapter 5

Additive	n	Value	$r_1$ [ps]	$r_2$ [ps]
-	4	Mean	3.25958	24.4735
		Median	3.21766	22.0906
		Standard Deviation	0.293787	5.59445
DMBQ 50 $\mu$ M	3	Mean	3.16017	19.3718
		Median	3.21141	19.7144
		Standard Deviation	0.235097	2.22661
DCBQ 200 $\mu$ M	3	Mean	3.24498	17.7529
		Median	3.26468	19.5854
		Standard Deviation	0.241729	4.56605
DCBQ 1 mM	3	Mean	17.7529	2.91984
		Median	19.5854	2.76074
		Standard Deviation	4.56605	0.496354

Table 7 TA lifetimes ( $r$ ) of isolated PSII and PSII with 2 mM DCBQ added (SI Figure 19 - Analysis of isolated PSII in the presence of DCBQ.)

Additive	n	Value	$r_1$ [ps]	$r_2$ [ps]
-	3	Mean	23.1305	986.478
		Median	20.7013	806.422
		Standard Deviation	9.94922	936.567
DMBQ 2 mM	3	Mean	12.1592	1822.44
		Median	11.622	1998
		Standard Deviation	2.26026	781.618

Table 8 TA lifetimes ( $r$ ) of PSII-less cells with different concentrations of DCBQ added (SI Figure 18 - Analysis of PSI-Less cells in the presence of DCBQ.)

Additive	n	Value	$r_1$ [ps]	$r_2$ [ps]	$r_3$ [ps]
-	5	Mean	1.37515	4.72576	33.3424
		Median	0.895146	4.29005	39.4114
		Standard Deviation	1.2489	1.32719	9.14994
DMBQ 1 mM	3	Mean	2.02068	3.67077	20.5342
		Median	1.723	3.75088	16.8731
		Standard Deviation	0.60698	0.360788	9.86783
DCBQ 5 mM	3	Mean	1.93172	3.20486	10.3788
		Median	2.60633	3.16679	10.0543
		Standard Deviation	1.24059	1.21283	2.65016

Table 9 TA lifetimes ( $r$ ) of wild-type cells with different concentrations of benzoquinone and benzoquinone with DCMU added (Figure 2D & SI Figure 15 – Lifetimes with different benzoquinones and DCMU combinations.)

## Chapter 5

Additive(s)	n	Value	$r_{quinone}/r_{cell}$ [ps]
<b>DCBQ 1 mM</b>	5	Mean	0.526043
		Median	0.494251
		Standard Deviation	0.19329
<b>DMBQ 1 mM</b>	5	Mean	1.22641
		Median	1.19472
		Standard Deviation	0.361439
<b>PPBQ 1 mM</b>	5	Mean	1.04763
		Median	1.03462
		Standard Deviation	0,438686
<b>DCMU &amp; DCBQ each 1 mM</b>	4	Mean	0.551711
		Median	0.636816
		Standard Deviation	0.224779
<b>DCMU &amp; DMBQ each 1 mM</b>	4	Mean	0.789561
		Median	0.917867
		Standard Deviation	0.197384
<b>DCMU &amp; PPBQ each 1 mM</b>	4	Mean	0.944083
		Median	0.904805
		Standard Deviation	0.281095

Table 10 TSCPC lifetimes of isolated PSII (SI Figure 28 - TCSPC analysis of biological samples treated with DCBQ or DCMU.)

## Chapter 5

Replicate number	Sample	Addition	Concentration	Illumination	Measurement	Lifetime $\tau_1$	Lifetime $\tau_2$
1	PSII	DCMU	-	470 nm	680 nm	4.67	1.05
2	PSII	DCMU	-	470 nm	680 nm	4.41	1.04
2	PSII	DCMU	-	470 nm	680 nm	4.21	1.09
1	PSII	-	-	470 nm	680 nm	3.40	1.40
1	PSII	-	-	470 nm	680 nm	3.20	1.20
1	PSII	-	-	470 nm	680 nm	3.51	1.04
1	PSII	DCBQ	10 uM	470 nm	680 nm	3.04	1.01
1	PSII	DCBQ	50 uM	470 nm	680 nm	1.77	0.29
2	PSII	DCBQ	50 uM	470 nm	680 nm	3.37	0.95
2	PSII	DCBQ	50 uM	470 nm	680 nm	2.77	0.79
1	PSII	DCBQ	200 uM	470 nm	680 nm	1.23	0.24
2	PSII	DCBQ	200 uM	470 nm	680 nm	2.14	0.46
2	PSII	DCBQ	200 uM	470 nm	680 nm	1.65	0.35
1	PSII	DCBQ	1 mM	470 nm	680 nm	1.39	0.16
1	PSII	DCBQ	1 mM	470 nm	680 nm	1.38	0.21

Table 11 TCSPC lifetimes of wild-type cells (SI Figure 28 - TCSPC analysis of biological samples treated with DCBQ or DCMU.)

Excitation 407 nm

Replicate number	Addition	Concentration	Illumination	Measurement	Lifetime $\tau_1$	Lifetime $\tau_2$
1	DCMU	1 mM	407 nm	680 nm	1.57	0.52
2	DCMU	1 mM	407 nm	680 nm	1.6	0.48
3	DCMU	1 mM	407 nm	680 nm	1.52	0.62
1	-	-	407 nm	680 nm	1.44	0.55
2	-	-	407 nm	680 nm	1.45	0.37
1	DCBQ	200 uM	407 nm	680 nm	1.24	0.42
2	DCBQ	200 uM	407 nm	680 nm	1.33	0.51
3	DCBQ	200 uM	407 nm	680 nm	1.26	0.38
1	DCBQ	1 mM	407 nm	680 nm	1.15	0.39
2	DCBQ	1 mM	407 nm	680 nm	1.19	0.43
3	DCBQ	1 mM	407 nm	680 nm	1.21	0.24

## Chapter 5

Excitation 470 nm

Replicate number	Addition	Concentration	Illumination	Measurement	Lifetime $\tau_1$	Lifetime $\tau_2$
1	DCMU	1 mM	470 nm	680 nm	2.15	0.70
1	-	-	470 nm	680 nm	2.03	0.62
2	-	-	470 nm	680 nm	2.01	0.55
1	DCBQ	1 mM	470 nm	680 nm	1.96	0.41
1	DCBQ	5 mM	470 nm	680 nm	1.84	0.32

Table 12 TCSPC lifetimes of control samples (SI Figure 29 - TCSPC controls.)

Replicate number	Addition	Concentration	Illumination	Measurement	Lifetime $\tau_1$	Lifetime $\tau_2$
1	DMSO	5%	407 nm	680 nm	1.39	0.38
1	DMSO	10%	407 nm	680 nm	1.42	0.37
1	DMSO	0.2%	470 nm	680 nm	1.98	0.59
1	DMSO	1%	470 nm	680 nm	2.00	0.58
2	DMSO	5%	470 nm	680 nm	1.80	0.62

## References

- [1] Schreiber, U., Endo, T., Mi, H. & Asada, K. Quenching analysis of chlorophyll fluorescence by the saturation pulse method: Particular aspects relating to the study of eukaryotic algae and cyanobacteria. *Plant Cell Physiol* (1995)
- [2] Hinrichsen, T. F. *et al.* Long-lived and disorder-free charge transfer states enable endothermic charge separation in efficient non-fullerene organic solar cells.
- [3] Mersch, D. *et al.* Wiring of Photosystem II to Hydrogenase for Photoelectrochemical Water Splitting. *J Am Chem Soc* **137**, 8541–8549 (2015).
- [4] Çoruh, O. *et al.* Cryo-EM structure of a functional monomeric Photosystem I from *Thermosynechococcus elongatus* reveals red chlorophyll cluster. *Commun Biol* **4**, 304 (2021).
- [5] Shen, G., Boussiba, S. & Vermaas, W. F. J. *Synechocystis* sp PCC 6803 Strains Lacking Photosystem I and Phycobilisome Function. *Plant Cell* **5**, 1853 (2007).
- [6] Ermakova-Gerdes, S., Yu, Z. & Vermaas, W. Targeted random mutagenesis to identify functionally important residues in the D2 protein of photosystem II in *Synechocystis* sp. strain PCC 6803. *J Bacteriol* **183**, 145–154 (2001).
- [7] Lea-Smith, D. J. *et al.* Phycobilisome-Deficient Strains of *Synechocystis* sp PCC 6803 Have Reduced Size and Require Carbon-Limiting Conditions to Exhibit Enhanced Productivity. *Plant Physiol* **165**, 705–714 (2014).
- [8] Berera, R., van Grondelle, R. & Kennis, J. T. M. Ultrafast transient absorption spectroscopy: Principles and application to photosynthetic systems. *Photosynth Res* **101**, 105–118 (2009).
- [9] Zhang, J. Z. *et al.* Photoelectrochemistry of Photosystem II in Vitro vs in Vivo. *J Am Chem Soc* **140**, 6–9 (2018).
- [10] Zamzam, N. *et al.* Femtosecond visible transient absorption spectroscopy of chlorophyll-f-containing photosystem II. *Proc Natl Acad Sci U S A* **117**, 23158–23164 (2020).
- [11] *Photosystem I*. vol. 24 (Springer Netherlands, 2006).
- [12] Karapetyan, N. V., Holzwarth, A. R. & Rögner, M. The photosystem I trimer of cyanobacteria: molecular organization, excitation dynamics and physiological significance. *FEBS Lett* **460**, 395–400 (1999).
- [13] Croce, R., Zucchelli, G., Garlaschi, F. M. & Jennings, R. C. A thermal broadening study of the antenna chlorophylls in PSI- 200, LHCI, and PSI core. *Biochemistry* **37**, 17355–17360 (1998).
- [14] Karapetyan, N. V. *et al.* Long-wavelength chlorophylls in photosystem I of cyanobacteria: Origin, localization, and functions. *Biochemistry (Moscow)* **79**, 213–220 (2014).
- [15] Molotokaite, E. *et al.* Trapping Dynamics in Photosystem I-Light Harvesting Complex i of Higher Plants Is Governed by the Competition between Excited State Diffusion from Low Energy States and Photochemical Charge Separation. *Journal of Physical Chemistry B* **121**, 9816–9830 (2017).
- [16] Russo, M., Casazza, A. P., Cerullo, G., Santabarbara, S. & Maiuri, M. Ultrafast excited state dynamics in the monomeric and trimeric photosystem I core complex of *Spirulina platensis* probed by two- dimensional electronic spectroscopy. *J Chem Phys* **156**, 164202 (2022).
- [17] Akhtar, P. *et al.* Two-Dimensional Electronic Spectroscopy of a Minimal Photosystem I Complex Reveals the Rate of Primary Charge Separation. *J Am Chem Soc* **143**, 14601–14612 (2021).
- [18] Shelaev, I. V. *et al.* Femtosecond primary charge separation in *Synechocystis* sp. PCC 6803 photosystem I. *Biochimica et Biophysica Acta (BBA) - Bioenergetics* **1797**, 1410–1420 (2010).
- [19] Cherepanov, D. A. *et al.* Mechanism of adiabatic primary electron transfer in photosystem I: Femtosecond spectroscopy upon excitation of reaction center in the far-red edge of the QY band. *Biochimica et Biophysica Acta (BBA) - Bioenergetics* **1858**, 895–905 (2017).

- [20] Hastings, G., Reed, L. J., Lin, S. & Blankenship, R. E. Excited state dynamics in photosystem I: effects of detergent and excitation wavelength. *Biophys J* **69**, 2044–2055 (1995).
- [21] Lee, Y., Gorka, M., Golbeck, J. H. & Anna, J. M. Ultrafast Energy Transfer Involving the Red Chlorophylls of Cyanobacterial Photosystem I Probed through Two-Dimensional Electronic Spectroscopy. *J Am Chem Soc* **140**, 11631–11638 (2018).
- [22] Anna, J. M., Ostroumov, E. E., Maghlaoui, K., Barber, J. & Scholes, G. D. Two-dimensional electronic spectroscopy reveals ultrafast downhill energy transfer in photosystem I trimers of the cyanobacterium *thermosynechococcus elongatus*. *Journal of Physical Chemistry Letters* **3**, 3677–3684 (2012).
- [23] Mülle, M. G., Niklas, J., Lubitz, W. & Holzwarth, A. R. Ultrafast Transient Absorption Studies on Photosystem I Reaction Centers from *Chlamydomonas reinhardtii*. 1. A New Interpretation of the Energy Trapping and Early Electron Transfer Steps in Photosystem I. *Biophys J* **85**, 3899–3922 (2003).
- [24] Melkozernov, A. N. *et al.* Specific Mutation Near the Primary Donor in Photosystem I from *Chlamydomonas reinhardtii* Alters the Trapping Time and Spectroscopic Properties of P700<sup>+</sup>. *Biochemistry* **36**, 2898–2907 (1997).
- [25] Russo, M. *et al.* Ultrafast excited-state dynamics in land plants Photosystem I core and whole supercomplex under oxidised electron donor conditions. *Photosynth Res* **144**, 221–233 (2020).
- [26] Slavov, C., Ballottari, M., Morosinotto, T., Bassi, R. & Holzwarth, A. R. Trap-Limited Charge Separation Kinetics in Higher Plant Photosystem I Complexes. *Biophys J* **94**, 3601–3612 (2008).
- [27] Santabarbara, S., Tibiletti, T., Remelli, W. & Caffarri, S. Kinetics and heterogeneity of energy transfer from light harvesting complex II to photosystem I in the supercomplex isolated from *Arabidopsis*. *Physical Chemistry Chemical Physics* **19**, 9210–9222 (2017).
- [28] Akhtar, P. *et al.* Excitation energy transfer between Light-harvesting complex II and Photosystem I in reconstituted membranes. *Biochimica et Biophysica Acta (BBA) - Bioenergetics* **1857**, 462–472 (2016).
- [29] Van Stokkum, I. H. M., Larsen, D. S. & Van Grondelle, R. Global and target analysis of time-resolved spectra. *Biochim Biophys Acta Bioenerg* **1657**, 82–104 (2004).
- [30] Dorlhiac, G. F., Fare, C. & van Thor, J. J. PyLDM - An open source package for lifetime density analysis of time-resolved spectroscopic data. *PLoS Comput Biol* **13**, e1005528 (2017).
- [31] van Stokkum, I. H. M., Larsen, D. S. & van Grondelle, R. Global and target analysis of time-resolved spectra. *Biochimica et Biophysica Acta (BBA) - Bioenergetics* **1657**, 82–104 (2004).
- [32] Berera, R., van Grondelle, R. & Kennis, J. T. M. Ultrafast transient absorption spectroscopy: Principles and application to photosynthetic systems. *Photosynthesis Research* vol. 101 105–118.
- [33] Mülle, M. G., Niklas, J., Lubitz, W. & Holzwarth, A. R. Ultrafast Transient Absorption Studies on Photosystem I Reaction Centers from *Chlamydomonas reinhardtii*. 1. A New Interpretation of the Energy Trapping and Early Electron Transfer Steps in Photosystem I. *Biophys J* **85**, 3899–3922 (2003).
- [34] Sugiura, M. & Inoue, Y. Highly purified thermo-stable oxygen-evolving photosystem II core complex from the thermophilic cyanobacterium *Synechococcus elongatus* having His-tagged CP43. *Plant Cell Physiol* **40**, 1219–1231 (1999).
- [35] El-Mohsawy, E. *et al.* Structure and Function of Intact Photosystem I Monomers from the Cyanobacterium *Thermosynechococcus elongatus*. *Biochemistry* **49**, 4740–4751 (2010).
- [36] Komenda, J. & Sobotka, R. Chlorophyll-binding subunits of photosystem I and II: Biosynthesis, chlorophyll incorporation and assembly. *Adv Bot Res* **91**, 195–223 (2019).
- [37] Boehm, M. *et al.* Investigating the Early Stages of Photosystem II Assembly in



- Synechocystis* sp. PCC 6803: ISOLATION OF CP47 AND CP43 COMPLEXES. *Journal of Biological Chemistry* **286**, 14812–14819 (2011).
- [38] Förster, T. Zwischenmolekulare Energiewanderung und Fluoreszenz. *Ann Phys* **437**, 55–75 (1948).
- [39] Scholes, G.D. Long-Range Resonance Energy Transfer in Molecular Systems.
- [40] Beljonne, D., Curutchet, C., Scholes, G. D. & Silbey, R. J. Beyond Förster resonance energy transfer in biological and nanoscale systems. *Journal of Physical Chemistry B* **113**, 6583–6599 (2009).
- [41] Dexter, D. L. A Theory of Sensitized Luminescence in Solids. *J Chem Phys* **21**, 836 (2004).
- [42] Köhler, A. & Bässler, H. *Electronic Processes in Organic Semiconductors*.
- [43] Laquai, F., Park, Y. S., Kim, J. J. & Basché, T. Excitation Energy Transfer in Organic Materials: From Fundamentals to Optoelectronic Devices. *Macromol Rapid Commun* **30**, 1203–1231 (2009).
- [44] Klessinger, M. & Michl, J. *Excited States and Photo-Chemistry of Organic Molecules*, Revised and Improved English-Language Edition. 537 (1995).
- [45] Vogel, P. & Houk, K. *Theory reactivity and mechanisms in modern synthesis*. 1382 (2019).
- [46] Marcus, R. A. On the Theory of Oxidation-Reduction Reactions Involving Electron Transfer. I. *J Chem Phys* **24**, 966 (2004).
- [47] Longatte, G. *et al.* Investigation of photocurrents resulting from a living unicellular algae suspension with quinones over time. *Chem Sci* **9**, 8271–8281 (2018).
- [48] Longatte, G. *et al.* Evaluation of photosynthetic electrons derivation by exogenous redox mediators. *Biophys Chem* **205**, 1–8 (2015).
- [49] Fu, H.-Y. *et al.* Redesigning the QA binding site of Photosystem II allows reduction of exogenous quinones. *Nat Commun* **8**, 15274 (2017).
- [50] Longatte, G., Rappaport, F., Wollman, F.-A., Guille-Collignon, M. & Lemaître, F. Mechanism and analyses for extracting photosynthetic electrons using exogenous quinones – what makes a good extraction pathway? *Photochemical & Photobiological Sciences* **15**, 969–979 (2016).
- [51] Trebst, A. The three-dimensional structure of the herbicide binding niche on the reaction center polypeptides of photosystem ii. *Zeitschrift für Naturforschung - Section C Journal of Biosciences* **42**, 742–750 (1987).
- [52] Bennett, T. *et al.* Elucidating the role of methyl viologen as a scavenger of photoactivated electrons from photosystem I under aerobic and anaerobic conditions. *Physical Chemistry Chemical Physics* **18**, 8512–8521 (2016).
- [53] Jones, R. W. & Garland, P. B. Sites and specificity of the reaction of bipyridylum compounds with anaerobic respiratory enzymes of *Escherichia coli*. Effects of permeability barriers imposed by the cytoplasmic membrane. *Biochemical Journal* **164**, 199 (1977).
- [54] Lawrence, J. M. *et al.* Synthetic biology and bioelectrochemical tools for electrogenic system engineering. *Sci Adv* **8**, 5091 (2022).
- [55] Sayegh, A. *et al.* Finding Adapted Quinones for Harvesting Electrons from Photosynthetic Algae Suspensions. *ChemElectroChem* **8**, 2968–2978 (2021).
- [56] Köhler, A. & Bässler, H. *The Electronic Structure of Organic Semiconductors*. Wiley-VCH Verlag GmbH & Co. KGaA vol. 1 (2015).
- [57] Marcus, R. A. & Sutin, N. Electron transfers in chemistry and biology. *BBA Reviews on Bioenergetics*
- [58] Watanabe, M., Iwai, M., Narikawa, R. & Ikeuchi, M. Is the Photosystem II Complex a Monomer or a Dimer? *Plant Cell Physiol* **50**, 1674–1680 (2009).
- [59] Young, I. D. *et al.* Structure of photosystem II and substrate binding at room temperature. *Nature* **540**, 453–457 (2016).
- [60] Boekema, E. J. *et al.* Evidence for a trimeric organization of the photosystem I complex from the thermophilic cyanobacterium *Synechococcus* sp. *FEBS Lett* **217**, 283–286 (1987).

- [61] Ivanov, A. G. *et al.* Iron Deficiency in Cyanobacteria Causes Monomerization of Photosystem I Trimers and Reduces the Capacity for State Transitions and the Effective Absorption Cross Section of Photosystem I in Vivo. *Plant Physiol* **141**, 1436–1445 (2006).
- [62] Kłodawska, K. *et al.* Elevated Growth Temperature Can Enhance Photosystem I Trimer Formation and Affects Xanthophyll Biosynthesis in Cyanobacterium *Synechocystis* sp. PCC6803 Cells. *Plant Cell Physiol* **56**, 558–571 (2015).
- [63] Kouřil, R., van Oosterwijk, N., Yakushevskaya, A. E. & Boekema, E. J. Photosystem I: a search for green plant trimers. *Photochemical & Photobiological Sciences* **4**, 1091 (2005).
- [64] Gardian, Z. *et al.* Organization of Photosystem I and Photosystem II in red alga *Cyanidium caldarium*: Encounter of cyanobacterial and higher plant concepts. *Biochimica et Biophysica Acta (BBA) - Bioenergetics* **1767**, 725–731 (2007).
- [65] Veith, T. & Büchel, C. The monomeric photosystem I-complex of the diatom *Phaeodactylum tricornutum* binds specific fucoxanthin chlorophyll proteins (FCPs) as light-harvesting complexes. *Biochimica et Biophysica Acta (BBA) - Bioenergetics* **1767**, 1428–1435 (2007).
- [66] Heinemeyer, J., Eubel, H., Wehmhöner, D., Jansch, L. & Braun, H.-P. Proteomic approach to characterize the supramolecular organization of photosystems in higher plants. *Phytochemistry* **65**, 1683–92 (2004).
- [67] Jordan, P. *et al.* Three-dimensional structure of cyanobacterial photosystem I at 2.5 Å resolution. *Nature* **411**, 909–917 (2001).
- [68] Fromme, P., Jordan, P. & Krauß, N. Structure of photosystem I. *Biochimica et Biophysica Acta (BBA)- Bioenergetics* **1507**, 5–31 (2001).
- [69] Fromme, P., Schubert, W.-D. & Krauß, N. Structure of Photosystem I: Suggestions on the docking sites for plastocyanin, ferredoxin and the coordination of P700. *Biochimica et Biophysica Acta (BBA)- Bioenergetics* **1187**, 99–105 (1994).
- [70] Stirbet, A. Excitonic connectivity between photosystem II units: What is it, and how to measure it? *Photosynthesis Research* vol. 116 189–214 Preprint at <https://doi.org/10.1007/s11120-013-9863-9> (2013).
- [71] Mirkovic, T. *et al.* Light absorption and energy transfer in the antenna complexes of photosynthetic organisms. *Chemical Reviews* vol. 117, 249–293
- [72] Dods, R. *et al.* Ultrafast structural changes within a photosynthetic reaction centre. *Nature* **589**, 310–314 (2021).
- [73] Ma, F., Romero, E., Jones, M. R., Novoderezhkin, V. I. & van Grondelle, R. Both electronic and vibrational coherences are involved in primary electron transfer in bacterial reaction center. *Nat Commun* **10**, 933 (2019).
- [74] Zouni, A. *et al.* Crystal structure of photosystem II from *Synechococcus elongatus* at 3.8 Å resolution. *Nature* **409**, 739–743 (2001).
- [75] Clifford, E. R. *et al.* Phenazines as model low-midpoint potential electron shuttles for photosynthetic bioelectrochemical systems. *Chem Sci* **12**, 3328–3338 (2021).
- [76] Zhang, J. Z. & Reisner, E. Advancing photosystem II photoelectrochemistry for semi-artificial photosynthesis. *Nat Rev Chem* **4**, 6–21 (2020).
- [77] Sokol, K. P. *et al.* Rational wiring of photosystem II to hierarchical indium tin oxide electrodes using redox polymers. *Energy Environ Sci* **9**, 3698–3709 (2016).
- [78] Saper, G. *et al.* Live cyanobacteria produce photocurrent and hydrogen using both the respiratory and photosynthetic systems. *Nat Commun* **9**, 2168 (2018).
- [79] Shlosberg, Y. *et al.* NADPH performs mediated electron transfer in cyanobacterial-driven bio- photoelectrochemical cells. *iScience* **24**, 101892 (2021).
- [80] Kato, M., Cardona, T., Rutherford, a W. & Reisner, E. Photoelectrochemical Water Oxidation with Photosystem II Integrated in a Mesoporous Indium Tin Oxide Electrode. *J Am Chem Soc* **134**, 8332–8335 (2012).
- [81] Ulas, G. & Brudvig, G. W. Redirecting Electron Transfer in Photosystem II from Water to

- Redox- Active Metal Complexes. *J Am Chem Soc* **133**, 13260–13263 (2011).
- [82] Sugiura, M. & Inoue, Y. Highly Purified Thermo-Stable Oxygen-Evolving Photosystem II Core Complex from the Thermophilic Cyanobacterium *Synechococcus elongatus* Having His-Tagged CP43. *Plant Cell Physiol* **40**, 1219–1231 (1999).
- [83] Onishi, A., Aikawa, S., Kondo, A. & Akimoto, S. Energy transfer in *Anabaena variabilis* filaments adapted to nitrogen-depleted and nitrogen-enriched conditions studied by time-resolved fluorescence. *Photosynth Res* **133**, 317–326 (2017).
- [84] Chukhutsina, V., Bersanini, L., Aro, E.-M., van Amerongen, H. & van Amerongen, H. Cyanobacterial flv4-2 Operon-Encoded Proteins Optimize Light Harvesting and Charge Separation in Photosystem II. *Mol Plant* **8**, 747–761 (2015).
- [85] Mascoli, V., Bersanini, L. & Croce, R. Far-red absorption and light-use efficiency trade-offs in chlorophyll f photosynthesis. *Nat Plants* **6**, 1044–1053 (2020).
- [86] Bar-Eyal, L. *et al.* An easily reversible structural change underlies mechanisms enabling desert crust cyanobacteria to survive desiccation. *Biochim Biophys Acta Bioenerg* **1847**, 1267–1273 (2015).
- [87] Lavergne, J. Improved UV-visible spectra of the S-transitions in the photosynthetic oxygen-evolving system. *Biochimica et Biophysica Acta (BBA) - Bioenergetics* **1060**, 175–188 (1991).
- [88] Lea-Smith, D. J., Bombelli, P., Vasudevan, R. & Howe, C. J. Photosynthetic, respiratory and extracellular electron transport pathways in cyanobacteria. *Biochim Biophys Acta Bioenerg* **1857**, 247–255 (2016).
- [89] Sétif, P., Boussac, A. & Krieger-Liszkay, A. Near-infrared in vitro measurements of photosystem I cofactors and electron-transfer partners with a recently developed spectrophotometer. *Photosynth Res* **142**, 307–319 (2019).
- [90] Longatte, G. *et al.* Investigation of photocurrents resulting from a living unicellular algae suspension with quinones over time. *Chem Sci* **9**, 8271–8281 (2018).
- [91] O'Reilly, J. E. Oxidation-reduction potential of the ferro-ferricyanide system in buffer solutions. *Biochimica et Biophysica Acta (BBA) - Bioenergetics* **292**, 509–515 (1973).

## Chapter 6: Discussion

## 6.1 Functional and structural significance of PSI in biocatalysis

Upon illumination, PSI absorbs light with nearly 100 % internal quantum efficiency (photon-to-electron conversion).<sup>[1]</sup> In PSI, the cofactors associated with electron transfer ( $F_x$ ,  $F_A$ ,  $F_B$ ) are very close to the surface of PSI.<sup>[2]</sup> The  $F_A$  and  $F_B$  Fe-S clusters are only 5-11 Å away from the surface of PSI.<sup>[2]</sup> This feature enables PSI to donate electrons to various soluble electron mediators as mentioned in section 1.4.1. The promiscuity of PSI towards electron donors and acceptors makes it an attractive candidate as a biological photoreductant.<sup>[2]</sup> Additionally, the non-membrane spanning nature of stromal subunits of PSI can be genetically modified or replaced in vitro easily.<sup>[3,4]</sup> All these features have motivated researchers across the globe to use PSI in the development of solar fuel cells and photovoltaic devices. Recent advancements in molecular biology and electrochemistry enabled to realize this potential of PSI.<sup>[2,5]</sup>

## 6.2 PSI-based light-driven biocatalysis

Effective use of photo-energized electrons obtained from PSI towards chemical production is a promising approach. In this PhD study, the use of PSI in biocatalysis was extended by fuelling various oxidoreductases. An attractive alternative approach in NADPH recycling systems is the use of photosensitizers.<sup>[6]</sup> With inspiration from photosynthesis, several research groups reported diverse photosensitizers, including diphenylalanine and porphyrin nanotubes<sup>[7]</sup>, proflavine<sup>[8]</sup>, cadmium sulfide (CdS)<sup>[9]</sup>, titanium oxide ( $TiO_2$ )<sup>[10]</sup> or carbon nitride ( $C_3N_4$ ).<sup>[11]</sup> All these photosensitizers mainly rely on electron donors like triethanolamine (TEOA) or mercaptoethanol and electron mediators, including pentamethylcyclopentadienyl rhodium bipyridine complexes ( $[Cp^*Rh(bpy)H_2O]^{2+}$ ).<sup>[6]</sup> With these photocatalytic NAD(P)H recycling systems, the TOF  $h^{-1}$  was reported to be 0.47 to 240,<sup>[6]</sup> indicating that all these approaches have very low to moderate efficiencies. The major problem with photosensitizers is the lack of specificity and the need of high energy wavelengths for operation.<sup>[6]</sup> On the contrary, the intriguing structure of PSI offers partially concealed cofactors, making PSI a moderately specific biological photosensitizer with the ability to function in the visible region of the light spectrum.

By mimicking nature, PSI was applied for NADPH recycling. To this end, we artificially reconstituted the photosynthetic electron transport chain using PSI, Fd, and FNR for light-driven NADPH regeneration (**Chapter 3, Figure 1**). In the PSI-Fd-FNR biocascade system,

## Chapter 6

the difference in the reduction potential of the proteins involved creates a paradigm for sequential electron transfer (**Figure 1A**). The series of electron transfer events that occur within the biocascade are represented below (**Figure 1B**). NADPH produced by the PSI-Fd-FNR biocascade was used to fuel three oxidoreductases.

To utilize isolated PSI efficiently, an optimal pH has to be established. However, as the biocascade has multiple enzymes, our objective was to find a suitable pH at which high NADPH production occurs within a reasonable period. To do so, the rate of NADPH production in the light-stimulated biocascade at three different pH conditions was examined. The NADPH production rate in the PSI-Fd-FNR biocascade at pH 7, pH 7.5, and pH 8 were 1.51, 1.73, and 1.17 mM/h, respectively (**Chapter 3, Figure 2**). A minor difference in NADPH production rate was noticed, possibly due to a minimal impact of the pH on the interaction between individual components of the PSI-Fd-FNR biocascade. This can be explained by the tightly coupled interaction events observed in the biocascade.

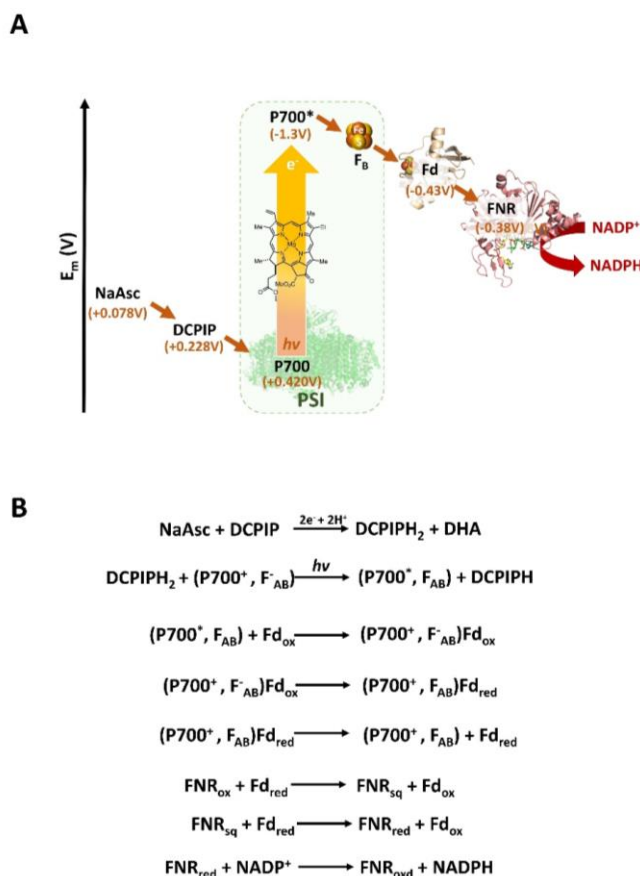


**Figure 1:** A) Illustration representing the varying midpoint potentials vs SHE of the PSI-Fd-FNR biocascade components that facilitates electron transfer.<sup>[12–17]</sup> B) Illustration representing the series of electron transfers within the PSI-Fd-FNR biocascade. Both illustrations were adapted from **Publication 2** (Chapter 3, Medipally et al., 2023, Fig. 2, and Fig. S2).

Due to the excess of NaAsc in the reaction solution, DCPIP was immediately reduced to form DCPIPH<sub>2</sub>.<sup>[13]</sup> The small size and hydrophobic nature of DCPIPH<sub>2</sub> enables it to interact with the luminal side of PSI, thus resulting in fast electron transfer between DCPIPH<sub>2</sub> and P700, the primary chlorophyll (Chl) molecule. The ratio of PSI: DCPIP was 1:1400, and the ratio of PSI: NaAsc was 1: 10<sup>6</sup>. As mentioned, the high concentrations of DCPIP and NaAsc are used for the faster reduction of P700.

Fd associates with PSI by interacting with three subunits of PSI, PsaA, PsaC, and PsaE. Most of the interactions are of electrostatic or hydrophobic nature.<sup>[18]</sup> According to Li et al., 2022, these electrostatic interactions primarily enable the association of Fd with PSI, contributing to the negative enthalpy.<sup>[18]</sup> On the other hand, upon binding of Fd with PSI, the displacement of water molecules on the interaction surfaces energetically favors an increase in enthalpy, leading to the complexation of Fd with PSI for electron transfer.<sup>[18]</sup> Thus, electron transfer between PSI and Fd is entropy-driven<sup>[18]</sup>, independent of slight changes in the pH. Fd interacts with FNR via salt bridges and hydrophobic interactions. The critical insight into the Fd-FNR interaction was derived from the crystallography and mutational study of maize leaf Fd and FNR.<sup>[19]</sup> The dissociation constant of the Fd-FNR complex hardly changes at ionic strength above 80 mM<sup>[20]</sup>, indicating that a slight change in pH may not impact the interactions between Fd and FNR. To conclude, under the given reaction conditions, the ratio of protein concentrations in the PSI-Fd-FNR biocascade and the ionic strength of the reaction are suitable to attain fast electron transfer and might explain why only a minor pH effect was noticed.

Further, PSI-Fd-FNR biocascade was coupled to three different oxidoreductases reaching upto 99% conversion and retaining the enantioselectivity. The possibility of large-scale application of PSI-Fd-FNR biocascade is discussed in the section 6.3.

### 6.3 Upscaling of PSI-Fd-FNR biocascade

The application of biocatalytic reactions for large-scale production depends mainly on the cost of biocatalyst, biocatalyst performance, biocatalyst stability and choice of starting materials. Cost of the biocatalyst is an important factor for large scale application<sup>[23]</sup>, which depending on the type of enzyme can vary from single-digit cent kg<sup>-1</sup> (hydratase or isomerase) to several hundred euros kg<sup>-1</sup> (cytochrome P450).<sup>[21]</sup> The enzymes used for NADPH recycling systems as mentioned in **Table 1** can be produced in sufficient amounts via recombinant over-expression from *E. coli*. In case of the PSI-Fd-FNR biocascade, Fd and FNR can be produced in sufficient



amounts via recombinant over-expression in *E. coli*, but PSI cannot be prepared from *E. coli*. In our study, PSI was isolated from *Synechocystis* sp. PCC 6803 (*Synechocystis* sp.) and *Thermosynechococcus vestitus* BP1 (*T. vestitus* BP1). This involves cell disruption, membrane solubilization and subsequently, three-column chromatography-based protein purification steps. This makes the current PSI isolation process very expensive and tedious. A large-scale application would require the steps of this process to be optimized.

In this study the disruption of the cells was realized by a high energy-consuming devices like the French press or Parr bomb and a bead mill. Recently, a biotechnological approach was reported to disrupt the cells without the need for mechanical pressure. In this method, lytic genes encoding holin and endolysin were expressed under green-light regulated *cpcG2* promoter. This has enabled cell disruption upon illumination with a green light.<sup>[22]</sup> In the future, implementing this method for cell disruption may reduce the economic and energy cost of the downstream process. The next required step in the PSI isolation process is membrane solubilization. It is necessary to isolate PSI in its purest form, because in nature, PSI is embedded in the thylakoid membrane. In our study, expensive detergent  $\beta$ -maltoside was used to solubilize the membrane, making the isolation of PSI highly unsustainable and cost-ineffective. Using cheap detergents, including triton X-100 was previously reported to isolate PSI from *Arthrospira platensis* without compromising the activity of PSI, which remains promising.<sup>[23]</sup> Alternatively, the use of styrene-maleic acid copolymer (SMA polymers) was reported to be cost-effective and non-detergent based approach.<sup>[24,25]</sup> Also, by using  $\alpha$ -olefin-maleic acid copolymers trimeric PSI was extracted from cyanobacterial membranes with high efficiency.<sup>[26]</sup> Apart from economic reasons, polymer based approaches are known to isolate the membrane protein complexes by preserving the native membrane composition around the protein complex, which may improve their functionality and stability.<sup>[24]</sup> In the future synchronizing, the lytic cell disruption followed by polymer-based PSI-Histag isolation may reduce the cost and tedious downstream process (**Figure 2**).<sup>[24,25]</sup>

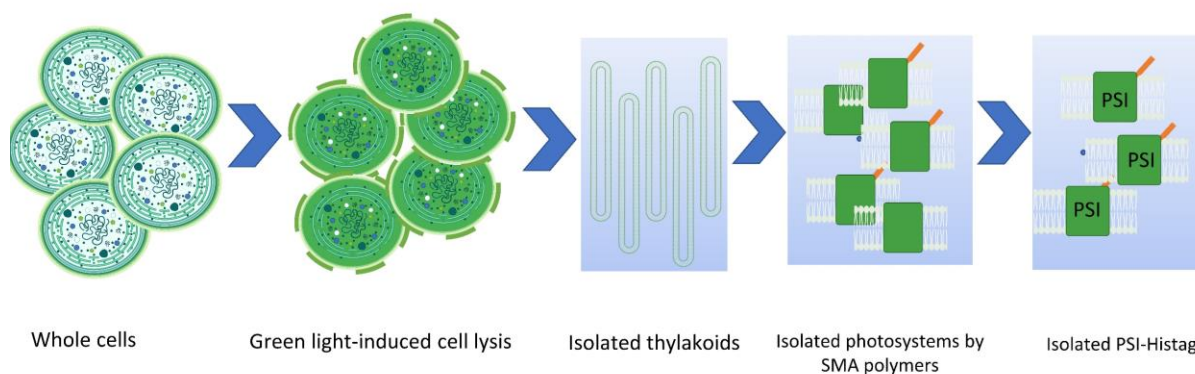


**Figure 2: Schematic representation of a proposed novel method for isolating PSI from Cyanobacteria.**

To reduce the cost of the biocatalyst further a clickable PSI model (see section 6.4) can be explored, which can be achieved by over-expression of E7-Fd-FNR gene fusion within *Synechocystis* sp. PCC 6803 PSI-Im7 mutant. With this approach, all the components of the PSI-Fd-FNR biocascade can be obtained from *Synechocystis* sp. Thereby, additional cost associated with over-expression of Fd and FNR in *E. coli* may be avoided.

For successful upscaling of biocatalytic reactions some of the key performance indicators are the following: speed of the reaction, selectivity/ enantiomeric excess (ee), substrate loading ( $\text{g L}^{-1}$ ), space-time yield (STY) ( $\text{g}_{\text{product}} \text{L}^{-1} \text{d}^{-1}$ ) and catalyst yield ( $\text{g}_{\text{product}}/\text{g}_{\text{cat}}$ ).<sup>[21]</sup> Speed of the reaction can be one of the important requirements considering the timelines in pharmaceutical industry.<sup>[23]</sup> The TOF of PSI-Fd-FNR biocascade at pH 7.5, was  $2.55 \text{ s}^{-1}$  and TOF of GDH with 260  $\text{s}^{-1}$  is far high and making it the better candidate for large-scale applications. In our study, PSI-Fd-FNR was successfully coupled with *Lactobacillus brevis* alcohol dehydrogenase (*LbADH*) which is known to produce chiral alcohols. To have deeper understanding of our system, PSI-Fd-FNR biocascade coupled to *LbADH* was compared to KRED (EC 1.1.1.184) coupled to GDH (EC 1.1.1.47). PSI-Fd-FNR biocascade coupled to *LbADH* showed successful production of phenylethanol. In case of KRED coupled to GDH, atorvastatin, the active ingredient of the drug Lipitor®, was produced.<sup>[27]</sup> Firstly, both the recycling methods used have maintained the ee of the biocatalytic reaction  $> 98\%$ .<sup>[21]</sup> Secondly, the substrate loaded in case of PSI-Fd-FNR biocascade was  $< 1 \text{ g L}^{-1}$ , whereas the substrate loaded in case of KRED coupled to GDH was  $> 160 \text{ g L}^{-1}$ .<sup>[21]</sup> Lastly, the STY of PSI-Fd-FNR biocascade coupled with *LbADH* was estimated to be  $< 1 \text{ g}_{\text{product}} \text{L}^{-1} \text{d}^{-1}$  whereas the KRED coupled to GDH process was estimated to be  $> 384 \text{ g}_{\text{product}} \text{L}^{-1} \text{d}^{-1}$ .<sup>[27]</sup> The good performance of KRED coupled to GDH serves as an example for the potential of improvement in PSI-Fd-FNR biocascade coupled to *LbADH*. The substrate loading capacity of PSI-Fd-FNR biocascade coupled to *LbADH* was not tested to

its limits, thereby a space for improvement can be expected. With series of further optimizations, the catalytic performance of PSI-Fd-FNR biocascade can be increased substantially. This includes optimization of biocascade with required amounts of electron donors, like DCPIP and NaAsc, addition of excess NADP<sup>+</sup>, enhancing the speed of the reaction by tuning the ratio of PSI, Fd, and FNR (currently 0.5:4:1). Additionally, the catalytic performance of PSI-Fd-FNR biocascade can be enhanced by enzyme engineering.

The operational stability of the biocatalyst used is also essential for large-scale applications. In the reaction conditions used for the PSI-Fd-FNR biocascade (< 30 °C, pH 7-8, red light, give timespan) there seemed to be no protein stability issue. However long-term stability could an issue. Here PSI is specially focused, which probably is the most sensitive protein component in the PSI-Fd-FNR biocascade. PSI is a membranal protein complex located in the thylakoid membrane of photosynthetic organisms. Reactive oxygen species (ROS) are the key players to influence the stability of PSI. The native environment of PSI consists of ROS scavenging agents, which circumvent the damage of PSI from ROS.<sup>[28]</sup> Jensen et al., reported that addition of catalase PSI reaction media would help avoiding the ROS formation, thereby the damage to PSI can be prevented.<sup>[29]</sup> Also, it is essential to build a reaction setup, which ensures the operational stability and long-term endurance of the system. In this regard, immobilization of the PSI-Fd-FNR biocascade could be an attractive strategy. This is because immobilized enzymes are reported to be stable then the soluble enzymes.<sup>[30]</sup> For instance, using clickable PSI model (see section 6.4), PSI, Fd and FNR can be coupled together and further immobilization on conductive surfaces improve the functional stability. Furthermore, Kiley et al., reported that the use of peptide detergents (A6K) to improve the structural stability of PSI on a dry surface for 21 days.<sup>[31]</sup> Additionally, the structural stability of PSI can be improved by physical interaction with surfaces via covalent linkages, encapsulation, and cross-linking. Both the approaches may palliate the effects of desorption, dissolution, and interaction with bulk electrolytes. In a study by Cherubin et al., PSI was encapsulated in polylactic-co-glycolic acid (PGA) and chitosan microparticles. PGA-encapsulated PSI was stable for > 34 days under continuous light.<sup>[32]</sup> In the future, assimilating the knowledge from previous studies and careful integration of fused PSI-Fd-FNR biocascade without compromising on the redox interface may enable the large-scale upscaling of PSI-Fd-FNR biocascade. However, all these methods also drive the cost of upscaling.

Reaction optimization is one of the crucial steps to be considered for large scale application of PSI-Fd-FNR biocascade. Recognizing and addressing the side reactions is essential. Under aerobic reaction conditions, all the components of the PSI-Fd-FNR biocascade are known to undergo side reactions with O<sub>2</sub>. Given the presence of dissolved oxygen, the PSI-Fd-FNR biocascade might produce reactive oxygen species, which may reduce the half-life of the enzymes in the PSI-Fd-FNR biocascade. Interestingly, we did not observe a significant difference in the rate of NADPH production in the PSI-Fd-FNR biocascade exposed to oxygen. This could be due to the efficient and tightly coupled electron transfer steps between the components of the PSI-Fd-FNR biocascade (**Chapter 3, Figure 2**) and also due the higher second-order rate constant between PSI and Fd than to O<sub>2</sub>, which are  $3.5 \times 10^8 \text{ M}^{-1} \text{ s}^{-1}$  and  $7.5 \times 10^4 \text{ M}^{-1} \text{ s}^{-1}$ , respectively.<sup>[33]</sup> Over time, a faster decline in NADPH in aerobic conditions than in anaerobic conditions was observed, indicating that the decline in NADPH is due to the FNR oxidase activity. Also, the decline in NADPH over time observed under oxygen-free conditions could be due to the influence of temperature and pH. Both NADPH and NADP<sup>+</sup> are susceptible to thermal decomposition at 19 °C the half-life of NADPH is 8 h at pH 7, whereas at 41 °C the half-life of NADPH was determined to be 1 h at pH 7.<sup>[34]</sup> During the PSI-Fd-FNR biocascade reaction, temperature was increased from 25 °C to 31 °C (**Chapter 3, Figure S9**) Thus, temperature might be one of the main factors responsible for influencing the decrease in NADPH over time. Furthermore, the pH has a significant effect on the stability of NADPH. At pH 7 the stability of NADPH is lower than at pH 8. Interestingly, this observation correlates with our results (**Chapter 3, Figure 2**), where the decline in NADPH concentration was higher at pH 7 compared to pH 8. At basic conditions, the pyridine nucleotide undergoes nucleophilic attack at the C2 or C4 position of the nicotinamide ring, thus leading to ring opening.<sup>[35,36]</sup> Whereas, in acidic pH, hydration of the 5,6 C=C bond by proton addition at C5 and nucleophile attack at C6 of the pyridine ring occurs.<sup>[35,37]</sup> Also, phosphate contributes to the breakdown of NADPH.<sup>[38]</sup> To conclude, though several components of the PSI-Fd-FNR biocascade can undergo side reactions with oxygen, the NADPH production rates remained the same in oxygen-exposed and oxygen-free samples due to the much higher second-order rate kinetics of electron transfer between the protein components of the PSI-Fd-FNR biocascade outperforming the intervention of oxygen. The faster decline in NADPH in long-term oxygen-exposed reactions compared to oxygen-free reactions is likely due to FNR oxidase activity, indicating that it may be advantageous to maintain an oxygen-free environment for large-scale application.

## Chapter 6

Also, light plays a crucial role in the biocatalytic performance of PSI-Fd-FNR biocascade. In this study, PSI was excited by red light ( $\lambda=685$  nm) with intensity of 500  $\mu\text{E}$ . Using high light conditions will improve the initial rates of PSI-Fd-FNR biocascade but may undermine the long-term operational stability of PSI-Fd-FNR biocascade. In future, optimization of light conditions would further improve the biocatalytic performance of PSI-Fd-FNR cascade. Also, in our reaction setup light was illuminated from the sides of the reaction vial, which may have compromised the performance of the PSI-Fd-FNR biocascade. In future designing a photobioreactor with uniform light distribution may improve the biocatalytic performance of the system. For instance, with wireless internal light illumination in bubble column reactor the light driven biocatalytic performance was shown to improved.<sup>[39]</sup> Also, sun light dependent flat plate bioreactor can be an attractive option for large-scale application of PSI-Fd-FNR biocascade.

Further, PSI-Fd-FNR biocascade was compared with other NADPH recycling systems in terms of cost of the substrate, atom efficiency, and easiness in product isolation. PSI-Fd-FNR biocascade and GDH utilizes NaAsc and glucose as a substrate and produces by-products dehydroascorbate and gluconic acid, respectively. The by-product formed will pose a challenge to separate the product from the reaction mixture. In the case of PTDH and FDH, utilizes phosphite and formate as substrate and produces the byproduct, phosphate and carbon dioxide, which can be easily removed by calcium precipitation and agitation, respectively. Thereby, product workup would be easy. However, all the above-mentioned byproducts are biodegradable. Additionally, both light-driven systems mentioned in Table 1 are atom inefficient, and product workup would also be difficult. All the mentioned systems are shown to exhibit low to moderate atom efficiency. Therefore, atom-efficient systems are needed. In nature, PSI obtains electrons from the water splitting activity of PSII. With inspiration from nature, developing an in vitro system, that enables PSI to function just on water and light would be an excellent alternative

Finally, by synchronizing all the approaches and methods, it is possible to apply PSI-Fd-FNR biocascade as a chemical production platform. However, a detailed economic and life cycle assessment is required to validate the applicability and sustainability of each process.

**Table 1: Comparison of PSI-Fd-FNR with other NADPH recycling system**

NADPH recycling	TOF <sup>a</sup>	cost of the substrate (in EUR) <sup>d</sup>	Atom efficiency	Ease of work-up	Reference
PSI-Fd-FNR	2.55 <sup>a</sup>	20	-	+	In this study
GDH	260	10	-	+	[40]
FDH	1.07	4	++	+++	[41]
PTDH	0.57	10	++	++	[42]
FNR-QD	0.40 <sup>b</sup>	20	-	+	[43]
Graphene-photocat-Rh	0.004 <sup>c</sup>	20	-	+	[44]

Note: [a] TOF = ([substrate]/[catalyst])/time, based on 10 min time points (0.57  $\mu$ M PSI, 3 mM NADP<sup>+</sup>). [b] TOF based on 2 h. [c] TOF based on 348 d<sup>-1</sup>. [d] prices were calculated based on the price value as of 02.10.23 obtained from Thermoscientific Ltd. and Sigma-Aldrich Ltd. and later divided by a factor of ten [e] Ranking order: + + +: Very good, + +: good, +: moderate, -: poor. n. a.: not available. Comparison adapted from reference [5] and this study.

## 6.4 Clickable PSI: A plug-and-play approach

Clickable PSI is an interesting option for the molecular confinement of a PSI-Fd-FNR biocascade together. Here, shortly, the other PSI fusion strategies that have been used for building semi-artificial photosynthetic devices are discussed.<sup>[2]</sup> A particular focus lies on the production of hydrogen. To this end, PSI was combined with inorganic catalysts, including a Pt ligand<sup>[45]</sup>, a nickel (II) diphosphine complex<sup>[46]</sup> or biocatalysts, including Fe-Fe hydrogenase<sup>[47,48]</sup> and Ni-Fe hydrogenase<sup>[49]</sup>

So far, four distinct approaches have been developed for in vitro modification of PSI. In the first approach, Greenbaum et al. and Sliver et al. coupled metal catalysts with PSI by directly precipitating a charged Pt ligand and a nickel (II) diphosphine complex onto PSI for hydrogen production (**Chapter 1, Figure 15**).<sup>[45,46]</sup> In the second approach, a dithiol linker connecting the F<sub>B</sub> cluster of PSI with the catalyst was developed by the ligand recuse method.<sup>[50]</sup> In this method, cysteine at position 13 was replaced with glycine in the PsaC subunit of PSI and later recombinantly expressed in *E. coli*.<sup>[50]</sup> Subsequently, this subunit was artificially reconstituted with the Fe-S cluster, which allows tethering of one end of the thiol linker to the F<sub>B</sub> cluster and the other end to the catalyst.<sup>[51,52]</sup> This method allows the tethering of metal catalysts, including Pt ligands, and biological catalysts, including hydrogenases (**Chapter 1, Figure 16 & 17**).<sup>[47,48,51]</sup> In the third approach, PSI-PsaE less complex was isolated from *Synechocystis* sp. PSI- $\Delta$ PsaE- mutant and later reconstituted with a Fd-PsaE fusion, resulting in the formation



of a PSI-Fd fusion complex (**Chapter 1, Figure 19**).<sup>[3]</sup> The fourth approach involves stromal stripping, as described in Wittenberg et al., where stromal subunits of PSI were stripped by exposing PSI to high salt concentration.<sup>[4]</sup> This disrupted the ionic interaction of stromal subunits with the PSI core, causing the stromal subunits dissociation. Subsequently, an Fd-PsaE fusion, along with heterologously expressed remaining stromal subunits (PsaD, PsaC), were artificially reconstituted with the PSI core, thereby transforming into a fully functional PSI-Fd fusion complex (**Chapter 1, Figure 18**).<sup>[4]</sup>

Clickable PSI is a genetically modified PSI complex that offers a unique possibility to fuse various biocatalytic modules. This was achieved in this PhD study by establishing the E7-Im7 affinity system. The PSI-Im7 complex could be successfully isolated from *Synechocystis* sp. PCC 6803 PSI-Im7 mutant and biochemically characterized (**Chapter 4, Figure 1**). E7-DNase (E7), Fd, fusion protein (EF) and E7-DNase (E7), Fd, FNR fusion protein (EFF) were prepared from *E. coli* and biochemically characterized (**Chapter 4, Figure 2**). Due to the strong affinity of the E7-Im7 system, EF or EFF were fused onto PSI-Im7 (**Chapter 4, Figure 3**). To our knowledge, this is the first-ever model that can allow fusing both mediator and biocatalyst onto PSI. PSI-Im7 is also interesting concerning the targeted orientation of biocatalysts onto PSI and its easiness of establishment in vivo. In this study, PSI-Im7 was coupled with EF with different linker lengths of 5, 10, and 15 (PSI-EF5, PSI-EF10, PSI-EF15). The efficiency of these chimeric proteins was tested based on the light-induced NADP<sup>+</sup> reduction rate by artificial reconstitution of the photosynthetic electron transport chain. The NADP<sup>+</sup> reduction rates of FPS1 (the free protein system), PSI-EF10, PSI-EF5, PSI-EF15 were observed to be  $2.05 \pm 0.22$ ,  $2.49 \pm 0.08$ ,  $2.02 \pm 0.29$  and  $1.51 \pm 0.20 \mu\text{M NADPH min}^{-1}$ , respectively (**Chapter 4, Figure.4**). PSI-EF10 was observed to perform best, indicating that a linker length of 10 AA is optimal for the electron transfer between PSI, Fd, and Fd, FNR.

PSI-Im7 was fused with EFF fusion proteins, consisting of a constant linker length of 10 AA between E7 and Fd, a variable linker of 5,10,15 between Fd and FNR (PSI-EFF5, PSI-EFF10, PSI-EFF15). The initial rates of NADP<sup>+</sup> photoreduction of FPS2, PSI-EFF5, PSI-EFF10, and PSI-EFF15 were  $5.30 \pm 0.62$ ,  $3.60 \pm 0.21$ ,  $1.63 \pm 0.15$ ,  $1.07 \pm 0.03 \mu\text{M NADPH min}^{-1}$ , respectively (**Chapter 4, Figure 5**). The electron transfer rates of all PSI-EFF chimeras were slightly lower compared to FPS2 (the free protein system 2). This is due to the two-sided tethering of Fd, which may have introduced steric hindrance that prevents the simultaneous exchange of Fd<sub>ox</sub> with Fd<sub>red</sub> at the Fd binding site of FNR.



Interestingly, we observed a clear decrease in NADP<sup>+</sup> reduction rate with an increase in linker length between Fd and FNR, indicating that longer linkers of 10 and 15 AA slow down the electron transfer between Fd and FNR.

Previously, protein-protein interaction in PSI-hydrogenase fusion protein was studied by Harris et al., using molecular dynamics (MD) simulation.<sup>[53]</sup> PSI was obtained from *T. vestitus* BP1 and Fe-Fe hydrogenase from *Clostridium pasteurianum*. This study is based on experimental data of PSI-hydrogenase, which is covalently linked by dithiol linkers, including decanedithiol, octanedithiol and hexanedithiol.<sup>[53]</sup> An analysis involving root-mean-squared fluctuations (RMSFs) and assessment of inter and intraprotein electron transfer within fusion proteins revealed that short-length hexanedithiol linker hinders the electron transfer. This insight helped elucidate the high hydrogen production of medium-length octanedithiol linkers.<sup>[53]</sup> Similarly, performing the MD simulations for PSI-EF and PSI-EFF chimeras might help to understand and redesign our PSI model for better electron transfer efficiency. Additionally, In PSI chimeras, the linkers consist of repeats of glycine (G) and serine (S) with a series of repetitive GGS motifs that offer flexibility and good stability. Recently however, the PSI-PsaE-HoxYH fusion with linker EKSSGSGSESKSTEKS was observed to be the best performing.<sup>[54]</sup> This shows that an in-depth understanding of the fusion/linker concept will be fruitful to build an optimal PSI fusion complex for particular application. Nevertheless, clickable PSI can be applied for building next generation biohybrid solar cell (see section 6.7).

## 6.5 Capturing electrons from whole cells

Isolated photosystems are excellent candidates for harvesting photo-energized electrons that can be channelized for chemical production (publications 2 and 3), CO<sub>2</sub> fixation<sup>[55]</sup> and H<sub>2</sub> production.<sup>[56]</sup> In parallel, using photosynthetic organisms to produce electricity has gained significant interest and emerged into a new field called biophotovoltaics (BPV). Photosynthetic organisms, including cyanobacteria, can be an excellent choice for BPV because they can act as exoelectrogen.<sup>[56]</sup> An exoelectrogen is a microorganism that can transfer electrons extracellularly.<sup>[56]</sup> The BPV approach is based on establishing an electron transfer process between the photosynthetic apparatus and extracellular electrodes.<sup>[56]</sup> Photosynthetic organisms expel electrons to maintain the redox state of cells by adapting to the changing external environment.<sup>[57]</sup> In Cyanobacteria, plastoquinone (PQ) and quinol oxidase plays an important

role in transferring electrons.<sup>[58]</sup> Additionally, NADPH is believed to be an endogenous electron mediator involved in electron transfer.<sup>[59,60]</sup>

Therefore, it is crucial to understand how the electrons escape from the photosynthetic apparatus. Baikie & Laura et al., studied the photodynamics of photosystems using in vivo ultrafast transient spectroscopy (TA spectroscopy) (**Chapter 5**, Baikie & Wey et al., 2023). In this study, *Synechocystis* sp. Wt strain, *Synechocystis* sp. without PSII or PSI, isolated PSI and PSII were subjected to TA spectroscopy. TA spectroscopy can be regarded as an extension of absorption spectroscopy. It measures the change in transmittance/absorbance of the sample upon excitation by a flash of light. In this technique, a broadband probe laser is used to measure sample absorbance after photoexcitation with a pump laser, enabling access to the photodynamics of the photosystems in a sub-picosecond timescale. The effect of exogenous electron mediators on the photodynamics of cyanobacterial cells by using dichlorobenzoquinone (DCBQ) was probed. Interestingly, it was found that DCBQ can alter the photosynthetic reaction centers and excited state decay on a sub-picosecond timescale. Previously, it was believed that DCBQ obtains electrons from the Q<sub>B</sub> pocket of PSII. However, with the mid-point potential of +315 V vs. SHE, it is possible to extract electrons from P700/P700\* or P680/P680\*, indicating that DCBQ can obtain electrons from PSI and PSII. Also, by further optical characterization of suspension cells with DCBQ, the reduction of DCBQ via fluorescence of intact cells was observed. It was resolved that Forster resonances are not active, indicating that the DCBQ interferes with the electron transfer mechanisms. With these considerations, it was proposed that upon photoexcitation, the Chl of photosystems enter highly delocalized intermediate charge transfer states followed by electron transfer. Additionally, cell absorption spectra remained unchanged even with an increase in the concentration of DCBQ. This suggests that DCBQ does not bind tightly to Chl in the core of the reaction center but interacts with peripheral Chls. A control experiment performed with 3-(3,4-Dichlorophenyl)-1,1-dimethylurea (DCMU) to support the proposed mechanistic insight. DCMU binds at the Q<sub>B</sub> binding site of PSII, which may compete with DCBQ (**Chapter 5, Figure.2d**). TA spectroscopy in the presence of DCMU and DCBQ yielded similar effects as DCBQ alone. An additional photoelectrochemistry experiment conformed the existence of an alternative binding site at Q<sub>B</sub> site.

It was long believed that the reaction centers within photosystems are insulated. However, using exogenous electron mediators, it is possible to obtain electrons from the protein scaffolds of PSI and PSII as they are leaky. This was proven by the electron extraction from the initial

photoexcited state of photosystems using DCBQ and Methyl viologen (MV). The interaction of photosystems is not just confined to a particular class of mediators. Hence, this study, helps us understand and design an electron transfer pathway between cells and electrode for building efficient biophotovoltaic systems.

Biophotovoltaics systems can provide power in milliwatt to watt.<sup>[56]</sup> To supply power for domestic purposes, substantial improvements are needed in the biophotovoltaics systems. This improvement should be achieved in a bottom-up approach, i.e. improvement through biophotovoltaic cell to biophotovoltaic panel.<sup>[56]</sup> Currently, biophotovoltaic systems are limited due to the mismatch between high quantum efficiency driven charge separation of photosystems with poor exoelectrogenicity. With our contemporary understanding of electron transfer from photosystems, we could improve the efficiency of exoelectrogenicity. This can be achieved by bioengineering the cells with novel endogenous electron mediators or by nanowiring in vivo photosystems with ex vivo electrodes. Recently, single-walled carbon nanotubes (SWCNTs) in combination with cyanobacteria has significantly improved exoelectrogenicity of cyanobacteria.<sup>[61]</sup> In this study, lysozyme coated SWCNTs were spontaneously penetrated the cell wall and cell membrane, subsequently found to be distributed on the peripheral regions.<sup>[61]</sup> Thereby, likely acting as an electron circuit. In future, by nanoengineering, a target-oriented internalization of SWCNTs near photosystems may allow electron extraction and conduction in a rapid fashion. This may improve the efficiency of biophotovoltaic systems.

### **6.6 Clickable PSI-based rational electron partitioning for efficient chemical production in cyanobacteria**

In recent years, an increased concern for the environment has led humanity to find sustainable alternatives for chemical production. Using cyanobacteria as a biocatalyst for chemical production provides an excellent option as cyanobacteria depend on abundant resources like water, carbon dioxide, and light. This has motivated to use cyanobacteria as a host for various enzymes, particularly reductases<sup>[62,63]</sup>, dehydrogenases<sup>[64]</sup> and monooxygenases.<sup>[65]</sup> These enzymes are mainly employed for the reduction of double bonds or the transformation of alcohols to ketones, and for various oxyfunctionalization reactions. These catalysts can be readily expressed in high amounts by heterologous gene expression.<sup>[64]</sup> The heterologously expressed enzymes rely on photosynthetic electron transport chain (PETC) for reductant (Fd, NADPH) generated by water oxidation of PSII.<sup>[63,65]</sup> In recent years, significant improvements have been made to divert the reductant flux of the PETC to the synthetic biocatalytic reaction.

## Chapter 6

One of the most significant and widely reported approaches was to knockout the genes coding for alternative electron sink sources (AES).<sup>[63,66]</sup> AES can act as an electron sinks in PETC that can dissipate the excess photosynthetic energy in case of highlight. These mechanisms are crucial for photosynthetic organisms as they experience dynamic light fluctuations, the so-called clouding effect, in nature.<sup>[67]</sup> AES in cyanobacteria are flavodiiron proteins, alternative respiratory oxidase, *bd*-quinol oxidase, and cytochrome c oxidase.<sup>[67,68]</sup> By genetic knockout of AES and simultaneously expressing the heterologous sink in photosynthetic organisms showed a significant increase in chemical production.<sup>[67]</sup> However, deleting multiple alternative electron sink sources is often a trade-off due to the slow growth.<sup>[68]</sup>

Further, the determined intracellular ratio of PSI, Fd, and FNR is 1:1.11:0.24, respectively, in *Synechocystis* sp.<sup>[3]</sup> Additionally, most of the reduced Fd in vivo are diverted to FNR because of the fair abundance of FNR in the cyanobacteria compared to other oxidoreductases, closer confinement of FNR towards PSI, and the high affinity of Fd towards FNR.<sup>[69–72]</sup> Due to this, the reductant flux diverted from PSI to FNR is almost one order of magnitude higher than for oxidoreductases.<sup>[73]</sup>

Mimicking nature by confining a protein of interest near the thylakoid membrane is a promising approach. Previously, cytochrome P450 (CYP79A1) with membrane-spanning protein Psam was expressed in *Synechococcus* sp. PCC 7002 for better access to reductants.<sup>[74]</sup> Masica et al., established cytochrome p450 (CYP110D1) fused to Fd in *Synechocystis* sp. for accessing electrons directly from PSI.<sup>[65]</sup> Yacoby et al., developed a hydrogenase fused to Fd with the aim of diverting the photosynthetic electrons towards hydrogen production in vitro.<sup>[75]</sup> Recently, Appel et al., and Kanygin et al., fused hydrogenase directly onto the Psad and Psac subunits of PSI, respectively.<sup>[49,76]</sup> The former was implemented in *Synechocystis* sp. and later in *Chlamydomonas reinhardtii*. Both approaches diverted the electrons towards hydrogen production directly from PSI.<sup>[49,76]</sup>

In contrast, Medipally et al., established a clickable PSI model that may allow fusing a myriad of enzymes onto PSI without interfering with the photosynthetic electron transport. With this approach, the mediator (usually Fd) and enzyme of interest can be fused onto PSI. Based on the physiological and biochemical characterization of PSI-Im7 mutant form *Synechocystis* sp. and isolated PSI-Im7, no compromise in the function of the mutant was observed (**Chapter 4, Supplementary Information Figure 1&2**). However, in the case of PSI-hydrogenase fusion,

several physiological constraints were noted in both the mutants, including slow growth and reduction in the binding ability of Fd binding to PSI. Moreover, this model cannot be translated and applied to other enzymes as each has a different reaction mechanism.<sup>[49,76]</sup> In light of the above considerations, implementing the PSI-Im7 model in vivo for hydrogen production could be a promising approach (**Figure 5**). Implementing this approach enables the Hyd to compete with other oxidoreductases and obtain electrons from PET. However, with the sensitivity of Hyd to oxygen and the typical low expression of exogenous enzymes in cyanobacteria, the impact of repair and recycling of photosynthetic machinery on the fusion can be identified as a potential risk.

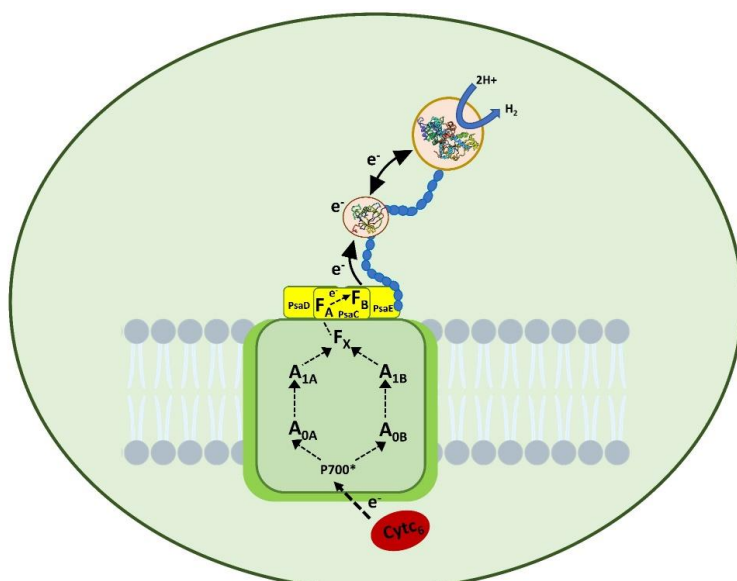


**Figure 5: Schematic representation of PSI-Fd-Hyd construct based whole cell hydrogen production.**

## 6.7 References

- [1] N. N. and A. Ben-Shem, *Nature reviews* **2004**, 5, 1–12.
- [2] K. Nguyen, B. D. Bruce, *Biochim Biophys Acta Bioenerg* **2014**, 1837, 1553–1566.
- [3] G. Moal, B. Lagoutte, *Biochim Biophys Acta Bioenerg* **2012**, 1817, 1635–1645.
- [4] G. Wittenberg, W. Sheffler, D. Darchi, D. Baker, D. Noy, *Phys. Chem. Chem. Phys* **1960**, 15, 19608–19614.
- [5] A. H. Teodor, B. D. Bruce, *Trends Biotechnol* **2020**, 38, 1329–1342.
- [6] X. Wang, T. Saba, H. H. P. Yiu, R. F. Howe, J. A. Anderson, J. Shi, *Chem* **2017**, 2, 621–654.
- [7] J. Hong Kim, M. Lee, J. Seok Lee, C. Beum Park, J. H. Kim, M. Lee, J. S. Lee, C. B. Park, *Angew. Chem. Int. Ed* **2012**, 51, 517–520.
- [8] D. H. Nam, C. B. Park, *ChemBioChem* **2012**, 13, 1278–1282.
- [9] J. Ryu, S. H. Lee, D. H. Nam, C. B. Park, *Adv Mater* **2011**, 23, 1883–1888.
- [10] Z. Jiang, C. Lü, H. Wu, *Ind Eng Chem Res* **2005**, 44, 4165–4170.
- [11] J. Liu, J. Huang, H. Zhou, M. Antonietti, *ACS Appl Mater Interfaces* **2014**, 6, 8434–8440.
- [12] N. Cassan, B. Lagoutte, P. Sétif, *J. Biol. Chem* **2005**, 280, 25960–25972.
- [13] A. Petrova, M. Mamedov, B. Ivanov, A. Semenov, M. Kozuleva, *Photosynth Res* **2018**, 137, 421–429.
- [14] D. Dvoranová, Z. Barbieriková, S. Dorotíková, M. Malček, A. Brincko, L. Rišpanová, L. Bučinský, A. Staško, V. Brezová, P. Raptá, *J Solid State Electrochem* **2015**, 19, 2633–2642.
- [15] J. S. Fruton, *J. Biol. Chem.* **1934**, 105, 79–85.
- [16] T. Kothe, N. Plumeré, A. Badura, M. M. Nowaczyk, D. A. Guschin, M. Rögner, W. Schuhmann, *Angew. Chem. Int. Ed* **2013**, 52, 14233–14236.
- [17] A. Badura, D. Guschin, T. Kothe, M. J. Kopczak, W. Schuhmann, M. Rögner, *Energy Environ Sci* **2011**, 4, 2435.
- [18] J. Li, N. Hamaoka, F. Makino, A. Kawamoto, Y. Lin, M. Rögner, M. M. Nowaczyk, Y.-H. Lee, K. Namba, C. Gerle, G. Kurisu, *Commun Biol* **2022**, 5, 951.
- [19] G. Kurisu, M. Kusunoki, E. Katoh, T. Yamazaki, K. Teshima, Y. Onda, Y. Kimata-Ariga, T. Hase, *Nat Struct Biol* **2001**, 8, 117–121.
- [20] A. N. Diakonova, S. S. Khrushchev, I. B. Kovalenko, Y. Riznichenko, A. B. Rubin, *Phys. Biol* **2016**, 13, 56004.
- [21] S. Wu, R. Snajdrova, J. C. Moore, K. Baldenius, U. T. Bornscheuer, *Angew. Chem. Int. Ed* **2021**, 60, 88–119.
- [22] K. Miyake, K. Abe, S. Ferri, M. Nakajima, M. Nakamura, W. Yoshida, K. Kojima, K. Ikebukuro, K. Sode, *Biotechnol Biofuels* **2014**, 7, 56.
- [23] D. Yu, G. Huang, F. Xu, M. Wang, S. Liu, F. Huang, *Photosynth Res* **2014**, 120, 311–321.
- [24] N. G. Brady, M. Li, Y. Ma, J. C. Gumbart, B. D. Bruce, *RSC Adv* **2019**, 9, 31781–31796.
- [25] O. Korotych, J. Mondal, K. M. Gattás-Asfura, J. Hendricks, B. D. Bruce, *Eur Polym J* **2019**, 114, 485–500.
- [26] C. E. Workman, P. Bag, B. Cawthon, F. H. Ali, N. G. Brady, B. D. Bruce, B. K. Long, *Angew. Chem. Int. Ed* **2023**, e202306572.
- [27] S. K. Ma, J. Gruber, C. Davis, L. Newman, D. Gray, A. Wang, J. Grate, G. W. Huisman, R. A. Sheldon, *Green Chem.* **2010**, 12, 81–86.
- [28] S. Khorobrykh, V. Havurinne, H. Mattila, E. Tyystjärvi, *plants* **2020**, 9, 1–63.

- [29] K. Jensen, J. B. Johnston, P. R. O. de Montellano, B. L. Møller, *Biotechnol Lett* **2012**, *34*, 239–245.
- [30] R. K. Singh, M. K. Tiwari, R. Singh, J.-K. Lee, *Int. J. Mol. Sci* **2013**, *14*, 14.
- [31] P. Kiley, X. Zhao, M. Vaughn, M. A. Baldo, B. D. Bruce, S. Zhang, *PLoS Biol* **2005**, *3*, 1180–1186.
- [32] A. Cherubin, L. Destefanis, M. Bovi, F. Perozeni, I. Bargigia, G. de La, C. Valbuena, || Cosimo D'andrea, A. Romeo, M. Ballottari, M. Perduca, *ACS Sustain Chem Eng* **2019**, *7*, 10435–10444.
- [33] G. E. Milanovsky, A. A. Petrova, D. A. Cherepanov, A. Y. Semenov, *Photosynth Res* **2017**, *133*, 185–199.
- [34] J. T. Wu, L. H. Wu, J. A. Knight, *Clin Chem* **1986**, *32*, 314–319.
- [35] S. L. Johnson, K. W. Smith, *J Org Chem* **1977**, *42*, 2580–2589.
- [36] S. L. Johnson, D. L. Morrison, *J. Biol. Chem.* **1970**, *245*, 4519–4524.
- [37] C. C. Johnston, J. L. Gardner, C. H. Suelter, D. E. Metzler, *Biochemistry* **1963**, *2*, 689–696.
- [38] S.G.A. Alivisatos, F. Ungar, G Abraham, *Nature* **1964**, *203*, 973–975.
- [39] M. Hobisch, J. Spasic, L. Malihan-Yap, G. D. Barone, K. Castiglione, P. Tamagnini, S. Kara, R. Kourist, *ChemSusChem* **2021**, *14*, 3219–3225.
- [40] K. Yamamoto, T. Nagao, Y. Makino, I. Urabe, H. Okada, *N Y Acad Sci* **1990**, *613*, 362–365.
- [41] H.T. Ding, D.F. Liu, Z.L. Li, Y.Q. Du, X.H. Xu, Y.H. Zhao, *J Appl Microbiol* **2011**, *111*, 1075–1085.
- [42] L. Zhang, E. King, W. B. Black, C. M. Heckmann, A. Wolder, Y. Cui, F. Nicklen, J. B. Siegel, R. Luo, C. E. Paul, H. Li, *Nat Commun* **2022**, *13*, 5021.
- [43] K. A. Brown, M. B. Wilker, M. Boehm, H. Hamby, G. Dukovic, P. W. King, *ACS Catal* **2016**, *6*, 2201–2204.
- [44] S. Choudhury, J.-O. Baeg, N.-J. Park, R. K. Yadav, *Green Chemistry* **2014**, *16*, 4389.
- [45] J. W. Lee, C. V. Tevault, S. L. Blankinship, R. T. Collins, E. Greenbaum, *Energy & Fuels* **1994**, *8*, 770–773.
- [46] S. C. Silver, J. Niklas, P. Du, O. G. Poluektov, D. M. Tiede, L. M. Utschig, *J Am Chem Soc* **2013**, *135*, 13246–13249.
- [47] C. E. Lubner, A. M. Applegate, P. Knörzer, A. Ganago, D. A. Bryant, T. Happe, J. H. Golbeck, *Proc Natl Acad Sci U S A* **2011**, *108*, 20988–20991.
- [48] C. E. Lubner, P. Knörzer, P. J. N. Silva, K. A. Vincent, T. Happe, D. A. Bryant, J. H. Golbeck, *Biochemistry* **2010**, *49*, 10264–10266.
- [49] J. Appel, V. Hueren, M. Boehm, K. Gutekunst, *Nat Energy* **2020**, *5*, 458–467.
- [50] M. L. Antonkine, E. M. Maes, R. S. Czernuszewicz, C. Breitenstein, E. Bill, C. J. Falzone, R. Balasubramaniam, C. Lubner, D. A. Bryant, J. H. Golbeck, *Biochimica Biophysica Acta Bioenerg* **2007**, *1767*, 712–724.
- [51] R. A. Grimme, C. E. Lubner, J. H. Golbeck, *Dalton Trans* **2009**, 10106–10113.
- [52] C. E. Lubner, R. Grimme, D. A. Bryant, J. H. Golbeck, *Biochemistry* **2010**, *49*, 404–414.
- [53] B. J. Harris, X. Cheng, P. Frymier, *J. Phys. Chem. B* **2016**, *120*, 599–609.
- [54] P. Wang, A. Frank, J. Appel, M. Boehm, N. Strabel, M. M. Nowaczyk, W. Schuhmann, F. Conzuelo, K. Gutekunst, *Adv Energy Mater* **2023**, *13*.
- [55] K. P. Sokol, W. E. Robinson, A. R. Oliveira, J. Warnan, M. M. Nowaczyk, A. Ruff, I. A. C. Pereira, E. Reisner, *J Am Chem Soc* **2018**, *140*, 16418–16422.
- [56] H. Zhu, Y. Li, *Green Carbon* **2023**, *1*, 14–19.
- [57] L. Darus, P. Ledezma, J. Keller, S. Freguia, *Photosynth Res* **2016**, *127*, 347–354.
- [58] J. M. Pisciotta, Y. Zou, I. V. Baskakov, *Appl Microbiol Biotechnol* **2011**, *91*, 377–385.



- [59] J. Hatano, S. Kusama, K. Tanaka, A. Kohara, C. Miyake, S. Nakanishi, G. Shimakawa, *Photosynth Res* **2022**, *153*, 113–120.
- [60] Y. Shlosberg, B. Eichenbaum, T. N. Tóth, G. Levin, V. Liveanu, G. Schuster, N. Adir, *iScience* **2021**, *24*, 101892.
- [61] A. Antonucci, M. Reggente, C. Roullier, A. J. Gillen, N. Schuergers, V. Zubkovs, B. P. Lambert, M. Mouhib, E. Carata, L. Dini, A. A. Boghossian, *Nat Nanotechnol* **2022**, *17*, 1111–1119.
- [62] H. C. Büchsenschütz, V. Vidimce-Risteski, B. Eggbauer, S. Schmidt, C. K. Winkler, J. H. Schrittwieser, W. Kroutil, R. Kourist, *ChemCatChem* **2020**, *12*, 726–730.
- [63] L. Assil-Companiononi, H. C. Büchsenschütz, D. Solymosi, N. G. Dyczmons-Nowaczyk, K. K. F. Bauer, S. Wallner, P. Macheroux, Y. Allahverdiyeva, M. M. Nowaczyk, R. Kourist, *ACS Catal* **2020**, *10*, 11864–11877.
- [64] H. C. Grimm, R. Kourist, in *Photosynthesis*, De Gruyter, **2021**, pp. 57–92.
- [65] F. Mascia, S. B. Pereira, C. C. Pacheco, P. Oliveira, J. Solarczek, A. Schallmey, R. Kourist, V. Alphand, P. Tamagnini, *Green Chemistry* **2022**, *24*, 6156–6167.
- [66] A. Torrado, H. M. Connabeer, A. Röttig, N. Pratt, A. J. Baylay, M. J. Terry, C. M. Moore, T. S. Bibby, *Plant Physiol* **2022**, *189*, 2554–2566.
- [67] D. J. Lea-Smith, N. Ross, M. Zori, D. S. Bendall, J. S. Dennis, S. A. Scott, A. G. Smith, C. J. Howe, *Plant Physiol* **2013**, *162*, 484–495.
- [68] M. Ermakova, T. Huokko, P. Richaud, L. Bersanini, C. J. Howe, D. J. Lea-Smith, G. Peltier, Y. Allahverdiyeva, *Plant Physiol* **2016**, *171*, 1307–1319.
- [69] H. Liu, D. A. Weisz, M. M. Zhang, M. Cheng, B. Zhang, H. Zhang, G. S. Gerstenecker, H. B. Pakrasi, M. L. Gross, R. E. Blankenship, *mBio* **2019**, *10*, 1–12.
- [70] M. Iwai, K. Takizawa, R. Tokutsu, A. Okamuro, Y. Takahashi, J. Minagawa, *Nature* **2010**, *464*, 1210–1213.
- [71] H. Fulgosi, L. Vojta, *Front Plant Sci* **2020**, *11*, 318.
- [72] D. Kannchen, J. Zabret, R. Oworah-Nkruma, N. Dyczmons-Nowaczyk, K. Wiegand, P. Löbbert, A. Frank, M. M. Nowaczyk, S. Rexroth, M. Rögner, *Biochimica et Biophysica Acta Bioenerg* **2020**, *1861*, 148208.
- [73] H. Medipally, M. M. Nowaczyk, M. Rögner, *Photosynthesis: Biotechnological Applications with Microalgae* **2021**, 13–42.
- [74] L. M. Lassen, A. Z. Nielsen, C. E. Olsen, W. Bialek, K. Jensen, B. L. Møller, P. E. Jensen, *PLoS One* **2014**, *9*, e102184.
- [75] I. Yacoby, S. Pochekailov, H. Toporik, M. L. Ghirardi, P. W. King, S. Zhang, *Proc Natl Acad Sci U S A* **2011**, *108*, 9396–9401.
- [76] A. Kanygin, Y. Milrad, C. Thummala, K. Reifschneider, P. Baker, P. Marco, I. Yacoby, K. E. Redding, *Energy Environ Sci* **2020**, *13*, 2903–2914.

## **Publications**

## Published research articles

**Hitesh Medipally\***, Marc M. Nowaczyk, Matthias Rögner (2021) Parameters of photosynthesis relevant for a biotechnological application (chapter 1). Photosynthesis: Biotechnological Applications with Microalgae, **De Gruyter**, 2021, 1-30 (**Publication 1**).

**Hitesh Medipally\***, Alice Guarneri, Lars Pospisil, Maurice C. R. Franssen, Willem J. H. van Berkel, Caroline E. Paul, Marc M. Nowaczyk (2023a) Light-driven NADPH cofactor recycling by photosystem I for biocatalytic reactions. **ChemCatChem**, e202300821, 1-7 (**Publication 2**).

**Hitesh Medipally\***, Marvin Mann, Carsten Kötting, Willem J. H. van Berkel, Marc M. Nowaczyk (2023b) A clickable photosystem I, ferredoxin, and ferredoxin NADP<sup>+</sup> reductase fusion system for light-driven NADPH regeneration. **ChemBioChem**, 24, e202300025, 1-10 (**Publication 3**).

Tomi K. Baikie\*, Laura T. Wey\*, Joshua M. Lawrence, **Hitesh Medipally**, Erwin Reisner, Marc M. Nowaczyk, Richard H. Friend, Christopher J. Howe, Christoph Schnedermann, Akshay Rao, Jenny Z. Zhang (2023). Photosynthesis re-wired on the pico-second timescale. **Nature**, 615, 836-840 (**Publication 4**).

Tomi K. Baikie, Darius Kosmützky, Joshua M. Lawrence, Victor Gray, Christoph Schnedermann, Robin Horton, Joel D. Collins, **Hitesh Medipally**, Bartosz Witek, Marc M. Nowaczyk, Jenny Zhang, Laura Wey, Christopher J. Howe, Akshay Rao (2023). Ultrafast In vivo Transient Absorption Spectroscopy. <https://doi.org/10.48550/arXiv.2307.09448> (**Publication 5**).

## Conference contributions

**Hitesh Medipally**, Marc M. Nowaczyk (2021): Redox-engineered photosystems and tailored made electron transfer pathway for in vitro photobiocatalysis. **French Photosynthesis Conference**, online (contribution: Poster).

**Hitesh Medipally**, Marc M. Nowaczyk (2021): Redox-engineered photosystems and tailored made electron transfer pathway for in vitro photobiocatalysis. **Perspectives of Bioenergetics Conference**, online (contribution: Poster).

**Hitesh Medipally**, Marc M. Nowaczyk (2022): Redox-engineered photosystems and tailored made electron transfer pathway for in vitro photobiocatalysis. **3<sup>rd</sup> Aachen Protein Engineering Symposium**, online (contribution: Poster).

## Contribution to the publications

**Hitesh Medipally\***, Marc M. Nowaczyk, Matthias Rögner (2021) Parameters of photosynthesis relevant for a biotechnological application. *Photosynthesis: Biotechnological Applications with Microalgae*, **De Gruyter**, 2021, 1-30. (**Publication 1**).

**Planning: 20%**

**Manuscript: 20%**

**Hitesh Medipally\***, Alice Guarneri, Lars Pospisil, Maurice C. R. Franssen, Willem J. H. van Berkel, Caroline E. Paul, Marc M. Nowaczyk (2023). Light-driven NADPH cofactor recycling by photosystem I for biocatalytic reactions. **ChemCatChem**, e202300821, 1-7 (**Publication 2**).

**Planning: 80%**

**Experimental contributions: 90%**

**Manuscript: 50%**

**Hitesh Medipally\***, Marvin Mann, Carsten Kötting, Willem J. H. van Berkel, Marc M. Nowaczyk (2023) A clickable photosystem I, ferredoxin, and ferredoxin NADP<sup>+</sup> reductase fusion system for light-driven NADPH regeneration. **ChemBioChem**, 24, e202300025, 1-10 (**Publication 3**).

**Planning: 70%**

**Experimental contributions: 90%**

**Manuscript: 50%**

Tomi K. Baikie\*, Laura T. Wey\*, Joshua M. Lawrence, **Hitesh Medipally**, Erwin Reisner, Marc M. Nowaczyk, Richard H. Friend, Christopher J. Howe, Christoph Schnedermann, Akshay Rao, Jenny Z. Zhang (2023). Photosynthesis re-wired on the pico-second timescale. **Nature**, 615, 836-840 (**Publication 4**).

**Planning: 0%**

### **Experimental contributions: 10%**

Purification of PSI trimers from *T. vestitus* BP1

Purification of PSII dimer from *T. vestitus* BP1

Biochemical and physiological characterization of PSI and PSII

### **Manuscript: 0%**

Tomi K. Baikie, Darius Kosmützky, Joshua M. Lawrence, Victor Gray, Christoph Schnedermann, Robin Horton, Joel D. Collins, **Hitesh Medipally**, Bartosz Witek, Marc M. Nowaczyk, Jenny Zhang, Laura Wey, Christopher J. Howe, Akshay Rao (2023). Ultrafast In vivo Transient Absorption Spectroscopy. <https://doi.org/10.48550/arXiv.2307.09448> (**Publication 5**).

### **Planning: 0%**

### **Experimental contributions: 10%**

Purification of PSI trimers from *T. vestitus* BP1

Purification of PSII dimer from *T. vestitus* BP1

Biochemical and physiological characterization of PSI and PSII

### **Manuscript: 0%**

### **Specifications on used illustrations**

Apart from the published data, all the graphs were made by Hitesh Medipally unless otherwise mentioned.

# Appendix



## Acknowledgements

I endlessly thank my supervisor **Prof. Dr. Marc Nowaczyk**, and all the members of our research group, "Molecular Mechanisms of Photosynthesis" at Ruhr University Bochum. Without them, this study would have not been possible. The helpful and shared nature of this group has encouraged me to learn and discuss science in a peaceful environment. I would also like to express my gratitude to **Assist. Prof. Dr. Caroline Paul** from Delft University of Technology, for assisting with the project progress and supplying enzymes. I also thank **Prof. Dr. Willem J H van Berkel** from Wageningen University for taking the responsibility as a second supervisor and thoroughly correcting the manuscripts and thesis. I also thank **Assoc. Prof. Dr. Maurice Franssen** and **Dr. Alice Guarneri** for supporting me to work at Wageningen University, and **Prof. Dr. Robert Kourist** from Technical University Graz for offering a job right after my graduate funding program and allowing me to focus on writing my thesis.

With immense gratitude, I thank **Prof. Dr. Rajagopal Subramaniam** from the University of Hyderabad for encouraging me to pursue a Ph.D. in Germany. He is the most generous person I have ever met. I thank him for all the encouragement and support during my Master of Sciences in India and recommending to work with **Prof. Dr. Marc Nowaczyk**.

My mother **M. Devendramma** is a crucial part of my life. Her unconditional love and dedication for raising me despite several socio-economic and mental challenges have inspired me. I would never substitute here love with anything. I thank my maternal grandparents, **B. Satyamma** and **B. Ram Reddy**, for continuous financial support and love in my upbringing. Without them, I would have never pursued my education. I have learned an important lesson from them: "*No matter what, be happy and continue forward.*"

I also thank my family members, **B. Saraswathi & Anand Reddy**, **Dr. B. Bhupathi Reddy**, **B. Samarasimha Reddy** for their support in my formative years. Here, I would like to emphasize the importance of my uncle **Dr. B. Bhupathi Reddy**. He greatly influenced me while growing up. The care and support I received from him, both in my personal life and in academics, are inexplicable.

I thank my sisters, **M. Sri Laxmi** and **M. Sri Priya**, for their support in my difficulty and happiness. I have unknown bondage with them. I appreciate their moral support and advice in making crucial decisions.

I specially thank **Dr. Tsvetan Tarnev (Swethan)** and **Dr. Arun Rachamalla** for being with me and encouraging me all the time.

Finally, I thank the PhotoBioCat research group, the MiCon research group, Ruhr University Bochum, Wageningen University and Research, and the Marie Skłodowska-Curie Actions-European Union Horizon 2020 MSCA ITN-EJD program under grant agreement number 764920 for funding and administrative help.

Hitesh Medipally

Curriculum vitae

# Hitesh Medipally

## Personal details

---

Date of birth: 16-06-1995

Spoken Languages: English/Hindi/Telugu

E-Mail: hitesh.medipally@rub.de

LinkedIn: <https://www.linkedin.com/in/hitesh-medipally-391a29136/>

## Working Experience and Achievements

---

**10/2018-Present      Ph.D. student (MSCA-ITN-JD program)**

*Ruhr University Bochum, Bochum, Germany*

**Ph.D. thesis:** Redox Engineered Photosystems and Tailored Electron Pathways for in-vitro Biocatalysis.

**10/2020-03/2021      Research intern at the Laboratory of Organic Chemistry,**

*Wageningen University and Research, Wageningen, Netherlands*

**Project title:** Exploring the Potential of Photosystem I as a Photocatalyst.

## Education

---

**07/2016-06/2018      M.Sc. in Plant Biology and Biotechnology**

*University of Hyderabad, Hyderabad, Telangana, India*

**Master thesis:** Studies on Photosynthesis in Protoplasts and Leaf discs of Pea.

**06/2013-05/2016      B.Sc. in Botany/Zoology/Chemistry**

*Osmania University College of Science Saifabad, Hyderabad, Telangana, India.*

Curriculum vitae

# Hitesh Medipally

## Achievement

---

- Secured 1<sup>st</sup> rank in national M.Sc. entrance examination for Plant Biology and Biotechnology conducted by University of Hyderabad.
- Secured 2<sup>nd</sup> rank in national M.Sc. entrance examination for Molecular Microbiology conducted by University of Hyderabad.
- Best Poster Prize for “The Chlorophylls Friend or Foe”.
- 1<sup>st</sup> prize for best essay on Life history of Sri Raja Bahadur Venkata Rama Reddy.

## Skills

---

- Molecular Biology (cloning, PCR, Primer design)
- FPLC for Protein Purification
- Gas Chromatography
- Microbiology (Cyanobacteria, *E. coli* culture handling, biotransformations)
- Dual-PAM (measuring Photosynthetic Parameters)
- Enzyme Kinetics
- Basic use of Bioinformatic tools

## Declaration

---

I hereby declare that all the information stated above is true. I take full responsibility for the factuality of documents and contents provided.

Hitesh Kumar Reddy Medipally

## Erklärung

ERKLÄRUNG Ich versichere, dass ich die eingereichte Dissertation selbstständig und ohne unzulässige fremde Hilfe verfasst, andere als die in ihr angegebene Literatur nicht benutzt und dass ich alle ganz oder annähernd übernommenen Textstellen sowie verwendete Grafiken und Tabellen kenntlich gemacht habe. Weiterhin erkläre ich, dass digitale Abbildungen nur die originalen Daten enthalten oder eine eindeutige Dokumentation von Art und Umfang der inhaltsverändernden Bildbearbeitung vorliegt. Außerdem versichere ich, dass es sich bei der von mir vorgelegten Dissertation (elektronische und gedruckte Version) um völlig übereinstimmende Exemplare handelt und die Dissertation in dieser oder ähnlicher Form noch nicht anderweitig als Promotionsleistung vorgelegt und bewertet wurde.

Es wurden keine anderen als die angegebenen Hilfsmittel verwendet.

Die Dissertation wurde gemäß der Promotionsordnung und der Betreuungsvereinbarung angefertigt.

Bochum, den

---

(Unterschrift)